Fe isotopes of a ca 2.4 Ga hematite-rich IF confirm oxygenation of the Transvaal basin in relation to the GOE

Margriet Lantink

Utrecht, May 2016

Abstract

The precise nature of ocean redox conditions is among the most uncertain aspects of the early Earth's surface zone. It is generally thought that Earth's atmosphere was anoxic until after ca 2.4 Ga, the Great Oxygenation Event (GOE), but there is less agreement about the timing and extent of the oxygenation of the oceans. Chemical sediments such as (banded) iron formations ((B)IFs) may allow us to reconstruct the evolution of the Precambrian oceans, since they bear information on the redox state and chemical composition of the ambient seawater. The widespread deposition of IF prior to and around the GOE suggests a genetic link with the rise of atmospheric oxygen: they might directly record the oxidation of aqueous Fe(II) in near-surface environments. However, large quantities of Fe could also have accumulated due to an increased influx of hydrothermal Fe(II) into the oceans. Tsikos et al. (2010) reported very depleted bulk-rock Fe isotope values (δ^{56}Fe of -1.6 ‰ down to -2.4 ‰) in the hematite- and Mn-rich samples of the ca 2.4 Ga Hotazel IF (Transvaal basin, South Africa), ascribing these data to deposition of Fe in a terminal, stratified basin that was depleted in heavy Fe isotopes due to earlier precipitation, evolved via Rayleigh fractionation. Here I present results from a unique drill-core (ca 3m) comprising the lowermost part of the Hotazel Fm. and its contact with the Ongeluk Fm. lava at the base. Overall textures, mineralogy and geochemistry of this hematite-rich rock suggest that in the lower part of the Hotazel ferric oxyhydroxides (hematite precursors) precipitated from seawater with a significant contribution of hydrothermal fluids directly sourced from the Ongeluk lava, whereas in the upper part of the drill-core precipitation took place from more open-marine seawater without a direct hydrothermal component. δ^{56}Fe values increasing from -0.50 ‰ for the hematite samples closest to the hydrothermally-altered Ongeluk lava (δ^{56}Fe of -0.7 ‰) to -0.26 ‰ for the uppermost hematite BIF part of the drill-core equally support this. Stratigraphically lower in the Transvaal Supergroup (Kuruman and Griquatown BIFs) near-zero to positive δ^{56}Fe have been reported for hematite (Johnson et al., 2003). The δ^{56}Fe of -0.26 of the most primary, seawater representative hematite BIF sample at the top of the drill-core may therefore represent the first position in the stratigraphy of the Transvaal basin where the isotopic signature becomes depleted and confirms the postulated link with a significant rise in the oxygen concentration of the basin. Moreover, the uniquely depleted δ^{56}Fe signal of the Ongeluk lava hydrothermal fluids (δ^{56}Fe of ≤ -0.7 ‰) illustrates the effect of progressive fluid-rock interactions under largely aerobic conditions in the shallowest parts of the Transvaal basin.

1. Introduction

Unravelling the oceanic redox conditions in the past has long been an important topic of paleoenvironmental research, since it is crucial for our understanding of the relationship between ocean chemistry and the evolution of the biosphere. Anoxic conditions likely prevailed in the deep oceans during most of the Earth's history, yet the precise nature and evolution of the ocean redox state is still unclear. There is widespread evidence in the rock record for a permanent rise in atmospheric O_2 levels between 2.45 Ga and 2.22 Ga, termed the Great Oxygenation Event (GOE); prior to the GOE O_2 did not constitute a significant portion (Holland, 1984; 1999; 2006; Farquhar et al., 2000; Bekker et al., 2004), although some authors argue that the atmosphere was oxic since ca 3.8 Ga (Ohmoto et al., 2006). Strong evidence is provided by the loss of mass independent fractionation of sulphur isotopes (MIF-S) at ca 2.32 Ga (Farquhar et al., 2000; Bekker et al., 2004), marking the time when O_2 started to accumulate in noticeable concentrations in the atmosphere, i.e. $pO_2 > 10^{-5}$ present atmospheric levels (21 vol. %). In contrast, there is far less agreement about the timing and extent of the oxygenation of the oceans.

The rise of atmospheric oxygen during the GOE should have similarly triggered oxygenation of the oceans. However, the widespread deposition of Fe-bearing chemical sediments such as banded iron formations (BIF) both before and after the GOE, until about 1.8 Ga, suggests that the oceans remained anoxic for a long time onwards (e.g. Bekker et al., 2010). Because Fe^{3+} is virtually insoluble at circumneutral pH (e.g. Kuma et al., 1996 and references therein), the large-scale BIF deposition obviously required the transport of Fe^{2+} through an anoxic water column, indicating that at least episodically the oceans were predominantly ferruginous (e.g. Planavsky et al., 2011; Poulton and Canfield, 2011; Reinhard et al., 2013). The majority of this Fe^{2+} is generally considered to have originated from hydrothermal systems (e.g. Derry and Jacobsen; Isley, 1995, Bau et al., 1997 and Krapež et al., 2003). The disappearance of BIFs after ca 1.8 Ga was initially ascribed to a transition towards more aerobic seawaters (Holland et al., 1984), although currently most scientists favour the idea of a euxinic ocean, i.e. anoxic and sulphidic (Canfield, 1998; Anbar et al., 2002; Shen et al., 2003; Arnold et al., 2004; Poulton et al., 2004). Accordingly, anoxic oceanic conditions prolonged until after a second rise in atmospheric O_2 at about 600 Ma, which was sufficiently powerful to oxygenate much of the deep oceans (Canfield, 1998; Scott et al., 2008; Sahoo et al., 2012; Lyons et al., 2014). See Figure 1.

Nevertheless, the exact behaviour of the global oceans around the GOE remains enigmatic. Because oxygenic photosynthesis is the only significant process responsible for the production of free O_2 in the Earth's near-surface environment, the atmospheric O_2 generated associated with the GOE most likely originated from marine eukaryotes (e.g. Buick, 2008; Campbell and Allen, 2008; Lyons et al., 2014), although a volcanic cause has also been proposed (Kasting et al., 1993; Holland, 2002). The peak in the worldwide deposition of iron formations (IF) prior to and around the GOE suggests that these sediments were inherently linked to the rise in photosynthetically-produced O_2 and precipitated *en masse* from oxidation of the large oceanic Fe^{2+} reservoir (see Figure 2). In particular the presence of hematite (i.e. $Fe^{3+}{}_2O_3$) has been used to argue for an O_2-bearing water column (e.g. James, 1954; Morris, 1993; Beukes and Gutzmer, 2008; Hoashi et al., 2009; Smith et al., 2013), either formed via inorganic oxidation of Fe(II) or aided by microaerophilic Fe(II) oxidisers (as summarized in Bekker et al., 2010; Konhauser et al., 2011). However, this

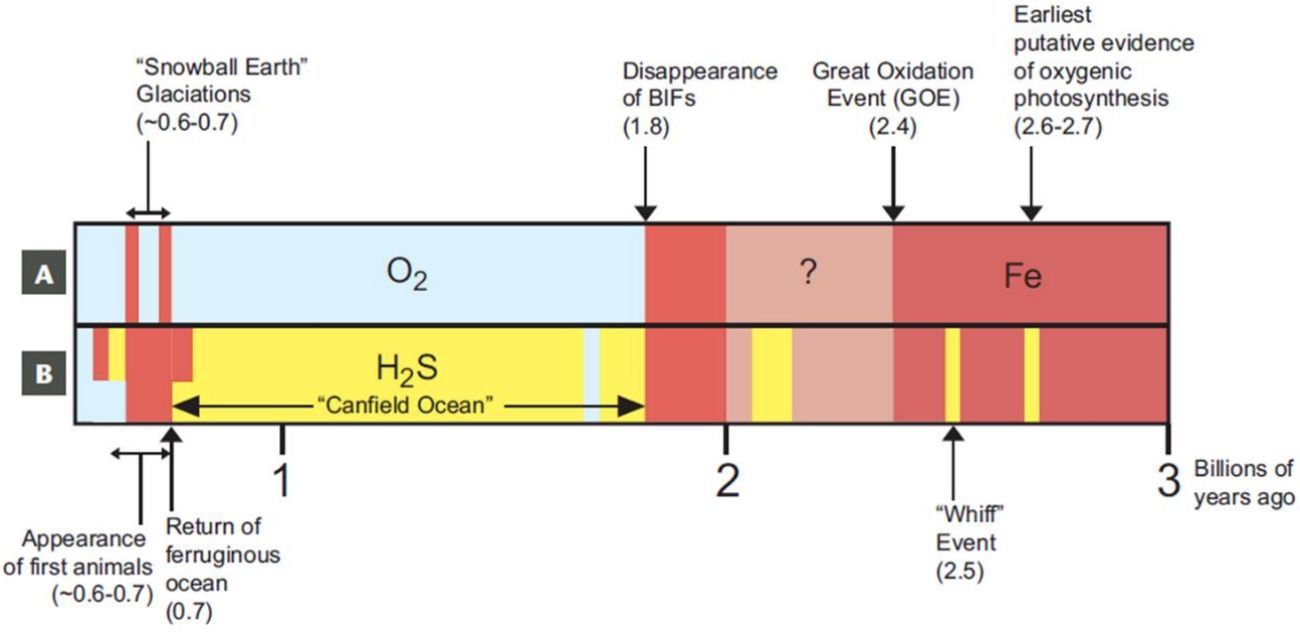

Figure 1: Schematic timeline of the Earth's deep ocean redox conditions since the past 3 Gyr, according to the model of **A)** Holland (2006) and **B)** Canfield (1998). Red, yellow and blue colours indicate ferruginous, euxinic and (sub)oxic conditions, respectively. From: Lyons and Gill (2010).

interpretation was challenged by the discovery of anaerobic photosynthetic bacteria (e.g. Widdel et al., 1993). These microbes are equally capable of oxidising Fe(II) and thus the presence of hematite in IF proves to be inconclusive for the availability of free O_2 (e.g. Kappler et al., 2005; Czaja et al., 2012; Li et al., 2013). In this view, the widespread deposition of iron formations prior to and around the timing of the GOE may instead predominantly reflect a genetic link with enhanced magmatism rather than with the global rise in O_2 levels (see Figure 2).

Stunning evidence for the emergence of oxygenic photosynthesis well before the GOE has shed new light on the IF depositional model. Molecular biomarkers (Brocks et al., 1999; 2003; Brasier et al., 2006; Eigenbrode and Freeman, 2006; Summons et al., 2006; Buick, 2008; Eigenbrode et al., 2008; Waldbauer et al., 2009) as well as inorganic data (Anbar et al., 2007) point to an at least ca 300 Myr earlier start of O_2-producing photosynthesis than the actual rise of atmospheric O_2 at ca 2.4 Ga. This allowed for the idea that global O_2 levels did not increase in a strictly step-wise fashion, but instead occurred as short pulses of small increases in the O_2 concentration well before the onset of the GOE (Anbar et al., 2007; Crowe et al., 2013). Because oxygenic photosynthesis is restricted to the photic zone, the accumulation of O_2 before the GOE must have been limited to the shallow parts of the oceans, creating local *oxygen oases* (e.g. Kasting, 1993; Olsen et al., 2013). This provides an elegant explanation for the rather paradoxical origin of IF, i.e. that they may reflect oxidation and precipitation of Fe(II) and Fe(III), respectively, in the near-surface environments of the anoxic oceans of the Archean.

Contrary studies, however, disagree with the existence of oxygenic photosynthesis before the GOE, arguing that the proposed biomarker evidence does not require the presence of O_2; others suggest that later contamination blurred the primary biomarker signal (Kirschvink and Kopp, 2008; Rasmussen et al., 2008; Brocks et al., 2011). Moreover, the partially constrained ca 300 Myr earlier appearance of O_2-producing marine eukaryotes (compared to the timing of the GOE) raises the question why oceanic and atmospheric O_2 levels did not increase much earlier in the Earth's history. The answer presumably lies in the balance between O_2 sources and sinks. Possibly prior to the GOE most of the produced O_2 was readily consumed by the large reducing potential of the Earth's ancient oceans; for some unknown reason this balance shifted at ca 2.4 Ga and the conditions allowed

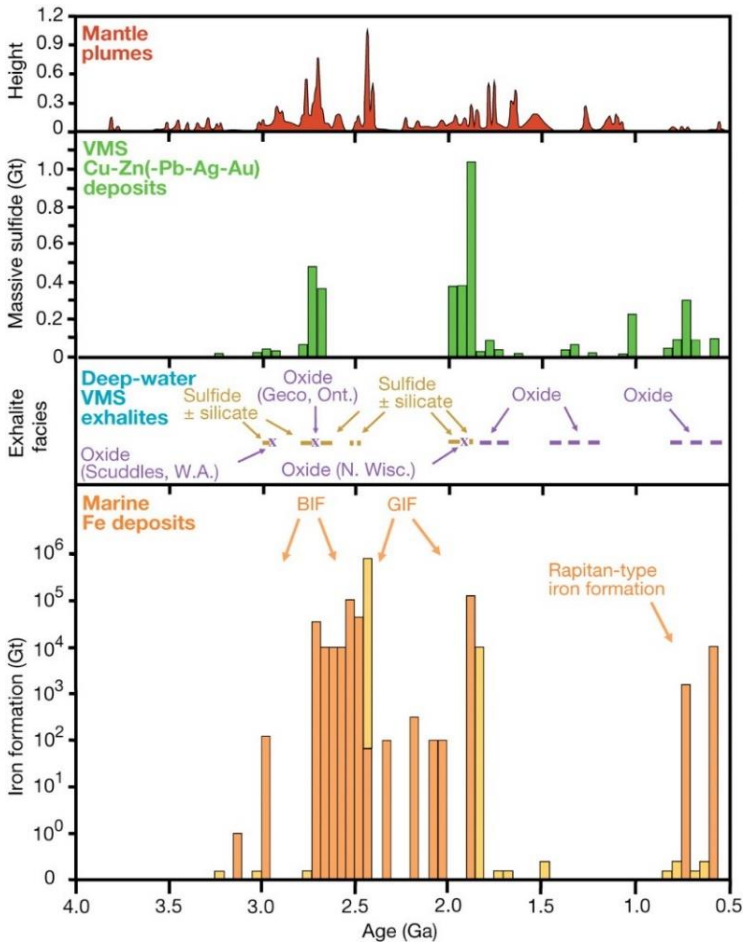

Figure 2: Summary of the global pattern of mantle superplume breakout events compared to trends in selected marine mineral deposits. From: Bekker et al. (2010).

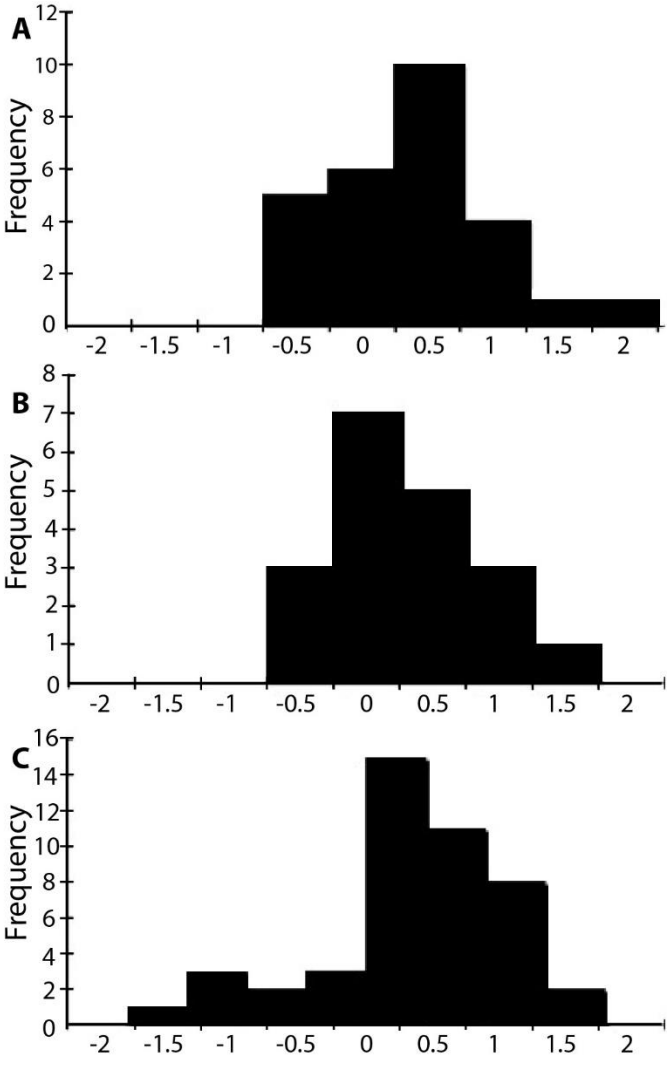

Figure 3: Distribution of bulk-rock $\delta^{56}Fe$ values for IFs of **A)** Meso-, Neoproterozoic and Phanerozoic age (0.1 ‰ average), **B)** 2.32 to 1.88 Ga (0.0 ‰ average) and **C)** 3.0 to 2.4 Ga (0.4 ‰ average). From: Planavsky et al. (2012).

for permanent accumulation of O_2 in the atmosphere. Several models have sought for an explanation lying in the composition of the atmosphere, in which changes in the volcanic input entail changes in the O_2 concentration (Claire et al., 2006; Zahnle et al., 2006; Kump and Barley, 2007; Gaillard et al., 2011). However, the role of the oceans at the timing of the GOE remains up to this point highly ambiguous, because geological evidence for oxygen oases and redox-stratification of the oceans has been difficult to find.

The recent advances in high-precision stable metal isotope ratio determinations have provided a great opportunity for the use of Fe isotopes in tracking natural redox cycling and hence as a key redox proxy for the evolution of O_2 in the oceans (e.g. Beard et al., 1999; 2003; Anbar et al., 2000; Zhu et al., 2000; Bullen et al., 2001; Sharma et al., 2001; Skulan et al., 2002; Welch et al., 2003; Johnson et al., 2002; 2005; Rouxel et al., 2003; 2005; Severmann et al., 2004). These studies have shown that many of the processes in nature involving Fe, such as redox reactions, mineral precipitations and metabolic processes, are capable of significant Fe isotope fractionation. Therefore, Fe isotopes are particularly useful for tracing abiogenic as well as biogenic Fe(II) oxidation and Fe(III) reduction in IF (e.g. Johnson et al., 2008a; 2008b).

The occurrence of positive Fe isotope compositions, i.e. enriched in the heavy ^{56}Fe isotope relative to the lighter ^{54}Fe and expressed as $\delta^{56}Fe$, in early Archean BIFs and Fe-rich cherts has been interpreted to reflect partial oxidation of an aqueous Fe(II) reservoir that had very low O_2 concentrations (Dauphas et al., 2004; Czaja et al., 2013; Li et al., 2013). The fact is that oxidation of dissolved Fe(II) produces (under equilibrium fractionation) $\delta^{56}Fe$ values for the Fe(III) (oxy)hydroxide product that are ca 1 ‰ higher (Polyakov and Mineev, 2000; Bullen et al., 2001; Croal et al., 2004; Beard and Johnson, 2004; Balci et al., 2006; Beard et al., 2010). Because the hydrothermal flux of dissolved Fe(II) to the Archean oceans must have had an average $\delta^{56}Fe$ of ca 0 ‰ (Yamaguchi et al., 2005), similar to that of the bulk crust (Beard et al., 2003; Poitrassen, 2004; Schoenberg et al., 2009; Craddock et al, 2013; Teng et al., 2013), the positive $\delta^{56}Fe$ values found in bulk-rock Archean IFs are thus associated with partial Fe(II) oxidation under generally reducing conditions. This is in contrast to the whole-rock $\delta^{56}Fe$ values from Fe-rich chemical sediments deposited in the later Proterozoic and Phanerozoic, i.e. after the GOE, which are overall tightly clustered around the 0 ‰ (Planavsky et al., 2012) reflecting essentially quantitative oxidation of the dissolved Fe(II) pool: if the fraction of oxidised Fe is large, the precipitate will obtain a $\delta^{56}Fe$ close to that of the source fluid (Beard et al., 2003; Rouxel et al., 2003; Anbar et al., 2005; Markl et al., 2006). See Figure 3.

Considering that the Archean and early Paleoproterozoic IFs apparently were a sink for high $\delta^{56}Fe$ compositions, there must be a corresponding reservoir for isotopically light Fe in the rock record. Previous authors have claimed that the consistently low $\delta^{56}Fe$ values in Archean pyritic shales appear to be this sink, embodying the residual isotopically light Fe(II) pool in the shallow parts of the ocean (Rouxel et al., 2005; Yamaguchi et al., 2005; Planavsky et al., 2012). However, and important problem with respect to the interpretation of these whole-rock Fe isotope studies is that they are often obscured by biogeochemical cycling during early sediment diagenesis (e.g. Yamaguchi et al., 2005; Johnson et al., 2008a; 2008b). The large variation of Fe isotope values, particularly very negative values, has accordingly been explained to be the result of dissimilatory iron reduction (DIR) (Johnson et al., 2008a; 2008b).

In 2010, Tsikos and associates brought alluring proof for an alternative fate of the ocean's isotopically depleted Fe(II) reservoir. Very depleted bulk-rock Fe isotope values were found in the hematite- and Mn-rich layers of the ca 2.4 Ga Hotazel Formation (Transvaal basin, South Africa) with $\delta^{57}Fe$ values down to -3.5 ‰, which is equivalent to a $\delta^{56}Fe$ of -2.4 ‰ (using the theoretical mass-dependent fractionation relationship $\delta^{57}Fe = 0.68 * \delta^{56}Fe$). In view of the enriched Fe isotope values of the hematite-rich samples from the Mn-poor Kuruman and Griquatown Fm. lower down in the stratigraphy of the Transvaal basin (Johnson et al., 2003), the depleted Fe isotopic signal of the Hotazel Fm. may therefore represent a Rayleigh fractionation process, in which the protracted oxidation of Fe(II) from the Transvaal basin and subsequent raining out of the heavy Fe isotopes eventually resulted in an isotopically depleted residual Fe(II) pool. These Fe isotopic characteristics may therefore constitute a potential link with the rise in atmospheric oxygen at the GOE. Moreover, since Mn(II) is after Fe(II) the next candidate on the redox ladder, the uniquely voluminous sedimentary Mn deposits in the Hotazel Fm. (Laznicka, 1992) are in conformity with an increasingly oxygenated, terminal depositional basin that had very high Mn-Fe ratios due to almost complete removal of aqueous Fe(II).

In a sense the proposed Rayleigh fractionation model for the Hotazel is analogous to the model of Rouxel et al. (2005), albeit on a spatially and temporally more restricted scale, but potentially tracks, regarding its supposed ca 2.4 Ga age (Bau et al., 1999; Gumsley et al., 2015) a crucial point in time: the Hotazel may have tracked one of the terminal Paleoproterozoic marine sinks for photosynthetic O_2 and actually have *caused* the onset of the GOE at ca 2.4 Ga (Tsikos et al., 2010). Earlier paleodepositional models placed the Hotazel Fm. in an oxygenated post-GOE world, proposing that the unique Mn(IV) deposits were directly sourced from hydrothermal exhalations of the Ongeluk lava, which lies stratigraphically beneath the Hotazel Fm (Cornell et al., 1996; Cornell and Schütte, 1995; Kirschvink et al., 2000; Kopp et al., 2005; Kirschvink and Kopp, 2008). Further detailed research is therefore required to check the validity of the proposed Rayleigh fractionation model.

This finally leads me to the reasons for carrying out this research project. Subject of this study is a roughly three-metre-thick drill-core that uniquely exposes the lowermost part of the Hotazel Fm. and its contact with the Ongeluk Fm. at the base. Because nobody has had access to this particular part of the stratigraphy before, or at least such unweathered, freshly exposed rocks, the Fe isotopic content of the *hematite* in this lowermost part of the Hotazel Fm. might have important constraints on the interpretation higher up in the stratigraphy. I want to find out whether the δ^{56}Fe signature of the hematite agrees with the Rayleigh distillation model of the Transvaal basin, and consequently agrees with the large-scale oxygenation of the Transvaal basin, or whether it indicates a predominantly volcanic exhalative origin of the Hotazel chemical sediments.

In order to answer these questions, I will measure the Fe isotope values of several (microdrilled) hematite samples distributed over the drill-core, together with some bulk-rock samples of the Ongeluk lava. Obtaining a purely hematitic δ^{56}Fe signature is desired, because contamination with other Fe-bearing minerals will complicate calculating back the initial seawater δ^{56}Fe composition: these minerals have different fractionation effects with respect to δ^{56}Fe (e.g. Schauble, 2004; Anbar and Rouxel, 2007). Upon the Fe isotope measurements, I will perform a detailed rock characterisation. A key issue that is often ignored in the analysis of redox proxies is that the primary hydrogenous signal may be easily obscured due to detrital input or overprinted by post-depositional mobilisation processes such as metamorphism and, in such vicinity to the Ongeluk lava in this case not unlikely, hydrothermal alteration. Therefore, I will examine the textures, mineralogy and geochemistry of Ongeluk and Hotazel rocks, with the aim to get insight into the following aspects:

1. What is the temporal and causal relationship between the formation of the Ongeluk lava and the deposition of the Hotazel sediments? Do my observations agree with the inferred subaqueous extrusion of the Ongeluk lava and its subsequent major hydrothermal alteration (Schütte, 1992; Cornell et al., 1996; Cornell and Schütte, 1995)?

2. Which parts of the Hotazel are composed of in situ formed sediments, and which parts are of detrital origin?

3. Which minerals are primary, and most importantly, is the hematite primary? That is, does the Fe incorporated in the hematite crystal lattice directly reflect initial oxidation of Fe(II) in the water column? “Dusty” hematite, i.e. minute inclusions of hematite within a chert matrix, has commonly been assumed to have formed via dehydration of ferric oxyhydroxides that precipitated from aqueous Fe(II) (Ayres, 1972; Ahn and Buseck, 1990; Beukes and Gutzmer, 2008; Smith et al., 2013). I want to check whether the hematite I use for Fe isotope analysis is also primary.

4. What is the nature of the source fluids from which the hematite was formed, i.e. is the Fe(II) predominantly derived from hydrothermal fluids of the Ongeluk lava, or does is reflect a more ambient seawater origin? Rare-earth elements (REE) form a particularly useful tool for tracing back the origin of the Fe in the Precambrian, allowing for comparison with modern analogues in which their behaviour is well studied (e.g. Bau and Dulski., 1996; Bau et al., 1997; Bolhar et al., 2004; Planavsky et al., 2010).

5. And finally, what is the primary δ^{56}Fe signature of the seawater, and what does this imply in respect of the redox state of the Transvaal basin? What other proxies, e.g. the rock’s Mn concentration, provide clues about the O_2 concentration of the water column upon formation of the Hotazel?

2. Geological setting

The drill-core originates from the Gloria Mine (borehole locality 36) in the Kalahari Manganese Field, situated 80 km west of Kuruman, Northern Cape Province, South Africa (see Figure 4). At the stratigraphic depth interval of interest, i.e. between 291.00 m and 294.14 m, it exposes the contact (at 293.79 m) between the Ongeluk Fm. and overlying Hotazel Fm. These units form together with the Kuruman and Griquatown BIFs part of the late Archean to early Proterozoic Transvaal Supergroup, a supracrustal sequence of the South-African Kaapvaal craton. Paleogeographic and lithostratigraphic reconstructions show that these IFs were deposited in a partly enclosed basin, the so-called Transvaal basin (e.g. Beukes, 1983), at the margins of the ancient supercontinent of Vaalbara (Button, 1976; Cheney, 1996; de Kock et al., 2009). The similarities in age, size and character of the IFs from the Transvaal basin with those of the Hamersley basin of the Australian Pilbara craton (e.g. Trendall, 1983) suggest that the two IF succession are broadly correlative, representing a combined Transvaal-Hamersley basin (Button, 1976; Cheney, 1996). The Transvaal Supergroup successions are laterally extending over hundreds of kilometres, covering the Kaapvaal craton from the Griqualand West sequence in the SW to the Transvaal-Bushveld basin in the NE (Beukes 1983; Eriksson et al. 1995). However, the Transvaal basin is very tiny compared to marginal basins in modern-day ocean systems and therefore its deposits are not strictly representative for the global ocean at that time period (Beukes and Gutzmer, 2008). Most paleoenvironmental studies, as well as this study, focus on the rocks in the Griqualand West basin, because these did not experience regional metamorphism and have only been subjected to burial temperatures in the range of 100 °C to 150 °C (Miyano and Beukes, 1984; Klein, 2005), corresponding to very low-metamorphic grade (up to lower greenschist facies).

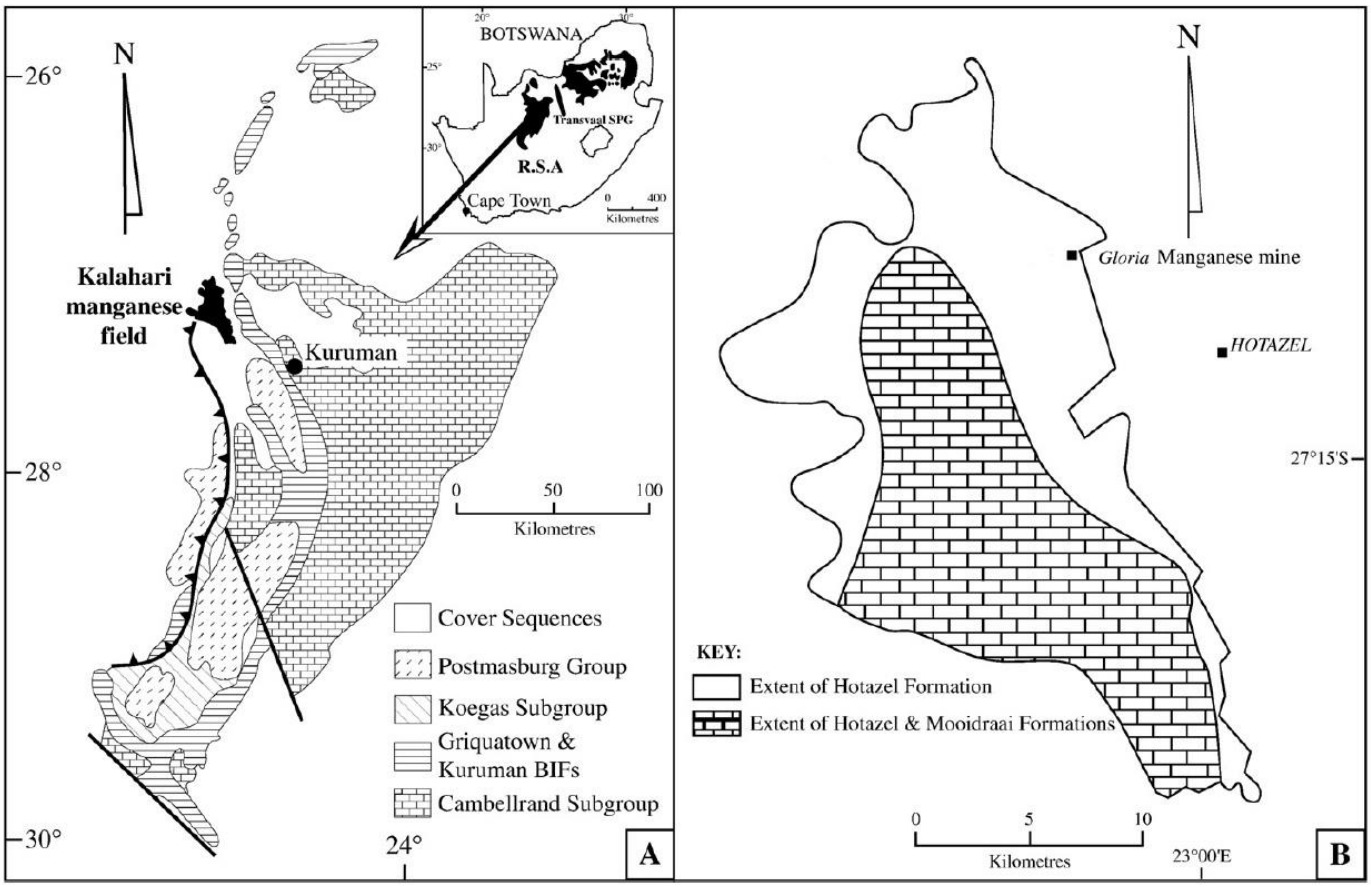

Figure 4: **A)** Geographical distribution of the Transvaal Supergroup in South Africa (inset) and a regional geological map (simplified) of the Transvaal Supergroup in the the Griqualand West Basin (Northern Cape Province); the outline of the Kalahari manganese field is indicated in black. **B)** Geological map of the Kalahari manganese field, including the locality of the Gloria manganese mine from which the drill-core in this study was taken. Modified from: Tsikos et al. (2010).

The stratigraphy of the Transvaal Supergroup in the Griqualand West Basin is divided into two parts (see also Figure 4). The lower portion consists of the ca 1.6 km thick Ghaap Group, which was deposited between 2.64 and 2.45 Ga (Pickard, 2003; Beukes and Gutzmer, 2008) and consists of a thick succession of mainly dolomitic carbonates at the base (Campbellrand subgroup), which are overlain by several hundreds of metres of BIF stratigraphy: the Kuruman and Griquatown Formation (Klein and Beukes, 1989; Beukes and Klein, 1990; Beukes and Gutzmer, 2008). Klein and Beukes (1989) interpreted this facies change to reflect progressive deepening of the basin, in which the Campbellrand carbonates were initially deposited in a shallow-marine environment and subsequent drowning caused deposition of shale, siderite-rich and magnetite-rich microbanded BIF. The upper portion of the Transvaal Supergroup (the Postmasburg Group) begins with the glacial diamictites of the Makganyene Fm., which, according to the model of Kirschvink et al. (2000), represent the earliest Snowball Earth event. These are overlain by a thick (300-900 m) package of tholeiitic-basaltic andesites from the Ongeluk Fm. Pillow lavas, as well as hyaloclastites and massive flows support subaqueous extrusion (Grobler and Botha, 1976; Schütte, 1992; Cornell and Schütte, 1995; Cornell et al., 1996). The Ongeluk lavas are followed by the chemical sediments of the ca 100-150-metre-thick Hotazel Fm. The Hotazel Fm. mainly comprises three distinct Mn layers, inter-layered with magnetite-carbonate BIF; at the contact between the BIF and Mn layers, transitional lutites occur, ranging in thickness from a few decimeters up to several metres (Gutzmer and Beukes, 1996; Tsikos et al., 2003; 2010). These lutites are rich in hematite and Mn-carbonates. The Hotazel Fm. is unconformably overlain by the Mooidraai dolomite, which represent shallow-marine platform carbonates (Swart, 2012). See Figure 5.

There is a large uncertainty about the depositional age of the Hotazel Fm., particularly with regard to the timing of the GOE. The Ongeluk lava was initially dated by Cornell et al. (1996) at ca 2222 ± 13 Ma. By implication, depositional models placed the timing of the Hotazel after the GOE (Schütte, 1992; Cornell and Schütte, 1995; Cornell et al., 1996; Kirschvink et al., 2000; Kopp et al., 2005; Kirschvink and Kopp, 2008). One model explains the Fe-Mn sediments of the Hotazel to reflect pulses of strong hydrothermal fluid input (related to the Ongeluk volcanic activity) and rapid precipitation upon oxidation with the oxygenated seawater (Schütte, 1992; Cornell and Schütte, 1995; Cornell et al., 1996). A more recent model relates the deposition of Mn ore bodies to primary precipitation of Mn(IV) in a post-Snowball Earth environment

(Kirschvink et al., 2000; Kopp et al., 2005; Kirschvink and Kopp, 2008) . Melting of the ice sheets would have allowed for oxidation of dissolved Fe(II) and Mn(II) by exposing the initially covered, anoxic waters to photosynthetically-produced O_2.

However, whole-rock Pb-Pb dating of the Mooidraai dolomites by Bau et al. (1999) suggests that the Ongeluk (and therefore the Hotazel Fm.) may be significantly older (i.e. ca 2394 ± 26 Ma). Moreover, age determination from detrital zircon grains of the Postmasburg group indicates a maximum age of 2436 ± 7 Ma, and a broad age range of the group somewhere between 2.43 and 2.38 Ga (Moore et al., 2012). This is also supported by very recent dating of the Ongeluk Fm., which yields a U-Pb age of ca 2.43 for the Ongeluk volcanic sills (Gumsley et al., 2015). As a consequence, the Makganyene diamictites were correlated to the glacial deposits of the Huronian Supergroup (Superior craton, Canada), and the Ongeluk lava to the Bushy Bend volcanics, which challenges the initial correlation to the Hekpoort lava (Reczko et al., 1995). Consequently, deposition of the Hotazel may have taken place ca 200 Ma earlier than initially thought: at the timing of the oxygenation of the atmosphere (ca 2.4 Ga). Elaborating on the early model of Beukes (1983) and Nel (1986), Tsikos et al. (2010) therefore proposed that the cyclic character of the Hotazel Fm., involving the characteristic succession of magnetite BIF-hematite lutite-Mn ore body, reflects transgression-regression cycles in a redox-stratified basin, in which the upper ocean layers were highly enriched in Mn(II) relative to Fe(II).

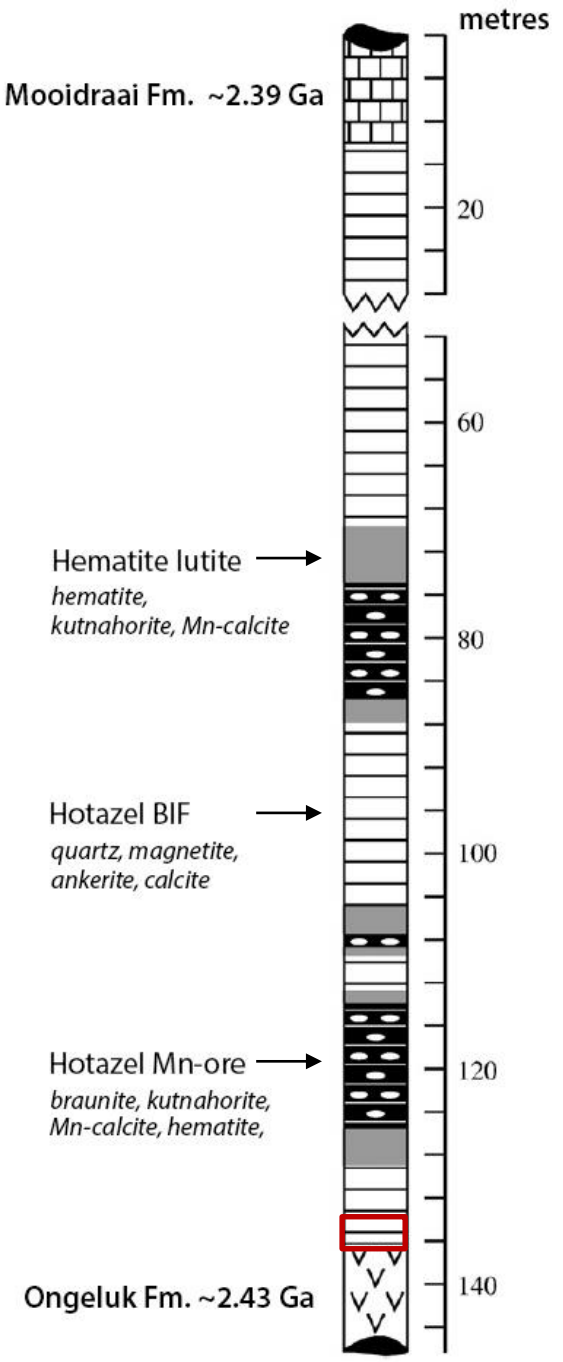

Figure 5: Schematic stratigraphic column of the Hotazel Formation and its adjacent stratigraphic units, i.e. the Ongeluk Fm. below and the Mooidraai Fm. above, as typically developed in the Griqualand West basin. The depositional ages for the Mooidraai Fm. and Ongeluk Fm. are from Bau et al. (1996) and Gumsley et al. (2015). The stratigraphy comprises three sequences of alternating BIF, hematite lutite and Mn ore, each with its own specific mineral content. The red box indicates the stratigraphic interval of interest in this study. Modified from: Tsikos et al. (2010).

3. Materials and methods

3.1 Rock characterisation

3.1.1 Drill-core description

From the interval between 291.00 m and 294.14 m depth, one half of the sliced drill-core GL36 (Gloria mine borehole locality 36) was transported to Utrecht University for research of the contact between the Ongeluk Fm. and the overlying Hotazel Fm. In order to keep a visual record of the original rock, the core was photographed with a scanner. To remove saw marks and to bring out the original, unweathered surface colour, several parts of the core were polished and scanned again. However, the mudstones were not polished because they were too brittle. Based on visual observation of the lithology, (igneous and sedimentary) textures, colours and presumed overall mineralogy, a description of the rock was made and displayed in a stratigraphic chart. In addition, the half-sliced drill-core was divided into halves again to keep one quarter for the record and to use the other quarter for making thin-sections and microdrilling Fe isotope samples.

3.1.2 X-ray fluorescence

To get a general overview of the absolute and relative concentrations of major elements throughout the drill-core in a non-destructive way, micro X-ray fluorescence

was applied using the *EDAX Orbis PC Silicon Drift Detector Analyzer.* With a 1-mm laser beam (1000 µA and 30 kV) line scan analysis was carried out along almost the entire Hotazel part of the drill-core applying a 5-seconds measurement time per point. A representative sample of the Ongeluk lava was also measured to compare the chemistry of the Hotazel rock with. Pieces of the core that were larger than 8 cm in length could not be analysed because these exceeded the instrument dimensions. Moreover, it was imperative that the samples were oriented with their flat surface perpendicular to the laser beam direction. Because the drill-core pieces had a rounded back they were put in a bin filled with sand to keep them in the right position.

The results were averaged out over 3 mm (three subsequent measurement points) to smooth the data and to average the composition. Accuracy and precision of the results are quite low because of the short measurement time and due to secondary X-ray interference. Therefore this technique should exclusively be treated in a qualitative way.

3.1.3 Optical microscopy

In addition to the broad-scale rock characterisation, several parts of the drill-core required further examination. Various areas distributed over the entire core that displayed specific petrographic features were selected for optical microscopy (see section 4.1.2, Table 2 for the sample location). Nineteen polished thin-sections were made of 30-µm-thick slices of rock oriented perpendicularly to the scanned surface of the core. Of all thin-sections the major mineral phases and relevant textures were identified with a *Polaris* optical microscope (maximum magnification of 787.5), under plane polarised (PPL), cross-polarised and transmitted light. Photomicrographs of the thin-sections were made with a *Leica MC170 HD* microscope camera (under PPL).

3.1.4 Electron microprobe analysis

Since optical microscopy was insufficient to identify the very fine-grained and opaque minerals present in the Ongeluk and Hotazel rocks, several thin-sections were selected for Electron microprobe analysis (EMPA). EMPA is an analytical technique that is used to establish the composition of microscopically small areas (e.g. individual mineral grains or parts of grains) by focusing of a beam of accelerated electrons. The electron beam produces X-rays with distinct energy levels that are diagnostic for the composition of the specimen. The X-rays are detected at particular wavelengths and their intensities are used to calculate the concentrations. All elements heavier than oxygen can be detected based on the specific set of X-rays they emit.

The *JEOL JXA-8530 Field emission Electron Probe Micro Analyzer* at Utrecht University was used for both qualitative mineral phase identification and mineral chemistry determination. Prior to EMPA thin-sections were carbon coated. Energy-dispersive spectrometry (EDS) was used only for rapid phase identification and wavelength-dispersive spectrometry (WDS) was applied for chemical composition analysis. With EDS analysis X-rays are collected and counted by a solid-state detector at once and are divided into different energy spectrums. The spectrum peaks displayed on the computer screen correspond to energies of elements present in the sample. The EDS technique is very rapid, but because of its limited sensitivity and the fact that element peaks are often overlapping, WDS is more desirable. With WDS analysis spectrometers are tuned to the characteristic X-ray of interest. The tuning is established by scattering of X-rays from a crystal positioned between a sample and the detector. By changing the angle of incidence of the X-rays, the crystal will consequently diffract X-rays of specific wavelengths. As a result, both the crystal and the detector move to adjust to the different incident angles.

WDS major element point analysis was applied on the Ongeluk alteration minerals and Hotazel Fe carbonates, Fe silicates and accessory (opaque) phases using a 1 to 3 µm laser diameter and 15 kV acceleration voltage; a 5 µm laser beam was used for hydrated minerals to reduce the effect of element vaporisation. Each thin-section was checked for chlorites, which were subsequently analysed (5-10 points per thin-section). Hematite and magnetite were chemically distinguished between based on the proportion of oxygen, expressed as a total weight percentage of 91 % or 94 %, respectively. In addition to single point measurements, four grid analyses (6x6 and 6x7, with 10 µm point spacing) were carried out on the pure hematite-chert layers in thin-section 2 and 14 to get an estimate the relative proportion of FeO to SiO_2 (wt %).

Apart from chemical analysis, the Microprobe was used to obtain highly magnified back-scattered electron (BSE) images of the various petrographic features, and specifically the mineral phase relations.

3.2 Hematite characterisation

3.2.1 Scanning electron microscopy

General rock characterisation was followed by a more detailed look at the hematite-rich sections in the Hotazel, in order to figure out the timing of hematite formation with respect to the other phases. The crystal size, morphology and cluster configurations of hematite particles from selected thin-sections in various settings were examined and photographed with a *FEI XL30 Field Emission Gun-Scanning Electron Microscope* in both BSE and SE (secondary emission) mode. Since the intensity of the BSE signal is strongly related to the atomic number of the specimen (i.e. bright areas correspond to heavy elements and dark areas to lighter elements), BSE images were useful for distinguishing hematite from the other mineral phases (primarily quartz). Combined with the SE view, which displayed the surface topography of the thin-sections, the hematite three-dimensional morphology could be discovered. Depending on the magnification a 10 or 15 V beam was applied.

3.2.2 Laser ablation

Laser ablation inductively coupled plasma mass spectrometry (LA-ICP-MS) was applied on eight hematite-chert sections distributed over the entire Hotazel-part of the drill-core, in order to determine their trace element and most importantly, their rare-earth element composition. Laser ablation is a rapid and sensitive technique for carrying out spatially-resolved in-situ (trace) element analysis. It is typically suitable for measuring trace elements at a concentration range of 1 µg/kg-100 mg/kg. A 193 nm wavelength *Lambda Physik COMPex 102 ArF excimer* laser ablation system connected to a *ThermoFischer Scientific Element 2 magnetic sector* ICP-MS with *GeoLas* optics was used for all LA-ICP-MS analyses of hematite-rich chert zones in various thin-sections. The ICP-MS was operated at low resolution (M/ΔM=400). The laser parameters were kept constant at a pulse repetition rate of 10 Hz, spot diameter of 60 µm and energy density of 5 J/cm^2 for the internal standards and 11.5 J/cm^2 for the samples. Laser ablation measurement time lasted ca 60 s of a total ICP-MS run time of 120 s. Several hematite-chert points were analysed per thin-section. After every five samples an internal calibration standard (NIST SRM610) and an external reference material (BCR-2G) were measured.

LA-ICP-MS data were processed with the *GEMOC Laser ICPMS Total Trace Element Reduction* (GLITTER) software package. Mean background values were obtained from the mean intensities of a circa 45 s interval prior to the start of the laser ablation measurement. These values were subtracted from the raw analyte intensities. Subsequently the background-corrected analyte intensities were calculated by correlation with the internal calibration standard and were thus corrected for changes in analytical conditions such as instrumental drift. NIST SRM610 reference values were taken from Pearce et al. (1997). In addition, the counting statistics 1 σ error and minimum detection limit with 99% confidence level were calculated. Element concentrations (in ppm) were determined relative to a known concentration of SiO_2, which had to be entered in GLITTER. The SiO_2 weight percentage was estimated from EMPA and XRD results, but the exact concentration could unfortunately not be established. Measurement bias (expressed in %) was determined from the relative difference between the BCG-2G measured concentrations and the GeoRem accepted values.

Since it was the aim to capture the trace element signature from the hematite and chert only, samples were checked for their purity before, during and after LA-ICP-MS. The laser was pointed on areas in the hematite-chert that were devoid of or poor in other minerals. In GLITTER (parts of) the measurement runs that showed a low Fe content or which were high in detrital element abundance were discarded. Spider diagram REE + Y profiles that were too spiky because of a low yield were similarly discarded.

REE and Y concentrations of all clean samples were normalized to PAAS (Post-Archean Australian shale, values from Pourmand et al., 2012). In order to increase the accuracy and reduce the spread in spider diagram REE profiles, an average REE concentration for each thin-section was created. This was only done for thin-sections of which the individual samples showed a similar REE profile but a varying total REE concentration.

3.3 Fe isotope samples

3.3.1 Sample selection

Seven locations in the Hotazel Fm. and three locations in the Ongeluk Fm. distributed over the whole stratigraphy were selected for Fe isotope analysis (see section 4.3.2-3 for the sample location). Samples from the Hotazel were obtained from the hematite-rich chert parts with the aim to track solely the Fe isotopic signal of hematite. Therefore, specific parts of the rock were chosen that looked mineralogically pure. Bulk-rock samples of the Ongeluk were analysed for Fe isotopes for comparison with crustal values (i.e. near-zero δ^{56} Fe). Small pieces of sample (ca 200-300 mg) were microdrilled from the selected areas with a 3-mm-width diamond coated core drill bit (or a diamond saw, depending on the accessibility of the desired piece of rock). The drill bit was cleaned in an ultrasonic bath for a few minutes for each sample to remove surface contamination. Cut samples were made to a fine powder in an agate mortar. The Hotazel samples were named Hotazel Fe (HF) 1 to 7 and the Ongeluk samples Ongeluk Fe (OF) 1 to 3, where the highest number indicated the stratigraphically lowest (deepest) sampling position.

3.3.2 X-ray diffractometry

X-ray diffraction (XRD) was carried out on the HF1-7 samples to check for the presence of minerals other than quartz and hematite. A few micrograms of sample powder was smeared uniformly onto a glass slide and analysed with *a Bruker-AXS D2 Phaser powder* X-ray diffractometer in *Bragg-Brentano* mode, equipped with a *Lynxeye* detector. Copper Kα1,2, λ = 1,^{54}1838 Å radiation was applied and operated at 30 kV and 10 mA.

With the XRD technique samples are subjected to X-rays at different angles (θ). If Bragg's Law is satisfied, the radiation is diffracted by the crystals in the sample: $2d(\sin\vartheta) = \lambda$. From the measured angle ϑ of the diffracted radiation of wavelength λ, the characteristic crystal lattice interplanar spacing d can be calculated and compared to a database.

Resulting 2θ plots were evaluated in the *Diffrac plus BASIC Evaluation package EVA* software. Background intensities were subtracted and the peaks were centered around the database quartz peaks. With "trial and error" the mineral phases that corresponded to the intensity peaks in the 2θ scan were identified: the minerals that were likely to be present in the samples (based on optical microscopy and EMPA results) were selected in software's

mineral database and it was verified whether the 2θ peaks from the software minerals matched the observed peaks in the sample spectrum.

A rough estimate of the relative mineral proportions in the samples was obtained by applying software semi-quantitative phase analysis. Semi-quantitative phase analysis is based on the hypothesis that all the phases are crystalline and detected and so their sum is 100 %. It was therefore essential that all phases were identified. By visual adjustment the Y-scale scale for each database pattern was matched to the peak height of the measured scan. Assuming the peak height was proportional to the net area, the relative mineral weight percentage was calculated.

3.3.3 Sample preparation

3.3.3-1 Sample digestion

Sample digestion was carried out in two ways, i.e. complete dissolution (total digestion) and partial dissolution (HCl digestion) according to the protocol described in Page et al. (1982) and in Tsikos et al. (2010), respectively. All Fe isotope samples were completely digested in HF-$HClO_4$-HNO_3, and for comparison samples HF3, 4, 6 and 7 were also treated with HCl so that only the Fe oxides and carbonates were dissolved. For the total digestion procedure ca 100 mg of sample was taken, together with a blank sample, five certified standards and a duplicate sample (of HF7). Lab standard ISE921 was used as processing standard, BHVO-1, AGV-1 and JB-2 as basalt reference materials and IF-G as iron formation reference material. The HCl dissolution sample sequence contained one blank and ISE921 processing standard. All sample digestions were performed in clean *Savillex Teflon PFA* beakers.

Samples that needed to be totally decomposed were digested in capped *Teflon* beakers using a 2.5 mL mixture of concentrated $HClO_4$-HNO_3 (in a 3:2 ratio) together with 2.5 mL of concentrated HF and were heated overnight on a hot plate at 90 ^oC. In this way the HF forms volatile silicate fluoride complexes that assist in dissolving the residue, while the $HClO_4$ ensures complete dissolution of insoluble fluoride complexes that may possibly have formed. The dissolved samples were subsequently dried down at 140 ^oC and consequently all silica and organic matter were removed. Finally, 25 mL of 1 M HNO_3 was added and heated overnight again at 90 ^oC. The HCl digestion was performed with 5 mL of ultrapure 9.5 M HCl and overnight heating at 85 ^oC. Afterwards, 10 mL of 6 M HCl was added and the undissolved parts were filtered out of the solution using 45 µm nylon syringe filters.

3.3.3-2 ICP-OES

A fraction of the solutions was taken for chemical analysis using inductively coupled plasma optical emission spectrometry (ICP-OES) to determine the Fe content of each solution and to establish indirectly the chemical composition of the (dissolved) dry rock. ICP-OES was performed with the *Perkin Elmer Optima 3000* ICP-OES instrument at Utrecht University in two runs with different dilution factors. For the first high concentration run ca 0.1 mL of sample solution was diluted to ca 5 mL in 1 M HCl; for the low concentration run a circa 2.5-3 mL aliquot was taken. The results of both runs were combined in order to discard measurements that were below the detection limit, below the background intensity or above the calibration range.

3.3.3-3 Preparation for chromatography

Preparation of pure Fe-bearing solutions was achieved following the protocol of Williams et al. (2004). Appropriate amounts of solution containing ca 300 µg of Fe were evaporated to dryness at 100 ^oC. Full oxidation of Fe from its divalent to trivalent state was achieved by stepwise addition of 4.5 mL concentrated HCl, 1.5 mL concentrated HNO_3 and 1 mL H_2O_2 and overnight reaction at 120 ^oC in capped *Teflon* beakers. After the reaction the samples were evaporated to dryness, dissolved in 2 mL of ultrapure 6 M HCl and evaporated again. Once dried down the samples were taken up in a specific amount of ultrapure 6 M HCl to get at least 0.5 mL of 600 µg/g Fe solution.

3.3.3-4 Anion-exchange chromatography

Separation of Fe from its sample matrix was achieved by anion-exchange chromatography. This technique uses a positively charged ion exchange resin with an affinity for negatively charged molecules. Anion-exchange chromatography was performed in *Biorad 1.8 mL reservoir columns* using 0.6 mL of *BioRad AG1-x4, 200-400 mesh resin* suspended in 0.05 M HCl, and with a total resin capacity of 0.6 mEq. The entire procedure took place in an airlock cleanroom. All individual column resins were cleaned thoroughly prior to column separation by complete filling of the reservoir (ca 0.7 mL) with ultrapure 6 M HCl and ultrapure water in the following order: 8 times with 6 M HCl, followed by 8 times with ultrapure water. The entire sequence was carried out twice.

Before sample loading the resin was pre-conditioned with 1 mL 6 M HCl. Subsequently 0.45 mL of each sample was loaded onto the resin whereby Fe was taken up in its chloride form ($FeCl_4^-$). In order to remove unwanted matrix ions the resin was further washed with four passes of 1 mL 6 M HCl. During this step it was checked whether the Fe (recognisable by its yellow colour) remained in the columns and was not washed out together with the matrix elements. The Fe was eluted with four passes of 0.5 mL 0.05 M HCl and evaporated to dryness. Columns were cleaned by two sequences of six passes 6 M HCl followed by six passes of 0.05 M HCl.

Oxidation of the Fe separates was achieved by reaction with concentrated HNO_3 and H_2O_2 on a hotplate for several hours; it was ensured that all the Fe was in solution. Dried down to small liquid drops the samples were transported into *Teflon* beakers to the Helmholtz

Centre Potsdam GFZ (German Research Centre for Geosciences) for Fe isotope measurements.

3.3.4 Fe isotope measurements

At the GFZ Fe isotope analysis was performed with a HNO_3 solution. Accordingly, to remove all HCl the samples were evaporated to total dryness, dissolved in 50 µL concentrated HNO_3 (13.9 M) and evaporated again, where after the dried samples were dissolved in 2 mL 0.3 M HNO_3. Solutions of internal Fe laboratory standard *HanFe* and the Fe isotopic bracketing standard IRMM-014 were similarly prepared. The 0.3 M HNO_3 solution was made at once in a separate bottle to ensure the same acid strength for each Fe analyte solution.

3.3.4-1 Purity check

Prior to the Fe isotope measurements an 80 µL fraction of the Fe samples, processing blanks and Fe standards was diluted to 4 mL for chemical analysis by ICP-OES (*Varian 720 ES*, GFZ Potsdam). Following the data acceptance protocol of Schoenberg and Von Blanckenburg (2005) the Fe separates were analysed for their Fe concentration and Fe purity.

Small differences in the matrix of the samples may affect the instrumental mass bias and thus the Fe isotopic signal of the samples. In the first place, the Fe concentration and acid molarity of the all geological samples has to be similar to that of the IRMM-014 bracketing standard, in this case 5 ppm Fe in 0.3 M HNO_3 respectively. Therefore, ICP-OES Fe concentration results of the 2 mL 0.3 M HNO_3 Fe separates were essential for calculating the appropriate fraction of each sample for making ca 4 mL of a 5 ppm Fe solution. Secondly, matrix effects due to sample impurities may additionally affect the instrumental mass bias drift. Fe separates may not be entirely matrix-free after anion-exchange chromatography and as a result these elements potentially shift the Fe isotopic composition of the samples. Accordingly, the samples were checked for metal impurities (Cr, Ni, Cd, Zn, Co and Cu) that can co-elute with Fe and some elements (e.g. Mg, Na) sensitive for contaminations after column chemistry. Further, procedural blanks were also analysed for Fe contents and contaminations.

Based on the OES results before and after column chemistry (before measured at UU, after measured at GFZ) column yields were calculated to ensure complete recovery of Fe for each sample during column separation, excluding the possibility of chromatographic Fe isotope fractionation. Because Fe yields for a few samples (based on ICP-OES results) unfortunately indicated significant loss, the Fe content of samples prior to column loading was re-measured with a *Shimadzu UV-1800 Spectrophotometer.* In addition, for each sample the total electrical charge loaded onto the columns was compared to the resin's capacity.

3.3.4-2 MC-ICP-MS

Fe isotopes were conducted using a *Thermo Neptune* multi-collector ICP-MS in medium-resolution mode. The multi-collector ICP-MS instrument is equipped with nine Faraday cups, so that the different masses can be collected simultaneously, making it much more precise for isotope measurements. The cup configuration and their corresponding atomic ions collected during Fe isotope analysis are listed in Table 1.

Table 1: Faraday cup setting for the Neptune MC-ICP-MS Fe isotope measurements.

Faraday cup	L4-F	L3	L2-F	L1-F	C-F	H1-F	H2-F	H3-F	H4-F
Atomic species	^{52}Cr	-	^{54}Fe	^{55}Mn	^{56}Fe	^{57}Fe	^{58}Fe	-	^{60}Ni

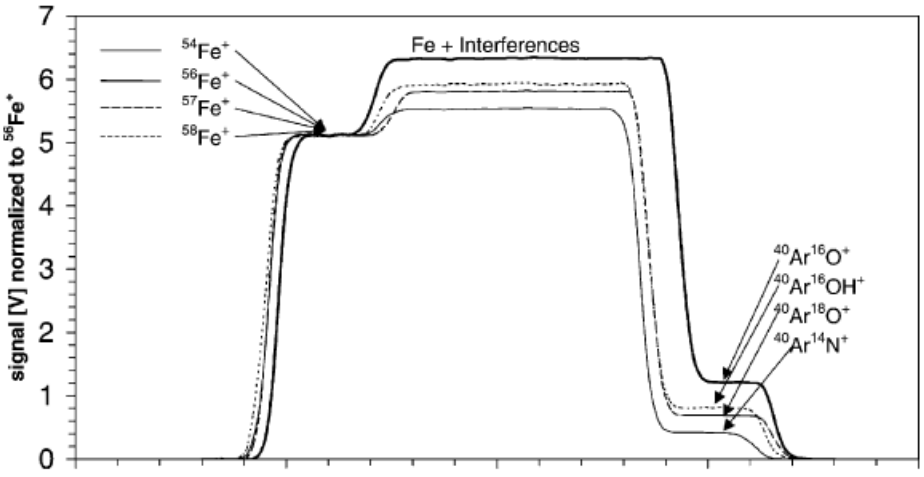

Figure 6: Typical mass scan obtained with a medium resolution entrance slit and a low-resolution detector slit, showing all lighter Fe isotopes entering the detector first and their corresponding heavier polyatomic interferences appearing later. The values on the x-axis represent the mass range for $^{56}Fe^+$ and $^{40}Ar^{16}O^+$. From: Weyers and Swieters (2003).

Unfortunately, most Fe masses suffer from mass interferences with isobaric polyatomic ions, which can limit the precision and accuracy of the isotope ratio measurement. The most important interferences for Fe isotopes are $^{40}Ar^{14}N^+$ on $^{54}Fe^+$, $^{40}Ar^{16}O^+$ on $^{56}Fe^+$, $^{40}Ar^{16}OH^+$ on $^{57}Fe^+$ and $^{40}Ar^{18}O^+$ on $^{58}Fe^+$. For high-precision isotope ratio measurements it is imperative that the intensities of the isotopes and their respective isobaric interferences that enter the detector (presented in a mass scan such as in Figure 6) can be distinguished from each other. The polyatomic interferences can be totally resolved, i.e. their intensity peaks can be completely separated, by applying a high resolution entrance and collector slit; in other words, by decreasing the size of the entrance slit and collector slit. However, in a mass scan this produces peaks with pointed tops; small drifts in the magnet that shift the position were the ion beams enter the detector would then result in large variations in the measured intensity. For high-precision isotope ratio measurements it is therefore necessary that the peaks have broad, flat plateaus. This is achieved by applying a medium-resolution entrance slit and a low-resolution detector slit, which does not result in total peak separation but produces a flat area on the Fe isotope peak that is interference-free. This is illustrated in Figure 6. In the Faraday cup, first the lighter Fe species enters the detector slit and forms the first plateau of the section peak. Subsequently the heavier isobaric interference enters the cup and creates a second, somewhat higher plateau in the intensity peak scan. Fe isotope ratios should thus be measured at the centre of the left plateau, which is free of interferences. In order to achieve this, the entrance slit must be small enough to separate the ion beams of the Fe isotopes and the polyatomic interferences, but at the same time produce a strong enough intensity for a high sensitivity. This is contrary to the collector slit, which is wider than the ion beam profiles on the Faraday detectors so that the beams are simultaneously collected at the edge position of the cups. However, the Fe ion beam is collected at the edge of the Faraday cup so that the polyatomic interference beam cannot enter the detector. See Figure 7. The three isotope plot (i.e. in which the results are plotted in $\delta^{57/54}Fe$ vs $\delta^{56/54}Fe$ space) is used after Fe isotope measurements to check there are no isobaric interferences: if present, these cause a shift (deviation) from the theoretical mass-dependent fractionation line.

Prior to the Neptune measurements extensive tuning of the instrument parameters (e.g. position of the focusing lenses, the magnet and the Faraday cups) was required to obtain good sensitivity, good peak shape (mass resolution) and complete interference suppression (peak position and ArO intensity). The mass scan (from a 5 ppm Fe solution) obtained after tuning is indicated in Figure 8.

A measure for the broadness of the flat plateau region and hence the mass resolution is the steepness of the peak slope of the ion beam profile, i.e. $m/\Delta m$, where m is the mass of the ion of interest and Δm the difference in mass between its 5% an 95% peak height. On the Neptune instrument a ca 30 µm diameter entrance slit was applied, resulting in a mass resolution of 8000-9000 ($m/\Delta m$). The sample solutions were nebulised and introduced by the *ThermoFinnigan* stable introduction

.

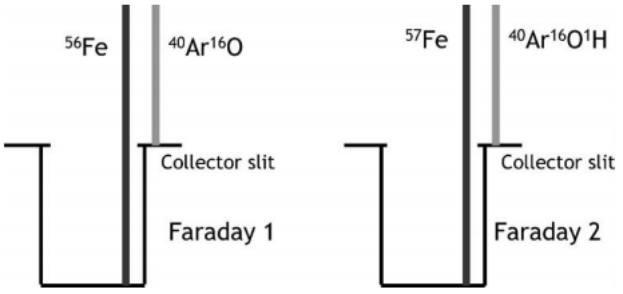

Figure 7 (above): Schematic picture of the setup for the simultaneous measurement of ^{56}Fe and ^{57}Fe. The high-resolution entrance slit has created space between the Fe isotope beams and their isobaric interference beams. Subsequently the Fe isotope beams are simultaneously collected at the edge of the Faraday cups, while the interference beam is blocked. From: Weyers and Swieters (2003).

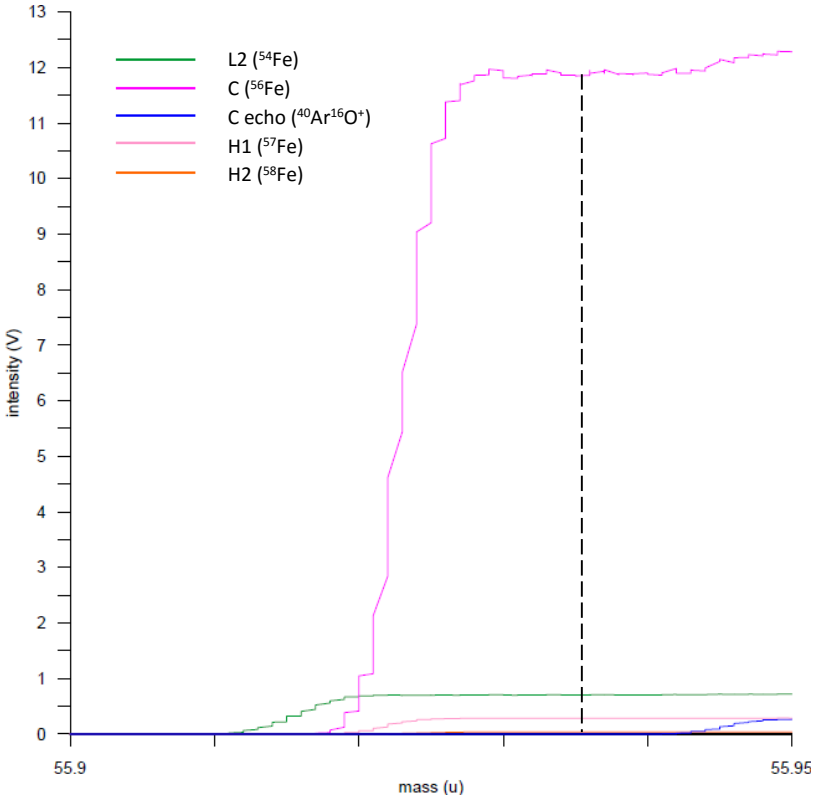

Figure 8 (right): Mass scan of a 5 ppm Fe solution performed after tuning of the Neptune MC-ICP-MS, showing all lighter Fe isotopes (this mass scan is a summary of all ions. Only the $^{40}Ar^{16}O^+$ interference on $^{56}Fe^+$ creating the right plateau is visible; those for $^{54}Fe^+$ and $^{58}Fe^+$ are too small to observe. Fe isotope ratios were measured in the middle of the interference-free left plateau (at the position of the dotted line in). The steepness of the $^{56}Fe^+$ peak slope corresponds to a mass resolution of 8000-9000.

system (SIS) spraychamber at a rate of ca 160 µL/min; sample uptake and washout time were 80 s and 100 s, respectively

The ions were transferred into vacuum using H- and N-type skimmer cones. Each analyte was measured in twenty cycles during a single run with a cycle integration time of 8.34 s. The analyses were carried out with the standard-sample bracketing method (SSB), in which measurements of a standard of known Fe (IRMM-014) isotope composition are alternated with measurements of the samples. During an entire session at each sample was measured three times; the HanFe standard was measured more frequently. In addition, blanks were included in each sequence.

3.3.4-3 Data evaluation and quality control

Raw isotope intensities were corrected for Ni and Cr interferences. Since these corrections are only applicable to low levels of Ni and Cr, samples were evaluated for their $^{54}Cr/^{54}Fe$ and $^{58}Ni/^{58}Fe$ content, which should not exceed 0.1 ‰ and 1 %, respectively. Samples were additionally corrected for the blanks intensities.

To correct for (small) fluctuations in the instrumental mass bias, the SSB method was applied, and accordingly $\delta^{56}Fe$ is reported as:

$$\delta^{56}Fe_{sample} = [^{56}Fe/^{54}Fe_{unbracketed\ sample} / (^{1}/_{2}*(^{56}Fe/^{54}Fe_{IRMM\text{-}014\ before} + {}^{56}Fe/^{54}Fe_{IRMM\text{-}014\ after}))\text{-}1] * 1000\ (‰);$$

$\delta^{57}Fe$ and $\delta^{58}Fe$ notations represent $^{57}Fe/^{54}Fe$ and $^{58}Fe/^{54}Fe$, respectively.

The SSB method assumes that the instrumental mass bias factor varies linearly over short periods of time. By interpolating between the $^{54/56}Fe$ of the two IRMM-014 bracketing standards, the $^{54/56}Fe$ of the unknown (bracketed) sample is corrected for this small mass bias drift. However, if this mass bias drift between two directly bracketing standard measurements is too large, this increases the uncertainty. Therefore (following the data acceptance criteria of Schoenberg and Von Blanckenburg (2005)) analytes for which the two directly bracketing standard measurements had an instrumental mass bias drift of 200 ppm or higher on the $^{56}Fe\text{-}^{54}Fe$ ratio were discarded. Moreover, the stability of the plasma was evaluated by calculating the mass bias drift between the IRMM-014 standards.

To avoid effects on the instrumental mass bias, samples for which the signal intensity of ^{56}Fe with respect to the bracketing standard IRMM-014 exceeded ±10 % were also rejected. In addition, the Fe isotope data were plotted in $\delta^{57}Fe\text{-}\delta^{56}Fe$ space; samples that did not overlap the mass-dependent fractionation line within their 95% confidence values (i.e. isobaric interferences) were removed.

Fe isotope data of all samples and standards were obtained during two measurement sessions divided over two days. During the first session the totally digested samples were analysed and during the second the HCl dissolved samples. For both sessions an average Fe isotope value was calculated from the three, two or one individual runs that were considered reliable according the criteria named above; from these runs an internal 2 σ standard deviation was obtained. The Fe isotope data of the reference materials were compared to the standard's accepted values and it was checked whether they were within the uncertainty limits. An external long-term reproducibility (2 S.D.) for the $\delta^{56}Fe$ measurements was obtained from the analysis of multiple HanFe 5 ppm solutions at the GFZ.

4. Results

4.1 Rock characteristics

4.1.1 Lithostratigraphy

Drill-core GL36 from 294.14 and 291.00 m depth contains the uppermost part of the Ongeluk and the lowermost part of the Hotazel Formation (see Appendix 1 for the drill-core scans). This transition zone consist of three major lithofacies, which are, from bottom to top (1) lava (Ongeluk); (2) (hematite-)lutite (Hotazel) and (3) BIF (Hotazel). In the following sections of the *Results* (and the *Discussion*), the term *Ongeluk* refers to the stratigraphic interval between 294.14 – 293.79 m depth and the term *Hotazel* to the interval between 293.79 – 291.00 m depth. See Figure 9.

(1) The Ongeluk Formation consists of dark green volcanic rock, occasionally cut by secondary carbonate veining. The original composition of the lava corresponds to that of a basaltic andesite (Schütte, 1992; Cornell et al., 1996) but later hydrothermal alteration and very low-grade metamorphism have markedly changed the rock's composition in terms of mineralogy and textures.

(2) The Ongeluk lava is immediately overlain by the dark red chemical sediments of the Hotazel Formation. Texturally, the rocks can be classified according to Simonson (1985) as iron-formation lutites (consisting of chemical mud) and the clastic-textured parts as iron-formation arenites (consisting of chemical sand). Mineralogically they consist predominantly of very fine-grained quartz mixed with Fe-rich minerals (cherty iron formation). Where very fine-grained hematite is the dominant Fe-bearing mineral present, the rock has a deep red colour; according to the classification of Beukes (1980) this rock type is called *jasper*. The rocks look similar to the "transitional lutitic lithologies" described by Tsikos et al. (2010), who found them higher up in the Hotazel at the contacts between the BIF and manganese subdivided into several subfacies. The stratigraphic chart in Figure 9 gives an overview of the broad mineralogical characteristics (i.e. dominant mineral constituent next to chert) and sedimentary textures (i.e. parallel, lenticular, wavy / chaotic bedding or crinkly lamination) of the Hotazel lutite. What stands out from this is the rhythmic alternation ("cycles" I, II and III) of hematite-rich and more clay-rich intervals (i.e. mudstones), which are typically separated by an interval of mixed composition. In general, the hematite-rich lutites and mudstones have relatively low-energy sedimentary features (i.e. parallel, fine lamination and small grainsizes), whereas the transition zones in between imply a high-energy depositional environment (i.e. wavy / chaotic bedding and more clastic-textured).

(3) In the upper part of the drill-core the lithology transitions from mudstone via hematite-rich BIF into magnetite-rich BIF. The BIF is characterised by mm- to cm-scale laminated assemblages of magnetite-rich bands that are interlayered with chert and Fe carbonates.

4.1.2 Sedimentological and petrographic observations

In this section each of the lithostratigraphic rock types identified in the drill-core is described in more detail with respect to their sedimentary structures, petrographic textures and (mineralogical) composition. Optical microscopy results are confirmed with EMPA. The microscopic observations are listed in Table 2 and petrographic images are displayed in Figure 10-11; the chemical composition of the mineral constituents is presented in Tables 3-5.

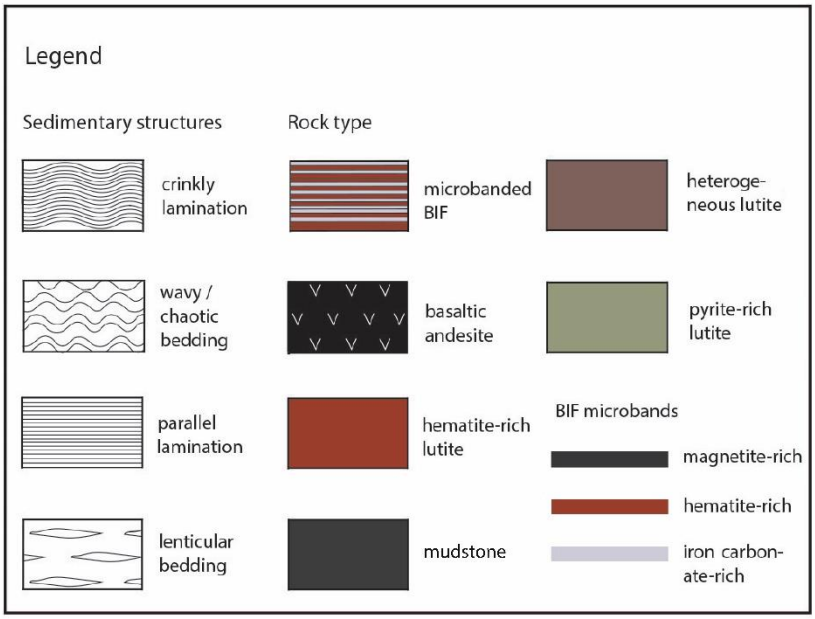

Figure 9 (next page): Stratigraphic chart of drill core GL36 at depth interval 294.14 m to 291.00 m. The contact between the Ongeluk and the Hotazel Formation is at 293.79 m depth. Photographs of the original drill-core are indicated on the right-hand side of the log (true scale). The positions of thin-sections (1-19) are indicated on the left. The lithology pictured in the stratigraphic chart is based on two characteristics: i) sedimentary structures and ii) mineralogy in combination with rock type. Above the Ongeluk lava three sequences occur (indicated by the vertical arrows I, II and III) of hematite-rich lutite transitioning into mudstone; in between the hematite lutite of cycle III a small pyrite-rich interval appears. Whereas the mudstone and hematite-rich units are often parallel laminated or lenticular bedded, the transition zones exhibit more chaotic structures. A small interval of crinkly lamination occurs in cycle III. At the end of cycle III, the mudstone transitions into a microbanded BIF, where magnetite instead of hematite becomes the most important Fe-rich mineral.

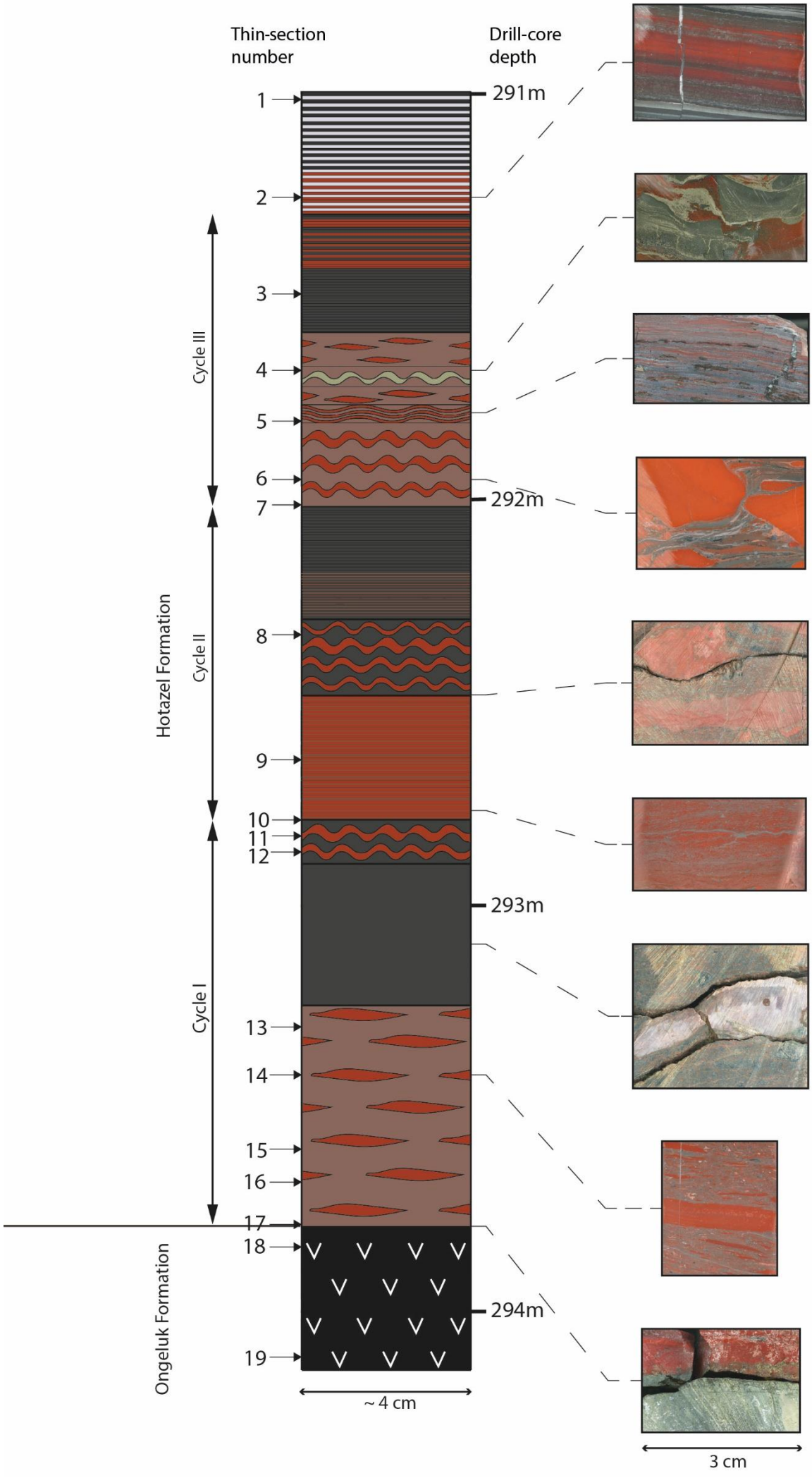
Thin-section number
Drill-core depth
1
2
3
4
5
6
7
8
9
10
11
12
13
14
15
16
17
18
19
291m
292m
293m
294m
Cycle III
Cycle II
Cycle I
Hotazel Formation
Ongeluk Formation
~ 4 cm
3 cm

Table 2: Overview of textures and mineral phases identified with the optical microscope and confirmed by EMPA.

Thin-section	Depth (m)	General texture	Mineral phases identified	Additional information
1	291.04	Banded iron formation. Black, opaque microbands alternating with light brown or grey microbands.	1. quartz 2. magnetite 3. ankerite 4. stilpnomelane 5. hematite	The black bands are made up of large, euhedral magnetite (up to 100 µm). The lighter coloured bands consist of chert, stilpnomelane and ankerite. Ankerite rhombohedra are large, but heavily altered (they contain many gaps).
2	291.51	Banded iron formation. Alternation of dark red (opaque) or black (opaque) and light brown or grey microbands or mesobands.	1. quartz 2. hematite 3. magnetite 4. stilpnomelane 5. chlorite	Fe-rich bands consist of either very fine-grained hematite sheets or euhedral magnetite crystals. Fe-poor layers contain predominantly chert or stilpnomelane.
3	291.51	Opaque, fine-grained mudstone with secondary veining.	1. quartz 2. magnetite 3. hematite 4. calcite (vein) 5. stilpnomelane (vein)	
4	291.69	Chaotically bedded purplish green (pyrite-rich) and dark red (hematite-rich) lutite. Granular features.	1. quartz 2. hematite 3. pyrite 4. calcite 5. magnetite 6. stilpnomelane	Abundance of euhedral pyrite. Grains consist predominantly of chert and calcite.
5	291.80	Crinkly lamination. Alternation of dark red, colourless, black and brown-greenish layers.	1. quartz 2. magnetite 3. hematite 4. stilpnomelane 5. minnesotaite 6. chlorite	Hematite-, minnesotaite-, magnetite- and stilpnomelane-rich bands. Stilpnomelane and minnosotaite needles have grown into the direction perpendicular to the bedding orientation.
6	291.95	Chaotically bedded hematite-chert sections surrounded by an opaque (mudstone) matrix. Many rounded and lense-shaped inclusions.	1. quartz 2. hematite 3. chlorite 4. stilpnomelane 5. minnesotaite 6. magnetite	Fine-grained hematite clusters form a network together with chert. Inclusions contain mixtures of minnesotaite, chert, stilpnomelane needles and anhedral chlorite patches.
7	292.01	Chaotically bedded hematite-chert sections surrounded by an opaque (mudstone) matrix. Some secondary veining.	1. quartz 2. hematite 3. chlorite 4. stilpnomelane 5. calcite (vein)	Opaque matrix contains nodules (ca 0.1-1 mm in diameter) of yellowish or blueish green chlorite needles showing radial growth.
8	292.33	Chaotically bedded hematite-chert units within a nodular (green) mudstone matrix (opaque).	1. quartz 2. hematite 3. chlorite 4. magnetite 5. stilpnomelane	Opaque matrix contains numerous radial chlorite nodules, with both an inner and outer rim. Some nodules show orange-blue pleochroism.
9	292.64	Hematite-rich lutite with small, lense-shaped inclusions.	1. quartz 2. hematite 3. chlorite 4. calcite	Inclusions contain (hematite-)chert or brownish green sheets of fine-grained, anhedral chlorite.
10	292.79	Transition between hematite-rich lutite and nodular mudstone.	1. quartz 2. hematite 3. chlorite 4. magnetite 5. stilpnomelane	
11	292.83	Chaotically bedded pale red hematite-chert unit.	1. quartz 2. hematite 3. calcite 4. stilpnomelane 5. magnetite 6. chlorite	Many small and discontinuous calcite veins or inclusions.

12	292.87	Green nodular mudstone.	1. quartz 2. chlorite 3. hematite	Radial chlorite nodules.
13	293.30	Granular and lense-shaped inclusions within a heterogeneous lutite. Some very pure hematite-chert lenses.	1. quartz 2. hematite 3. calcite 4. minnesotaite 5. stilpnomelane 6. magnetite 7. pyrite	Inclusions are rich in subhedral calcite crystals and minnesotaite.
14	293.42	*Idem as thin-section 13.*	*Idem*	*Idem*
15	293.60	Granular and lense-shaped inclusions within a heterogeneous lutite.	1. quartz 2. hematite 3. calcite 4. minnesotaite 5. stilpnomelane 6. chlorite 7. magnetite 8. pyrite	Large (ca 1 mm) radial aggregates of pyrite. Inclusions and lenses contain calcite, minnesotaite, chlorite and stilpnomelane.
16	293.68	Granular and lense-shaped inclusions within a heterogeneous lutite.	1. quartz 2. hematite 3. calcite 4. minnesotaite 5. magnetite 6. pyrite	Inclusions are rich in subhedral calcite crystals together with minnesotaite.
17	293.78	Contact of Ongeluk lava with the Hotazel Formation: abrupt transition from green lava to dark red lutite.	*Ongeluk:* 1. chlorite 2. feldspar 3. calcite *Hotazel:* 4. quartz 5. hematite 6. calcite 7. chlorite	Several chlorite-calcite veins (100-400 µm wide) with a thick opaque (hematite) rim are branching from the lava towards the contact. Minute dendritic crystals are growing out of these veins. Chlorite occurs in both anhedral and fibrous crystal habit; at the contact, fibres are aligned perpendicularly to the orientation of the contact.
18	293.84	Pale green lava with a porphiritic texture: phenocrysts of 1-2 mm, but much smaller grainsizes for the groundmass minerals.	1. chlorite 2. feldspar 3. calcite	Most of the lava consists of anhedral to elongate chlorite pseudomorphs or interstitial patches; colourless relicts of feldspar phenocrysts (they contain many hollows and gaps).
19	294.11	*Idem as thin-section 18.*	*Idem*	*Idem*

Ongeluk lava

The Ongeluk lava mainly consists of the minerals chlorite, quartz, feldspar, titanite and calcite. The rock has a uniform, dark green colour that is caused by the abundance of the chlorite minerals. The original igneous texture was porphyritic, but this is somewhat obscured by the secondary chlorite and quartz patches covering the very fine-grained groundmass. The original groundmass minerals of the Ongeluk lava have grainsizes much smaller than 1 mm, but some (feldspar) phenocrysts are up to 1-2 mm long.

The chlorites are typically pale green under plane-polarised light and they show an anomalous blue interference colour under cross-polarised light. They often occur in irregular aggregates that have replaced the groundmass minerals or as pseudomorphs after euhedral phenocrysts (clinopyroxenes according to Schutte, 1992); see Figure 11a. EMPA data reveal the chemical composition of the chlorites resembles that of chamosite or clinochlore (Table 3a). Quartz is one of the most abundant minerals developed in the Ongeluk. It occurs as small irregular patches in the groundmass of the lava, surrounding the chlorite aggregates and feldspars. Feldspar phenocrysts may reach up to 2 mm length, but most of the crystals are much smaller than 1 µm and are (partly) covered by the chlorites. The phenocrysts are sub- to euhedral, but at the same time are heavily altered: they contain numerous small gaps and caved-in rims (see Figure 11a). EMPA results show that the feldspar contains significant amounts of Al and K indicating orthoclase, but also of Fe and Mg, which does not agree with the composition of orthoclase (Table 3a). Secondary calcite forms irregularly shaped patches

cutting across the chlorites and feldspars. Microprobe results show that the calcite contains some Mn (1.2 wt %). Occasionally it occurs in large, randomly oriented veins that cross-cut the rock. The veins thus likely represent the fillings of once open cracks. Titanite occurs as minute aggregates at the edges of chlorite and quartz patches.

Contact between the Ongeluk and Hotazel

At the contact with the overlying Hotazel Formation the Ongeluk lava has a different appearance (see Figure 9 and 10, thin-section 17). No feldspars are found here, and the rock consists almost completely of chlorite minerals. Optical microscopy reveals several veins that are branching from the Ongeluk towards the contact with the Hotazel. The veins are typically 100-400 µm wide, and contain a thick opaque rim of hematite crystals (based on EMPA). Inside the veins mainly chlorite, calcite and some titanite are found. Minute dendritic chlorite crystals grow out of these veins, perpendicular to the veining direction. Perpendicular to the contact with the Hotazel, an approx. 100-µm thick layer of uniformly directed chlorite needles has developed (see Figure 11b).

Hotazel lutite

The Hotazel lutite is subdivided into three major lithofacies, namely hematite lutite, mudstone and a *transition zone*, i.e. the chaotically bedded interval where hematite lutite changes into mudstone. The Hotazel stratigraphy displays a (more or less) rhythmic alternation of hematite lutite - transition zone - mudstone - transition zone - hematite lutite, as indicated by cycles I, II and III in Figure 9. Each of these cycles with its corresponding lithological succession is described here
in more detail.

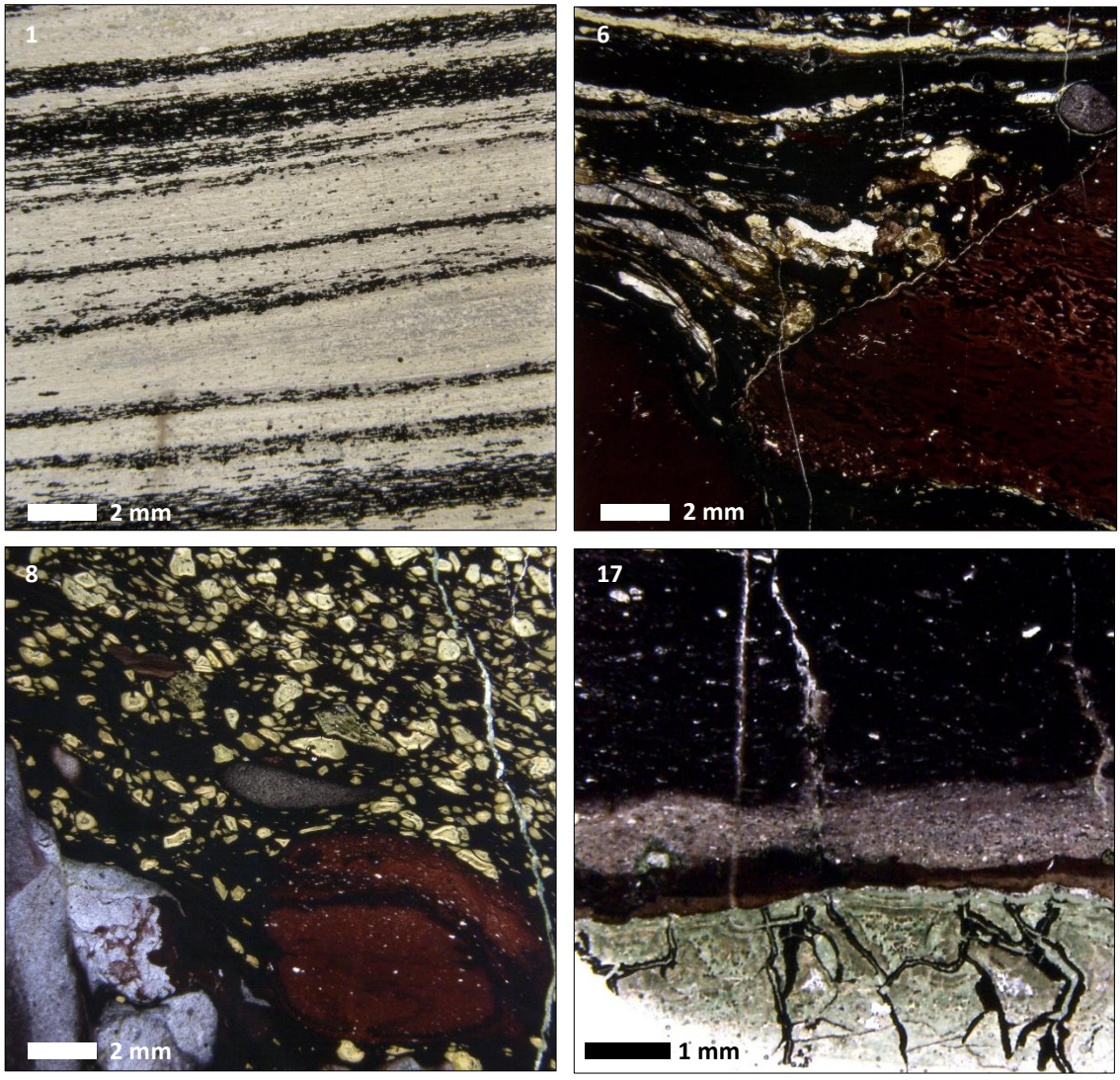

Figure 10: Plane-polarised light images of details of thin-section 1, 6, 8 (magnification 4.6x) and 17 (magnification 11.5x). For description see Table 2.

Hematite lutite (cycle I)

The lowermost hematite lutite contains deep red jasper (hematite-chert) lenses consisting predominantly of minute hematite particles finely disseminated within a microcrystalline quartz groundmass (for a detailed description, see section 4.2.1). The lenses have a wide variety in size (a thickness of < 1 mm up to 1 cm), but they have the same bedding-parallel orientation. Grains forming trains of discontinuous lenses is called *lenticular bedding* (after Reineck and Wunderlich, 1968) and originates from deposition of isolated or starved bedforms on a firm mud substrate (Pettijohn, 1975). The matrix in between the jasper lenses has a more brown-purplish to dark grey colour and is both texturally and mineralogical heterogeneous. It is made up of a mixture of both chemical mud and sand; especially the lowermost part nearest to the Ongeluk contains many clasts and is classified as an iron-formation arenite. The clasts are (similar to the jasper lenses) oval to lenticularly shaped and stratified parallel to their longest dimension. Optical microscopy and Microprobe data show that, apart from quartz as the main mineral constituent, various amounts of Fe oxides (hematite and magnetite), Fe silicates (chlorite, stilpnomelane and minnesotaite), pyrite, apatite, manganoan ilmenite (Mn-ilmenite), and manganoan calcite (Mn-calcite) occur (see Table 2, 3b and 4). Mn-ilmenite and apatite occur in much smaller modal amounts and are more abundant in the clay-rich parts.

Magnetite is usually present as large (1-100 µm, typically 10-50 µm) and well-crystallised opaque, rhombohedral crystals, disseminated in the matrix in random orientation or as crystals grouped together to form microbands; rarely it forms small (< 3 cm in diameter) magnetite ore bodies. Magnetite crystals are almost universally coarser grained than their surrounding minerals. Moreover, they frequently intersect the other phases. In parts of the matrix where magnetite is the major Fe oxide instead of hematite, the rock has a characteristic dark grey colour and metallic lustre. This is particularly the case for the upper part of the hematite-lutite, where the rock transitions into mudstone.

Stilpnomelane, chlorite and minnesotaite (ferrroan talc) are typically concentrated in the clastic-textured sections. Although some recrystallization of the minerals has taken place, this has not obliterated the original sedimentary features. The grains are composed of mixtures of these minerals in variable proportions (as in Figure 10, thin-section 6). Stilpnomelane crystals occur as coarse-grained sprays of yellowish-brown needles (ca 10-200 µm in length) or as finer-grained sheaves or needles (< 10 µm) scattered throughout the heterogeneous matrix. EMPA data show that stilpnomelane contains traces of K (see Table 3b). Minnesotaite occurs as radiating, “bow-tie” needles or plates, locally replacing stilpnomelane. Minnesotaite is particularly abundant in this part of the drill-core (close to the Ongeluk lava) and is often associated with or growing over Mn-calcite. Anhedral chlorite patches are present but minor in this part of the rock and are similarly overgrown by minnesotaite (see Figure 11g).

EMPA data reveal that all diagenetic calcite in the Hotazel consistently contains a few wt % of Mn and is therefore called *manganoan calcite* (see Table 3b). Mn-calcite occurs as large, anhedrally shaped sheets (> 100 µm) covering a substantial area of the hematite lutite closest to the Ongeluk lava. They commonly make up clastic textures together with the Fe silicates. At many places the Mn-calcite sheets seem to be partially dissolved: they contain rounded hollows and gaps were calcite is absent and is replaced by the groundmass chert. This dissolution feature is particularly common in this part of the Hotazel (see Figure 11c and g).

Minor pyrite is present in the form of polycrystalline nodules (*spherulitic* pyrite) with a diameter of up to hundreds of microns (see Figure 11d). Their internal structure consists of radial, bladed crystals which have bended the initial lamination of the surrounding matrix during their growth.

Traces of chalcopyrite and galena occur together with barite in small grains composed of Ongeluk chlorite and Mn-calcite. The sulphides and sulphates are situated directly above the contact with the Ongeluk (< 1mm). See Table 3, 4 and Figure 11c.

Mudstone (cycle I)

The mudstone interval displays no obvious lamination but is largely composed of small nodules. Its uniform dark grey-greenish colour is in marked contrast to the deep red hematite-rich rock from below and reflects a difference in mineralogy (see Figure 9). The mudstone mineralogy is dominated by very fine-grained quartz, magnetite, hematite, chlorite, stilpnomelane, Mn-ilmenite and F-apatite.

The dark-green nodules in the mudstone are ca 0.1-1 mm in diameter and almost entirely composed of chlorite. The internal structure of the nodules varies: chlorite fibres occur either as randomly oriented clusters, or in radial orientation producing spherulites. The chlorites are high in aluminium compared to the other Fe silicates; they have an average Al concentration of ca 13 wt %, although this varies significantly (see Table 3b and Figure 12). Their overall appearance and chemistry are quite similar to that of the chlorites in the Ongeluk lava, i.e. their composition is close to that of chamosite or clinochlore, though the average Al content of the Ongeluk chlorites is a few percentages higher (ca 18-19 wt %).

Several of these spherulites display concentric growth rims, along which Mn-ilmenite has formed trains of individual crystals of 10-30 µm in length (see thin-section 8 in Figure 10, and Figures 11e and f). Whereas Mn-ilmenite is virtually absent in hematite-chert sections, it occurs more frequently in the more clay-rich and clastic-textured parts of the Hotazel. The ilmenite minerals present in the Hotazel contains more than 10 wt % of Mn

(see Table 3b). Apatite is another minor phase which is more abundant in the clay-rich parts. It occurs as randomly scattered anhedrally to euhedrally shaped crystals of ca 5 µm.

Hematite is still present but to a lesser extent and it is intermixed with the other mineral phases instead of concentrated in hematite-chert aggregates. Moreover, it occurs as rod-like crystals of up to 5 µm instead of < 1 µm subrounded particles, locally replacing stilpnomelane or chlorite (see Figure 13).

Transition zone (cycle I)

The transition zone between the mudstone of cycle I and the hematite lutite of cycle II consists of chaotically bedded bulges of pale red jasper and dark green nodular mudstone. Further, it contains a large, angular fragment of magnetite ore body floating into the matrix. The bulges resemble load casts formed by soft-sediment deformation (SSD) shortly after burial and prior to lithification (see Figure 9).

Figure 11: BSE and SE images of various minerals found in the Ongeluk (A-B) and Hotazel formation (C-L), illustrating the crystal habits, textures and inter-mineral relationships. **A**: Heavily altered feldspar (fsp) phenocryst surrounded by anhedral chlorite (chl) patches (thin-section 19). **B**: Veins at the Ongeluk – Hotazel contact with a thick rim of massive, microplaty (ca 5 µm) hematite (hem). The dendritic structures growing perpendicular from these veins (see Table 2 and Figure 10, thin-section 17) are composed of chlorite minerals. **C**: Detrital grains close to the contact (thin-section 17), containing barite (bar) and chalcopyrite (chalc), surrounded by a chlorite and Mn-calcite (Mn-calc) rim. Holes of dissolved calcite sheets are replaced by the quartz (qtz) matrix. **D**: Pyrite (pyr) spherulites within heterogeneous hematite-chert matrix (thin-section 15). **E**: Radial chlorite nodules within a mudstone matrix (thin-section 8). **F**: SE image of a detail in E, illustrating the crystal habit and orientation of the chlorites and the interior rim of Mn-ilmenite (Mn-ilm). **G**: Grain consisting of various Fe-bearing minerals: minnesotaite (minn), chlorite, stilpnomelane (stilp), together with a randomly oriented euhedral magnetite (mnt) crystal. Similar to in C, partially dissolved Mn-calcite sheets are replaced by chert. This calcite-dissolution feature is quite common in the Hotazel close to the Ongeluk (thin-section 16). **H**: Detrital grains showing the phase relationships between Mn-calcite, stilpnomelane and magnetite mineral growth (thin-section 6). Euhedral magnetite crystals cut through the calcite sheet and stilpnomelane laths; the stilpnomelane needles in turn clearly intersect the calcite sheet. **I-J**: Crinkly laminated stilpnomelane-, minnesotaite-, chlorite-, hematite- and magnetite layers, locally interbedded with detrital grains (thin-section 5). The minerals are euhedral (apart from the submicrometer-sized hematite particles) and concentrated in particular layers. **K**: Euhedral magnetite and ankerite (ank) (overlain by stilpnomelane needles) BIF layers within a chert background (thin-section 1). **L**: Close-up of an ankerite rhomb. The crystal is heavily altered and replaced by chert; the outer rim is more Fe-rich than the crystal centre (thin-section 1).

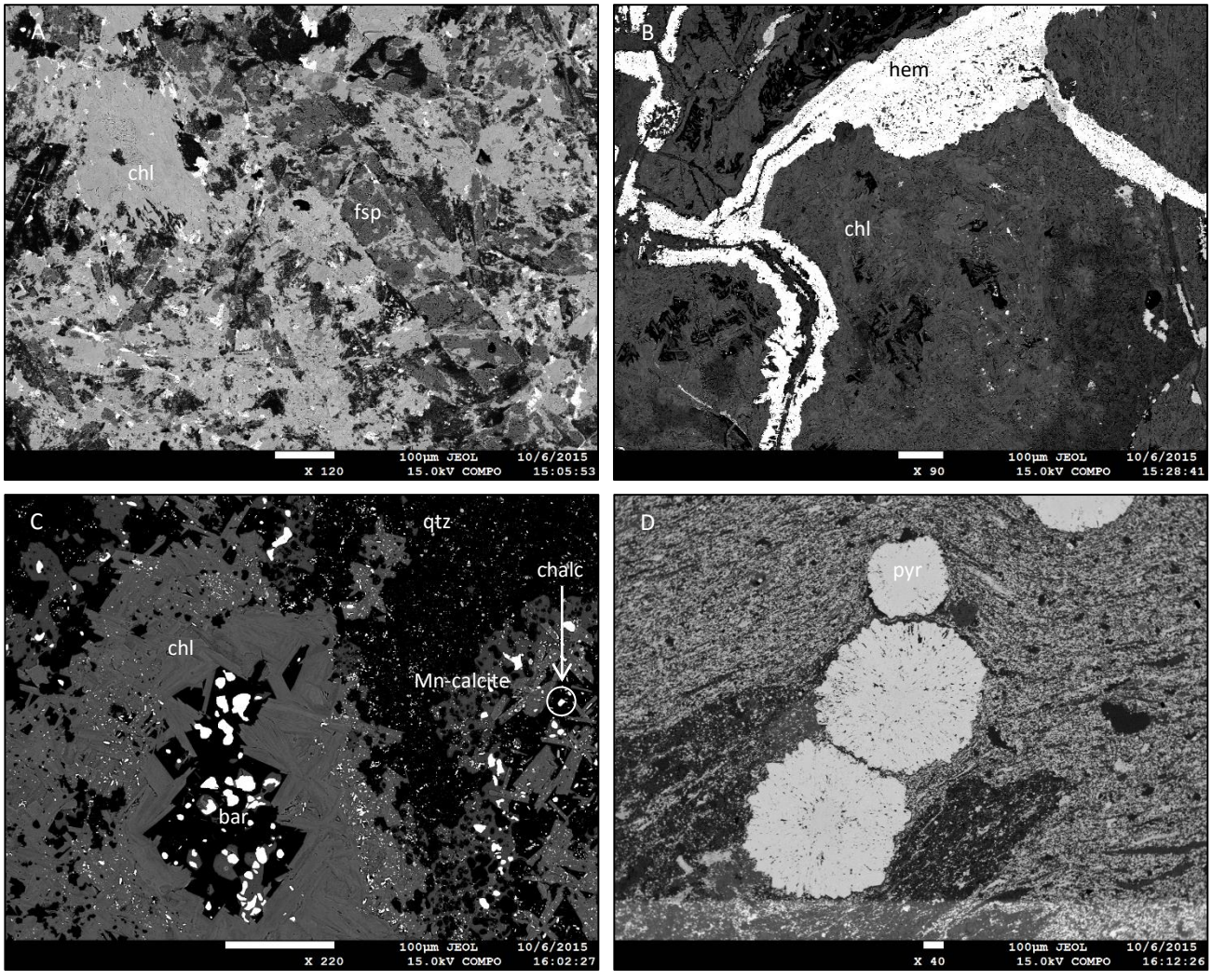

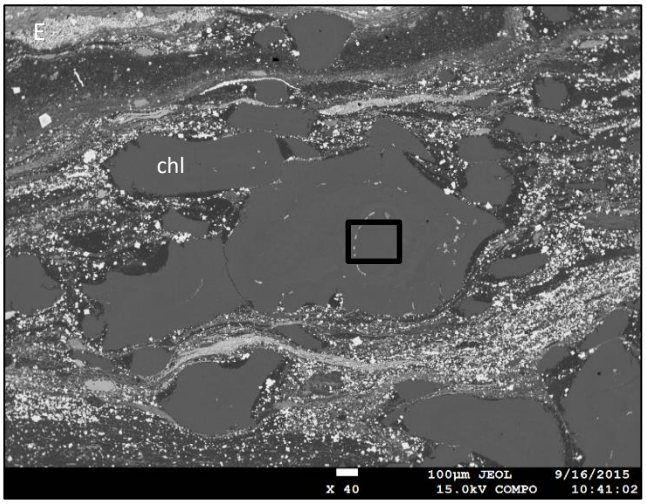
E
chl
X 40
100µm JEOL
15.0kV COMPO
9/16/2015
10:41:02

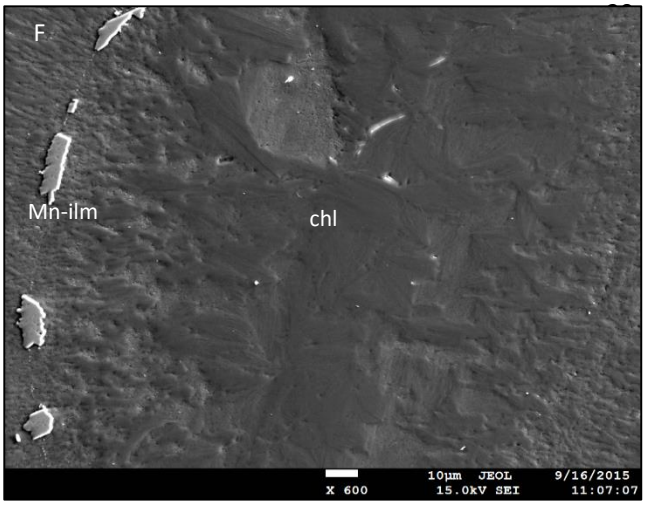
F
Mn-ilm
chl
X 600
10µm JEOL
15.0kV SEI
9/16/2015
11:07:07

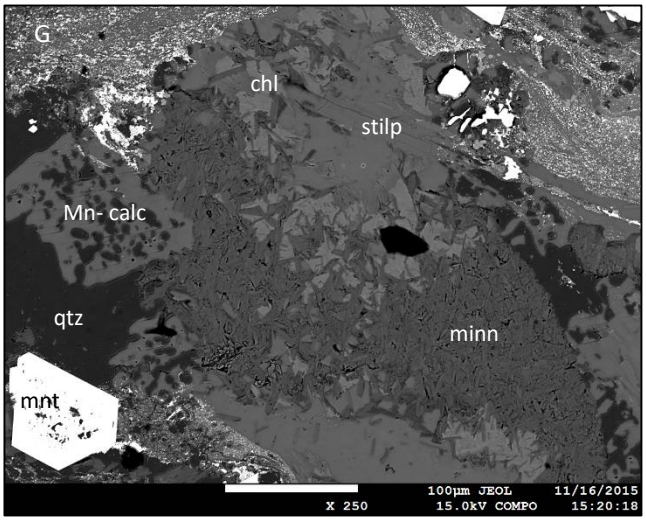
G
chl
stilp
Mn- calc
qtz
minn
mnt
X 250
100µm JEOL
15.0kV COMPO
11/16/2015
15:20:18

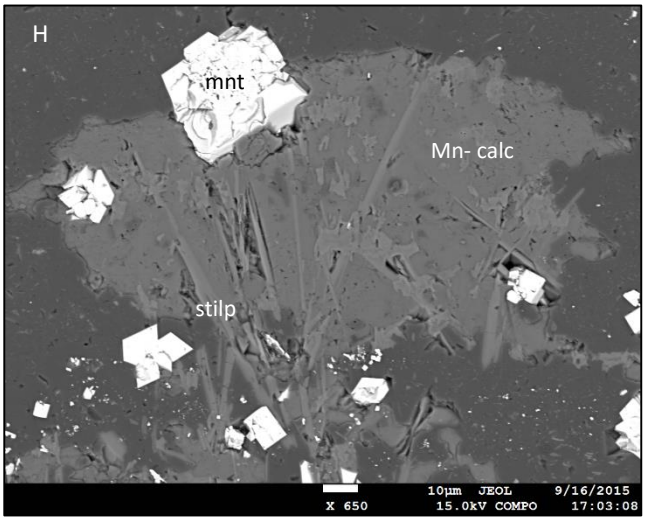
H
mnt
Mn- calc
stilp
X 650
10µm JEOL
15.0kV COMPO
9/16/2015
17:03:08

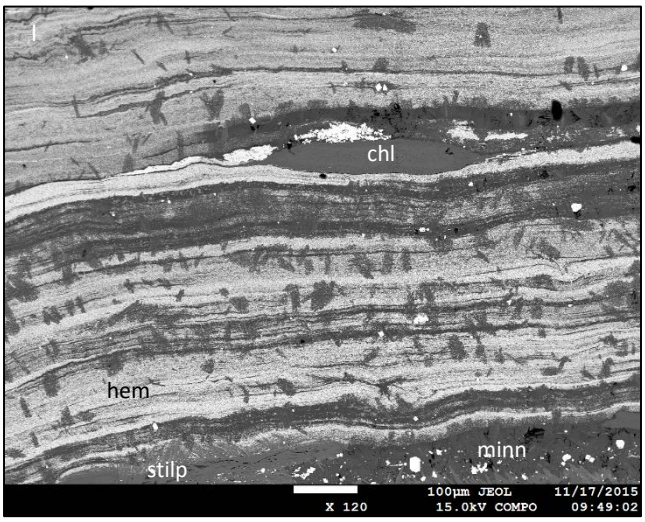
I
chl
hem
minn
stilp
X 120
100µm JEOL
15.0kV COMPO
11/17/2015
09:49:02

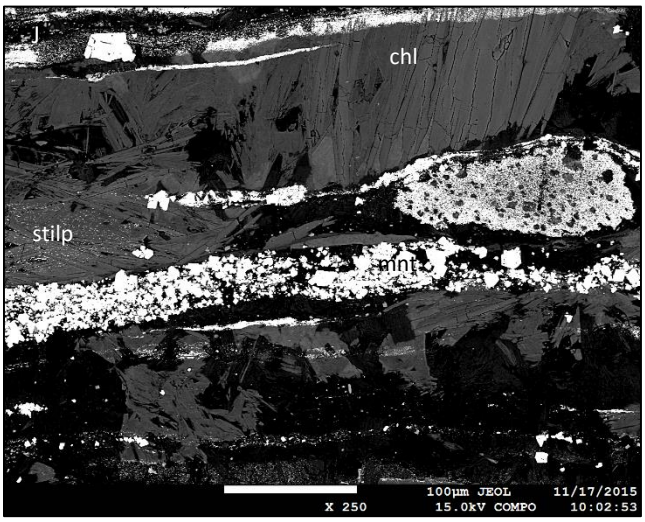
J
chl
stilp
mnt
X 250
100µm JEOL
15.0kV COMPO
11/17/2015
10:02:53

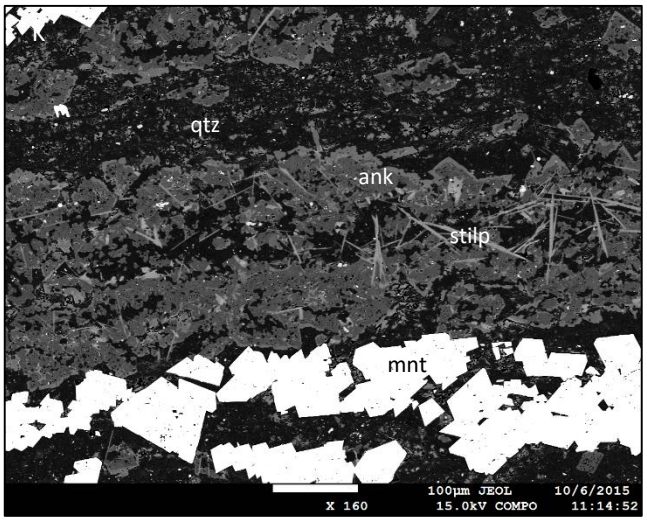
K
qtz
ank
stilp
mnt
X 160
100µm JEOL
15.0kV COMPO
10/6/2015
11:14:52

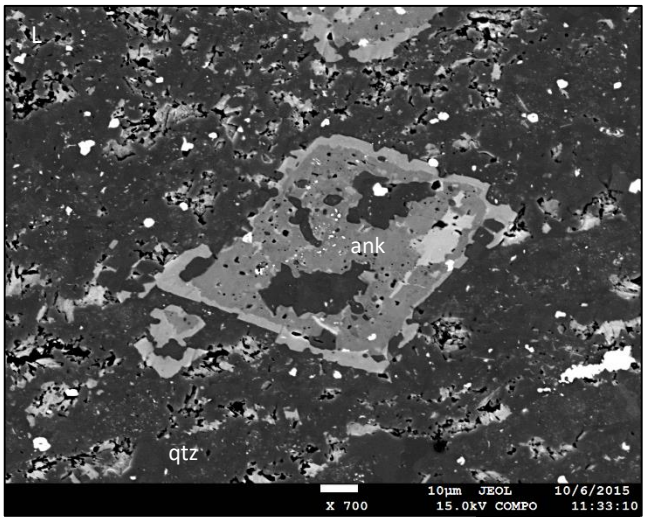
L
ank
qtz
X 700
10µm JEOL
15.0kV COMPO
10/6/2015
11:33:10

The major minerals present in the more clay-rich parts are similar to those in the mudstone described in the section above (cycle I). The bulges of jasper in this particular section are lighter coloured compared to pure hematite-chert due to a lower hematite content. In addition, the jasper displays several discontinuous microcracks of Mn-calcite.

Hematite lutite (cycle II)

This second hematite lutite is devoid of any clastic textures and consists almost entirely of parallel laminated dark red jasper. Millimetre-scale hematite-rich chert layers are alternated with darker, more magnetite-rich chert (see Figure 9). Despite the difference in mineralogy, the individual laminae have poorly defined graded contacts resulting in a uniform dark red colour of the rock rather than a banded character. Therefore, *hematite lutite* is still a more appropriate term than *banded iron formation*.

Apart from the sedimentary textures, the mineralogy of the rock is very similar that of the lenticular bedded hematite lutite of cycle I, although minnesotaite and Mn-calcite are present in far lower volumes. Pyrite occurs rarely as cubic euhedral to subhedral aggregates within the magnetite-rich layers.

Transition zone (cycle II)

Textures, sedimentary structures and mineral content are very similar to those in the transition zone of cycle I, apart from the absence of the Mn-calcite microcracks (see Figure 9 and 10, thin-section 8).

Mudstone (cycle II)

The lower stratigraphic part of the mudstone consists of brownish red, parallel laminated and fine-grained chemical mud, which changes in the upper part into a dark grey-greenish laminated but coarser-grained rock. The colour difference is due to the relative abundance of hematite: the lower part contains more hematite, whereas the upper part is poorer in hematite but richer in magnetite and chlorite nodules. The clastic-textured parts of the mudstone consist of submillimetre-sized ellipsoidal or lenticular grains of heterogeneous mineralogy that are closely packed together.

Transition zone (cycle III)

The transition zone of cycle III is more hematite-rich than those (cycle I and II) stratigraphically below. The lithology is made up of jasper load casts and heterogenous clasts floating in a heterogeneous matrix of chemical mud, and is best described as a “chaotic intraformational breccia” (Simonson et al., 1984 and references therein). See Figure 9. The clasts have a subrounded, angular or tabular shape and are sometimes oriented discordantly to the overall lamination. The jasper bulges are subrounded to lenticular and show a variety of colours, from bright red to dark brown or purple. The bright red sections are purely made up of hematite-chert, whereas the other colours reflect various proportions of magnetite, stilpnomelane, minnesotaite and Mn-calcite impurities. The clastic-textured matrix in between the jasper lobes contains elongate, mineralogically homogeneous lenses and heterogeneous grains of (mixed) chert, magnetite, stilpnomelane, minnesotaite, chlorite or Mn-calcite (see Figure 10, thin-section 6). The wavy appearance of these elongate lenses is caused by sediment loading prior to lithification, which has obscured the original bedding direction.

Hematite lutite (cycle III)

The third hematite lutite is not characteristically more hematite-rich compared to the (cycle III) transitional interval stratigraphically below. However, it is horizontally bedded and contains no SSD textures except for a short, pyrite-rich interval in the middle (see Figure 9). The lithology consists of small hematite-rich grains or lenses within a heterogeneous matrix of both chemical mud and sand, which are relatively rich in minnesotaite associated with Mn-calcite. Compared to cycle I the lenses are smaller, less elongate and have a brighter red colour.

At the base, a short interval of *crinkly lamination* is present. The individual lamina (1 mm - 50 µm) are homogeneous with regard to their mineralogy and they have a characteristic curved-wrinkled appearance (see Figure 9). A typical sequence consists of alternating microbands of concentrated hematite, minnesotaite and stilpnomelane, occasionally together with microbands of magnetite or chlorite. The edges of the microbands are distinctly defined by an abrupt change in mineralogy. The hematite particles occur either in densely packed hematite-chert layers, or in minnesotaite microbands, thereby almost entirely covering the minnesotaite crystals (see Figure11i and j). The Fe silicate crystals are also preferentially concentrated in individual, mono-mineralogical layers and oriented perpendicular to the bedding orientation. Tiny detrital grains have locally been incorporated in the lamination (see also 4i and j).

In the middle part several bulges of greenish coloured pyrite-rich lutite occur. In contrast to the spherulitic form of pyrite close to the Ongeluk lava, here, the pyrite crystals occur as euhedral cubes of ca 5-10 µm disseminated within the magnetite-chert matrix. F-apatite is also relatively common in this section.

Mudstone (cycle III)

The third mudstone interval is devoid of any clastic textures or SSD and consists exclusively of parallel laminated chemical mud. It transforms from a uniformly coloured, dark greenish-grey mudstone at the base into a banded mudstone of alternating brownish red and dark grey lamina which are relatively hematite-rich or hematite-poor, respectively. The mineral content is very similar to that of the other mudstones lower in the stratigraphy. However, chlorite does not occur isolated in nodules or spherulites but as small patches scattered in the matrix. EMPA results reveal also a slight increase in

the mineral's Al concentration compared to nodular chlorite further down in the stratigraphy (see Figure 13).

Hotazel BIF

The Hotazel BIF is composed of rhythmic alternations of distinct, fine-grained Fe-rich and Fe-poor microbands and is devoid of any clastic textures. The Fe-rich bands are made up of Fe oxides (i.e. magnetite or hematite) and the Fe-poor bands consist of Fe silicates and carbonates (i.e. stilpnomelane, minnesotaite, chlorite and ankerite). Very fine-grained quartz is constantly present as major groundmass mineral. The lower part of the BIF is more hematite-rich whereas in the upper part the Fe oxide bands are almost entirely made up of magnetite. The Fe-poor bands are predominantly composed of fine-grained stilpnomelane-rich chert at the base but become progressively more ankerite-rich towards the upper part. Accordingly, the upper BIF part of the Hotazel consists of a well-banded magnetite-Fe silicate-ankerite assemblage (see Figure 10, thin-section 1). On a larger scale, the individual microbands of homogeneous mineralogy are concentrated together and consequently display BIF mesobanding (millimetre- to centimetre-scale lamina thicknesses).

Microprobe data show that the rock is devoid of any siderite; ankerite is the only identified Fe carbonate phase. It occurs as large (10-100 µm) rhombohedra which show chemical zoning: the crystal core has a lower Fe / (Fe + Mg + Mn) ratio compared to the outer rim (see Table 3b and Figure11k and l). The ankerite rhombs are heavily altered according to the multiple gaps inside the crystal structure which are replaced by chert. Ankerite is also regularly overlain by Fe silicates (typically stilpnomelane) and magnetite. Chlorite is present but minor and occurs exclusively as small patches aligned to the overall bedding direction similar to the laminated mudstone below the BIF. It has a different Al-content and shape compared to the nodular form (see Figure 3).

Table 3a

Oxide (wt %)	chlorite	feldspar	calcite	titanite	hematite
SiO_2	25.9	52	0.15	30	1
1 S.D.	0.6	1.4	0.05	2.0	1.1
CaO	0.4	< 0.1	57	26	0.11
1 S.D.	0.7	-	1.1	1.6	0.05
SO_3	< 0.1	< 0.1	< 0.1	< 0.1	< 0.1
1 S.D.	-	-	-	-	-
K_2O	< 0.1	3.8	< 0.1	< 0.1	< 0.1
1 S.D.	-	0.3	-	-	-
TiO_2	0.1	0.10	< 0.1	33	1.4
1 S.D.	0.2	0.02	-	2.1	0.8
Al_2O_3	18.6	27.6	< 0.1	3.8	0.7
1 S.D.	0.9	0.6	-	1.7	0.7
MgO	14	2.8	0.11	1.2	0.5
1 S.D.	1.0	0.3	0.05	0.9	0.6
FeO	28	5.2	0.8	3	87
1 S.D.	1.1	0.8	0.5	1.4	3.5
MnO	0.6	< 0.1	1.2	< 0.1	< 0.1
1 S.D.	0.1	-	0.6	-	-
Na_2O	< 0.1	< 0.1	< 0.1	< 0.1	< 0.1
1 S.D.	-	-	-	-	-
Total	88	91.3	59	97	90.6
1 S.D.	1.2	0.6	1.2	2.0	0.3

Table 3b

Oxide (wt %)	magne-tite	stilpno-melane	minne-sotaite	chlorite	Mn-calcite	pyrite	ankerite (centre)	ankerite (rim)	Mn-ilmenite
SiO_2	1.3	49	56	30	0.7	0.2	0.8	2	0.9
1 S.D.	0.3	2.2	1.3	1.6	0.7	0.1	0.8	1.9	0.8
CaO	< 0.01	0.2	< 0.01	0.14	53	< 0.1	28	26	< 0.1
1 S.D.	-	0.5	-	0.1	4.2	-	0.3	-	-

Table 3a (left) and **b** (below): WDS-measured average chemical composition of the mineral phases present in **a)** the Hotazel Fm. part and **b)** the Ongeluk Fm. part of drill-core GL36. For each mineral composition, several crystals were measured in different thin-sections (see Appendix 2 for the entire dataset). 1 S.D. is the standard deviation for this mean composition. Elements are indicated with their oxide form, but it is important to note that the given weight percentages only represent the measured mass of the elements (atoms) and not that of oxygen. Elements lighter than F (i.e. mainly H and O) cannot be measured properly with WDS, but their total contribution to the mineral mass can be deduced from the deviation of the Total (mass %) from 100 %. Hematite could not be analysed in the Hotazel because grainsizes were too low. Quartz is not listed in this table but is ubiquitous in both the Hotazel and the Ongeluk

Table 3b (continued)

Oxide (wt %)	magne-tite	stilpno-melane	minne-sotaite	chlorite	Mn-calcite	pyrite	ankerite (centre)	ankerite (rim)	Mn-ilmenite
SO_3	< 0.1	< 0. 1	< 0.1	< 0.1	0.1	68	< 0.1	< 0.1	< 0.1
1 S.D.	-	-	-	-	0.1	1.3	-	-	-
K_2O	< 0.1	2	< 0.1	< 0.1	< 0.1	< 0.1	0.2	< 0.1	< 0.1
1 S.D.	-	1.1	-	-	-	-	0.2	-	-
TiO_2	< 0.1	< 0.1	< 0.1	0.1	< 0.1	< 0.1	< 0.1	< 0.1	50
1 S.D.	-	-	-	0.2	-	-	-	-	1.2
Al_2O_3	< 0.1	5	1.0	12	0.1	< 0.1	0.1	< 0.1	0.2
1 S.D.	-	0.3	0.8	1.7	0.2	-	0.1	-	0.1
MgO	< 0.1	11	21	18	1	< 0.1	17	11.2	0.4
1 S.D.	-	2.0	1.0	1.6	1.8	-	1.6	0.6	0.4
FeO	93	24	16	25	0.9	31.0	3.8	9	38
1 S.D.	0.5	1.3	1.3	1.9	0.3	0.2	0.6	2.0	0.4
MnO	< 0.1	1.2	0.10	0.37	3.7	< 0.1	11	8	10.4
1 S.D.	-	0.1	0.02	0.07	0.3	-	0.8	2.0	0.2
Na_2O	-	-	< 0.1	< 0.1	-	< 0.1	< 0.1	< 0.1	< 0.1
1 S.D.	-	-	-	-	-	-	-	-	-
Total	94.3	92	94.3	87.0	60	99	60	56	99.6
1 S.D.	0.5	1.1	0.5	0.8	2.3	1.4	1.4	1.4	0.4

Table 5 (lower left): Chemical composition of hematite-chert in thin-section 2 and 14, determined from the average of 98 and 72 WDS grid points (10 µm spot size), respectively. 1 S.D. is the standard deviation of the mean of all grid points.

Oxide (wt %)	Hematite-chert 2	Hematite-chert 14
SiO_2	89	72
1 S.D.	5.8	7.2
CaO	0.1	0.1
1 S.D.	0.2	0.3
SO_3	< 0.1	< 0.1
1 S.D.	-	-
K_2O	< 0.1	< 0.1
1 S.D.	-	-
TiO_2	< 0.1	< 0.1
1 S.D.	-	-
Al_2O_3	0.19	0.2
1 S.D.	0.1	0.1
MgO	1	0.3
1 S.D.	2.1	0.4
FeO	8	26
1 S.D.	3.6	6.5
MnO	0.2	< 0.1
1 S.D.	0.1	-
Na_2O	< 0.1	< 0.1
1 S.D.	-	-
Total	98	99
1 S.D.	2.1	0.8

a

(wt %)	CaO	F	P_2O_5	SO_3	FeO	BaO
F-apatite	54	4	40	*n.d.*	2	*n.d.*
F-apatite	55	4	40	*n.d.*	*n.d.*	*n.d.*
F-apatite	52	5	39	*n.d.*	*n.d.*	*n.d.*
barite	1	*n.d.*	*n.d.*	35	*n.d.*	64
barite	2	*n.d.*	*n.d.*	34	2	62
barite	*n.d.*	*n.d.*	*n.d.*	33	*n.d.*	67
barite	*n.d.*	*n.d.*	*n.d.*	33	*n.d.*	67
barite	*n.d.*	*n.d.*	*n.d.*	33	*n.d.*	67
barite	1	*n.d.*	*n.d.*	35	*n.d.*	64
barite	1	*n.d.*	*n.d.*	35	*n.d.*	64
barite	2	*n.d.*	*n.d.*	34	*n.d.*	64

b

(wt %)	Pb	S	Fe	Cu
galena	91	9	*n.d.*	*n.d.*
chalcopyrite	*n.d.*	37	31	33

Table 4 (above): Semi-quantitative EMPA results (EDS) of minor phases present in the Hotazel Fm.; *n.d.* stands for *not determined*. **a)** Apatite occurs in virtually every thin-section, but particularly in the opaque, clay-rich parts. Barite is only found close to the contact with the Ongeluk Fm. **b)** Sulphide minerals are only identified close to the contact with the Ongeluk Fm. (in association with barite).

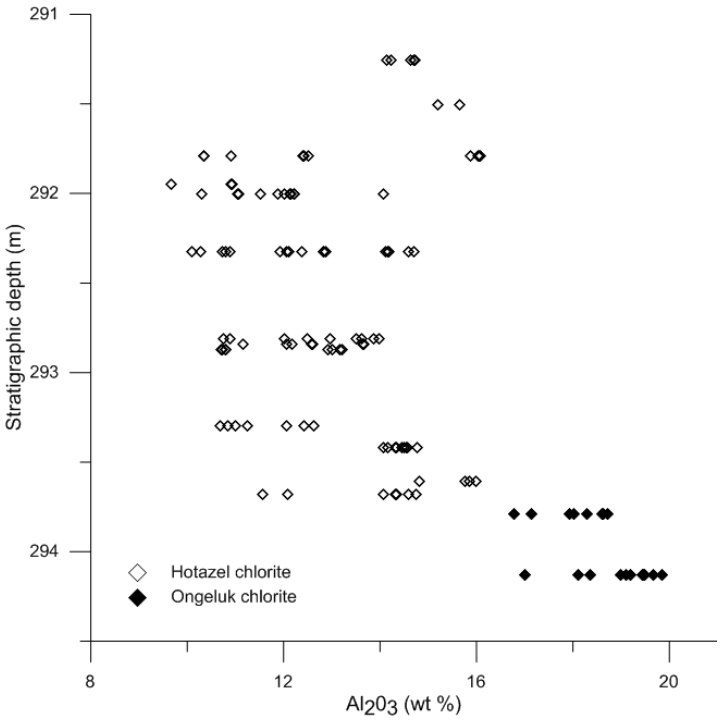

Figure 12: Al_2O_3 weight percentage of chlorite (WDS data) versus stratigraphic depth. Notice the decrease in the chlorite Al_2O_3 content from the Ongeluk to the Hotazel Fm., and the subtle increase in the upper Hotazel again.

4.1.3 Major element geochemistry

Vertical geochemical trends of the major elements (Si, Fe, Mg, Ca, Mn, Al, Ti, S, P, K and Na) in the Hotazel stratigraphy (and uppermost Ongeluk) are given in Appendix 3, of which a selection is presented in Figure 14. It is important to note that these results should exclusively be regarded in a qualitative way (see section 3.2.1). The relative elemental mass fractions are plotted along with the element/Al-ratios, in order to filter out the effect of dilution by sedimentary phases devoid of Al.

Along the whole depth profile Si and Fe constitute the major mass fraction of the rock, followed by Mg, Al and Ca; Mn, Na, K, Ti and P are only present in minor amounts (not more than a few wt %); S is only abundant in the pyrite-rich lutite interval. Analogous to the cyclic behaviour of changes in the sedimentary facies, the concentration profiles of several elements show a rhythmic behaviour along the stratigraphy.

In general, the mudstones and transition zones are highly enriched in Al relative to the hematite lutites and BIF. For these Al-rich intervals, the Al-Ti ratio remains at a rather constant high level (the Al-poor parts have near-zero Al/Ti values), altough the lowermost part of the hematite lutite shows a gradual decline in the Al/Ti with distance from the Ongeluk lava. In terms of mineralogy, Al is mainly hosted in the Fe silicate minerals chlorite and stilpnomelane; hence these minerals constitute a considerable portion of the mudstones and transition zones (clastic textured parts), in accord with the observations reported in section 4.1.2. This is also demonstrated in the Mg and Mn wt % profile, which correlates positively with that of Al in regard to these intervals, since Mg and Mn are also incorporated in the crystal lattices of the Fe silicates.

The Fe/Al diagram clearly shows a stratigraphic variation which is 180° out of phase with that of the Al content and Al/Ti plots. In the mudstones and clastic-textured transition zones the Fe content over the aluminosilicate component is very low compared to that of the hematite lutite and BIF facies, which evidently results from the large difference in the Al concentration between these two groups. Apparently, in the mudstone and clastic textured parts the rocks' Fe content is predominantly hosted in chlorite and stilpnomelane, whereas in the relatively aluminosilicate-free parts Fe is mostly bound to the other Fe-bearing phases (i.e. oxides, carbonates, pyrite and minnesotaite). Areas in the stratigraphy which display a positive correlation between Fe/Al and Ca/Al, Mg/Al or S/Al are rich in Fe carbonate (i.e. ankerite), Al-poor Fe silicate (i.e. minnesotaite) and Fe sulphide (i.e. pyrite).

Areas which only show Fe/Al enrichment (i.e. no elevated element/Al values for the other elements) are predominantly constituted of Fe oxides, for example the uppermost part of cycle I hematite lutite. Stratigraphically somewhat lower, peaks in the Fe/Al correlate well with those in the Ca/Al; the same applies for Hotazel BIF at the top of the Hotazel. At these stratigraphic intervals, the Al-normalised Mn and Mg content (i.e. corrected for dilution of aluminosilicates) are also considerably high. Apparently, these zones of the Hotazel stratigraphy are affected by an increased supply of Mn- or Mg-bound carbonate. The increased Mn/Al is in accord with the high modal abundance of Mn-calcite observed in the hematite lutite part of the Hotazel and of ankerite in the BIF part (see section 4.1.2). Although no Mg-rich carbonate (i.e. ankerite) is found in the hematite lutite, the Mn-calcite is in close association with minnesotaite. The large bulge in the Fe/Al and Mg /Al profile thus corresponds to the large volume of the Mg-rich (and Al-poor) Fe silicate minnesotaite. The occurrence of pyrite is clearly demonstrated by the correlation between the Fe/Al distribution and the three S-rich intervals, i.e. occurring in the hematite lutites of cycle I and II and in the pyrite-rich lutite of cycle III.

Figure 14: Overview of selected micro-XRF data showing vertical geochemical trends along the GL36 drill-core, from the upper part of the Ongeluk lava towards the Hotazel BIF at the top. The XRF data are presented as three-point averages of 1-mm laser point measurements (i.e. 3 mm averages) to enhance smoothness of the profile, but still locally some strong spikes occur. At several stratigraphic intervals XRF data are missing; for those parts no line has been plotted. **A**: The Al weight % compared with the Al-Ti ratio. **B**: The Al normalised profile of Fe (x 10^2). **C**: The Mg weight % compared with its Al-normalised profile. **D**: The Al normalised profile of S. **E**: The Ca weight % compared with its Al-normalised profile. **F**: The Mn weight % compared with its Al-normalised profile. The micro-XRF method has a large uncertainty (> 10%) and therefore element weight percentages are semi-quantitative. See Appendix 3 for the entire major element dataset obtained from micro-XRF.

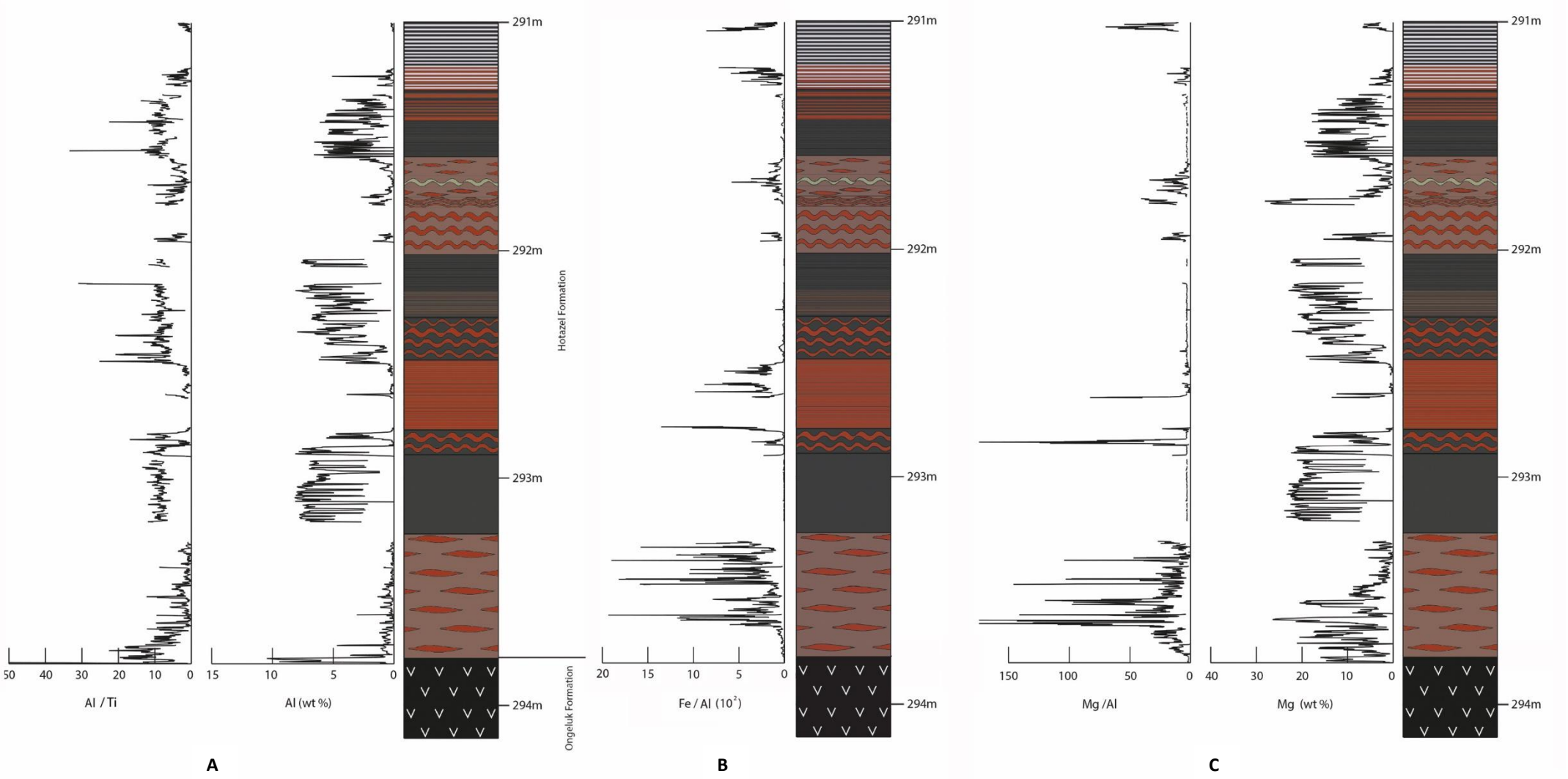

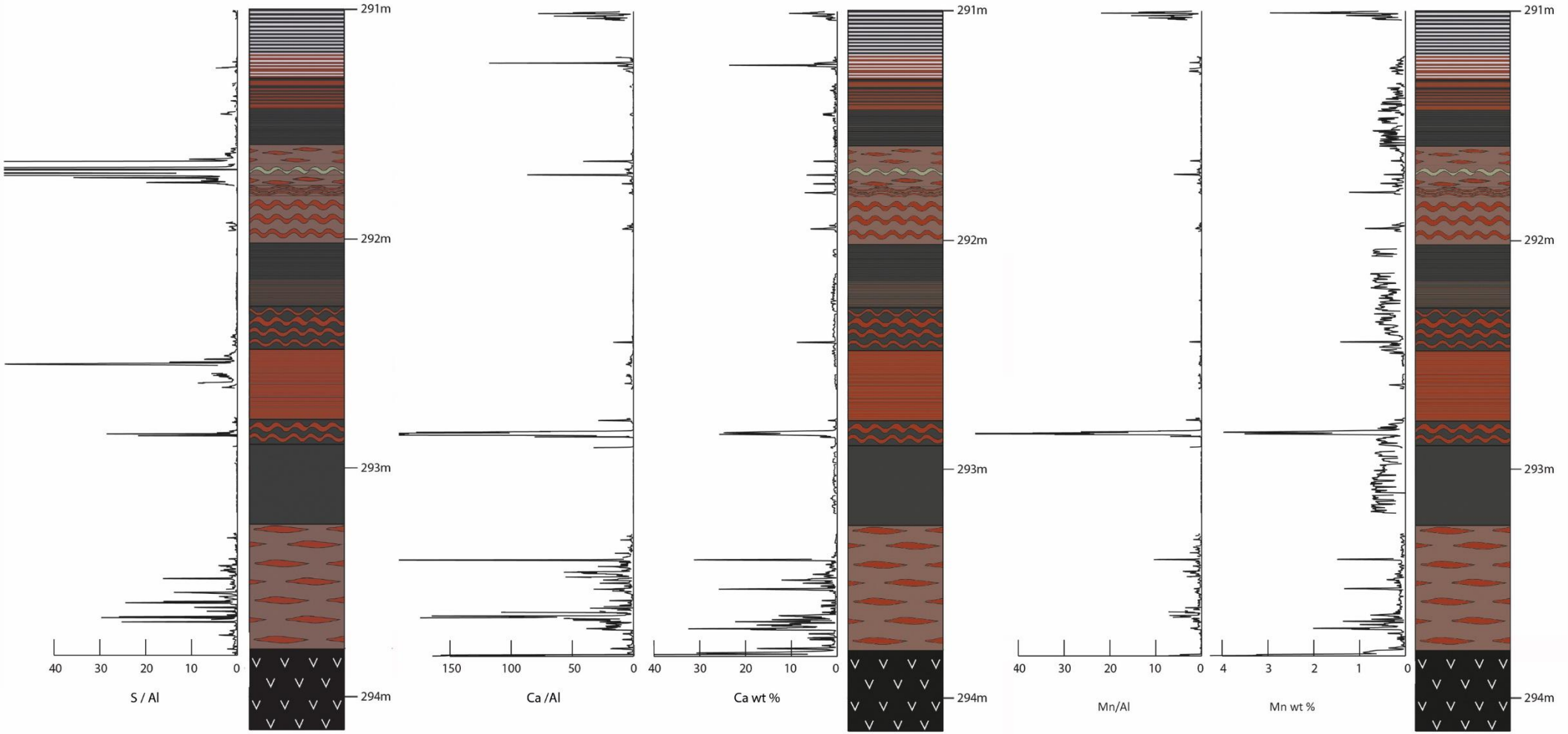
291m
292m
293m
294m
40
30
20
10
0
S / Al
150
100
50
0
Ca /Al
Ca wt %
Mn/Al
4
3
2
1
Mn wt %

D **E** **F**

4.2 Characterisation of hematite

4.2.1 Configuration, size and crystal habit

BSE images of the Hotazel jasper sections show that hematite occurs as minute crystals, often forming concentric networks around spherical globules of chert (see e.g. Figure 15d). The chert spheres (< 5 µm) show no internal lamination or structure and are therefore likely to be relict colloidal textures. The hematite occurs as scattered individual crystals ranging from 100 to 800 nm in diameter, with a morphology ranging from subrounded to hexagonal plates to more elongate forms as shown from BSE and SE images (see Figure 13b and 15a-e). The particles seem to be slightly aligned with their longest dimension to the direction of the concentric network structure. In the crinkly laminated part of the Hotazel, the individual submicrometre hematite crystals are preferentially aligned to the horizontal lamination (see Figure 13a). The crystals are densely packed in monomineralic layers, which have a much higher hematite concentration than normal jasper bands (which are primarily composed of chert).

In thin-section 2, which contains BIF microbands of hematite-chert (see also Table 2), the individual subrounded hematite crystals that are observed on the BSE images are seemingly of submicrometre scale (see Figure 15a-b), but the SE image shows that these are actually composed of aggregates of numerous, ultrafine (< 10 nm) hematite spheres (see Figure 15c). These nanospheres have not been observed in the other hematite-chert sections of the Hotazel, i.e. in jasper bulges or lenses further down in the stratigraphy, implying that this feature is specific for the BIF layers only. On the contrary, it may be possible that these nanospheres are present in the other jasper sections, but that they were not visible due to a low surface relief of the studied polished thin-sections (i.e. thin-sections 5, 8 and 14, of which the images are shown in Figures 13a-b and 15d-e).

Compared to in the pure jasper sections of the Hotazel, hematite has a different crystal morphology and size in the more heterogeneous parts (i.e. hematite-poor) and mudstones. It occurs as small clusters of randomly or radially oriented rod-like micrometre-sized crystals (typically 5 µm in length) disseminated in the mudstone matrix or in chlorite nodules (see Figure 13c-d). Locally it has overgrown stilpnomelane or chlorite needles (see Figure 13c). In the veins at the contact with the Ongeluk lava hematite occurs at the rim as massive aggregates of radiating microplaty crystals of > 10 µm in length (see Figure 11b).

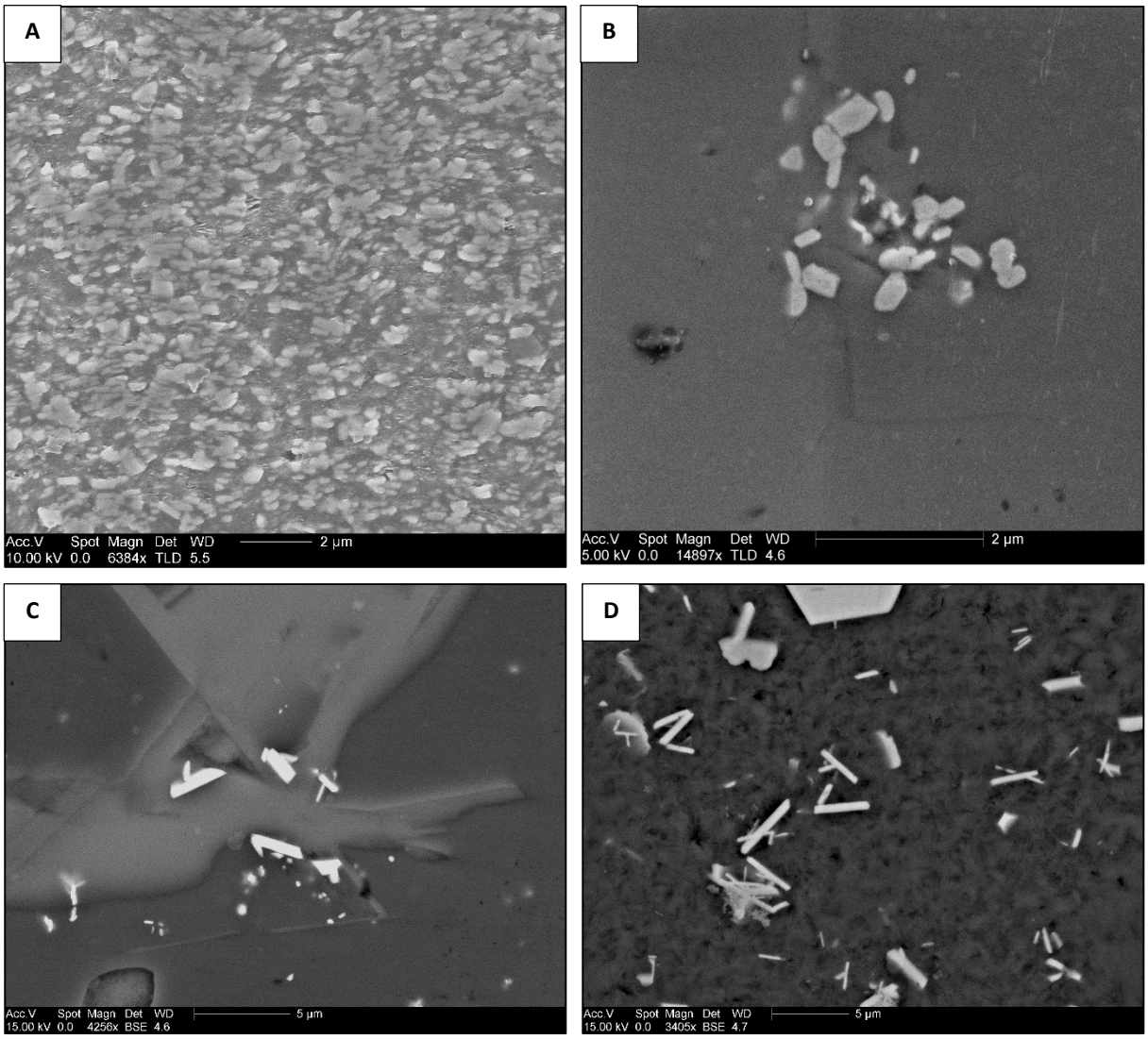

Figure 13 (previous page): SEM images of hematite crystals at various locations in the Hotazel Fm. **A**: SE (UHD) image of a detail of a hematite-rich crinkly laminated layer (thin-section 5). The hematite crystals (< 1 µm) have a subrounded to platy morphology and are aligned to each other in the horizontal plane. Compared to the hematite-chert sections in Figure 15 the concentration of hematite particles is considerably higher. **B**: SE (UHD) image of a hematite-chert inclusion (thin-section 8). The inclusion is relatively calcite- and stilpnomelane-rich and hematite-poor. The picture shows a small cluster of subrounded to platy hematite crystals (submicron scale) standing out from the background surface. Again, no nanospherules are visible. **C**: BSE image of the same (hematite)-chert inclusion in B, but here showing stilpnomelane fibres overlain or replaced by large (> 1 µm), secondary hematite. **D**: BSE image of a detrital grain composed of tiny chlorite fibres (thin-section 8). Micron-sized, rod-like (radial) hematite particles are scattered randomly. In the upper left corner, Mn-ilmenite and euhedral magnetite are present.

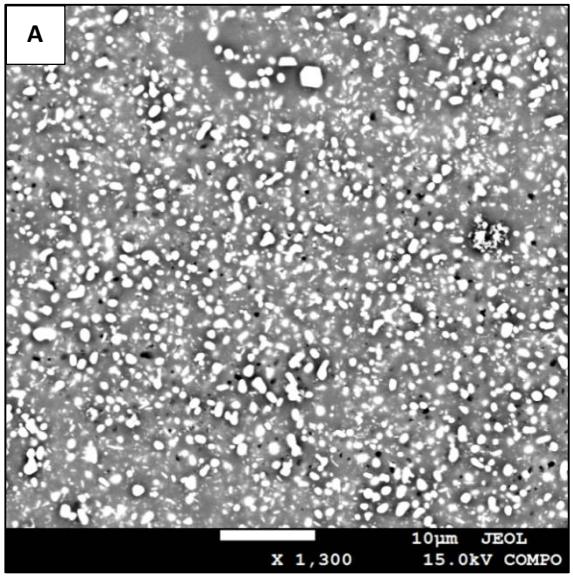

Figure 15: SEM images of hematite crystals in the hematite-chert sections of the Hotazel. **A**: Back-scattered electron (BSE) image of a detail of a jasper BIF microband (thin-section 2). The grey scale implies that the apparent individual hematite crystals (white) are subrounded and range in size from ca 2 µm to < 1 µm. The grey matrix is composed of silica. **B**: Secondary emission (SE) image of the same BIF layer as in A, showing the surface relief. Here, the (seemingly) individual hematite particles are visible not by composition but based on their crystal size and morphology. **C**: An ultra-high definition (UHD) SE image of a detail from B. The picture reveals that the seemingly subrounded hematite crystals of (sub)micron scale identified in A and B are in fact composed of nanosized spherules, intermingled with nanosized silica. **D**: BSE image of a detail of a hematite-chert lens (thin-section 14). The hematite crystals are < 1 µm and have a subrounded to elongate habit. Clusters of hematite display a network around chert spheres (ca 5 µm in width). **E**: SE (UHD) image of a detail from D. Here, no nanospherules are visible.

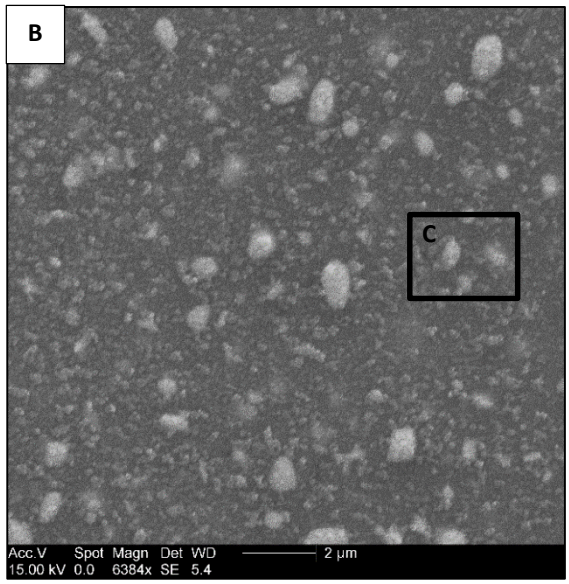

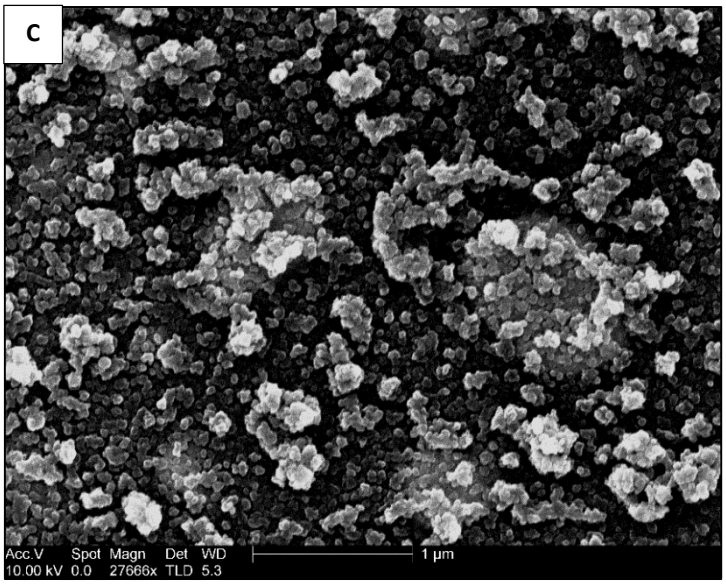

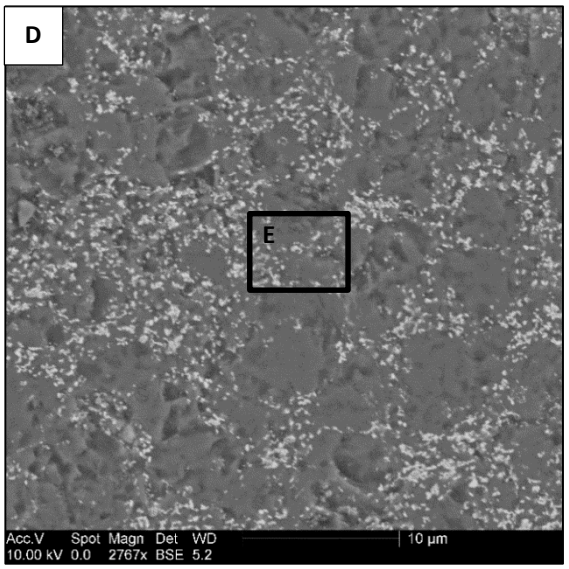

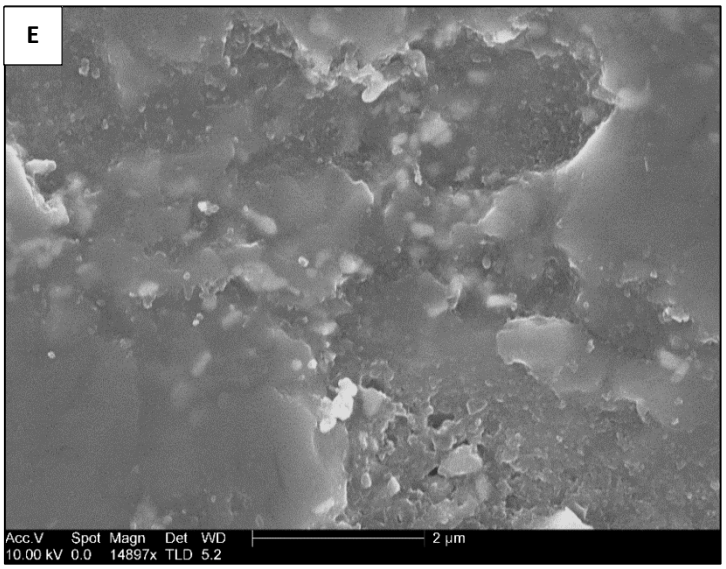

4.2.2 Major and trace element geochemistry

Microprobe grid data (see Table 5) together with LA-ICP-MS data (Appendix 4) give an indicatation of the relative major and trace element concentrations of the hematite-chert sections. Jasper consists mainly of silica (73-91 wt % SiO_2) and Fe oxide (7.8-26 wt % FeO), with low concentrations of Mg, Al, Ca, Mn and Ti.

Rare-earth elements and Yttrium (REE + Y) concentrations and patterns of jasper obtained from eight thin-sections at different stratigraphic levels of the Hotazel are presented in Table 6 and Figure 16a, normalised to the Post-Archean Average Shale (PAAS) values from Pourmand et al. (2013). Bau and Dulski (1996; and references therein) have shown the advantage of combining REE with Y value for interpreting their behaviour and therefore Y is inserted in between Dy and Ho, in accord to its ionic radius. Minor amounts of lithogenic material incorporated in the hydrogenous sediment are sufficient for obscuring the original trace elemental signature and therefore only REE + Y data of clean jasper samples are presented here (see section 3.2.2 for sample purity determination procedure). The concentrations listed in Table 16a represent the average values that were constituted of several individual laser ablation points; due to large differences in the trace element concentration between the individual measurement points, the 1 σ standard deviations are very high. However, the relative REE + Y distribution patterns of all accepted laser point analyses are quite consistent (see Appendix 4.3).

Selected geochemical data that are relevant for comparison with the REE + Y signal of (ancient) seawater are listed in Table 7, following the approach of Bolhar et al. (2004). In principle, REE anomalies are defined as the relative enrichment or deficiency of the concerning element relative to its neighbouring elements, expressed as $(REE_n/REE_n^*)_{SN} = 2REE_n /(REE_{n-1} + REE_{n+1})$, where REE_{SN} stands for shale-normalised REE abundance and *n* indicates the lanthanide number of the concerning REE. Exceptions to this rule are the anomalies of La, Ce and Gd, which are defined as La / (3Pr – 2Nd), Ce / (2Pr – 1 Nd) and Gd / (2Tb – 1Dy), respectively. This extrapolation is applied to avoid arriving at apparent (i.e. incorrect) enrichments or deficiencies of the elements which are actually caused by anomalies in the abundances of their neighbouring REE (Ce, La and Eu, respectively). In addition, La and Ce anomalies are graphically displayed in $(Ce/Ce^*)_{SN}$ versus $(Pr/Pr^*)_{SN}$ space in Figure 17, for which Ce anomalies are calculated after Bau and Dulsk (1996). Moreover, the sample's Y/Ho is plotted along their Zr content in Figure 18.

Figure 16a clearly shows REE + Y abundances of < 0.015 to 0.4 times PAAS values, depletion in the light REE (LREE) relative to the heavy REE (HREE), insignificant to large positive Eu anomalies and positive Y anomalies for all samples; Table 7 indicates the presence of positive anomalies for La and Gd but no convincing Ce anomaly. On the basis of the LREE depletion, the samples are subdivided into two separate groups. Sample 2 displays a distinctly more LREE depleted profile compared to the other samples (6, 8, 9, 11, 13, 14 and 16). Its average $(Pr / Yb)_{SN}$ of 0.03 is more than a factor 10 lower than for the other thin-sections, which have an average $(Pr / Yb)_{SN}$ of 0.38. However, both groups have a similar HREE (Yb and Lu) content. The REE +Y patterns of the less LREE depleted samples are almost parallel to one another, apart from small variations in the positive Eu anomalies. Sample 2 is derived from a hematite-chert BIF layer in the upper Hotazel stratigraphy, whereas the other samples are coming from jasper lenses or bulges in the Hotazel lutite part further down in the stratigraphy (see Table 2 and Figure 9). Therefore, in Figure 16b the two sample groups are indicated with *BIF hematite* and *lutite hematite*, respectively.

In Figure 16b trace element features of BIF hematite and lutite hematite are compared to the REE + Y distribution of modern seawater (Bau et al., 1996) and modern hydrothermal vent fluids (Bao et al., 2008). Modern seawater shows LREE depletion relative to HREE: the shale-normalised Pr–Yb ratio of the Pacific Ocean plotted in Figure 16b has a value of 0.13, but typical values for the open ocean are usually in the range of 0.10-0.28 (Johannesson et al., 2006 and references therein). Further, the modern (oxygenated) oceans show a distinctly negative Ce anomaly and positive La, Gd and Y anomalies, whereas the high-T vent fluids are LREE enriched and show a conspicuous Eu anomaly. In Figure 16c the REE + Y distribution of BIF hematite and lutite hematite samples are compared to ancient and modern marine precipitates. The REE signal of the Hotazel oxide facies reported higher up in the Hotazel stratigraphy (Tsikos and Moore., 1997; no Y data) displays are pattern very much alike the lutite hematite data from this study, albeit the fact that it exhibits slightly more LREE depletion. The REE profile (no Y data) of the hydrothermal plume-derived Fe oxide sediments of the TAG hydrothermal field (German et al., 1993) shows a very prominent Eu anomaly similar to that of the high-T hydrothermal fluids in Figure 16b, but is somewhat LREE depleted instead of enriched. The hydrothermal Fe crusts from the Hawaii Rift zone are relatively rich in trace elements compared to the other deposits (Bau et al, 2014), although its $(Pr / Yb)_{SN}$ of 0.37 is similar to that of the average lutite jasper samples. Their REE + Y distribution displays a negative Ce anomaly, a superchondritic Y/Ho and a vague Eu anomaly.

Thin-section	2	1 S.D.	6	1 S.D.	8	1 S.D.	9	1 S.D.	11	1 S.D.	13	1 S.D.	14	1 S.D.	16	1 S.D.
	n = 9		n = 4		n = 2		n = 2		n = 2		n = 8		n = 8		n = 5	
La	5.5	1.9	109.7	171.6	66.7	44.5	84.5	36.9	97.1	61.6	50.9	30.3	85.6	33.2	69.4	44.6
Ce	5.0	1.3	83.1	127.4	55.0	32.6	61.0	29.1	90.8	57.2	43.4	23.3	68.0	23.6	52.1	32.7
Pr	5.6	1.5	67.3	102.3	51.0	32.1	53.3	24.5	75.6	43.6	45.1	24.2	71.7	27.5	53.0	34.0
Nd	5.9	1.5	67.5	100.5	57.6	36.9	65.1	32.4	77.8	40.1	49.8	27.3	82.7	30.7	60.0	36.7
Sm	8.4	3.4	75.5	115.9	58.4	36.5	72.8	39.1	98.9	53.7	58.1	26.9	91.6	33.1	59.1	36.8
Eu	18.9	5.9	190.3	298.9	127.6	90.1	204.1	93.0	148.6	90.1	83.0	40.1	178.3	75.7	262.4	194.2
Gd	14.2	3.8	90.1	135.3	88.6	58.1	98.5	45.5	138.1	60.5	82.9	43.2	151.6	54.7	94.5	61.5
Tb	23.7	6.3	89.9	142.5	83.6	53.5	96.6	44.7	142.0	67.8	80.9	36.6	163.0	56.3	87.9	54.7
Dy	36.9	9.1	128.3	195.9	111.9	73.5	128.5	55.5	206.7	99.4	103.8	53.1	197.7	62.3	104.2	54.1
Y	67.4	14.8	202.1	289.6	174.7	118.3	262.9	101.1	312.2	154.3	163.8	95.3	383.5	126.8	224.3	114.0
Ho	54.5	18.9	146.0	216.3	129.6	94.2	151.9	62.7	229.3	121.1	112.8	55.6	241.8	82.2	129.0	54.5
Er	76.9	25.6	146.0	210.5	136.9	852.3	166.7	70.7	250.1	123.9	123.0	65.4	245.3	73.5	127.5	64.6
Yb	175.4	39.5	142.2	197.9	130.0	528.6	133.0	49.6	253.5	111.7	120.5	47.2	216.8	65.4	125.8	55.9
Lu	209.0	41.0	175.3	264.7	139.2	99.7	163.5	50.8	299.9	146.9	136.5	73.8	221.3	77.0	149.7	57.6

Table 6 (above): PAAS-normalised hematite-chert REE + Y concentrations (ppb) per thin-section. 1 S.D. is the 1 σ standard deviation of the individual laser ablation point concentrations with respect to the mean value for each thin-section. The number of laser ablation point measurements is indicated with *n.* Due to large differences in the trace element concentration between the individual measurement points, the 1 S.D. values are very high. For the relative REE + Y distribution patterns of all accepted laser point analyses, see Appendix 4.3.

Table 7 (below): Averages of selected geochemical data for the hematite-chert samples. The REE anomalies are calculated as defined by Bolhar et al. (2004) and as explained in the text. 1 S.D. is calculated from the individual laser ablation point concentrations with respect to the mean value for each thin-section.

Thin-section	2	1 S.D.	6	1 S.D.	8	1 S.D.	9	1 S.D.	11	1 S.D.	13	1 S.D.	14	1 S.D.	16	1 S.D.
(Ce/Ce*)sn	0.94	0.64	1.24	4.61	1.24	2.18	1.47	2.19	1.24	1.80	1.07	1.58	1.12	1.23	1.13	2.03
(Pr/Pr*)sn	1.03	0.33	0.89	1.67	0.91	0.69	0.85	0.49	0.90	0.64	0.97	0.64	0.95	0.44	0.95	0.73
(Eu/Eu*)sn	1.67	0.65	2.30	4.37	1.74	1.47	2.38	1.37	1.25	0.87	1.18	0.71	1.47	0.73	3.42	2.99
(La/La*)sn	1.09	1.23	1.64	9.33	1.76	5.75	2.83	9.39	1.36	3.06	1.42	3.72	1.73	3.64	1.78	5.83
(Gd/Gd*)sn	1.36	2.06	1.75	12.06	1.60	3.91	1.52	2.57	1.79	3.97	1.43	2.35	1.18	1.26	1.32	2.40
Y/Ho	32.1	45.4	35.9	45.5	34.9	39.4	44.9	42.1	35.3	30.6	37.6	18.9	41.1	27.8	45.1	29.8
(Pr/Yb)sn	0.03	0.01	0.47	0.98	0.39	1.62	0.40	0.24	0.30	0.22	0.37	0.25	0.33	0.16	0.42	0.33
Zr (ppm)	0.77	0.77	0.91	1.11	0.15	1.36	1.06	1.14	0.85	1.20	1.31	0.80	2.70	1.34	1.19	0.62
total REE (ppm)	4.1		24.1		18.0		22.6		29.4		15.4		28.8		19.5	

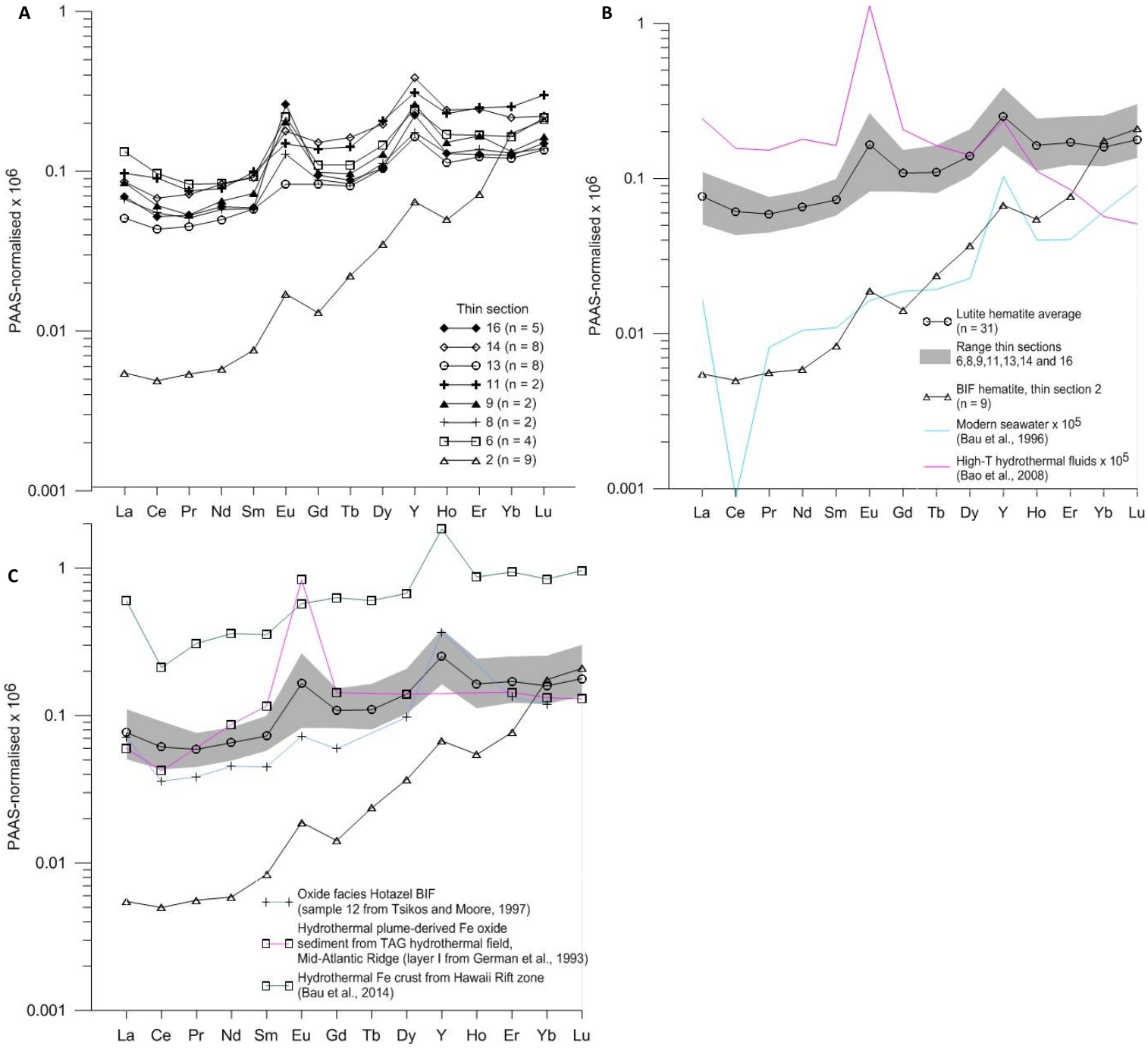

Figure 16: Plots or rare-earth element data normalised to post-Archean Australian shale (PAAS). **A**: REE + Y concentrations (ppb) of hematite-chert from several parts of the Hotazel (see Table 2 and Figure 9 for thin-section description and stratigraphic location). All samples clearly have a positive Eu and Y anomaly. Further, all samples are LREE depleted, but the REE + Y profile of hematite-chert in thin-section 2 is distinctly more LREE depleted than the rest. This hematite-chert sample originates from the Hotazel BIF; the other samples were acquired from the Hotazel lutite part. In B and C, the samples and subdivided into and named after one of these two groups. **B**: Comparison of the two distinct REE + Y profiles from the Hotazel lutite and BIF parts (data from this study) with modern seawater x 10^5 and with modern high-temperature hydrothermal fluids x 10^5 from the Juan de Fuca Ridge (Bao et al, 2008). **C**: Comparison of the Hotazel lutite and BIF hematite-chert REE + Y from this study with the Hotazel BIF oxide facies data from higher up in the stratigraphy (Tsikos and Moore (1997); with modern hydrothermally derived Fe crust (Bau et al., 2014) and with modern hydrothermal plume-derived Fe oxide sediment from the TAG hydrothermal field (German et al., 1993).

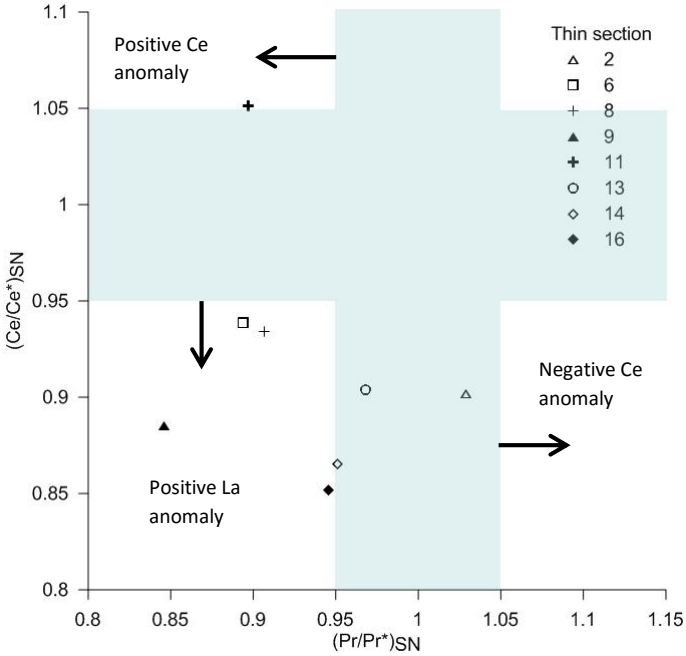

Figure 17: Hematite-chert averaged samples from the Hotazel in a graph of $(Ce/Ce^*)_{sn}$ versus $(Pr/Pr^*)_{sn}$ (after Bau and Dulski, 1996).The shaded area represents the field in which samples have neither La nor Ce anomalies. None of the samples has a negative Ce anomaly. All thin-sections except for 11 have a positive La anomaly; sample 11 has a slightly positive Ce anomaly. The 1 S.D. error bars are exceeding the limits of this graph and therefore are not indicated. See Appendix 4.3 for the individual sample anomalies.

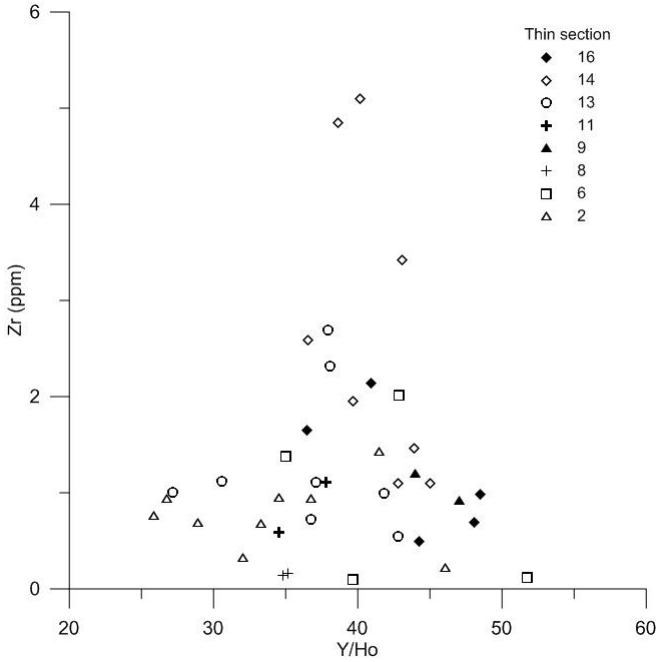

Figure 18: Diagram of Zr versus Y/Ho showing all hematite-chert samples (averages per thin-section are listed in Table 7). Y/Ho (wt) ratios range from 26 to 52. The Zr content of thin-section 14 is somewhat elevated but falls well below 6 ppm; for the rest of the samples the Zr concentration is lower than 3 ppm.

4.3 Fe isotope sample data

4.3.1 Sample characteristics

4.3.1-1 Mineral content

The mineral content of the jasper samples selected for Fe isotope analysis (HF1-HF7) is presented in Table 8, and the raw XRD 2θ plots are displayed in Appendix 5. It is important to note that these results should only be regarded in a qualitative way (see also section 3.3.2). Chert (quartz) fractions are evidently the highest for all samples, with prominent intensity peaks in the diffraction spectra (see Appendix 5) and estimated abundances of more than 70 wt % for HF7, above 80 wt % for HF1 and > 85 wt % for HF2, 3, 4, 5 and 6. Hematite is the second most abundant mineral phase in most of the samples, with the largest values for HF7 (ca 19 wt %). In contrast, in HF5 chlorite (chamosite) comprises a larger portion of the sample's weight than hematite. Both minerals show similar diffraction peak heights. In HF3 hematite displays more obvious peaks in the diffraction spectrum compared to the accessory minerals, i.e. minnesotaite (talc), ankerite and magnetite, but is in terms of weight fraction also richer in minnesotaite than hematite. Samples HF1, 2, 4 and 6 have hematite as second most important mineral constituent, but similarly are contaminated with various amounts of magnetite, chlorite and ankerite; HF6 also contains calcite. With regard to the hematite purity of the Fe isotope samples, HF7 accordingly has the highest fraction of hematite relative to the total amount of accessory Fe-bearing phases.

4.3.1-2 Chemistry

ICP-OES major and trace element data for the bulk-rock (HF1-7 and OF1-3) and HCl-fraction (HF3, 4, 6 and 7 HCl) Hotazel and Ongeluk Fe isotope samples are listed in Appendix 6. The results represent the dry, dissolved rock fractions and therefore Si is only present in trace amounts (silica was removed during the rock digestion procedure). Fe constitutes the major part, followed by minor amounts of Mg, Al, Ca and Mn; the other elements only occur in trace amounts. Accordingly, in Table 9 the major oxide weight fractions for each sample are summarised. For the HCl-fraction samples these values should correspond to the dissolved oxide and carbonate fractions.

For the Hotazel samples, the results are mainly in agreement with the XRD mineralogy data. The FeO content of bulk-rock sample HF7, i.e. 21-22 wt %, is considerably higher than for the other samples, i.e. 9-10 wt % for HF1 and 2 and 5-6 wt % for HF3, 4 and 6. The HCl dissolved equivalent of HF7 contains slightly less FeO compared to the bulk rock value, indicating most of the samples' Fe is hosted in the oxide (and carbonate) phase,

as is confirmed by the high hematite content inferred from XRD results. In contrast, the FeO fraction of the other HCl-treated samples (HF3, 4 and 6 HCl) is much lower, implying that a substantial part of the original jasper sample did not dissolve in HCl. Because Fe silicates should not dissolve in HCl, this presumably reflects the presence of Fe silicate impurities. These Fe silicate impurities were not identified in the XRD plots of samples HF4 and 6 as distinct peaks, but may perhaps be reflected by the broad bulge at the outer left of the spectra (between 5 and 15 2θ). HF5 contains very little FeO (2.8 wt %) and is relatively rich in MgO (1.4 wt %) and Al_2O_3 (0.8 wt %), which is also in accord with the high chlorite content reported by XRD data. HF6 contains a considerable amount of CaO (1.4 wt %) relative to FeO (5.4 wt %), which is similarly reflected in its high ankerite and calcite content. Ongeluk samples OF1-3 are predominantly composed of SiO_2, FeO, Al_2O_3 and MgO. OF1 and 3 have a very similar chemistry, but OF2 slightly is different from them because it has a lower FeO-SiO_2 ratio.

Table 8: List of minerals present in samples HF1-7 according to XRD 2θ plots (see Appendix 5). For each sample the spectrum peaks of quartz (chert) and hematite are prominent, but the peaks of the minor mineral phases are often hardly to detect from the background level and thus their presence is questionable. The relative mineral abundances (wt %) were obtained by XRD semi-quantitative analysis (see section 3.3.2) and should be regarded merely as a rough estimate.

	quartz	hematite	magnetite	chlorite	ankerite	minnesotaite	calcite
Sample	wt %	wt %	wt %	wt %	wt %	wt %	wt %
HF1	81	8	2	7	2	-	-
HF2	86	8	4	-	3	-	-
HF3	87	4	1	-	2	7	-
HF4	94	5	-	-	2	-	-
HF5	95	2	-	5	-	-	-
HF6	90	5	-	-	2	-	3
HF7	74	19	2	-	4	-	-

Table 9: Major oxide fractions present in the Hotazel Fe isotope (HF1-7) and Ongeluk Fe isotope (OF1-3) samples, calculated from ICP-OES data of the digested rock solutions. HF1-7 and OF1-3 are bulk-rock samples and hence the ICP-OES element data represent bulk-rock concentrations. Except for Fe, Mg, Mn, Al and Ca, the element concentrations in HF1-7 are very low (see Appendix 6.1), and thus the remaining (unmeasured) rock mass is assumed to have consisted of SiO_2 (which has been lost during acid digestion). OF1-3 additionally contain traces of K, P and Ti (see Appendix 6.1). HF3, 4, 6 and 7 HCl are partially dissolved in HCl and thus ICP-OES results only relate to the HCl-dissolved fraction (presumably the oxide and carbonate fraction) of the bulk rock. HF7a and HF7b (HCl) are duplicate samples.

	FeO	MgO	MnO	Al_2O_3	CaO	SiO_2 + trace elements
Sample	wt%	wt%	wt%	wt%	wt%	wt %
HF1	9.6	0.2	0.0	0.1	0.1	90.0
HF2	9.9	0.3	0.0	0.3	0.4	89.1
HF3	5.3	0.5	0.0	0.1	0.2	93.9
HF4	5.0	0.2	0.0	0.5	0.1	94.2
HF5	2.8	1.4	0.0	0.8	0.0	95.0
HF6	5.4	0.3	0.1	0.1	1.4	92.7
HF7a	22.4	0.4	0.1	0.2	1.1	75.9
HF7b	21.3	0.4	0.1	0.2	1.0	77.0
OF1	20.4	9.5	0.4	12.9	2.1	54.7
OF2	15.5	10.2	0.5	11.2	2.0	60.6
OF3	20.6	9.9	0.5	15.6	5.0	48.4
HCl-fraction:						
HF3 HCl	2.6	0.1	0.0	0.1	0.2	
HF4 HCl	1.8	0.1	0.0	0.6	0.1	
HF6 HCl	2.4	0.2	0.1	0.0	1.3	
HF7a HCl	17.1	0.3	0.1	0.2	1.1	
HF7b HCl	18.6	0.3	0.1	0.3	1.4	

4.3.2 Fe isotope data

4.3.2-1 Quality control of column chemistry

An overview of the sample digestion and subsequent processing data prior to column separation is presented in Appendix 6.2. ICP-OES results for Fe purity check of the samples and standards after anion-exchange chromatography are listed in Appendix 6.3. Most samples are devoid of any contaminants; only HF4 and OF3 contain some Na. The two procedural blanks are contaminated with traces of Na, Al and S, but this is not seen in any of the samples or standards. The total Fe content of the procedural blanks is listed in Appendix 6.3, Table 8.

Column yields are listed in Table 10. Preferably all yields are above 90 % to ensure no significant Fe loss occurred during anion-exchange chromatography, which could provoke considerable Fe isotope fractionation (Anbar et al., 2000); the > 90 % yield is based on the fact that the ICP-OES measurements have about 10 % uncertainty and thus 90% cannot be distinguished from 100 % within analytical uncertainty. Unfortunately, yields of standard ISE921 and samples HF3, 4, 5, 6 and OF1-3 are < 90 %. The low yield of OF2 can be explained by accidental loss of Fe solution directly after chromatography. Photospectrometry measurements of the sample solutions prior to column separation reveal that a small portion of the ISE921 solution was lost during the processing steps after sample dissolution, but this still does not result in a > 90 % column yield. In addition, the total amount of electrical charge per sample that was loaded onto the columns is listed in Table 10, next to the column yield. There is no correlation between the total amount of Fe and electrical charge loaded onto the columns and the column yield. Moreover, the total resin' capacity is 0.6 mEq (see section 3.3.3-4); 10 % of the total resin capacity is only exceeded by samples ISE921 and AGV-1. AGV-1 has a very high column yield, and it is therefore unlikely that Fe isotope fractionation has occurred during column separation. Accordingly, for some samples considerable amounts of solution must have been lost *after* column separation, for example by spatting of solution out of the Teflon beakers during evaporation steps.

Sample	Amount of Fe loaded (µg)	Total Fe collected (µg)	Column yield (%)	Max. mEq loaded
blank	0	0	-	<0.012
ISE921	286	234	**82**	0.14
BHVO-1	237	221	93	0.069
JB-2	412	383	93	0.099
HF1	221	217	98	0.015
HF2	226	225	99	0.017
HF3	287	205	**71**	0.019
HF4	304	212	**70**	0.021
HF5	427	327	**77**	0.048
HF6	338	260	**77**	0.025
HF7a	264	252	95	0.017
HF7b	248	246	99	0.016
blank HCl	0	0	-	<0.010
AGV-1	258	254	98	0.12
OF1	159	138	**87**	0.040
OF2	240	119	**49**	0.044
OF3	289	255	**88**	0.055
HF3 HCl	398	406	102	0.027
HF4 HCl	553	537	97	0.049
HF6 HCl	479	473	99	0.044
HF7 HCl a	235	236	101	0.016
HF7 HCl b	532	514	97	0.032
IF-G	255	248	97	

Table 10: Anion-exchange column separation data for Fe. Preferably column yields are above 90 % for each sample, in order to rule out Fe isotope fractionation during chromatography. Unfortunately, for several samples (indicated in bold) the yield is below 90 %. However, there is no correlation between the column yield and the amount of Fe loaded onto the column, nor is there a correlation with the total electrical charge (mEq) loaded. Moreover, 10 % of the total resin capacity is only exceeded by samples ISE921 and AGV-1. It is therefore unlikely that Fe isotope fractionation occurred during column separation; low column yields are presumably the effect of loss of Fe solution after chromatography.

4.3.2-2 MC-ICP-MS data quality control

Raw analyte MC-ICP-MS results are listed in Appendix 8.1. Information about the behaviour of the instrumental parameters and samples during the MC-ICP-MS measurements required for Fe isotope data acceptance is visualised in Appendix 8.2 (see also section 3.3.4-3). Mean δ^{56}Fe and δ^{57}Fe values of HF1-7 and OF1-3 from measurement session 1 (including internal 2 S.D. uncertainties) are presented in Table 11 along their stratigraphic sampling height. The values for the duplicate samples HF7a and HF7b are the same within uncertainty, i.e. they differ 0.004 ‰ and 0.006 ‰ in their δ^{56}Fe and δ^{57}Fe, respectively (see Appendix 8.1). The RMs of both measurement sessions are listed in Table 12 together with their GeoRem accepted value and resulting bias %.

All the δ^{56}Fe and δ^{57}Fe values of the RMs of session 1 are within their accepted uncertainty limits (except for those of AGV-1, which is more than fifty years old, and for the δ^{57}Fe of JB-2, which has a very narrow GeoRem uncertainty range). On the contrary, the RMs measured during session 2 highly deviate from both their accepted value and the values obtained during session 1. HanFe of session 2 has a δ^{56}Fe (0.23 ‰) and δ^{57}Fe (0.33 ‰) that is 0.07 ‰ and 0.10 ‰ lower than the mean δ^{56}Fe and δ^{57}Fe values of HanFe measured during session 1 (0.30 ‰ and 0.44 ‰, respectively), though they are still the same to each other within their internal 2 S.D. uncertainties. However, the duplicate samples HF7a HCl and HF7b HCl are relatively similar (i.e. a difference of 0.02 and 0.03 % for δ^{56}Fe and δ^{57}Fe, respectively), suggesting that the

Sample	δ^{56}Fe ‰	internal 2 S.D. ‰	δ^{57}Fe ‰	internal 2 S.D. ‰	Stratigraphic depth (m)
HF1	-0.26	0.05	-0.34	0.07	291.259
HF2	-0.31	0.02	-0.42	0.05	291.625
HF3	-0.38	-	-0.52	-	291.837
HF4	-0.49	0.01	-0.76	0.02	291.937
HF5	-1.07	0.11	-1.58	0.20	292.322
HF6	-0.93	0.08	-1.36	0.13	292.900
HF7a	-0.50	0.07	-0.70	0.08	293.425
HF7b	-0.50	-	-0.70	-	293.425
OF1	-0.70	0.03	-1.06	0.10	293.854
OF2	-0.73	0.02	-1.08	0.01	294.000
OF 3	-0.65	0.03	-0.99	0.03	294.137

Table 11: Fe isotope compositions of the bulk-rock hematite-chert samples from the Hotazel (HF1-7) and Ongeluk Fm. (OF1-3), together with their sampling stratigraphic depth (MC-ICP-MS session 1). All samples are normalised against the IRMM-014 standard. The internal 2 S.D. represents the standard deviation calculated from the Fe isotopic values of the individual analytes (usually n = 3); HF3 and HF7b have no standard deviation because they represent the Fe isotopic value of just one analyte (the other two analytes were rejected). See also Appendix 8.1 for the raw MC-ICP-MS Fe isotopic data. The **external 2 S.D. uncertainties** for δ^{56}Fe and δ^{57}Fe are ±**0.11 ‰** and ±**0.20 ‰**, respectively.

inaccuracy is relatively consistent for each measured sample from session 2. Therefore, the mean Fe isotope values of HF3, 4, 6 and 7 HCl presented in Table 13 have been corrected for this with a factor of +0.07 ‰ and +0.10 ‰, respectively. The shift in δ^{56}Fe and δ^{57}Fe values between session 1 and 2 for BHVO-1 is even larger (±0.11 and 0.18 ‰, respectively), and here the mean Fe isotopic values of the two different sessions are not even within each other's uncertainty range. However, the measured Fe isotopic composition of HanFe is much better constrained than that of BHVO-1, that is, the number of individual HanFe analytes of which the HanFe mean value is calculated is much higher than for BHVO-1 (see Appendix 8.1). Therefore, the correction is based on the difference in the Fe isotopic composition of HanFe (between measurement session 1 and 2) rather than on that of BHVO-1.

An indication of the overall external reproducibility of δ^{56}Fe and δ^{57}Fe values is achieved from multiple MC-ICP-MS measurements of internal lab standard HanFe and corresponds to 0.059 ‰ and 0.087 ‰, respectively (see Table 14). However, for a few samples the internal standard deviations obtained during session 1 are larger than these two values (see Table 11 and Appendix 8.1). The largest 2 S.D. is of sample HF5 and corresponds to 0.106 and 0.204 ‰ for δ^{56}Fe and δ^{57}Fe, respectively. Therefore, the external uncertainties for the δ^{56}Fe and δ^{57}Fe results from HF1-7 and OF1-3 reported here are ±0.11 ‰ and ±0.20 ‰, respectively. Since the correction applied to the δ^{56}Fe and δ^{57}Fe values of the HCl-fraction samples is questionable, an external 2 S.D. uncertainty of ±0.11 ‰ and ±0.20 ‰ for these HCl-fraction δ^{56}Fe and δ^{57}Fe results, respectively, may therefore be an underestimation: the +0.07 ‰ and +0.10 ‰ correction is based on the difference in the measured Fe isotopic composition of HanFe between MC-ICP-MS session 1 and 2, and not on that of BHVO-1, which would yield a larger correction, i.e. +0.11 and +0.18 ‰, respectively. Taking this possibly larger correction factor (based on BHVO-1) into account, the uncertainty range for the δ^{56}Fe and δ^{57}Fe of samples HF3,4, 6 and 7 HCl would be at least ±0.04 and 0.08 ‰ larger (respectively) than for the bulk-rock samples.

Session	Standard	δ^{56}Fe ‰	internal 2 S.D. ‰	RM accepted value ‰	*Bias* *%*	δ^{57}Fe ‰	internal 2 S.D. ‰	RM accepted value ‰	*Bias* *%*
1	HanFe	0.30	0.07	0.29 ± 0.05	*n.a.*	0.44	0.12	0.43 ± 0.07	*n.a.*
1	BHVO-1	0.08	0.07	0.11 ± 0.04	*n.a.*	0.11	0.12	0.156 ± 0.07	*n.a.*
1	JB-2	0.05	0.01	0.067 ± 0.02	*n.a.*	0.08	0.08	0.096 ± 0.01	*19*
1	AGV-1	-0.03	0.07	0.122 ± 0.05	*126*	-0.06	0.09	0.113 ± 0.15	*153*
1	IF-G	0.64	0.07	0.65 ± 0.07	*n.a.*	0.93	0.07	0.936 ± 0.10	*n.a.*
2	HanFe	0.23	0.01	0.29 ± 0.05	*20*	0.33	0.05	0.43 ± 0.07	*22*
2	BHVO-1	-0.02	0.002	0.11 ± 0.04	*119*	-0.07	0.02	0.156 ± 0.07	*142*

Table 12: MC-ICP-MS data of all standards (measured during session 1 and 2) compared with their corresponding accepted reference material values (from GeoRem). All standard δ^{56}Fe and δ^{57}Fe values from session 1 are within the 2 S.D. range of the accepted RMs except for AGV-1 and JB-2 (only δ^{57}Fe). Additionally, HanFe and IF-G values are very close to the RM's accepted mean. On the contrary, the standards measured during session 2 highly deviate from both their RM value and the results from session 1. For the standards of which the Fe isotope value falls outside the 2 S.D. range of the accepted RM value, the bias (%) is indicated; *n.a.* stands for *not applicable.*

4.3.2-3 $\delta^{56}Fe$ values

The $\delta^{56}Fe$ values of all bulk-rock hematite-chert samples range from -0.26 ‰ to -1.07 ‰, which corresponds to a $\delta^{57}Fe$ from -0.34 ‰ and -1.58 ‰, respectively (see Table 11). These values are considerably higher than those ($\delta^{57}Fe$) of bulk-rock BIF (from -0.07 to -2.74 ‰, with a mean of -1.70 ‰) and transitional hematite lutite (from -2.24 to -3.52‰) samples reported higher up in the Hotazel stratigraphy (Tsikos et al., 2010). The $\delta^{56}Fe$ of the Ongeluk samples lies in between -0.65 ‰ and -0.73 ‰, which is significantly lower than the near-zero values (±0.05 ‰) for normal igneous rocks (Beard et al., 2003; Poitrassen et al., 2004). The HCl-fraction hematite-chert samples have $\delta^{56}Fe$ (corrected) values in the range of -0.11 ‰ to -0.50 ‰. Duplicate samples HF7a HCl and HF7b HCl have an approximately similar Fe isotope composition (-0.50 ‰ to -0.48 ‰) as the equivalent bulk-rock duplicate samples (both -0.50 ‰), whereas the (corrected) $\delta^{56}Fe$ value of HCl-fraction samples of HF3, 4 and 6 HCl (-0.11 ‰, -0.19 ‰ and -0.61 ‰) is far higher than for their corresponding bulk-rock samples (-0.38 ‰, -0.49 ‰ and -0.93 ‰, respectively).

The $\delta^{56}Fe$ values of all bulk-rock and (corrected) HCl-fraction samples from the Ongeluk lava and Hotazel hematite-chert are plotted along their sampling stratigraphic depth in Figure 19, in combination with a visualisation of their characteristic chemical composition, i.e. their relative FeO, MgO, MnO, Al_2O_3 and CaO wt %. Whereas the $\delta^{56}Fe$ of the Ongeluk lava remains rather constant, the Hotazel part of the diagram displays a conspicuous stratigraphic trend of decreasing $\delta^{56}Fe$ from HF7 towards samples HF6 and 5 and a subsequent increase from HF5 towards samples HF4, 3, 2 and 1 at the top. Moreover, relatively low $\delta^{56}Fe$ values, e.g. of samples HF5 and 6 seem to be characterised by a relatively low FeO content. The HCl-fraction samples exhibit a more or less similar pattern as the bulk-rock samples, although the $\delta^{56}Fe$ values for HF 6, 4 and 3 HCl are much higher.

	$\delta^{56}Fe$ ‰	$\delta^{57}Fe$ ‰	$\delta^{56}Fe$ corrected + 0.07 ‰	$\delta^{57}Fe$ corrected + 0.10 ‰
HF3 HCl	-0.18	-0.26	-0.11	-0.16
HF4 HCl	-0.26	-0.38	-0.19	-0.28
HF6 HCl	-0.68	-1.02	-0.61	-0.92
HF7a HCl	-0.57	-0.83	-0.50	-0.73
HF7b HCl	-0.55	-0.86	-0.48	-0.76

Table 13: Fe isotope data of the HCl-fraction hematite-chert samples from the Hotazel Fm. (HF3, 4, 6 and 7) of MC-ICP-MS session 2. Because the $\delta^{56}Fe$ and $\delta^{57}Fe$ results of reference materials HanFe and BHVO-1 measured during session 2 were lower than their results from session 1 and their accepted values (see Table 12), all Fe isotopic data of session 2 (i.e. HCl-fraction samples) have been corrected with a factor of +0.07 ‰ and +0.10 ‰ for $\delta^{56}Fe$ and $\delta^{57}Fe$, respectively (see section 4.3.2-2 for explanation).

	$\delta^{56}Fe$	2 S.D.	$\delta^{57}Fe$	2 S.D.	number
HanFe	0.299	0.059	0.437	0.087	99

Table 14: Summary of Fe isotope values for internal lab standard HanFe obtained from multiple analyses conducted with the ThermoFinnigan Neptune MC-ICP-MS of the GFZ, Potsdam. The 2 S.D. gives an indication for the overall instrumental uncertainty of $\delta^{56}Fe$ and $\delta^{57}Fe$ values**.**

Figure 19: Overview of $\delta^{56}Fe$ results of samples from the Hotazel (HF1-7) and Ongeluk (OF1-3) versus stratigraphic depth, combined with their major chemical composition (relative oxide weight %). $\delta^{56}Fe$ of both the bulk-rock (TD, i.e. totally destructed) and HCl-fraction (HCl) samples are plotted. The 2 S.D. external uncertainty of all bulk-rock $\delta^{56}Fe$ values is ±0.11 ‰, as indicated with the error bars. Because the Fe isotope values of the HCl-fraction samples were corrected (see section 4.3.2-2), they are more prone to uncertainty. Hence, the proposed external 2 S.D. uncertainty that is based on the bulk-rock samples may actually be an underestimation for the HCl-fraction samples and therefore their error bars are not indicated.

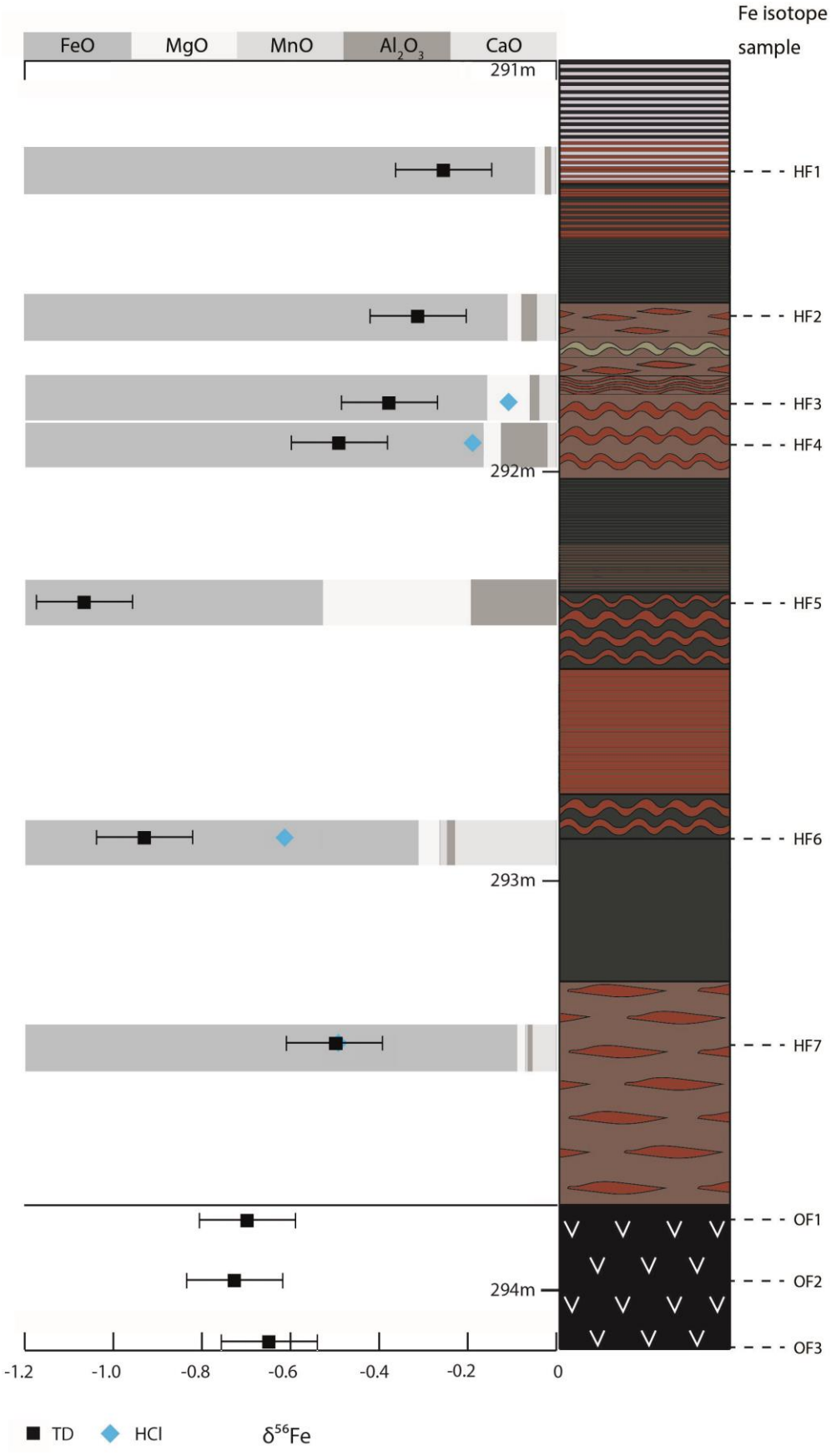

5. Discussion

5.1 Subaqueous extrusion and hydrothermal alteration of Ongeluk lava

The porphyritic texture and very fine-grained matrix (crystal sizes < 1 µm) of the Ongeluk lava (see section 4.1.2) confirm its supposed extrusive origin (Reczko et al., 1995). In surface outcrops of the Ongeluk Fm. Schütte (1992) and Cornell et al. (1996) reported the widespread occurrence of pillow lavas and hyaloclastites, implying that the lavas extruded into a marine setting. In the drill-core of this study no diagnostic features of subaqueous extrusion were found, but the conformable contact with the stratigraphically overlying Hotazel chemical sediments (i.e. precipitates from a water body) supports extrusion directly into the sea rather than subaerial extrusion and later submergence. Textural, mineralogical and chemical evidence imply that subsequent hydrothermal activity pervasively altered the originally basaltic-andesitic composition (Schutte, 1992; Cornell and Schütte, 1995; Cornell et al., 1996). The profoundly altered character of the relict feldspar phenocrysts (see Figure 11) and their anomalous chemical composition (see Table 3a) indicate that the original elements incorporated in the crystal lattice were partially removed and replaced by other ones. Virtually all primary igneous phases were altered to secondary, hydrothermal minerals, predominantly chlorite (together with quartz, calcite and titanite). The glassy matrix as well as the original phenocrysts (with a clinopyroxene composition according to Schütte (1992)) are covered by chlorite patches or chlorite pseudomorphs, respectively. In addition, several veins are branching between the contact with the overlying Hotazel Fm. and the uppermost altered Ongeluk. These veins are probably preserved pathways through which fluids interacted with the lava. Here, the surrounding rock is almost entirely made up of chlorite (no relict feldspars are present), which indicates even more extensive alteration. Moreover, in the Hotazel Fm. directly above the contact with the Ongeluk (< 1mm distance), traces of barite, chalcopyrite and galena are present, concentrated in little grains made up of chlorite. This mineral assemblage is typical for modern hydrothermal chimneys spouting fluids with a temperature < 350 ^{o}C (Haymon and Kastner, 1981) and was presumably derived by reworking of laterally exposed vents.

The remarkably low δ^{56}Fe composition of the Ongeluk lava Fe isotope samples OF1-3 is in agreement with the inferred hydrothermal alteration (see Table 11). Relatively large Fe isotopic variations occur (up to 1.1 ‰) in the Earth's mantle (Williams et al., 2005), yet the igneous rocks of the crust are generally very homogeneous, showing slightly positive δ^{56}Fe values with an average of ca 0.13 ‰ relative to IRMM-014 (e.g. Beard et al., 2003; Poitrassen, 2004; Schoenberg et al., 2009; Craddock et al, 2013; Teng et al., 2013). This is in marked contrast to the average value for the Ongeluk lava (ca -0.69 ‰). Studies have shown that the extensive redox reactions, dissolution and precipitation of Fe-bearing minerals that occur during modern-day seawater-basalt alteration, comprising both low-T oceanic crust hydrothermal alteration (Rouxel et al., 2003) as well as high-T hydrothermal systems (Sharma et al., 2001) should result in significant Fe isotope fractionation. The anomalous δ^{56}Fe composition of the Ongeluk lava thus clearly reflects this phenomenon. During hydrothermal circulation, dissolution of the original igneous (basaltic) phases coincides with the preferential removal of ^{54}Fe over ^{56}Fe, resulting in Fe isotopically enriched basalts of up to +1-2 ‰ and isotopically light hydrothermal fluids ranging from −0.69‰ to −0.12‰, and with an average of ca -0.3 ‰ (Sharma et al., 2001; Beard et al., 2003; Severmann et al., 2004, 2008; Rouxel., 2008). The dissolved Fe^{2+} load of these fluids becomes more and more isotopically depleted during progressive alteration, not only due to the kinetic effect during dissolution of the primary minerals but also due to the precipitation of isotopically heavier secondary minerals out of these fluids, i.e. equilibrium fractionation. The depleted δ^{56}Fe of samples OF1-3 thus indicates that the uppermost part of the Ongeluk lava is actually the chemical product of isotopically evolved hydrothermal source fluids due to earlier fluid-rock interaction in the deeper parts of the lava. As the rising fluids approached the top of the Ongeluk lava, their isotopically depleted mobilised Fe(II) load also produced negative δ^{56}Fe values for the Fe-bearing alteration products (i.e. ca -0.7 ‰).

The temporal relationship between the initial (subaqueous) extrusion of the lava and its hydrothermal alteration has important implications for the fate of the Hotazel rocks. If hydrothermal alteration commenced long *after* extrusion, hence, after deposition of the Hotazel sediments, in the first place the initial chemical precipitation of the Hotazel sediments would not have a genetic relation with the hydrothermal fluids (i.e. they could not have precipitated from these fluids), and secondly, they might have formed part of the hydrothermal circulation system that was formed later. This consequently would have altered the original Hotazel sediments and thus have obscured the primary features, in particular the Fe isotopic composition. However, the occurrence of chlorite grains in the Hotazel (very close to the contact), which are very similar in appearance and chemistry to those found in the altered Ongeluk lava (see Figure 11 and Table 3a-b), indicates that hydrothermal alteration of the Ongeluk lava started *prior to* sedimentation onto the seafloor, i.e. before accumulation of the Hotazel sediments. Accordingly, this suggests that hydrothermal activity was coeval with subaqueous extrusion.

The fact that veins are descending from the Ongeluk-Hotazel Fm. contact and subsequently branch downwards in the direction of the Ongeluk lava suggests that they represent fractures through which seawater interacted with the lava and with hydrothermal fluids from below, rather than a post-depositional feature. This process thus

also happened *before* the initiation of the Hotazel Fm. deposition. The veins contain a thick rim of microplaty hematite, implying that the seawater that interacted with the lava and / or discharging fluids from below was rich in dissolved O_2 and subsequently reacted with Fe(II) released from dissolved primary and / or secondary Fe-bearing minerals. The dendritic textures observed with the optical microscope (see Table 2) presumably reflect supercooling and subsequent dendritic mineral growth due to interactions from the relatively cool seawater with hot lava.

In addition to the presence of hematite in the vein rims, the occurrence of barite closely above the contact may also indicate that O_2 was present in the seawater, since sulphur is in its oxidised rather than reduced form. However, in magmatic systems at temperatures above 400°C, hydrolysis of SO_2 forms H_2S as well as H_2SO4 upon cooling (Ellis and Giggenbach, 1971; Ohmoto and Goldhaber, 1997), and therefore the presence of barite is not conclusive for the presence of free O_2 in the water column. Still the fact that barite is more abundant than galena and chalcopyrite (see section 4.1.2) hints at the possibility that oxidation occurred after release of the hydrothermal fluids into the sea. In addition, Schütte (1992) and Cornell et al. (1996) reported that alteration of the Ongeluk lava included oxidation (*hematitisation*), especially in the upper part of the stratigraphy, which similarly points to the oxidising role of down flowing seawater. However, if these are all *primary*, i.e. not post-depositional features, they are not directly conclusive for large-scale oxygenation of the ocean. Based on chemical analysis, Cornell and Schütte (1996) ascribed the alteration of the Ongeluk lava to a shallow marine (< 400 m) process. In addition, the relicts of starved wave ripples (lenticular bedding) observed in the hematite lutite directly above the Ongeluk consequently imply above fair-weather wave base conditions (e.g. Pettjiohn, 1975; Simonson, 1985; Beukes and Gutzmer, 2008). Hence, the oxidised parts of the Ongeluk lava might very well represent oxidation in the ocean's surface layer with O_2 derived from photosynthetically-produced O_2 oases.

5.2 Detrital versus hydrogenous origin of the Hotazel sediments

The Hotazel sequence is largely composed of Fe-rich chemical sediments that have precipitated from the water column, i.e. *hydrogenous* sediments, and therefore potentially bears information about the chemistry and redox state of the seawater. The occurrence of clastic sedimentary textures and Al-rich, i.e., crustal-derived material unfortunately signifies that the Hotazel sediments contain a substantial *detrital* contribution, which as a consequence obscures this seawater component. As will be discussed below, however, I consider the hematite-chert sections used for rare-earth element and Fe isotope analysis to be generally poor in allochtonous material.

5.2.1 Textural evidence for authigenic versus allogenic sediment

In terms of sedimentary textures, the fine-grained and finely laminated parts of the Hotazel stratigraphy originate from more energetically quiet areas / periods and hence reflect slow pelagic sedimentation, but this might comprise both sedimentation of fine-grained chemical (i.e. hydrogenous) precipitates as well as detrital clays (see Figure 9) and therefore chemical data are required to distinguish between the two (see section 5.2.2). In contrast, the chaotic breccias of transition zone cycle III (as defined in section 4.1.2) comprise soft-sediment deformation (chaotic bedding) together with poorly sorted and matrix supported granules of angular to subrounded shape, and are therefore certainly considered detrital, although the granules themselves could initially have been derived from comparable chemical sediments deposited elsewhere (Simonson, 1985 and references therein). The breccias were formed by transport of sedimentary reworked material and subsequent early lithification of the chert matrix, which preserved these floating textures. It is important to note that SSD textures alone do not necessarily indicate the input of reworked allochtonous material. Rather, SSD could only have deformed the original lamination by sediment loading prior to lithification due to e.g. differences in density, but without causing significant sediment transport. Moreover, most of the small ellipsoidal or irregular bodies found in iron formations are diagenetic concretions rather than primary features (Simonson, 1985 and references therein). Therefore I consider the large jasper load casts and concretions from which most of the Fe isotope samples (i.e. HF3, 4, 5 and 6) and REE + Y data (i.e. thin-section 6, 8 and 11) in this study were obtained, to be in situ deposited. However, the discordant orientation, subrounded to angular shape and mineralogical heterogeneity of several granules in the transition zone of cycle III is certainly secondary and reflects displacement of unconsolidated sediments. The occurrence of parallel laminated intervals alternated with chaotically bedded transition zones in the Hotazel stratigraphy thus either reflects sediment loading due to a change in density of the sediment type (e.g. between hematite lutite and nodular mudstone), or (especially for the chaotic breccia of cycle III) it reflects episodes of sedimentary reworking and transport, possibly due to a change in the relative sea level.

The supposed current-generated origin of the lenticular bedding (e.g. Pettjiohn, 1975; Simonson, 1985; Beukes and Gutzmer, 2008) observed in the hematite lutites of cycle I and III equally implies transport of sediment. Hence, both the jasper lenses and their surrounding heterogeneous matrix might not be formed in situ. However, the compositional homogeneity of the jasper lenses (that is, predominantly hematite and chert) argues against a detrital origin. Rather, the bedforms are relicts of an originally flat bed which was partially removed by currents, but the firm, immobile parts remained attached

to the substrate. The small heterogeneous grains in the surrounding matrix though imply a more mobile behaviour. I therefore conclude that the REE + Y (i.e. thin-section 13, 14 and 16) and Fe isotope sample(s) (i.e. HF7) obtained from these jasper lenses similarly are in situ-derived.

5.2.2 Source of chlorite

From a mineralogical and geochemical perspective, the mudstones and (clay-rich parts of) the transition zones of the Hotazel stratigraphy are rich in Al (see Figure 14), which is hosted into the crystal lattice of chlorite (ca 13 wt % Al) and to a lesser extent in stilpnomelane (ca 5 wt %; see Table 3b). Lithophile elements such as Al are characteristic for terrigenous detrital material, although Al may also have a hydrogenous component reflecting seawater adsorption processes (Ederfield and Holland, 2004). However, considering the marked contrast to the very low Al content of the hematite lutites and BIF, it is more likely that these are predominantly hydrogenous and that the increased Al concentration of the mudstones and transition zones represents a large lithogenic contribution. Local increases in the Al content in the hematite lutite and BIF intervals represent smaller influxes of terrigenous material, preserved as grains composed of randomly oriented Al-bearing Fe silicates. The close association of stilpnomelane with chlorite in the mudstones and clastic textures suggest that the relatively Al-poor mineral is also of detrital origin, although several authors have argued that stilpnomelane is the metamorphic product of a precursor hydrogenous Fe silicates such as greenalite (e.g. Konhauser et al., 2002, 2007; Klein et al., 2005; Rasmussen et al., 2013, 2015). The increased abundance of euhedral apatite in the clay-rich parts of the Hotazel similarly hints to a detrital source.

Because Ti and Al are generally immobile elements during weathering and diagenesis (Goldschmidt, 1954), the constant Al-Ti ratio of the mudstones indicates that they were formed from a rather constant flux of detrital material of relatively similar composition (see Figure 14). Considering the striking similarities between the mineral characteristics and chemical composition of chlorite occurring in the Ongeluk Fm. and in the Hotazel Fm., it may very well be the case that the chlorite in (the mudstone intervals of) the Hotazel is a detrital product of eroded Ongeluk lava material. This automatically means that erosion, transport and sedimentation of the chlorites (or their metamorphic precursors) onto the seafloor started after hydrothermal alteration of the primary igneous minerals of the Ongeluk lava. Further, the replacement of chlorite spherulites by euhedral Mn-ilmenite (see Figure 11) suggests that Mn-ilmenite was formed after a metamorphic reaction of chlorite together with some precursor Ti-bearing mineral; it is very probable that this Ti-bearing mineral also originated from the Ongeluk lava, e.g. from secondary titanite (or its precursor igneous phase). Hence, detrital chlorite, and in general the (nodular) mudstone intervals of the Hotazel were predominantly sourced from reworked material of the Ongeluk lava. The highly elevated Al/Ti in the hematite lutite directly above the contact with the Ongeluk Fm. (compared to the relatively low Al wt %) and its gradual decrease towards low Al/Ti values (see Figure 14) possibly reflects a difference in the Al/Ti composition of the sediment source. BSE images in Figure 11a and b indicate that titanite is virtually absent in the Ongeluk lava part at the contact with the Hotazel (thin-section 17 in Figure 11b) compared to somewhat lower in the stratigraphy (thin-section 19 in Figure 11a). Perhaps this signifies that the top layer of the Ongeluk lava is slightly more felsic in composition and hence poorer in Ti, which accordingly results in elevated Al/Ti values for reworked material from this top part of the Ongeluk lava.

The mudstone intervals could basically have formed by any type of process that provoked the erosion of the exposed parts of the Ongeluk lava and (lateral) transport and sedimentation of the eroded material. Their cyclic occurrence suggests that they could be inherently linked to sea level fluctuations, which episodically provoked erosional events that acted at the site of the Ongeluk lava and subsequently allowed for accumulation of the reworked material in the broader surrounding area. Since the mudstones are well-sorted and fine-grained, this indicates that the exposed parts of the Ongeluk lava were situated at a location quite far-off. In an alternative scenario, however, the mudstone intervals may be deposited via volcanic ash fall associated with the Ongeluk volcanism. Although the nodular character of the chlorite aggregates seems to be the result of a sedimentary reworking process, rounded and spherical aggregates have also been found in the Ongeluk lava itself by Schütte (1992), who interpreted these to represent former volcanic glass spherules or refiled vesicles. The chlorite nodules may thus be directly derived from these preserved (but already hydrothermally altered) igneous features. Therefore, the mudstone intervals could very well be linked to episodes of increased volcanic eruptions from the active Ongeluk volcanic centre. As a consequence, the relatively volcaniclastic-free hematite lutite intervals in between the clay-rich parts of the Hotazel sequence, together with the BIF part at the top of the drill-core (from which Fe isotope sample HF1 and REE + Y thin-section 2 were obtained) would represent chemical precipitation from the water column during periods of volcanic quiescence; the highly elevated Al-normalised Fe concentration profiles along these hematite lutite zones clearly demonstrate a large hydrogenous Fe contribution.

Irrespective of the sedimentation mechanism, the influx of volcanic material decreases with increasing height through the stratigraphy of the Hotazel: the mudstone interval of cycle III is devoid of any nodular chlorite and only contains smaller chlorite patches and fibres indicating a more remote source of the Ongeluk lava or of its volcanic centre. Moreover, chlorite becomes virtually absent in the upper BIF part of the Hotazel. Regarding the

paleoenvironmental interpretation that BIF sediments were deposited in the more deep-water, basinal setting of the Transvaal basin (Beukes and Gutzmer, 2008), the absence of Ongeluk volcanic material in the upper Hotazel sediments might signify a spatial and temporal shift towards a deeper-marine paleoenvironment, distant from the shallow-marine Ongeluk (volcanism). Stagnation of the activity of the Ongeluk volcanism itself might also be a likely cause.

5.3 Primary versus secondary features of the Hotazel

5.3.1 Origin of hematite

Considering the very small grainsize (< 1 µm) of the hematite particles compared to the other Fe-bearing minerals, and the fact that they occur in isolated hematite-chert lenses, bulges or layers suggests that submicron-scale hematite is left rather unaffected by post-depositional alteration processes (see section 4.1.2). Larger grainsizes and euhedral, well-mineralised crystal shapes (of e.g. magnetite) ultimately arise from mineral recrystallisation or replacement during diagenesis and low-grade metamorphism; the absence of other Fe minerals in the hematite-chert sections further argues against secondary replacement of precursor Fe-bearing minerals. Therefore, I propose that submicrometre-sized hematite is the most primary Fe-bearing mineral present in the Hotazel rocks (see Figure 13a-b and 15), analogous to the interpretation of hematite in other (B)IFs (e.g. Ahn and Buseck, 1990; Hoashi et al., 2009; Sun et al., 2014). The term *primary* refers here to the aqueous Fe signal acquired from the particles that initially precipitated from the water column and subsequently experienced mineral dehydration during burial. The primary hematite is in marked contrast to the larger (> 1 µm), rod-like hematite crystals showing radiating forms, which are disseminated in the mudstones in close association with other Fe minerals (e.g. magnetite) or replacing stilpnomelane and / or chlorite fibres (see Figure 13c-d). These characteristics are clearly attributed to mineral replacement reactions by secondary hematite, possibly formed via infiltration of O_2-bearing fluids after lithification (e.g. Rasmussen et al., 2014). The microplaty hematite observed in the veins at the contact with the Ongeluk is analogous to secondary hematite ore (e.g. Morris, 2012).

The occurrence of ultrafine (< 10 nm) hematite spheroids in the BIF jasper layer in Figure 15c is strongly supportive for the widely accepted idea that hematite is the early diagenetic (dehydration) product of ferric oxyhydroxide colloidal particles (e.g. Ahn and Buseck, 1990; Morris, 1993; Bekker et al., 2010), formed via oxidation of Fe(II) with free O_2 produced by cyanobacteria (e.g. Klein and Beukes, 1989) or anaerobically / microaerobically by enzymatic Fe(II) oxidation (e.g. Widdel et al., 1993; Konhauser et al., 2002; Kappler et al., 2005). In the SE images of the lutite jasper lenses and bulges no tiny colloidal hematite spheroids, but larger (<1 µm), subrounded to hexagonal plates were identified (see Figure 13a-b, 15d-e). This might indicate that the particles have undergone a coarsening process during burial lithification by structural water released from the surrounding chert during the transformation from amorphous silica to quartz (e.g. Frondel, 1982; Meng et al., 2009; Sun et al., 2015). Alternatively, the hematite nanospheres indeed could also be present in the lutite jasper sections, but were simply not be identified due to a low surface relief of the studied (polished) thin-sections. Hence, the submicrometre-sized hematite crystals observed in the jasper lenses and bulges in the Hotazel are also likely to be primary.

The chain configuration of the hematite particles forming a surrounding network around chert globules in Figure 15d might very well be a preserved primary texture, representing flocculated silica gels with co-precipitated ferric oxyhydroxide particles. In silica-supersaturated waters, flocculation of silica is catalysed by the bridging effect of adsorbing ferric oxyhydroxide particles onto the surface of the colloidal silica (Williams and Crerar, 1985). Accordingly, the hematite-chert networks observed in several jasper sections in the Hotazel might depict the well-preserved primary texture of a process analogous to that in modern hydrothermal systems described by Williams and Crerar (1985), and provides robust evidence that the submicron-scale and nanosized hematite in the Hotazal is a direct product of precursor water column-derived ferric oxyhydroxide particles.

An additionally noteworthy feature is the preferential alignment of hematite particles (< 1 µm) observed in the hematite microbands of the crinkly laminated part of the Hotazel (see Figure 15a). The crinkly character of the lamination, the clay mineral enrichment (i.e. stilpnomelane, minnesotaite and chlorite) and the lamina-specific distribution of the minerals are indicative of microbial mats (Schieber, 1999). The specific ordering of the hematite particles in microlamina might therefore signify oxidation of aqueous Fe(II) promoted by the microbial mat community.

5.3.2 Mineral paragenesis

Apart from the hematite-chert, Mn-calcite seems to be a relatively primary phase, covering a substantial area of the heterogeneous matrix in the lower part of hematite lutite cycle I. The dissolution textures and replacement by chert in Figure 11c and g imply that Mn-calcite growth predated silicification of the rock, which started during burial diagenesis (Siever, 1992); Figure 11c and g clearly show that the Fe silicates similarly postdate Mn-calcite formation. Mn-calcite could be a direct precipitate from the water column, or it could have replaced an early carbonate precursor (e.g. Ayres, 1972).

The dissolution textures inside the ankerite rhombs and replacement by chert indicate that it formed at the same time as Mn-calcite; their large crystal size suggests that they experienced a coarsening process during sediment burial prior to silicification (see Figure 11k-l). The overlying stilpnomelane needles also hint at a primary,

early diagenetic origin of ankerite. The chemical zoning of the ankerite rhombs, i.e. the fact that the crystal cores have a lower Fe / (Mg + Mn) than the outer rims may signify more than one period of crystal growth, which is also supported by the absence of the chert dissolution textures in the outer rim. The somewhat rhombohedral shape of the Mn-calcite sheet in Figure 11l and the common association with minnesotaite in the entire lower part of hematite lutite I could potentially indicate that they are both secondary minerals formed from precursor ankerite, whereby Mn and Ca were incorporated into Mn-calcite and Mg and Fe eventually into the crystal lattice of the minnesotaite. Ankerite could also be an early diagenetic phase after fine-grained siderite, which is by several authors interpreted to be a primary precipitate from seawater (Klein and Beukes, 1989; Klein, 2005; Konhauser et al., 2002, 2007). Regardless of the exact mineral formation pathway, ankerite is a relatively early, hydrogenous phase.

Although chlorite in the Hotazel is evidently detrital, the phase relations between chlorite and the other Fe silicates (see section 4.1.2) demonstrate that stilpnomelane and minnesotaite have developed at a later stage than the deposition of chlorite (or its metamorphic precursor). In the granular textures, chlorite is commonly overgrown by stilpnomelane, which in turn is replaced by minnesotaite, in agreement with the inferred (diagenetic or) low-grade metamorphic origin of stilpnomelane and minnesotaite (e.g. Ayres, 1972; Klein, 2005; Bekker et al., 2010. Regarding the approx. 5 wt % decrease in Al content for the Hotazel chlorites compared to the Ongeluk chlorites (see Figure 12 and Table 3a-b), I suspect that this might consequently be the effect of the incorporation of Al into the crystal lattice of stilpnomelane needles after deposition and burial of the chlorite and subsequent stilpnomelane formation. Minnesotaite is usually formed at the expense of stilpnomelane with increasing metamorphic grade (Klein, 2005), but its abundance in the Mn-calcite and ankerite-rich parts of the Hotazel (see section 4.1.2) suggests it is also a metamorphic product of a Mg-rich carbonate precursor mineral.

The occurrence of stilpnomelane in the absence of chlorite, particularly in the mudstone of cycle III and the upper BIF part of the Hotazel (see section 4.1.2), indicates stilpnomelane could have entirely consumed all precursor chlorite, or alternatively, that it could be the metamorphic product of a different precursor mineral than chlorite. It may potentially have formed from Fe-rich hydrothermal clays (Krapez et al., 2003; Bekker et al., 2010), or after the Al-poor Fe silicate greenalite, which is considered to be have been formed from originally precipitated amorphous Fe-silicate gels (Konhauser et al., 2002, 2007; Rasmussen et al., 2015). However, the relatively high Al content (ca 5 wt %) of the Hotazel stilpnomelane needles argues against a fully hydrogenous precursor phase, and signifies at least partial contribution from a preceding Al-bearing clay.

Coarse-grained and euhedral-shaped magnetite crystals commonly occur dispersed in the heterogeneous matrix or concentrated in BIF microbands, typically cross-cutting or overgrowing (hematite-)chert, Mn-calcite, ankerite and the Fe silicates, indicating that magnetite is evidently a very late-stage mineral, as concluded by many previous studies on very low-grade metamorphosed BIFs (e.g. Ayres, 1972; Bekker et al., 2010; Sun et al., 2015). However, some authors argue that it formed during early diagenesis or low-grade metamorphism from incomplete oxidation of aqueous Fe(II) (e.g. Klein et al., 2005; Johnson et al., 2008) or from reduction of an initially fully oxidised ferric oxyhydroxide precursor, either biologically mediated (Johnson et al., 2008; Lovley et al., 1987) or abiogenic (Frost et al., 2007). The latter could apply to the magnetite crystals concentrated in mono-mineralic BIF microbands, but the occurrence of randomly disseminated magnetite rhombs that are e.g. cross-cutting stilpnomelane (see Figure 11g-h) evidently points to a metamorphic origin.

The randomly scattered and euhedral-outlined cubic pyrite occurring in the pyrite-rich lutite interval (hematite lutite cycle III) is, similar to magnetite, a rather late-stage mineral. In contrast to these cubic pyrite crystals, the pyrite spherulites in hematite lutite cycle I (see Figure 11d) seem to represent a more primary feature. The original horizontal lamination of the surrounding matrix bends around the pyrite spherulites, implying that the spherulites predate sediment compaction. A similarly early diagenetic origin for spherulitic pyrite was proposed by e.g. Raiswell (1982) and Bekker et al. (2004). The occurrence of pyrite in (modern) organic-rich marine sediments is typically thought to be the result of microbial reduction (bacterial sulphate reduction) via the conversion of preceding Fe monosulphide (e.g. Berner, 1970; Canfield et al., 1989). On the other hand, under anoxic conditions pyrite could be formed abiotically in both low-T sedimentary environments (e.g. Raiswell, 1982) or from higher-T hydrothermal fluids (Xu and Scott, 2005).

5.4 Hydrothermal fluids versus ambient seawater origin of Hotazel

Previous researchers have proposed a volcanic-exhalative origin of the Hotazel Fm. (Cornell et al., 1996; Cornell and Schütte, 1995; Kirschvink et al., 2000; Kopp et al., 2005; Kirschvink and Kopp, 2008), reflecting rapid deposition of Fe-Mn sediments in the proximity of the Ongeluk hydrothermal vent site (Cornell and Schütte, 1995) or primary precipitation of Mn(IV) sourced from the Ongeluk hydrothermal system in the aftermath of a Snowball Earth Event (Kischvink et al., 2000). This is in contrast to the proposed ambient seawater origin of Tsikos et al. (2010). Although the model of Cornell and Schütte (1995) received major criticism because it fails to explain the cyclic development of BIF, hematite lutite and Mn-ore (Beukes and Gutzmer, 1996) and both the models of Cornell and Schütte (1995) and Kischvink et al. (2000) do

not account for the uniquely high Mn content of the Hotazel Fm. (Laznicka, 1992; Tsikos et al., 2010), it is not inconceivable that the lowermost chemical sediments of the Hotazel sequence were sourced by the delivery of hydrothermal fluids into the Transvaal basin, since they directly cover the hydrothermally altered Ongeluk lava. As a consequence, these fluids may also have contributed to the seawater Fe(II) inventory from which the hematite was formed.

5.4.1 Major element constraints on hydrothermal influx

The elevated carbonate concentration of hematite lutite cycle I, as reflected by the high modal abundance of Mn-calcite and minnesotaite (which both presumably formed after an originally water column-derived precursor carbonate phase), and the good correlation between the Al-normalised concentration profiles of Ca, Mg, Mn and Fe (as previously described in section 4.1.3) imply that this lowermost part of the Hotazel Fm. was sourced from rather carbonate-rich fluids. Although the (modern) oceans comprise the largest part of the Earth's carbonate reservoir and marine carbonate deposition thus mostly originates from the seawater, the conspicuous enrichment close to the Ongeluk lava hints towards a different source. The fact that the hydrothermally-derived sulphides and sulphates in Figure 11c are surrounded by Mn-calcite suggests a hydrothermal origin of the enhanced carbonate input. Schütte (1992) and Cornell and Schütte (1995) previously reported the role of CO_2-rich fluids in the Ongeluk hydrothermal system, thereby suggesting that the CO_2 was partially derived from de-carbonation of Campbellrand dolomite from lower down in the stratigraphy of the Transvaal basin due to deep percolation of the hydrothermal fluids. The increased carbonate content of the lowermost part of the Hotazel might thus very well have recorded the input of CO_2-rich vent fluids. By implication, the carbonate-bound Ca, Mn and Mg may similarly have a direct hydrothermal origin. This is in contrast to the upper BIF part of the drill-core, where these elements are concentrated in distinct microlamina, bound to ankerite (see Figure 11k). The specific ordering, together with the stratigraphically more remote position with respect to the Ongeluk lava makes the interpretation of direct exhalation from the Ongeluk hydrothermal fluids less tempting.

The positive correlation of the Al-normalised Ca, Mg, Mn and Fe concentration profiles compared to that of S in hematite lutite cycle I equally supports a large contribution of hydrothermal exhalations. The fact that in this part of the rock pyrite occurs in the form of large spherulites (see Figure 11d) might reflect rapid crystallisation due to mixing between hot vent fluids and cold ambient seawater, as has been observed at outer parts of hydrothermal chimneys (Xu and Scott, 2005). By implication, this points to a rather close position of the Ongeluk extrusive vent with respect to the chemical sediments observed here in the studied drill-core, though there are alternative explanations for the occurrence of pyrite spherulites. For example, in low-T sedimentary systems spherulitic pyrite is formed at a high degree of supersaturation with respect to Fe sulphide (Raiswell, 1982; Wang and Morse, 1996), or it may be the product of bacterial sulphate reduction during early diagenesis (e.g. Bekker et al., 2004). The very pronounced euhedral pyrite-rich interval in hematite-lutite cycle III (see Figure 9) might also suggest an enhanced hydrothermal influx in this part of the stratigraphy, analogous to that in hematite-lutite cycle I. Xu and Scott (2005) concluded that in hydrothermal vent systems, the cubic crystal shape of pyrite might reflect near-equilibrium crystallisation due to a lower temperature of the vent fluids, and hence might indicate a lower-T or more distal hydrothermal origin of the pyrite-rich interval in cycle III. However, cubic-shaped pyrite is essentially ubiquitous in modern euxinic marine sedimentary settings and thus I find the hydrothermal interpretation for the increased S content here less convincing. By any means, the occurrence of $Fe(II)S_2$ hints at more reducing conditions, whereas the occurrence of Mn(II) carbonates suggests a tendency towards an increasing oxidation potential of the water column and perhaps forms a prelude to the build-up of Mn in the hematite lutite and Mn ore bodies higher up in the Hotazel sequence (Tsikos et al., 2010).

5.4.2 Rare-earth element and Y characteristics of Paleoproterozoic seawater

The REE + Y content of ferric oxyhydroxide is largely controlled by adsorption onto the particles' surfaces during settling through the water column (Byrne and Sholkovitz, 1996 and references therein). Assuming that minimal fractionation occurs within the REE + Y group during oxidation of Fe(II) and co-precipitation with ferric oxyhydroxides from seawater, the REE + Y distribution pattern of Fe-bearing chemical sediments directly reflects that of the water body in which the Fe precipitated, and hence tracks the origin of Fe. Based on this assumption, the REE + Y signature of many very low-grade metamorphosed Archean and Paleoproterozoic BIFs and other Fe-rich chemical sediments (consisting of a shale-normalised total REE + Y concentration below unity, LREE depletion, positive La, Gd and Y anomalies and insignificant to large positive Eu anomalies) has been inferred to directly have trapped the REE + Y signature of the ancient seawater (e.g. Derry and Jacobsen, Bau et al., 1996, Bolhar et al., 2004). In the light of this, the REE + Y profiles of all the jasper samples from the Hotazel Fm. analysed in this study point towards a predominant seawater origin of the lanthanides and hence of Fe, regarding their typical BIF-like signature (see Figure 16); yet the lutite samples seem to reveal a noteworthy contribution of hydrothermal fluid-derived REE + Y.

i) Different to the REE + Y signature of modern seawater but typical for high-T hydrothermal vent fluids, small to moderately positive Eu anomalies (1.18 – 3.42) are present in all hematite-chert samples (see Figure 16 and Table 7). This is a common feature for Precambrian IF, since the oceans at that time were enriched in mantle-

derived REE + Y compared to the modern ocean due to an increased supply of black smoker-type high-T hydrothermal activity (e.g. Derry and Jacobsen, 1990). Hydrothermal fluids show Eu (and LREE) enrichment (provided that Eu occurs as Eu^{2+}) due to preferential release by the source rock of ions with a larger radius (Bau, 1991). The Eu anomaly observed in all hematite-chert samples thus clearly reflects the contribution of REE + Y from hydrothermal fluids to the dissolved REE + Y load of the ancient seawater. Small-scale variability in the intensity of the Eu anomaly in BIF has been inferred to reflect variations in the dilution of hydrothermal fluids by seawater (Bau and Dulski, 1996). Here, the largest $(Eu/Eu^*)_{SN}$ occurs in thin-section 16, which is stratigraphically situated closest to the Ongeluk lava and might therefore indeed correspond to the largest high-T hydrothermal influx. This agrees with the previously discussed carbonate and sulphur enrichment in the lowermost part of the Hotazel. However, the uncertainties for the $(Eu/Eu^*)_{SN}$ values are very large and thus the strength of the Eu anomaly is unsuitable for quantitative comparison between individual samples (see Table 7).

ii) A second, important difference in the REE + Y pattern of ancient compared to modern seawater is the lack of a vastly negative Ce anomaly, and which is equally absent in the hematite-chert samples. Negative Ce anomalies arise from the oxidation of Ce^{3+} to less soluble Ce^{4+} and subsequent removal from the water column by scavenging from settling particles (Sholkovitz et al., 1994), and are therefore indicative for aerobic waters. This is in contrast to suboxic to anoxic waters, which lack large negative Ce anomalies (e.g. German and Ederfield, 1990). BIF hematite-chert (thin-section 2) shows a slightly negative Ce anomaly (0.94) according to the definition of Bolhar et al. (2004), in contrast to the lutite samples, which show positive $(Ce/Ce^*)_{SN}$ (see Table 7). However, according to the approach of Bau and Dulski (1996) these are apparent Ce anomalies are caused by positive La anomalies, although thin-section 2 still has a tendency towards a negative Ce anomaly (see Figure 17). This might suggest that the hematite in the BIF part of the Hotazel could be derived from a marginally more oxygenated water body compared to the lower lutitic part, or alternatively, from more evolved seawater with respect to removal of Ce(IV) from the dissolved REE + Y load. This is in agreement with the paleoenvironmental interpretation of BIF being deposited in a more deep-marine setting and hence precipitated from a larger and "older" water body compared to the lutitic, i.e. shallower part of the Hotazel which was more prone to new hydrothermal REE + Y influxes.

iii) The positive La and Gd anomalies present in the hematite-chert samples are also characteristic for modern (and ancient) seawater (see Table 7). Enrichments in La compared to the other LREE arise from its enhanced stability in seawater related to its empty inner 4f electron shell (Byrne and Kim, 1990; De Baar et al., 1991); positive Gd anomalies are similarly attributed to increased solution stability and decreased surface complexation related to a half-filled inner 4f shell of Gd (e.g. Byrne and Kim, 1990; Kim et al., 1991). The Gd anomalies in the samples, ranging from 1.18 to 1.79, are roughly analogous to the modern seawater signature, i.e. $(Gd/Gd^*)_{SN}$ = 1.09 for the open ocean and 1.21 for enclosed bays (Johannesson et al., 2006 and references therein). The La enrichment is not very distinct compared to the strong positive La anomaly of the modern ocean, i.e. $(La/La^*)_{SN}$ = 4.8 (Bau et al., 1996). This is demonstrated both with the $(La/La^*)_{SN}$ values presented in Table 7 (calculated by the definition of Bolhar et al., 2004) and by the $(Ce/Ce^*)_{SN}$ versus $(Pr/Pr^*)_{SN}$ plot in Figure 17 (according to the method of Bau and Dulski (1996)). However, as mentioned previously for the Eu anomaly, the $(Gd/Gd^*)_{SN}$ and $(La/La^*)_{SN}$ have very large 1 σ error bars and thus should be regarded merely in a qualitative way.

iv) Because Y and Ho have a near-identical ionic radius and occur both in the trivalent oxidation state, they should behave geochemically in a similar fashion and hence occur in ratios equal to average shale or continental crust. However, strongly superchondritic Y/Ho values (ca 40-80) are characteristic for seawater, whose Y-Ho ratio decreases with water depth (Høgdahl et al., 1968; Bau et al., 1995; Nozaki et al., 1997). Several mechanisms have been proposed to be responsible for their fractionation in seawater: differences in solution and surface complexation behaviour, variable solubility of Y and Ho phosphate minerals and fractionation during chemical weathering of continental material (Nozaki et al., 1997; Bolhar et al., 2004). In this study, the BIF hematite-chert and lutite hematite-chert samples have Y-Ho (wt) ratios of 32.1 and 34.9– 45.1, respectively, which is (for some samples) in between those of terrestrial rocks (Y/Ho ≈ 27) and modern seawater (Y/Ho > 40; see Table 7). The Y/Ho of BIF jasper (thin-section 2) is actually closer to the chondritic value. This could imply crustal contamination, except for the fact that there exists no correlation between the Zr content and the Y-Ho ratio, which hence argues against contamination with detrital material (see Figure 18). Bau et al. (2014) showed that the preferential scavenging of Ho relative to Y during formation of modern hydrogenetic Fe-Mn crusts results in lower Y/Ho values than that of their strongly superchondritic seawater source. The mixed Y/Ho signature of the hematite-chert samples from this study possibly represents this process. Given the fact that the Y/Ho of the ocean decreases with increasing water depth, the lower Y/Ho of the BIF compared to the lutitic samples might further be attributed to a lower Y/Ho of the inferred deeper-marine source water of the BIF jasper.

In an alternative scenario, the lower Y/Ho of the BIF sample points towards a hydrothermal origin, regarding the chondritic Y/Ho of hydrothermal fluids (Bau and Dulski, 1999). Paradoxically, the high-T hydrothermal fluids of Bao et al. (2008) indicated in Figure 16 have elevated Y/Ho compared to PAAS, but this is due to

conservative behaviour of Y during REE scavenging on precipitating ferric oxyhydroxides close to the vent. Apparently, the chondritic Y/Ho signal of hydrothermal fluids is rapidly lost, suggesting that fast precipitation of ferric oxyhydroxides close to the vent site is required in order to maintain a hydrothermally-derived Y-Ho ratio. The lowest Y/Ho value of 32.1 of BIF hematite-chert would accordingly have been formed from rapid formation after the release of hydrothermal fluids into the ocean, but this is in marked contrast to the previously discussed similarity of its REE + Y signature with that of (ancient) seawater. The different possible scenarios for varying Y/Ho discussed here thus have contrasting implications for the origin of the hematite-chert samples, and therefore I conclude that this REE + Y proxy is unriable, especially because of its relatively poor precision (see Table 6 and 7).

v) The conspicuous LREE depletion of the hematite-chert samples, specifically of the BIF jasper, agrees very well with the distinct LREE depletion of modern (and ancient) seawater (see Figure 16). This characteristic LREE (and MREE) depletion of modern seawater reflects competition in particle-solution interactions due to lanthanide contraction, in which the larger particles, i.e. the light REE are forming carbonate ion complexes to a lesser extent than the heavier REE. As a result, the LREE are more easily scavenged from the seawater by adsorption processes (e.g. Byrne and Kim, 1990; Quinn et al., 2004). The same process occurs in rivers and estuaries, hence their dissolved HREE enriched signature deliverance to the open ocean contributes to the LREE / HREE depletion (e.g. Hoyle et al., 1984; Ederfield et al., 1990). The BIF hematite-chert $(Pr/Yb)_{SN}$ value of 0.03 implies that it is even more LREE depleted than that of modern seawater, with a $(Pr/Yb)_{SN}$ of 0.13. The average $(Pr/Yb)_{SN}$ value of 0.38 for the lutite hematite-chert samples still indicates LREE depletion but is significantly higher than that of modern seawater and of the BIF jasper samples. This might simply mean that the lutite sample REE + Y were partially derived from a LREE-enriched high-T hydrothermal fluid source, which as a result shifted the overall REE + Y distribution towards a less steep LREE-depleted pattern. However, several studies have shown that the REE + Y distribution of high-T hydrothermal plume particles rapidly scavenge the REE + Y signature from the surrounding seawater and therefore quickly lose their initial hydrothermal signature, except for their positive Eu anomaly (e.g. German et al., 1990; Bau and Dulski, 1999; Sherrel et al., 1999). This suggests that it is only possible to detect a hydrothermal fluid contribution in the REE + Y pattern of ferric oxyhydroxide particles close to the vent site. Bau et al. (2014) stated that modern hydrothermal Fe-Mn oxyhydroxide deposits from the Hawaii Rift zone display shale-normalised REE + Y patterns very similar to those of seawater, so it is difficult to distinguish between a seawater and an additional hydrothermal fluid origin based on REE + Y of the ferric oxyhydroxide precipitate alone. Therefore I will discuss in the next section the other potential mechanisms that might have caused the clear dissimilarity between the $(Pr/Yb)_{SN}$ of BIF and lutite jasper REE + Y signature.

5.4.3 Possible causes of disparate LREE depleted patterns

Contamination of the lutite samples with detrital material would evidently explain the clear difference in $(Pr/Yb)_{SN}$ compared to the BIF samples, because this accordingly would shift the REE + Y signature towards a more horizontal distribution pattern. Although samples or analyses that showed an elevated concentration of lithophile elements (e.g. Al, Ti, Cr, Zr) or major elements other than Fe (e.g. Mg and Mn) were discarded from the results (see also section 3.2.2) for sample purity determination procedure), the accepted samples presented in the *Results* (section 4.2.2) were not purely made up of hematite-chert. Indeed, there is a positive correlation between the total REE + Y abundance and the amount of lithogenic material (see Appendix 4.1). Moreover, most of the lutite jasper samples, i.e. from thin-section 16, 14, 11, 9, 8 and 6 have a higher lanthanide content than the BIF jasper sample (thin-section 2). However, thin-section 13 has a detrital component (i.e. Al, Ti, Cr and Zr concentration) in the same order of magnitude as that of thin-section 2 (see Appendix 4.1 and Figure 18). Apparently, this resulted in a slightly lower total REE + Y content relative to the other lutite samples, but it did not affect the LREE depletion: the $(Pr/Yb)_{SN}$ of sample 13 has an average of 0.37, similar to the mean value for all lutite samples (see Table 7). Therefore I discard the possibility that detrital contamination is responsible for the disparate REE + Y signal of the BIF and lutite hematite-chert samples.

Secondly, the REE + Y pattern may not be a primary signal but represent a post-depositional alteration feature. The REE + Y pattern of BIF hematite-chert could have been shifted towards a steeper profile due to preferential removal of LREE during anoxic burial diagenesis (Byrne and Sholkovitz, 1996). However, this argument is not applicable here since the samples are composed of primary hematite, and hence the ferric oxyhydroxide particles and their co-precipitated REE + Y presumably remained undisturbed during diagenesis. However, post-diagenetic mobilisation of REE + Y during burial metamorphism or metasomatism is still probable, especially considering the (stratigraphic) proximity of the hematite-chert sediments to the pervasively altered Ongeluk lava. In high-T fluid-rock interactions under mildly acidic conditions, the REE + Y pattern of the fluids is mainly controlled by sorption processes, which leads to preferential release of the LREE due to the lanthanide contraction (Bau, 1991). Consequently, this process could have shifted the REE + Y profile of the lutite samples towards a less LREE-depleted pattern. Previous authors though established that the low water-rock ratio associated with the very low-grade metamorphism (i.e. greenschist facies) the Transvaal BIFs experienced was unsuitable for considerable mobilisation of REE + Y (Bau and Dulski, 1996; Slack et al., 2007). Regarding the

similarly immature sediments of the Hotazel sediments it is thus also unlikely that burial metamorphism significantly affected its REE + Y content. On the other hand, it is not inconceivable that hydrothermal fluids from the Ongeluk hydrothermal circulation system could have penetrated the lower part of the Hotazel Fm. and consequently added their increased dissolved load of LREE to the sediments. The SE picture Figure 15d of the jasper lens in thin-section 14 (in hematite lutite cycle I) displays coarser hematite grains than found in the BIF microband from thin-section 2, which might reflect a coarsening process induced by these hydrothermal fluids. However, the hematite particles are still regarded to be very primary because of their submicron-scale crystal size and the supposed silica flocculation texture they exhibit. Potentially, the hydrothermal fluids could have affected the co-precipitated REE + Y only, and have left the silica and ferric oxyhydroxide deposits unaltered. The consistency in the REE + Y patterns of all lutite hematite-chert samples, and more specifically the constant $(Pr/Yb)_{SN}$ values they exhibit, argues against this scenario, although all samples might of course have experienced an identical degree of fluid alteration. Consequently it is not possible to rule out the chance of a metasomatic effect on the hematite-chert REE + Y signature, but the evidence against significant hydrothermal mobilisation of the primary REE + Y content is more convincing.

An alternative cause for the two distinct levels of LREE depletion might involve a difference in the scavenging behaviour of the REE + Y during formation of ferric oxyhydroxides in the water column. It is widely demonstrated by experimental studies (e.g. Byrne and Kim, 1990; Koeppenkastrop and De Carlo, 1993; Bau, 1999) as well as studies of modern natural systems (e.g. Bau and Koschinsky, 2009 and references therein) that precipitation of ferric oxyhydroxide particles is accompanied by fractionation within the REE + Y group. Partitioning coefficients between modern hydrogenetic Fe-Mn crusts and seawater decrease towards the HREE. Accordingly, the lower degree of LREE depletion of the lutite hematite-chert compared to that of modern seawater might actually be the effect of preferential adsorption of the LREE onto the ferric oxyhydroxide particles and subsequent scavenging from the seawater. But it remains unclear why this scavenging process would not identically apply to the formation of the BIF part.

Because the alternative scenarios discussed above all fail to convincingly explain the clear division in lutite and BIF hematite-chert $(Pr/Yb)_{SN}$ values, I conclude that the two REE + Y distribution patterns most likely represent a difference in the REE + Y of the source fluid. The identical $(Pr/Yb)_{SN}$ of the Hotazel lutite jasper and that of modern hydrothermal fluid-derived Fe crust from the Hawaii Rift zone (see also section 4.2.2 and Figure 16c) indicates a significant hydrothermal origin for the lower part of the Hotazel. In accordance with the previously discussed sedimentary and petrographic features of the Hotazel, the lutite hematite-chert REE + Y could represent deposition in a shallow marine setting which was more influenced by the contribution of a hydrothermally-derived REE + Y load from the Ongeluk system. The freshly released Fe(II) was readily oxidised and precipitated as ferric oxyhydroxide particles. In modern hydrothermal settings, the adsorption of seawater-sourced REE + Y onto hydrothermal plume takes place at the scale of days: the REE + Y distribution of the plume gradually evolves from a more vent-dominated pattern close to the vent towards a more seawater-like pattern in the neutrally buoyant plume part (e.g. German et al., 1990; Sherrel et al., 1999; Bau and Dulski, 1999; Edmonds and German, 2004). Hence, the dissolved hydrothermal Fe(II) must have experienced rapid flocculation with amorphous silica so that there was little time for the REE + Y of the ambient seawater to adsorb onto them and thus the hydrothermal REE + Y signal was partially maintained. This is in contrast to the formation of the BIF hematite-chert, which originates from a deeper part of the ocean, less influenced by hydrothermal influxes. Due to long-term removal of LREE by e.g. preferential scavenging onto ferric oxyhydroxide, the $(Pr/Yb)_{SN}$ value of the remaining seawater had considerably decreased, and accordingly this LREE depletion is reflected by the distinct LREE depleted distribution pattern of the BIF jasper. The fact that the $(Pr/Yb)_{SN}$ value of BIF jasper (thin-section 2) is even lower than that of average modern seawater may signify that the LREE in the seawater of the Transvaal basin were scavenged to a much higher degree than in modern ocean water. This accordingly could support the idea that the dissolved Fe(II) pool of the Transvaal basin experienced protracted oxidation in relation to the rise of photosynthetically-produced O_2; the extensive removal of Fe(II) would have co-occurred with enhanced (preferential) LREE scavenging.

At last, it remains unclear why the REE distribution pattern of the sample from Tsikos and Moore (1997), i.e. the “Hotazel oxide facies” in Figure 16c, does not show an equal degree of LREE depletion as the BIF hematite sample from this study, but more like that of the lutite hematite samples. The oxide facies sample was derived from higher up in Hotazel stratigraphy, but of the same BIF interval as from which the BIF hematite sample originates, and should therefore also embody more open-marine REE characteristics. However, the sample consisted of various other minerals, which presumably obliterate the hematite-chert REE signal, and therefore its REE cannot be compared to that of the samples from this study.

5.5 Fe isotope constraints on the redox state of the ocean

Tsikos et al. (2010) proposed that the very negative $\delta^{56}Fe$ values and extensive Mn precipitation reported higher up in the Hotazel sequence represent the last stages of the Fe isotopic and geochemical evolution of the Transvaal basin, associated with increasing (dissolved) O_2 levels. The depleted $\delta^{56}Fe$ values of the hematite- and Mn-rich layers

signify the removal of the residual (Rayleigh-distillated) Fe(II) pool from the ocean due to an overwhelm of photosynthetically produced O_2, potentially marking the onset of the GOE. The $\delta^{56}Fe$ values measured in the hematite-rich samples presented in this study are correspondingly depleted, if only moderately, but might very well satisfy this Rayleigh fractionation scenario (see Table 11). Because these $\delta^{56}Fe$ values were measured in primary hematite they cannot be the result of microbial Fe(III) reduction, which is similarly capable of producing very depleted $\delta^{56}Fe$ values in the sediment (e.g. Johnson et al., 2008). However, the measured $\delta^{56}Fe$ values in the jasper samples do not directly represent the $\delta^{56}Fe$ of the Transvaal seawater but they also depend on fractionation processes in the water column. Moreover, most of the samples are contaminated with other Fe-bearing minerals that obscure the original $\delta^{56}Fe$ value of hematite. In addition, the nature of the aqueous Fe(II) source remains an important issue: as suggested by its REE + Y partitioning behaviour, hematite from the lutite part of the Hotazel may largely originate from hydrothermally sourced Fe(II). This would mean that the $\delta^{56}Fe$ values of the Fe isotope samples derived from the lutitic part (i.e. HF3-7) represent a relatively isolated, shallow part of the Transvaal basin with its local, hydrothermal fluid-dominated Fe isotopic signature; only the $\delta^{56}Fe$ of sample HF1 (from the BIF part) would be more representative for the $\delta^{56}Fe$ of the entire basin. Consequently, the $\delta^{56}Fe$ results from Table 11 need further evaluation before a seawater $\delta^{56}Fe$ composition can be deduced from them.

5.5.1 Fe isotope signature of source fluids

In the most ideal case, the samples HF1-7 constitute purely hematite and chert, without the contribution of additional phases in which the Fe is hosted. The $\delta^{56}Fe$ value of (primary) hematite then represents 1) isotopic fractionation during the redox change from aqueous Fe(II) to Fe(III) and subsequent ferric oxyhydroxide formation (assuming that no fractionation occurred during further hematite formation); and 2) the $\delta^{56}Fe$ value of the source fluid. Following standard practice, the Fe isotopic fractionation between to components A and B is described as:

$$\alpha_{A\text{-}B} = (^{56}Fe/^{54}Fe)_A/(^{56}Fe/^{54}Fe)_B$$

Because this α value is very small, I prefer to use here the following approximation for $\alpha_{A\text{-}B}$, that is:

$$10^3 ln\alpha_{A\text{-}B} \approx \delta^{56}Fe_A - \delta^{56}Fe_B \approx \Delta^{56}Fe_{A\text{-}B}$$

The theoretically predicted and experimentally determined fractionation effects (i.e. $\Delta^{56}Fe_{A\text{-}B}$) for equilibrium fractionation (under low-T and circumneutral pH) of Fe(II)aq → Fe(III) and Fe(III) → $Fe(OH)_3$ are ca -3 ‰ and +2 ‰, resp., resulting in overall $Fe(II)_{aq}$ → ferrihydrite fractionation effect of ca -1.0 ‰ (Bullen et al., 2001; Beard and Johnson, 2004; Beard et al., 2010). At higher temperatures (T > 250°C) the absolute value of this cumulative fractionation effect decreases (e.g. Polyakov and Mineev, 2000). Furthermore, the degree of fractionation induced by microbially mediated Fe(II) oxidation is approximately similar to that of abiotic oxidation (Croal et al., 2004; Balci et al., 2006). In conclusion, from the $\delta^{56}Fe$ values of the Hotazel Fe isotope samples that, apart from chert, purely consist of primary hematite, I estimate that the $\delta^{56}Fe$ of the source fluid would have been ca 1.0 ‰ lighter (i.e. $\Delta^{56}Fe_{Fe(II)aq\text{ - hematite}} = \delta^{56}Fe_{Fe(II)aq} - \delta^{56}Fe_{hematite}$ = -1.0 ‰).

Unfortunately, this assumption is far from trivial and only applies in the case of partial oxidation of the aqueous Fe(II) reservoir; the $\delta^{56}Fe$ of samples that reflect complete oxidation of the entire dissolved Fe(II) load would be identical to that of the initial fluid prior to oxidation. Another caveat in determining the $\delta^{56}Fe$ of the source fluid is the uncertainty about whether chemical equilibrium has been fully achieved, or whether the measured $\delta^{56}Fe$ values also result from a kinetic fractionation effect. Therefore, estimates of the source fluid $\delta^{56}Fe$ composition based on samples HF1-7 should only be considered as an indication.

Based on both XRD and ICP-OES data (and as discussed previously in section 4.3.1), Fe isotope sample HF7 has the highest hematite content of all Hotazel samples and only contains a relatively minor Fe carbonate (ankerite) and magnetite contribution. The fact that bulk-rock and the HCl-fraction of HF7 both have a very similar FeO concentration and $\delta^{56}Fe$ value, further supports the finding that Fe silicates are virtually absent and that the majority of the Fe in sample HF7 is hosted in hematite. In order to deduce from this an Fe isotopic signature of the initial aqueous source, the equilibrium isotope fractionation effect for $Fe(II)_{aq}$ oxidation and subsequent ferric oxyhydroxide formation (i.e. $\Delta^{56}Fe_{Fe(II)aq\text{ - hematite}}$ = -1.0 ‰) can thus directly be applied. Accordingly, the sample's bulk-rock $\delta^{56}Fe$ value of -0.50 ‰ likely corresponds to a $\delta^{56}Fe$ value of the initial fluid as low as circa -1.5 ‰.

In contrast to sample HF7, the other Fe isotope samples of the Hotazel (HF6-1) contain various amounts of Fe-bearing minerals other than hematite (see section 4.3.2). Because these minerals have different redox states and bonding types, they have different fractionation factors with respect to Fe (Schauble, 2004; Anbar and Rouxel, 2007). Micro-analytical techniques have established that this Fe isotopic heterogeneity and these inter-mineral fractionations can be preserved during diagenesis and metamorphism (Frost et al., 2007; Whitehouse and Fedo, 2007). Although the $\delta^{56}Fe$ of the Fe(II) source might be the same for all samples, variations in the sample's mineral content (either reflecting primary or diagenetic processes) may thus result in a different $\delta^{56}Fe$ composition of the sample that is attributed to the different mineral-specific fractionation factors.

This is for example illustrated by sample HF6, which has a bulk-rock $\delta^{56}Fe$ of ca -0.93 ‰ (see Table 11). Regarding the sample's relatively high (bulk-rock and HCl-fraction) CaO and slightly elevated MgO and MnO content (see

Table 9 and Figure 19), together with the identification of ankerite in its XRD spectrum (see Table 8), sample HF6 presumably contains (apart from hematite) a significant portion of Fe carbonates. As previously discussed, Fe carbonates either formed directly from seawater Fe(II) (Klein and Beukes, 1989; Klein, 2005; Konhauser et al., 2002, 2007) or during diagenesis by (a)biogenic reduction of ferric oxyhydroxides coupled to the oxidation of organic matter, and subsequent magnetite formation (Lovley et al., 1987; Frost et al., 2007; Johnson et al., 2008). Because the fractionation effect between aqueous Fe(II) and $FeCO_3$ (i.e. $\Delta^{56}Fe_{Fe(II)aq - FeCO3}$) is much higher than between Fe(II) and $Fe(OH)_3$, that is, experimentally determined $\Delta^{56}Fe_{Fe(II)aq - FeCO3}$ values range from 0.0 ‰ up to +1.0 ‰ (e.g. Wiesli et al., 2004; Johnson et al., 2005), the Fe carbonate impurities in sample HF6 therefore complicate the interpretation of the initial seawater $\delta^{56}Fe$. Moreover, this fractionation effect is also highly dependent on the carbonate composition, in which the presence of Ca in ankerite further increases the fractionation factor compared to Ca-free siderite (Steinhoefel et al., 2009). Supposing that the ankerite in HF6 formed diagenetically from a primary Fe carbonate precursor, its $\delta^{56}Fe$ value thus presumably would be around 1-2 ‰ lower than that of the ferric oxyhydroxide precipitates. Secondary Fe carbonate formation after Fe(III) hydroxide would alternatively result in the formation of $Fe(II)_{aq}$ fluids with a 2–3 ‰ lighter $\delta^{56}Fe$ value than the $\delta^{56}Fe$ of the precursor Fe(III) substrate (e.g. Bullen et al., 2001; Beard and Johnson, 2004; Beard et al., 2010). Carbonate $\delta^{56}Fe$ that precipitated from this released Fe(II) would thereupon be between 0 and 1 ‰ lighter, whilst magnetite would be 1.3‰ heavier (Johnson et al., 2005). Altogether, the Fe incorporated into secondary ankerite could be down to 4 ‰ lighter than that of the original ferric oxyhydroxide precipitates.

Both scenarios consequently lead to preferential incorporation of ^{54}Fe into Fe carbonate, but according to the literature the extent to which this happens varies highly (e.g. Wiesli et al., 2004; Johnson et al., 2005) and makes it thus very difficult to decipher the Fe isotope composition of the initial fluid source of sample HF6. However, to get a rough idea of the extent to which the Fe carbonate portion of sample HF6 may have affected its bulk-rock $\delta^{56}Fe$ value, I make the following assumptions: (i) First of all, I presume that ankerite is a rather primary mineral (based on the mineral phase relationships established earlier in section 5.3.2). Hence, this yields an Fe(II) → ankerite fractionation effect (i.e. $\Delta^{56}Fe_{Fe(II)aq - FeCO3}$) of only between 0.0 ‰ and +1.0 ‰. (ii) Furthermore, I assume that, apart from Fe carbonate impurities, the rest of sample HF6 consists of hematite only. If the Fe carbonate fraction in sample HF6 then would have an Fe(II) → ankerite fractionation effect of 0.0 ‰, this would result in a carbonate-corrected $\delta^{56}Fe$ value (i.e. corresponding to a purely hematitic composition) of -0.9 ‰ and a $\delta^{56}Fe$ of the aqueous source Fe(II) reservoir down to ca -1.9 ‰; taking +1.0 ‰ as the fractionation effect between Fe(II) and ankerite, the carbonate-corrected $\delta^{56}Fe$ value of sample HF6 would be ca -0.8 ‰, corresponding to a ca -1.8 ‰ value of the water column (see Table 15 for the calculation). This means that the presence of ankerite would have shifted the $\delta^{56}Fe$ of sample HF6 towards lower values with a maximum of +0.1 ‰. It is important to note though that this calculation (in Table 15) is based on the assumption that all Ca in HF6 HCl is bound to Fe. However, the XRD data show that calcite is more abundant than ankerite, meaning that the majority of the measured Ca is hosted in (Mn-)calcite. This indicates that the influence of the Fe carbonate fraction in sample HF6 on the overall $\delta^{56}Fe$ is far lower than the calculated shift of -0.1 ‰ and is moreover of little importance regarding the ±0.11‰ external uncertainty limits of $\delta^{56}Fe$. Therefore, the difference between the $\delta^{56}Fe$ of samples HF7 (ca -0.5 ‰) and HF6 (ca -0.9 ‰) may signify an real change in the Fe isotopic composition of the water column with time towards a slightly more depleted signature, which might have been as low as -1.9 ‰.

However, the assumption that bulk-rock sample HF6 only contains hematite and Fe carbonate needs to be re-evaluated. The FeO wt % of sample HF6 HCl is more than 50 % lower than that of bulk-rock sample HF6 (see Table 9), indicating that a considerable amount of Fe was not dissolved during HCl-treatment of the initial rock powder. Because Fe silicates, in contrast to Fe oxides and Fe carbonates, are generally thought to be insoluble in HCl, this undissolved Fe may thus be bound to Fe silicate impurities. Considering the higher (corrected) $\delta^{56}Fe$ value of circa -0.6 ‰ for sample HF6 HCl, the Fe silicate fraction could have shifted the bulk-rock sample's $\delta^{56}Fe$ towards more negative values than would have been the case if Fe was exclusively hosted in hematite. Following this interpretation, instead of using the $\delta^{56}Fe$ value of bulk-rock sample HF6, the $\delta^{56}Fe$ of sample HF6 *HCl* would be more suitable for back-calculating the $\delta^{56}Fe$ of the sample's original hematite fraction and hence that of the initial Fe(II) pool. Following the same procedure as I did for bulk-rock sample HF6, the carbonate-corrected $\delta^{56}Fe$ value (i.e. corresponding to a purely hematitic composition) would accordingly be ca -0.5 ‰ (in the case of $\Delta^{56}Fe_{Fe(II)aq - FeCO3}$ = 0.0 ‰) and ca -0.4 ‰ (for $\Delta^{56}Fe_{Fe(II)aq - FeCO3}$ = +1.0 ‰; see Table 16). This proposed maximum correction of +0.2 ‰ is again an overestimation because part of the CaO was presumably hosted in Mn-calcite instead of ankerite. As a result, the Fe isotopic signature of the hematite fraction of HF6 (HCl) would be similar to that of HF7 within the external 2 S.D. uncertainty limits of ±0.11 ‰, instead of ca 0.3-0.4 ‰ lower.

The other Fe isotope samples from the Hotazel Fm. have a much lower CaO-FeO ratio than sample HF6 (see Table 9 and Figure 19), so I consider the additional effect of Fe carbonate fractionation on the total $\delta^{56}Fe$ value of these samples (bulk-rock as well as HCl-fraction) to be of minor importance. More specifically, changes in $\delta^{56}Fe$ caused by the presence of Fe carbonate are likely to remain within

the ±0.11‰ external uncertainty limits of the measured bulk-rock $\delta^{56}Fe$ values. What instead seems to have a considerable influence on the samples' $\delta^{56}Fe$ values is the earlier mentioned contribution of Fe silicates. Not only does sample HF6 exhibit a large difference between its bulk-rock and HCl-fraction $\delta^{56}Fe$ value, but the same is shown for samples HF4 and HF3. The measured $\delta^{56}Fe$ of the HCl-fraction of samples HF6, 4 and 3 is approx. +0.3‰ higher than that of their bulk-rock equivalent. In these samples at least half of the total Fe concentration in the original rock powder did not dissolve into the HCl solution, as demonstrated by the difference in Fe concentration between the bulk-rock and HCl-fractions (see Table 9). Because Fe silicates are generally insoluble in HCl, the ±0.3 ‰ difference in the Fe isotopic composition between the bulk-rock and HCl-leach samples could thus be related to the presence or absence of Fe silicates. This interpretation is supported by the fact

Table 15: Correction of the bulk-rock $\delta^{56}Fe$ composition of sample HF6 (i.e. -0.93 ‰) for the additional $\delta^{56}Fe$ fractionation effect of ankerite impurities that are present in the sample. From the typical FeO/CaO of ankerite (obtained from EMPA results) I can estimate how much FeO in sample HF6 is bound to ankerite and how much is bound to hematite (assuming that only ankerite and hematite are present). From the fractionation effect between aqueous Fe(II) and ankerite (i.e. $\Delta^{56}Fe_{HF6\ carbonate}$ = 0.0 ‰ to + 1.0 ‰) and between aqueous Fe(II) and hematite (i.e. $\Delta^{56}Fe_{Fe(II)aq\ -\ HF6\ oxide}$ = -1.0 ‰) I can finally obtain an estimate of the $\delta^{56}Fe$ composition of the initial seawater Fe(II), .i.e $\delta^{56}Fe_{Fe(II)\ aq}$ = -1.9 to -1.8‰.

	Mean ankerite composition (EMPA results) wt %			Mean ankerite composition *Recalculated*** wt %	HF6 composition (ICP-OES results) wt %
Fe	6.25	→	FeO	10.81	5.44
Ca	27.02		CaO	46.72	1.41
Total*	57.84				

* The term *Total* indicates the total mass % obtained from WDS results (see also Table 3b and Appendix 2.1).
** Recalculated assuming a total mass of 100 wt % in order to convert the relative atomic wt % of Fe and Ca in ankerite to FeO and CaO wt %.

Assuming that all CaO of sample HF6 is hosted in ankerite, the distribution of the sample's total Fe content over the carbonate and oxide fractions is:

Carbonate Fe (wt %) = $(FeO/CaO)_{ankerite} * CaO_{HF6}$ = (10.81 / 46.72) * 1.41 = 0.33

Oxide Fe (wt %) = FeO_{HF6} - carbonate Fe = 5.44 – 0.33 = 5.11

Following standard practice, the isotopic fractionation between two components, A and B, is described as:

$\alpha_{A-B} = (^{56}Fe/^{54}Fe)_A/(^{56}Fe/^{54}Fe)_B$

As previously mentioned in section 5.5.1, a useful approximation for the fractionation factor is α_{A-B}:

$10^3 ln\alpha_{A-B} \approx \delta^{56}Fe_A - \delta^{56}Fe_B \approx \Delta^{56}Fe_{A-B}$

Following this definition, I obtain:

$\delta^{56}Fe_{Fe(II)\ aq} - \delta^{56}Fe_{HF6\ total} = \Delta^{56}Fe_{Fe(II)aq\ -\ HF6\ total}$, where *Fe(II)aq* represents the initial seawater Fe(II) and where *HF6 total* represents all Fe in sample HF6, i.e. hosted in both the oxide and carbonate fraction

Accordingly:

$\delta^{56}Fe_{Fe(II)\ aq} = \Delta^{56}Fe_{Fe(II)aq\ -\ HF6\ total} + \delta^{56}Fe_{HF6\ total}$

$\delta^{56}Fe_{Fe(II)\ aq} = (\Delta^{56}Fe_{Fe(II)aq\ -\ HF6\ oxide} * \text{oxide Fe/total Fe} + \Delta^{56}Fe_{Fe(II)aq\ -\ HF6\ carbonate} * \text{carbonate Fe/total Fe}) + \delta^{56}Fe_{HF6\ total}$

I assume that $\Delta^{56}Fe_{Fe(II)aq\ -\ HF6\ oxide}$ = -1.0 ‰; $\delta^{56}Fe_{HF6\ total}$ has a (corrected) value of circa -0.93 ‰ (see Table 13)

Therefore:

If $\Delta^{56}Fe_{Fe(II)aq\ -\ HF6\ carbonate}$ = 0.0 ‰, then $\delta^{56}Fe_{Fe(II)\ aq}$ = (-1. 0 ‰ * 5.11/5.44 + 0.0 ‰ * 0.33/5.44) – 0.93 ‰ = **-1.9 ‰**

If $\Delta^{56}Fe_{Fe(II)aq\ -\ HF6\ carbonate}$ = +1.0 ‰, then $\delta^{56}Fe_{Fe(II)\ aq}$ = (-1.0 ‰ * 5.11/5.44 + 1.0 ‰ * 0.33/5.44) – 0.93 ‰ = **-1.8 ‰**

Table 16: Correction of the bulk-rock $\delta^{56}Fe$ composition of sample HF6 **HCl** (ca -0.6 ‰) for the additional $\delta^{56}Fe$ fractionation effect of ankerite impurities that are present in the sample.

	Mean ankerite composition (EMPA results) wt %			Mean ankerite composition *Recalculated*** wt %	HF6 HCl composition (ICP-OES results) wt %
Fe	6.25	→	FeO	10.81	2.36
Ca	27.02		CaO	46.72	1.28
Total*	57.84				

* The term *Total* indicates the total mass % obtained from WDS results (see also Table 3b and Appendix 2.1).

** Recalculated assuming a total mass of 100 wt % in order to convert the relative atomic wt % of Fe and Ca in ankerite to FeO and CaO wt %.

Assuming that all CaO of sample HF6 HCl is hosted in ankerite, the distribution of the sample's total Fe content over the carbonate and oxide fractions is:

Carbonate Fe (wt %) = $(FeO/CaO)_{ankerite} * CaO_{HF6\ HCl}$ = (10.81 / 46.72) * 1.28 = 0.30

Oxide Fe (wt %) = $FeO_{HF6\ HCl}$ - carbonate Fe = 2.36 – 0.30 = 2.06

Following standard practice, the isotopic fractionation between two components, A and B, is described as:

$\alpha_{A-B} = (^{56}Fe/^{54}Fe)_A/(^{56}Fe/^{54}Fe)_B$

As previously mentioned in section 5.5.1, a useful approximation for the fractionation factor is α_{A-B}:

$10^3 ln\alpha_{A-B} \approx \delta^{56}Fe_A - \delta^{56}Fe_B \approx \Delta^{56}Fe_{A-B}$

Following this definition, I obtain:

$\delta^{56}Fe_{Fe(II)\ aq} - \delta^{56}Fe_{HF6\ HCl\ total} = \Delta^{56}Fe_{Fe(II)aq\ -\ HF6\ HCl\ total}$, where *Fe(II)aq* represents the initial seawater Fe(II) and where *HF6 HCl total* represents all Fe in sample HF6 HCl, i.e. hosted in both the oxide and carbonate fraction

Accordingly:

$\delta^{56}Fe_{Fe(II)\ aq} = \Delta^{56}Fe_{HF6\ HCl\ total} + \delta^{56}Fe_{HF6\ HCl\ total}$

$\delta^{56}Fe_{Fe(II)\ aq} = (\Delta^{56}Fe_{Fe(II)aq\ -\ HF6\ HCl\ oxide} * \text{oxide Fe/total Fe} + \Delta^{56}Fe_{HF6\ HCl\ carbonate} * \text{carbonate Fe/total Fe}) + \delta^{56}Fe_{HF6\ HCl\ total}$

I assume that $\Delta^{56}Fe_{Fe(II)aq\ -\ HF6\ HCl\ oxide}$ = -1.0 ‰; $\delta^{56}Fe_{HF6\ HCl\ total}$ has a (corrected) value of circa -0.6 ‰ (see Table 13)

Therefore:

If $\Delta^{56}Fe_{Fe(II)aq\ -\ HF6\ HCl\ carbonate}$ = 0 ‰, then $\delta^{56}Fe_{Fe(II)\ aq}$ = (-1.0 ‰ * 2.06/2.36 + 0.0 ‰ * 0.30/2.26) – 0.6 ‰ = **-1.5 ‰**

If $\Delta^{56}Fe_{Fe(II)aq\ -\ HF6\ HCl\ carbonate}$ = + 1 ‰, then $\delta^{56}Fe_{Fe(II)\ aq}$ = (-1.0 ‰ * 2.06/2.36 + 1.0 ‰ * 0.30/2.26) – 0.6 ‰ = **-1.4 ‰**

that there is no difference in the Fe isotopic composition of the bulk-rock and HCl-leach of sample HF7 (see also Table 11 and Figure 19), which was concluded to be a very pure hematite-chert sample. Its FeO / ($MgO + Al_2O_3$) is far higher (i.e. ca 36) than that of bulk-rock samples HF6, 4 and 3, i.e. ca 14, 7 and 9, respectively (see also Table 9 and Figure 19). As a result, from the samples that are rather poor in hematite and rich in Fe silicate impurities (based on their MgO and Al_2O_3 content), the $\delta^{56}Fe$ value of their HCl-fraction would be more suitable for deducing an Fe isotopic signature of the initial Fe(II) pool from rather than that of the bulk-rock sample. HF4 HCl has a (corrected) $\delta^{56}Fe$ of ca -0.2 ‰, which is significantly higher than lower down in the Hotazel stratigraphy; HF3 HCl has an even higher value of ca -0.1 ‰. Following the same procedure as for samples HF7 and HF6, the $\delta^{56}Fe$ of their source fluids would yield values down to around -1.2 and -1.1 ‰, respectively.

However, the presumption that Fe silicates are insoluble in HCl is challenged by the relatively high MgO and Al_2O_3 concentrations that were measured in the HCl-fraction of samples HF7, 6, 4 and 3 (see Table 9), and therefore also the interpretation of their $\delta^{56}Fe$ values is challenged. Apart from sample HF6 HCl, all HCl-leach samples have an approximately similar Al_2O_3 concentration as in their corresponding bulk-rock leach. Not only does this suggest that the Fe silicates *were* dissolved in HCl, either partially or even fully, but it also implies that the portion of Fe that remained inert during HCl digestion was mainly hosted in the Fe oxides, that is, a substantial portion of the Fe oxides was dissolved during the HCl digestion procedure.

This is also illustrated in Table 17, in which the chemistry of the undissolved fraction of samples HF7, 6, 4 and 3 is given (obtained by subtracting the HCl-fraction data from the bulk-rock data, listed in Table 9).

Table 17: Chemistry of the rock fraction of sample HF3, 4, 6 and 7 that did not dissolve in HCl, obtained from subtracting the chemistry of the HCl-fraction samples from that of the equivalent bulk-rock samples (based on the ICP-OES data presented in Table 9).

Undissolved fraction:	FeO	MgO	MnO	Al_2O_3	CaO	FeO/(MgO + Al_2O_3)
HF3	2.7	0.4	0.0	0.0	0.0	6.8
HF4	3.2	0.1	0.0	-0.1	0.0	32.0
HF6	3.0	0.1	0.0	0.1	0.1	15.0
HF7a	5.3	0.1	0.0	0.0	0.0	53.0
HF7b	2.7	0.1	0.0	-0.1	-0.4	27.0

The Fe / (Mg + Al_2O_3) of the samples is too high compared to the typical ratios for chlorite, stilpnomelane and minnesotaite (i.e. Fe / (Mg + Al_2O_3) < 1; see EMPA data in Table 3b). Provided that these ICP-OES data are correct, incomplete dissolution of the Fe oxides, i.e. hematite, must have been responsible for the +0.3 ‰ shift in the δ^{56}Fe values of samples HF6, 4 and 3 HCl rather than the contribution of Fe silicates. This +0.3 ‰ difference could in the first place be explained when the bulk-rock sample's Fe silicate fraction would involve much higher δ^{56}Fe values than the hematite fraction. If subsequently the Fe silicates were dissolved in HCl but a substantial part of the Fe oxides was not, the higher relative abundance of Fe silicates over hematite could have caused a shift towards an overall heavier Fe isotopic composition. However, the δ^{56}Fe value of HF5 (i.e. -1.07 ‰), which is the lowest of all samples presented in this study, might suggest that the Fe silicate fraction is expected to show the opposite. This δ^{56}Fe value of -1.07 ‰ may not necessarily indicate enhanced δ^{56}Fe depletion (relative to the -0.50 ‰ of HF7) of the hematite fraction and thus of the initial seawater Fe(II), but instead it may largely reflect the δ^{56}Fe effect of Fe silicate impurities: XRD data suggest that the sample's relative hematite concentration is low (i.e. ca 2 wt %) compared with chlorite (i.e. ca 5 wt; see Table 8). Even though Fe constitutes only ca 30 wt % of chlorite, which is more than two times lower than the Fe concentration in the crystal lattice of hematite (ca 70 wt %), this certainly hints at a substantial contribution of chlorite. This is further supported by the large MgO, and more importantly, large Al_2O_3 content of HF5 relative to FeO (see Table 9 and Figure 19). Because these chlorite / Fe silicate impurities are very minor in sample HF7, the large difference in the δ^{56}Fe value between samples HF7 and HF5 (i.e. ca 0.6 ‰) hints at the possibility that this may reflect (at least in part) a difference in mineralogy rather than intrinsic changes in the seawater δ^{56}Fe composition only. Previously I concluded that chlorite in the Hotazel is a detrital mineral derived from the hydrothermally altered Ongeluk lava. Although no individual Fe isotope data of chlorite exist, the average bulk-rock δ^{56}Fe value of the Ongeluk samples OF1-3 is ca -0.7 ‰. Considering the fact that the majority of the Ongeluk lava is composed of secondary chlorite (as stated in section 4.1.2 and as supported by the very high Al_2O_3 content of OF1-3 in Table 9), I find it unlikely that the chlorite fraction in the Hotazel samples would have a much higher δ^{56}Fe composition. Therefore I assume that the detrital chlorite in the Hotazel Fe isotope samples generally has a depleted δ^{56}Fe composition. Coming back to the initially postulated explanation for the ±0.3 ‰ shift between the bulk-rock and HCl-fraction δ^{56}Fe values of samples HF6, 4 and 3, simply the dissolution of Fe silicates and incomplete Fe oxide dissolution probably did not cause a +0.3 ‰ heavier δ^{56}Fe value of the HCl-fraction.

In an alternative scenario, the presence of MgO and Al_2O_3 impurities in sample HF5 (and in the other samples) might not reflect that of chlorite but of stilpnomelane, since Mg and Al are also incorporated in the crystal lattice of stilpnomelane. This would mean that the δ^{56}Fe signature of Fe silicate impurities not necessarily represents a directly detrital signal from the Ongeluk lava. In none of the sample's XRD spectra stilpnomelane was identified (see Table 8), but this is highly unlikely regarding the widespread distribution of stilpnomelane in the entire Hotazel sequence (see section 4.1.2). Moreover, only in the XRD spectra of sample HF1 and HF5 chlorite peaks reached above the detection limit, although in each sample Al_2O_3 was detected with ICP-OES. Because Al is mainly hosted in the crystal lattice of chlorite, the fact that sample HF4 has a far larger Al_2O_3 concentration (i.e. 0.5 wt %) than HF1 (0.1 wt %) implies that chlorite or stilpnomelane certainly are present in HF4 but did not produce distinct peaks in the corresponding XRD spectrum plot. It is thus very difficult to identify the presence of and distinguish between individual peaks of chlorite, stilpnomelane (or minnesotaite) in XRD plots; rather all the Fe silicates form a broad bulge at the lower 2θ end of the XRD spectrum plot. Therefore the XRD data are not very suitable for identification of the Fe silicates in the Hotazel samples; instead the chemical composition of the bulk-rock Fe isotope samples is more helpful. Samples of which a relatively large portion is composed of Fe silicates but which have relatively low Al_2O_3 and high MgO concentrations are more likely to contain more stilpnomelane and / or minnesotaite than chlorite. For example, HF5 has a MgO-Al_2O_3 ratio of ca 1.8, which lies in between the typical MgO / Al_2O_3 values for stilpnomelane (ca 2.1) and chlorite (ca 1.4; see Table 3b). Given the fact that little CaO is present in sample HF5 and thus no Mg is hosted in the Fe carbonate fraction, this indicates that the Fe of the sample originates from both chlorite and stilpnomelane. Because of the relatively large uncertainty in the ICP-OES data (±10 %), this method is less suitable for samples which have a lower MgO and Al_2O_3 concentration but this example perfectly illustrates that stilpnomelane may be present in all jasper samples even though they were not detected with XRD.

This has important implications for the interpretation of the Fe isotope effect of Fe silicate contributions, because their $\delta^{56}Fe$ values then do not strictly represent a detrital $\delta^{56}Fe$ signature but may also reflect fractionation processes during stilpnomelane (and minnesotaite) formation. For example, during burial diagenesis and metamorphism stilpnomelane could have grown from precursor clays (i.e. chlorite) and thereby preferentially incorporated ^{54}Fe in its crystal lattice. In the absence of detrital chlorite, stilpnomelane could alternatively originate from hydrogenous Fe silicate gels (Konhauser et al., 2002, 2007; Rasmussen et al., 2015); then its $\delta^{56}Fe$ might be inherently linked to the $\delta^{56}Fe$ of the water column. No data about the fractionation factors between aqueous Fe(II) and greenalite exist, which is the supposed primary precursor mineral to stilpnomelane, but in general silicates that contain Fe(II) are predicted to obtain light Fe in equilibrium as compared to Fe(III) fluids and minerals (Polyakov and Mineev 2000). Hence, regardless of whether MgO and Al_2O_3 impurities in the Hotazel hematite-chert samples represent a hydrogenous or detrital $\delta^{56}Fe$ signature, their presence indicates that they shifted the sample's overall $\delta^{56}Fe$ composition presumably towards lower values, and certainly not towards heavier ones.

Returning to the previously mentioned uncertainty about what happened during HCl dissolution - that is, did incomplete dissolution of the Fe oxide fraction and dissolution of Fe silicates in HCl (in contrast to what would be expected) cause the +0.3 ‰ difference between the bulk-rock and the HCl-fraction $\delta^{56}Fe$ value of samples HF6, 4 and 3? – the mechanism that was initially put forward (i.e. the Fe silicates have a much higher $\delta^{56}Fe$ composition than the Fe oxides) hence fails to explain this. As a consequence, the only other option that remains is that significant isotope fractionation occurred during incomplete dissolution of the hematite fraction, which obscured the samples natural $\delta^{56}Fe$ signal. Preferential dissolution of the heavy isotopes (^{56}Fe) with respect to the lighter isotopes (^{54}Fe) would accordingly have created a +0.3 ‰ heavier Fe isotopic composition of the HCl-fraction sample. This isotopic shift is not visible in sample HF7 (HCl), because the portion of oxide-bound Fe that was not dissolved in HCl (i.e. ca 3-5 wt %; see Table 17) is much lower than the total amount of Fe in the sample (i.e. ca 22 wt %; see Table 9); the relative amount of isotope fractionation during HCl-dissolution of HF7 would thus be much lower than for samples HF6, 4 and 3. Evidence for quantitative Fe isotope fractionation during HCl digestion has so far not been reported, but in a general sense, isotope fractionation is expected during equilibration between any two metal complexes with different bonding energetics, in which the heavy isotopes are preferentially incorporated in the stronger bonding environment (Bigeleisen and Mayer, 1947, Urey, 1947; Polyakov and Mineev, 2000). Anbar et al. (2000) demonstrated that Fe isotopes can be fractionated during column separation (between dissolved $FeCl_4^-$ and resin-bound $FeCl_4^-$), in which the heavy Fe isotopes preferentially partitioned into the dissolved phase. During HCl dissolution also $FeCl_4^-$ complexes are formed from solid $Fe(III)_2O_3$, but because this is crystalline material, isotope fractionation is not expected to happen: incongruent dissolution, i.e. dissolution of the surface layers of minerals will cause the release of the isotopes that were randomly incorporated in the mineral's crystal lattice. Yet if the hematite-chert samples lost all there crystallinity during to the powdering, fractionation may indeed have taken place. To conclude, it is not possible to predict here whether HCl digestion would have involved isotope fractionation or not. As a consequence, there are two contrasting theories that could explain the ±0.3 ‰ difference between bulk-rock samples HF6, 4 and 3 and their HCl-fraction equivalents. Because of the uncertainty about the processes that play a role in HCl digestion, it is not possible to confidently rule out one of the two, so I will discuss here the implications for both scenarios.

In the first scenario (*option 1*), I assume that the $\delta^{56}Fe$ values of the HCl-fraction samples represent that of the Fe oxide and carbonate fraction only (and consider the ICP-OES results of Table 17 to be not convincing); the +0.3 ‰ shift is related to the Fe silicates, which shifted the bulk-rock $\delta^{56}Fe$ towards more depleted values. Accordingly, the $\delta^{56}Fe$ values of samples HF 4 and 3 HCl (i.e. ca -0.2 and -0.1 ‰, respectively), and the carbonate-corrected $\delta^{56}Fe$ value of sample HF6 (i.e. between -0.6 and -0.4 ‰) should represent that of the sample's hematite fraction only. No HCl-fraction data exist of sample HF5, and so I cannot deduce any tightly constrained Fe isotope composition of the hematite fraction only; yet it would presumably be much higher (> +0.3 ‰) than its bulk-rock $\delta^{56}Fe$ value (ca -1.07 ‰). In the alternative scenario (*option 2*), the $\delta^{56}Fe$ value of the HCl-fraction samples does not represent that of the sample's pure Fe oxide and carbonate fraction, but instead reflects that of significant Fe isotope fractionation during partial dissolution of the Fe oxide fraction (in contrast to what is expected to happen). In this case, the sample's bulk-rock $\delta^{56}Fe$ value would be more suitable for tracing back the Fe isotopic signature of the (pure) hematite fraction and subsequently of the initial seawater Fe(II) source. As a result, the carbonate-corrected bulk-rock $\delta^{56}Fe$ value of sample HF6, i.e. between ca -0.9 and -0.8 ‰, would represent that of its hematite fraction, which is considerably lower than its value according to *option 1* (i.e. between -0.6 and -0.4 ‰) and that of HF7 (i.e. ca -0.5 ‰). Unfortunately, the lack of information about the precise Fe isotope characteristics and fractionation effects of the Fe silicates does not allow me here for deciphering the $\delta^{56}Fe$ composition of the hematite fraction of samples HF5, 4 and 3. They presumably shifted the sample's bulk-rock $\delta^{56}Fe$ values (i.e. -1.07 ‰, -0.49 ‰ and -0.38 ‰, respectively) towards lower values, but the extent to which this happened remains unclear.

Having elaborated on the different interpretations of the Fe isotope values of samples HF6-3, I will now move on to

the next sample of the Hotazel stratigraphy, i.e. HF2. The ca 0.4 wt % CaO in sample HF2 indicates the presence of some ankerite, but this is much lower than the 1.4 wt % CaO in HF6 and so its effect on the sample's $\delta^{56}Fe$ is of minor importance (see Table 9 and Figure 19). In addition, the Al_2O_3 content of HF2 is slightly elevated (ca 0.3 wt %) and thus proves that Fe silicates are present. No HCl-fraction $\delta^{56}Fe$ data exist for this sample, but compared to HF4, sample HF2 has a three times higher FeO- Al_2O_3 ratio and hence, following *option 1*, the relative effect of the Fe silicates on the sample's bulk-rock $\delta^{56}Fe$ composition must have been lower than for HF4 (that is, lower than a ±0.3 ‰ shift). This means that the silicate-corrected $\delta^{56}Fe$ value of sample HF2 (i.e. without the presence of Fe silicate impurities) would be higher than -0.31 ‰ (the sample's uncorrected $\delta^{56}Fe$ value) but lower than 0.0 ‰. Following *option 2*, this silicate-corrected value would presumably lie more towards the lighter end of this (-0.3 to 0.0 ‰) range.

Sample HF1 has a similar FeO concentration as HF2, but far lower Fe silicate and carbonate contributions (see Table 9 and Figure 19), which means that the bulk-rock $\delta^{56}Fe$ value of HF1 presumably closely represents that of the hematite only. Though, XRD data suggest that a portion of the Fe oxide fraction of HF1 (and of HF2) constitutes magnetite instead of hematite (see Table 8). Because magnetite is most likely a very late-stage mineral, the Fe incorporated in its crustal lattice could have had various mineral sources with a diversity of $\delta^{56}Fe$ compositions, so the $\delta^{56}Fe$ contribution of magnetite is rather uncertain. The only thing that is known is the approx. -1.3 ‰ cumulative fractionation effect between aqueous Fe(II) and magnetite (Johnson et al., 2005). Supposing that the Fe hosted in magnetite was provided by reductive dissolution of primary ferric oxyhydroxides (which produced Fe(II) with a 2-3 ‰ lighter $\delta^{56}Fe$ composition than the Fe(III) mineral source), the overall $\delta^{56}Fe$ of magnetite would be 0.7-1.7 ‰ lower than the original ferric oxyhydroxide minerals. If magnetite on the contrary formed directly from partial oxidation of aqueous Fe(II) in the water column, this would produce positive $\delta^{56}Fe$ values, such as also have been reported in the Kuruman and Griquatown BIFs (Johnson et al., 2003). However, regarding the fact that the majority of the samples contain hematite, I prefer a more late-stage interpretation of magnetite. As a consequence this must have shifted the bulk-rock $\delta^{56}Fe$ of sample HF1 (ca -0.26 ‰). But regarding the very faint magnetite peak in the XRD spectrum plot of sample HF1 (see Appendix 5), I consider the contribution of magnetite to the $\delta^{56}Fe$ of HF1 to be irrelevant, certainly regarding the $\delta^{56}Fe$ external uncertainty limits of ±0.11 ‰. Therefore I conclude that the bulk-rock $\delta^{56}Fe$ of -0.26 ‰ directly reflects oxidation of Fe(II) in the water column and thus presumably corresponds to a seawater $\delta^{56}Fe$ down to circa -1.3 ‰. In contrast to HF1, the magnetite contribution in sample HF2 is potentially more important (see Table 8). This implies that, similarly as for the Fe silicate impurities, the sample's bulk-rock $\delta^{56}Fe$ value (ca -0.31 ‰) should be corrected (with a positive $\delta^{56}Fe$ correction factor) in order to obtain the $\delta^{56}Fe$ signature of the original ferric oxyhydroxide precipitates. Unfortunately, the exact magnitude of this + $\delta^{56}Fe$ correction factor is unknown, but I estimate that the final silicate- and magnetite-corrected $\delta^{56}Fe$ value would stay within the previously proposed range of -0.3 to 0.0 ‰, which would consequently still correspond to a depleted seawater $\delta^{56}Fe$ signal.

5.5.2 Oxygenation of the entire Transvaal basin?

The negative $\delta^{56}Fe$ composition of all hematite samples in the Hotazel unambiguously signifies (despite the large uncertainties in that I encountered in the previous section) that at the time of ferric oxyhydroxide deposition the dissolved Fe(II) pool was isotopically depleted, since partial oxidation of Fe(II) from a normal reservoir ($\delta^{56}Fe$ = 0 ‰) would ultimately produce positive $\delta^{56}Fe$ values for hematite (i.e. ca +1.0 ‰). In view of the fact that the lowest $\delta^{56}Fe$ found in sample HF7 (i.e. ca -0.5 ‰) is depleted, yet to a much lower degree than in the hematite- and Mn-rich layers higher up in the Hotazel stratigraphy (down to -3.5 ‰), this might imply that the Fe isotopes presented here report the first stratigraphic point where the isotopic signature of the Transvaal basin starts to become depleted, in agreement with the proposed Rayleigh distillation effect (Tsikos et al., 2010). However, the REE + Y distribution patterns of hematite-chert as outlined earlier in the *Discussion* (in sections 5.4.2 and 5.4.3) suggest that the hematite in the lower lutite part of the Hotazel originates directly from exhalations of hydrothermal fluids released in a shallow marine, oxygenated environment. Accordingly, the $\delta^{56}Fe$ value of sample HF7 (and those of HF2-6) should at least partly report the $\delta^{56}Fe$ signature of these hydrothermal fluids instead that of the bulk seawater signal only. This seems to be supported by the stratigraphic trend the $\delta^{56}Fe$ of the Fe isotope samples of the Hotazel Fm. show:

The lowermost sample from the Hotazel lutite part, sample HF7, has an approx. 0.24 ‰ *lower* $\delta^{56}Fe$ value than sample HF1 from the upper BIF part of the Hotazel. Although this 0.24 ‰ difference is not very large, it certainly reaches beyond the sample's $\delta^{56}Fe$ external uncertainty limits (±0.11 ‰) and therefore depicts a detectable change. Assuming that a similar Fe isotope fractionation mechanism was responsible for the formation of hematite in samples HF1 and 7, this stratigraphic difference in $\delta^{56}Fe$ may directly reflect a difference in the source fluid $\delta^{56}Fe$ composition. The *increase* in hematite $\delta^{56}Fe$ with *increasing* height in the stratigraphy and hence with time demonstrates the opposite of what would be expected for a Rayleigh fractionation effect induced by progressive oxidation and removal of heavy Fe from the dissolved Fe(II) pool. Therefore, the change in $\delta^{56}Fe$ from HF7 to HF1 can only be explained by an additional influx of isotopically more enriched Fe towards the top, or vice versa, a decrease in the input of an isotopically more depleted Fe(II) source.

Given that the lutite part of the Hotazel is interpreted to represent more a shallow-marine paleoenvironment compared to the BIF part, the shift towards slightly higher δ^{56}Fe values from HF7 to HF1 may be attributed a change towards a deeper-marine Fe(II) source with a different, slightly higher δ^{56}Fe. This interpretation requires that the ocean was stratified with respect to δ^{56}Fe, but concerning the emerging evidence for redox stratification of the ancient oceans this was probably the case (Kasting, 1992; Olsen et al., 2013; Planavsky et al., 2014; Riding et al., 2014; Satkoski et al., 2015). Most of the O_2 was produced in the photic zone through high biological primary productivity and so oxidation rates of Fe(II) in the shallowest part of the ocean were highest; further down in the water column sunlight penetration decreased and consequently photosynthetically-produced O_2 levels became lower. By analogy, Satkoski et al. (2015) argued for Fe isotope evidence of a redox-stratified ocean based on much older (ca 3.2 Ga) sediments. They reported an average δ^{56}Fe value of +0.55 ‰ for fine-grained chert samples (i.e. deeper marine) and an average of +0.18 ‰ for granular samples (i.e. shallow-marine), arguing (by modelling) that these reflected a maximum O_2 content of 0.4 µM and ca 10 µM, respectively.

However, the very low Fe isotopic signature of the Ongeluk lava alteration products, that is having an average δ^{56}Fe value of -0.7 ‰, indicates that the associated hydrothermal fluids yielded δ^{56}Fe values even lower than -0.7 ‰. When these fluids subsequently entered the ocean, oxidation of their dissolved Fe(II) load must have similarly resulted in low δ^{56}Fe values of the ferric oxyhydroxide products. The fact that hematite Fe isotope composition sample HF7, which was derived from a stratigraphically close position to the Ongeluk lava is similarly low (ca -0.5 ‰) and moreover, since it is more depleted than in the upper BIF part (i.e. HF1 has a δ^{56}Fe of ca -0.26 ‰) hints at a substantial contribution of isotopically depleted hydrothermal fluids to the lower part of the Hotazel hematite deposits. The mixture between the hydrothermally-derived δ^{56}Fe (< -0.7 ‰) and the ambient seawater-derived δ^{56}Fe (< -0.26 ‰) contribution must have ultimately produced the ca -0.5 ‰ composition of HF7.

The Fe isotopic difference between HF7 and HF1 thus suggests that it reports the decrease in contribution of Fe from these isotopically depleted Ongeluk-derived hydrothermal fluids through time, accompanied by a transition towards a more open marine setting with a slightly heavier δ^{56}Fe signature. However, the δ^{56}Fe values of the interstitial Fe isotope samples (HF6-2) only partly support this. According to *option 1* (as defined in section 5.1.1), the hematite in sample HF6 has a rather similar δ^{56}Fe value (corrected for Fe silicate and carbonate impurities) to that of HF7 and thus indeed points to an additional hydrothermal fluid source, analogous to HF7. The even more depleted δ^{56}Fe value of the hematite in sample HF6 as suggested by *option 2* (i.e. ca -0.8 or -0.9 ‰) also confirms this; the decrease in the seawater δ^{56}Fe from HF7 to HF6 could in fact indicate an enhanced hydrothermal influx (which temporarily increased the hydrothermal fluid-seawater ratio), or perhaps the influx of an even further depleted hydrothermal source, isotopically evolved via Rayleigh fractionation. The uncertainty about the original δ^{56}Fe signal of the hematite fraction in sample HF5 is too high to draw direct conclusions from, but it presumably also indicates a relatively low seawater δ^{56}Fe composition (that is, ≤ -0.5 ‰). In contrast to the three lowermost Hotazel Fe isotope samples, however, the δ^{56}Fe compositions of the next samples in the stratigraphy, i.e. HF4, 3 and 2 (corrected for Fe silicate and carbonate impurities) are considerably higher, i.e. > -0.4 ‰ according to *option 2* and ≥ -0.2 ‰ according to *option 1*, which means that they may even exceed the proposed δ^{56}Fe value for sample HF1 (ca -0.26‰), which lies stratigraphically above them. Regardless of their exact values, samples HF4, 3 and 2 show a stratigraphic trend of increasing δ^{56}Fe with increasing height through the stratigraphy (see Figure 19). Possibly this may signify the dilution of the hydrothermal δ^{56}Fe signal by enhanced input from an isotopically heavier water body, upwelling from the deeper parts of the ocean. However, this is in conflict with the REE + Y distribution pattern of thin-section 6, which corresponds to the same jasper layer as Fe isotope sample HF4 (and close to sample HF3), but which still exhibits a LREE depletion trend that is similar to the other lutite hematite samples from lower down in the sequence and different to the steeper profile of the BIF hematite (from which laser ablation sample 2 and Fe isotope sample HF1 were derived). The influx of Fe and REE + Y from a more open marine water body would evidently result in a steeper REE + Y profile analogous to the BIF sample. This suggests that either of the two explanations is incorrect. In the first place, there may be an alternative explanation for the REE + Y results. The relatively high $(Pr/Yb)_{SN}$ value for the REE + Y pattern in sample 6, and in general for that of all lutite jasper samples compared to that of the BIF sample may not necessarily track an increased hydrothermal REE + Y source, but could also predominantly reflect (for unknown reasons) a difference in REE + Y scavenging behaviour. Potentially the LREE are more easily adsorbing onto Fe(III) oxyhydroxide particles in more oxygenated settings, but to date evidence for this is lacking. And even if this were the case, it fails to explain the heavier δ^{56}Fe value for HF4 (and HF3). So I conclude that the Fe isotopic compositions of samples HF4 and 3 instead do reflect (rapid oxidation of) a hydrothermal Fe(II) source (mixed with ambient seawater). A second explanation might be that the δ^{56}Fe of these hydrothermal fluids changed composition. However, this is rather unlikely considering the fact that the δ^{56}Fe of hydrothermal fluids decreases with time and distance from the hydrothermal centre (Sharma et al., 2001; Beard et al., 2003; Severmann et al., 2004, 2008; Rouxel., 2008). An alternative scenario explaining the heavier δ^{56}Fe values in HF4-2 compared to HF7-5 may lie in the Fe isotope fractionation process itself rather than in differences in the δ^{56}Fe of the source

water. Very rapid oxidation of Fe(II) followed by ferric oxyhydroxide precipitation produces smaller Fe isotope fractionation because isotopic equilibrium is not reached (Johnson et al., 2002). Accordingly, this might suggest that the lower part of the hematite samples reflects faster precipitation than higher up. Unfortunately it is not possible to prove or disprove this theory; the same applies to the potential role of microbial reduction processes in the sediment, which cause the release of isotopically enriched fluids (Johnson et al., 2008a; b). From these fluids subsequent oxidation could once again form new ferric oxyhydroxide minerals with a heavier δ^{56}Fe signature. Nevertheless, the uncertainty about the origin of the δ^{56}Fe composition of samples HF4-2 does not affect my statement regarding the contrasting origin and significance of the δ^{56}Fe signature of samples HF7 and HF1; that is the ca -0.50 ‰ value of HF7 is derived from seawater mixed with a hydrothermal Fe contribution (δ^{56}Fe < -0.7 ‰) which can be directly linked to the high-T fluid-rock interactions in the Ongeluk lava, whereas the ca -0.26 ‰ value of HF1 represents a rather "clean" seawater signal.

The depleted Fe isotopic composition of the Ongeluk hydrothermal fluids, i.e. lower than -0.7 ‰, provides strong evidence for the presence of considerable volumes of O_2, which overwhelmed the hydrothermal supply of reductants. Under the suboxic conditions of modern MOR-type hydrothermal alteration fluids have negative δ^{56}Fe values ranging from −0.69‰ to −0.12‰, largely due to the formation of secondary, isotopically heavier (ferric) minerals (Sharma et al., 2001; Beard et al., 2003; Severmann et al., 2004, 2008; Rouxel, 2008). However, the higher heat flow in Archean probably produced MOR hydrothermal fluxes with near-zero δ^{56}Fe (Yamaguchi et al., 2005; Johnson et al., 2008a). Because precipitation of hematite from these fluids (at equilibrium) is predicted to contain Fe with a δ^{56}Fe of around +0.5 to +1.0 ‰, the -0.50 ‰ value of HF7 indicates that the hydrothermal fluids may have had extremely low δ^{56}Fe values of down to -1.5 ‰ (given that the fraction of Fe(II) that was oxidised and precipitated was relatively small). Their actual value was presumably far lower than -1.5 ‰, considering the fact that the δ^{56}Fe of HF5 represents a mixture with less isotopically depleted seawater. Consequently, the dissolved Fe(II) load in the Ongeluk hydrothermal fluids released into the ocean must have experienced extensive oxidation and continuous removal of the isotopically heavier Fe further down along the seawater-Ongeluk lava reaction pathway. As the rising hydrothermal fluids progressively mixed with downward circulating (oxidising) seawater from above, they began to precipitate out secondary minerals such as Fe(III) oxyhydroxides and Fe(III)-rich secondary clays such as caledonite (Polyakov and Mineev, 2000). According to the Rayleigh fractionation model of Rouxel et al. (2003), the first ferric precipitates would have positive δ^{56}Fe values at the start of the precipitation but with the ongoing alteration would become gradually more negative and could eventually produce δ^{56}Fe values down to -3.0 ‰ when only 10 % of the dissolved Fe(II) pool remained. Similarly low δ^{56}Fe values were achieved in low-T (< 50 ^{o}C) spring fluids that were oxidised upon contact with the atmosphere (Bullen et al., 2001). The δ^{56}Fe values in the uppermost part of the Ongeluk lava (ca -0.7 ‰) thus reflect an intermediate stage in the Rayleigh evolution of the hydrothermal fluids.

The Rayleigh-evolved Fe isotopic signature of the lutite part of the Hotazel is in close agreement with the previously discussed textural and mineralogical clues about the existence of free dissolved O_2 produced by oxygenic photosynthesis, which are: *i)* the secondary hematite in the inferred seawater interaction pathways through the upper part of the Ongeluk lava, *ii)* the hydrothermally-sourced barite close to the Ongeluk-Hotazel Fm. contact and *iii)* the primary hematite found in the microbial mat structures. These features seem not diagnostic for the rest of the Transvaal basin: the transition from hematite lutite cycle I towards the (hematite-rich) BIF part of the Hotazel ultimately depicts a change from rather isolated towards more open-marine, deeper water conditions. However, considering the similarly evolved Fe isotopic signature of these more ambient seawaters (i.e. a seawater δ^{56}Fe down to -1.3 ‰), the amount of O_2 that was initially produced in these restricted O_2 oases in uppermost surface zones must eventually have outpaced the locally available Fe(II) and started to oxidise larger volumes of the dissolved Fe(II) reservoir.

The few Fe isotope results reported in this study would in themselves have a limited scientific meaning with regard to the genetic link of the Hotazel sediments with the rise of atmospheric O_2 levels around the GOE, except that they perfectly fit in with the previously outlined Rayleigh fractionation scenario: large-scale BIF deposits of the Kuruman and Griquatown Fm., comprising near-zero to positive δ^{56}Fe values for the primary hematite fractions at the bottom (Johnson et al., 2003), and the profoundly depleted hematite- and Mn-rich layers of the Hotazel higher up in the stratigraphy of the Transvaal basin (Tsikos et al., 2010). The Fe isotope data presented in this study, specifically that of sample HF1, may thus mark the first (identified) position in space and time where the Fe isotopic signature in the sediment is depleted and remains depleted throughout the entire following ca 100 metres of stratigraphy. The (previously mentioned) high level of LREE depletion measured in hematite from the BIF part ($(Pr/Yb)_{SN}$ = 0.03) compared to that of average modern ocean water ($(Pr/Yb)_{SN}$ = 0.13) may add to the interpretation of an Fe isotopically and geochemically evolved Transvaal seawater composition due to a long-term oxidation of the aqueous Fe(II) reservoir. In addition, the fact that Mn is virtually absent in the Kuruman and Griquatown BIFs but starts to appear in the primary carbonate phases of the lower Hotazel (i.e. Mn-calcite and ankerite) is perfectly in line with the protracted removal of Fe(II) as O_2 levels started to accumulate. Yet the bulk-rock Mn concentrations (XRF data indicate < 2

wt%) are lower than reported in the hematite lutite layers higher up in the Hotazel (2.05-25.77 wt % Mn) from Tsikos et al. (2010), and Mn occurs in its reduced (Mn(II)) rather than oxidised (Mn(III) and Mn(IV)) state. Initially this may indicate that seawater O_2 concentrations were still fairly low at the base of the Hotazel compared to higher up in the stratigraphy, because oxidation rates of Fe(II) are faster than those of Mn(II). This is similarly supported by the absence of true negative Ce anomalies in the hematite REE + Y distribution patterns. Alternatively, the rather low Mn concentration at the lowermost three metres of the Hotazel Fm. may not necessarily indicate lower O_2 concentrations compared to higher up the sequence but reflect a difference in the *maturity* of the aerobic seawater conditions instead. In other words, the contribution of hydrothermal fluids from the Ongeluk system most likely shifted the water column's Fe/Mn content temporarily towards a higher, near-crustal composition (i.e. 50/1; Qin and Humayun, 2008). At this point, the presence of free dissolved O_2 would involve preferential oxidation of Fe(II) above Mn(II), and moreover, cause Mn(III) to be recycled back into the water column (Tsikos et al., 2010): Mn(III) is a thermodynamically favourable electron acceptor upon oxidation of Fe(II) (Canfield et al., 2005). Proceeding aerobic conditions and hence removal of dissolved Fe(II) would dramatically enrich the seawater's Mn(II) content and eventually give rise to precipitation of Mn-rich deposits.

Conclusion

The roughly three metres of drill-core stratigraphy that formed the subject of this study encompass a wealth of textural, mineralogical and geochemical information that enabled me to draw the following conclusions:

The Ongeluk lava underwent major hydrothermal alteration upon extrusion into the shallow parts of the Transvaal basin, a finding which supports previous work (Schütte, 1992; Cornell and Schütte, 1995; Cornell et al., 1996). The peculiar Fe isotopic depletion of the rock's alteration minerals, i.e. with a mean δ^{56}Fe value of -0.7 ‰, uniquely depicts the effect of progressive fluid-rock interactions with relatively O_2-rich seawater, entailing a Rayleigh fractionation process such as the process that is observed in modern mid-ocean ridges (e.g. Sharma et al., 2001; Rouxel et al., 2003). The thick rim of secondary hematite that fences the cracks through which seawater percolated the upper part of the Ongeluk lava, along with the occurrence of hydrothermally-derived barite directly above the contact with the Hotazel Fm. similarly hint at the presence of free dissolved O_2.

The upper part of the Ongeluk lava exhibits a strong genetic link with the directly overlying sediments from the Hotazel Fm. The cyclic occurrence of (three) mudstone intervals, and specifically, the abundance of Al-rich secondary chlorite in these intervals, reflects episodes of enhanced detrital input from already highly altered Ongeluk lava. Hydrothermal exhalations also constitute a major portion of the hydrogenous sediments of the lower (lutite) part of the Hotazel Fm., as suggested by the increased carbonate and pyrite content of hematite lutite cycle I, the elevated $(Pr/Yb)_{SN}$ composition of jasper samples and the peculiar *decrease* in the δ^{56}Fe of hematite with *increasing* proximity to the Ongeluk lava: the more depleted Fe isotopic composition of hematite at ca 0.37 m distance from the contact (sample HF7 has a δ^{56}Fe of ca -0.50 ‰) relative to the Fe isotopic composition at ca 2.53 m distance (sample HF1 has a δ^{56}Fe of -0.26 ‰) involves the contribution of strongly depleted hydrothermal fluids to a slightly heavier ambient seawater δ^{56}Fe composition. In view of the convincing textural evidence for a primary origin of the hematite-chert sections in the Hotazel, the REE + Y and Fe isotope characteristics acquired from this hematite unequivocally represent a primary signal, relating to the initial process of ferric oxyhydroxide formation from oxidation of dissolved Fe(II) in the water column rather than post-depositional alteration features.

Inasmuch as the sedimentary textures, e.g. the lenticular bedding and crinkly lamination, signify that the lower lutite part of the Hotazel was deposited in a shallow-marine setting, and thus the redox conditions deduced from these sediments are presumably more representative of a restricted part of the Transvaal basin instead of open-marine seawater, I propose that the highly oxidising conditions in this shallow part of the ocean must have played an important role in oxygenation of the entire Transvaal basin. The δ^{56}Fe value of the Fe isotope sample from the top BIF part of the drill-core (i.e. -0.26‰) certainly reflects precipitation from deeper, more ambient seawater conditions with a corresponding δ^{56}Fe composition down to approx. -1.3 ‰. Without any doubt, this value embodies the incipient isotopic evolution of the Transvaal basin in the run-up to the end-member geochemical and isotopic characteristics of the basin as expressed in the very depleted δ^{56}Fe values (down to -2.4 ‰) and the vast accumulation of Mn higher up in the Hotazel Fm. (Tsikos et al., 2010). The placement of the Hotazel depositional event at ca 2.4 Ga indicates its direct significance for the global oxygenation of the atmosphere, i.e. the GOE: it may have recorded the progressive rise of dissolved O_2 produced by photosynthesis, which initially was consumed by the large volume of dissolved Fe(II) in the Transvaal seawater, but which ultimately overwhelmed this reducing power, giving rise to large-scale accumulation of free O_2. The miniature paleoenvironmental reconstruction that I presented in this study may therefore have not only provided important insights in the redox conditions of the Transvaal basin, but also in the still poorly constrained evolution of global oceanic O_2 levels and their relation to the GOE.

Acknowledgements

I would like to thank the following people and institutions for their assistance in the undertaking of this thesis:

My first supervisor Dr Paul Mason from Universiteit Utrecht and my second supervisor dr Harilaos Tsikos from Rhodes University for their guidance and scientific contribution throughout the entire project;

Paul Oonk for his skills and assistance with all the Fe isotope laboratory work, as well as his feedback on my thesis;

Dr Geerke Floor for her intensive technical guidance during the Fe isotope measurements at the German Research Centre for Geosciences GFZ and with the data analysis afterwards;

All people from the technical staff of the Earth Sciences Department, Universiteit Utrecht: Helen de Waard, Ton Zalm, Tilly Bouten, Otto Stiekema, Leonard Bik, Peter van Krieken en Anita van Leeuwen-Tolboom;

And finally I am thankful to Guus Lantink for his feedback on my English writing.

References:

Ahn, J. H., & Buseck, P. R. (1990). Hematite nanospheres of possible colloidal origin from a Precambrian banded iron formation. *Science*, *250*(4977), 111-113.

Anbar, A. D., Roe, J. E., Barling, J., & Nealson, K. H. (2000). Nonbiological fractionation of iron isotopes. *Science*, *288*(5463), 126-128.

Anbar, A. D., & Knoll, A. H. (2002). Proterozoic ocean chemistry and evolution: a bioinorganic bridge? *Science*, *297*(5584), 1137-1142.

Anbar, A. D., Jarzecki, A. A., & Spiro, T. G. (2005). Theoretical investigation of iron isotope fractionation between Fe $(H_2O)_6^{3+}$ and Fe $(H_2O)_6^{2+}$: implications for iron stable isotope geochemistry. *Geochimica et Cosmochimica Acta*, *69*(4), 825-837.

Anbar, A. D., & Rouxel, O. (2007). Metal stable isotopes in paleoceanography.*Annu. Rev. Earth Planet. Sci.*, *35*, 717-746.

Anbar, A. D., Duan, Y., Lyons, T. W., Arnold, G. L., Kendall, B., Creaser, R. A., ... & Buick, R. (2007). A whiff of oxygen before the great oxidation event?.*Science*, *317*(5846), 1903-1906.

Arnold, G. L., Anbar, A. D., Barling, J., & Lyons, T. W. (2004). Molybdenum isotope evidence for widespread anoxia in mid-Proterozoic oceans. *Science*, *304*(5667), 87-90.

Ayres, D. E. (1972). Genesis of iron-bearing minerals in banded iron formation mesobands in the Dales Gorge Member, Hamersley Group, Western Australia.*Economic Geology*, *67*(8), 1214-1233.

Balci, N., Bullen, T. D., Witte-Lien, K., Shanks, W. C., Motelica, M., & Mandernack, K. W. (2006). Iron isotope fractionation during microbially stimulated Fe (II) oxidation and Fe (III) precipitation. *Geochimica et Cosmochimica Acta*, *70*(3), 622-639.

Bao, S. X., Zhou, H. Y., Peng, X. T., Ji, F. W., & Yao, H. Q. (2008). Geochemistry of REE and yttrium in hydrothermal fluids from the Endeavour segment, Juan de Fuca Ridge. *Geochemical Journal*, *42*(4), 359-370.

Bau, M., Dulski, P., & Moller, P. (1995). Yttrium and holmium in South Pacific seawater: vertical distribution and possible fractionation mechanisms. *Oceanographic Literature Review*, *11*(42), 955.

Bau, M., & Dulski, P. (1996). Distribution of yttrium and rare-earth elements in the Penge and Kuruman iron-formations, Transvaal Supergroup, South Africa. *Precambrian Research*, *79*(1), 37-55.

Bau, M., Koschinsky, A., Dulski, P., & Hein, J. R. (1996). Comparison of the partitioning behaviours of yttrium, rare earth elements, and titanium between hydrogenetic marine ferromanganese crusts and seawater. *Geochimica et Cosmochimica Acta*, *60*(10), 1709-1725.

Bau, M., Höhndorf, A., Dulski, P., & Beukes, N. J. (1997). Sources of rare-earth elements and iron in Paleoproterozoic iron-formations from the Transvaal Supergroup, South Africa: evidence from neodymium isotopes.*The Journal of Geology*, 121-129.

Bau, M. (1999). Scavenging of dissolved yttrium and rare earths by precipitating iron oxyhydroxide: experimental evidence for Ce oxidation, Y-Ho fractionation, and lanthanide tetrad effect. *Geochimica et Cosmochimica Acta*, *63*(1), 67-77.

Bau, M., & Dulski, P. (1999). Comparing yttrium and rare earths in hydrothermal fluids from the Mid-Atlantic Ridge: implications for Y and REE behaviour during near-vent mixing and for the Y/Ho ratio of Proterozoic seawater. *Chemical Geology*, *155*(1), 77-90.

Bau, M., Romer, R. L., Lüders, V., & Beukes, N. J. (1999). Pb, O, and C isotopes in silicified Mooidraai dolomite (Transvaal Supergroup, South Africa): implications for the composition of Paleoproterozoic seawater and 'dating'the increase of oxygen in the Precambrian atmosphere. *Earth and Planetary Science Letters*, *174*(1), 43-57.

Bau, M., Schmidt, K., Koschinsky, A., Hein, J., Kuhn, T., & Usui, A. (2014). Discriminating between different genetic types of marine ferro-manganese crusts and nodules based on rare earth elements and yttrium. *Chemical Geology*, *381*, 1-9.

Beard, B. L., Johnson, C. M., Cox, L., Sun, H., Nealson, K. H., & Aguilar, C. (1999). Iron isotope biosignatures. *Science*, *285*(5435), 1889-1892.

Beard, B. L., Johnson, C. M., Skulan, J. L., Nealson, K. H., Cox, L., & Sun, H. (2003). Application of Fe isotopes to tracing the geochemical and biological cycling of Fe. *Chemical Geology*, *195*(1), 87-117.

Beard, B. L., & Johnson, C. M. (2004). Fe isotope variations in the modern and ancient earth and other planetary bodies. *Reviews in Mineralogy and Geochemistry*, *55*(1), 319-357.

Beard, B. L., Handler, R. M., Scherer, M. M., Wu, L., Czaja, A. D., Heimann, A., & Johnson, C. M. (2010). Iron isotope fractionation between aqueous ferrous iron and goethite. *Earth and Planetary Science Letters*, *295*(1), 241-250.

Bekker, A., Holland, H. D., Wang, P. L., Rumble, D. I. I. I., Stein, H. J., Hannah, J. L., ... & Beukes, N. J. (2004). Dating the rise of atmospheric oxygen. *Nature*, *427*(6970), 117-120.

Berner, R. A. (1970). Sedimentary pyrite formation. *American journal of science*, *268*(1), 1-23.

Beukes, N. J. (1980). Suggestions towards a classification of and nomenclature for iron-formation. *Trans. Geol. Soc. S. Afr*, *83*, 285-290.

Beukes, N. J. (1983). Palaeoenvironmental setting of iron-formations in the depositional basin of the Transvaal Supergroup, South Africa. *Developments in Precambrian Geology*, *6*, 131-198.

Beukes, N. J., & Klein, C. (1990). Geochemistry and sedimentology of a facies transition—from microbanded to granular iron-formation—in the early Proterozoic Transvaal Supergroup, South Africa. *Precambrian Research*, *47*(1-2), 99-139.

Beukes, N. J., & Gutzmer, J. (1996). A volcanic-exhalative origin for the world's largest (Kalahari) manganese field. *Mineralium Deposita*, *31*(3), 242-245.

Beukes, N. J., & Gutzmer, J. E. N. S. (2008). Origin and paleoenvironmental significance of major iron formations at the Archean-Paleoproterozoic boundary. *Reviews in Economic Geology*, *15*, 5-47.

Bigeleisen, J., & Mayer, M. G. (1947). Calculation of equilibrium constants for isotopic exchange reactions. *The Journal of Chemical Physics*, *15*(5), 261-267.

Bolhar, R., Kamber, B. S., Moorbath, S., Fedo, C. M., & Whitehouse, M. J. (2004). Characterisation of early Archaean chemical sediments by trace element signatures. *Earth and Planetary Science Letters*, *222*(1), 43-60.

Brasier, M., McLoughlin, N., Green, O., & Wacey, D. (2006). A fresh look at the fossil evidence for early Archaean cellular life. *Philosophical*

Transactions of the Royal Society of London B: Biological Sciences, *361*(1470), 887-902.

Brocks, J. J., Logan, G. A., Buick, R., & Summons, R. E. (1999). Archean molecular fossils and the early rise of eukaryotes. *Science*, *285*(5430), 1033-1036.

Brocks, J. J., Buick, R., Summons, R. E., & Logan, G. A. (2003). A reconstruction of Archean biological diversity based on molecular fossils from the 2.78 to 2.45 billion-year-old Mount Bruce Supergroup, Hamersley Basin, Western Australia. *Geochimica et Cosmochimica Acta*, *67*(22), 4321-4335.

Brocks, J. J. (2011). Millimeter-scale concentration gradients of hydrocarbons in Archean shales: Live-oil escape or fingerprint of contamination? *Geochimica et Cosmochimica Acta*, *75*(11), 3196-3213.

Buick, R. (2008). When did oxygenic photosynthesis evolve? *Philosophical Transactions of the Royal Society of London B: Biological Sciences*, *363*(1504), 2731-2743.

Bullen, T. D., White, A. F., Childs, C. W., Vivit, D. V., & Schulz, M. S. (2001). Demonstration of significant abiotic iron isotope fractionation in nature.*Geology*, *29*(8), 699-702.

Button, A. (1976). *Transvaal and Hamersley Basins: Review of basin development and mineral deposits* (No. 107). University of the Witwatersrand, Economic Geology Research Unit.

Byrne, R. H., & Kim, K. H. (1990). Rare earth element scavenging in seawater.*Geochimica et Cosmochimica Acta*, *54*(10), 2645-2656.

Byrne, R. H., & Sholkovitz, E. R. (1996). Marine chemistry and geochemistry of the lanthanides. *Handbook on the physics and chemistry of rare earths*, *23*, 497-593.

Canfield, D. E., Raiswell, R., & Bottrell, S. H. (1992). The reactivity of sedimentary iron minerals toward sulfide. *American Journal of Science*,*292*(9), 659-683.

Canfield, D. E. (1998). A new model for Proterozoic ocean chemistry. *Nature*, *396*(6710), 450-453.

Canfield, D. E., Kristensen, E., & Thamdrup, B. (2005). *Aquatic geomicrobiology*. Gulf Professional Publishing.

Cheney, E. S. (1996). Sequence stratigraphy and plate tectonic significance of the Transvaal succession of southern Africa and its equivalent in Western Australia. *Precambrian Research*, *79*(1), 3-24.

Claire, M. W., Catling, D. C., & Zahnle, K. J. (2006). Biogeochemical modelling of the rise in atmospheric oxygen. *Geobiology*, *4*(4), 239-269.

Cloud, P. (1973). Paleoecological significance of the banded iron-formation.*Economic Geology*, *68*(7), 1135-1143.

Cornell, D. H., & Schütte, S. S. (1995). A volcanic-exhalative origin for the world's largest (Kalahari) manganese field. *Mineralium Deposita*, *30*(2), 146-151.

Cornell, D. H., Schütte, S. S., & Eglington, B. L. (1996). The Ongeluk basaltic andesite formation in Griqualand West, South Africa: submarine alteration in a 2222 Ma Proterozoic sea. *Precambrian Research*, *79*(1), 101-123.

Craddock, P. R., Warren, J. M., & Dauphas, N. (2013). Abyssal peridotites reveal the near-chondritic Fe isotopic composition of the Earth. *Earth and Planetary Science Letters*, *365*, 63-76.

Croal, L. R., Johnson, C. M., Beard, B. L., & Newman, D. K. (2004). Iron isotope fractionation by Fe (II)-oxidizing photoautotrophic bacteria. *Geochimica et cosmochimica acta*, *68*(6), 1227-1242.

Crowe, S. A., Døssing, L. N., Beukes, N. J., Bau, M., Kruger, S. J., Frei, R., & Canfield, D. E. (2013). Atmospheric oxygenation three billion years ago. *Nature*, *501*(7468), 535-538.

Czaja, A. D., Johnson, C. M., Beard, B. L., Roden, E. E., Li, W., & Moorbath, S. (2013). Biological Fe oxidation controlled deposition of banded iron formation in the ca. 3770Ma Isua Supracrustal Belt (West Greenland). *Earth and Planetary Science Letters*, *363*, 192-203.

Dauphas, N., van Zuilen, M., Wadhwa, M., Davis, A. M., Marty, B., & Janney, P. E. (2004). Clues from Fe isotope variations on the origin of early Archean BIFs from Greenland. *Science*, *306*(5704), 2077-2080.

De Baar, H. J. W., Schijf, J., & Byrne, R. H. (1991). Solution chemistry of the rare earth elements in seawater. *Eur J Solid State Inorg Chem*, *28* (Suppl S), 357-373.

de Kock, M. O., Evans, D. A., & Beukes, N. J. (2009). Validating the existence of Vaalbara in the Neoarchean. *Precambrian Research*, *174*(1), 145-154.

Derry, L. A., & Jacobsen, S. B. (1990). The chemical evolution of Precambrian seawater: evidence from REEs in banded iron formations. *Geochimica et Cosmochimica Acta*, *54*(11), 2965-2977.

Edmonds, H. N., & German, C. R. (2004). Particle geochemistry in the Rainbow hydrothermal plume, Mid-Atlantic Ridge. *Geochimica et Cosmochimica Acta*, *68*(4), 759-772.

Eigenbrode, J. L., & Freeman, K. H. (2006). Late Archean rise of aerobic microbial ecosystems. *Proceedings of the National Academy of Sciences*, *103*(43), 15759-15764.

Eigenbrode, J. L., Freeman, K. H., & Summons, R. E. (2008). Methylhopane biomarker hydrocarbons in Hamersley Province sediments provide evidence for Neoarchean aerobiosis. *Earth and Planetary Science Letters*, *273*(3), 323-331

Elderfield, H., Upstill-Goddard, R., & Sholkovitz, E. R. (1990). The rare earth elements in rivers, estuaries, and coastal seas and their significance to the composition of ocean waters. *Geochimica et Cosmochimica Acta*, *54*(4), 971-991.

Elderfield, H., Holland, H. D., & Turekian, K. K. (Eds.). (2006). *The oceans and marine geochemistry* (Vol. 6). Elsevier.

Ellis, A. J., & Giggenbach, W. (1971). Hydrogen sulphide ionization and sulphur hydrolysis in high temperature solution. *Geochimica et Cosmochimica Acta*, *35*(3), 247-260.

Eriksson, P. G., Hattingh, P. J., & Altermann, W. (1995). An overview of the geology of the Transvaal Sequence and Bushveld Complex, South Africa. *Mineralium Deposita*, *30*(2), 98-111.

Eugster, H. P., & Chou, I. M. (1973). The depositional environments of Precambrian banded iron-formations. *Economic Geology*, *68*(7), 1144-1168.

Farquhar, J., Bao, H., & Thiemens, M. (2000). Atmospheric influence of Earth's earliest sulfur cycle. *Science*, *289*(5480), 756-758.

French, B. M. (1973). Mineral assemblages in diagenetic and low-grade metamorphic iron-formation. *Economic Geology*, *68*(7), 1063-1074.

Frost, C. D., Von Blanckenburg, F., Schoenberg, R., Frost, B. R., & Swapp, S. M. (2007). Preservation of Fe isotope heterogeneities during diagenesis and metamorphism of banded iron formation. *Contributions to Mineralogy and Petrology*, *153*(2), 211-235.

Gaillard, F., Scaillet, B., & Arndt, N. T. (2011). Atmospheric oxygenation caused by a change in volcanic degassing pressure. *Nature*, *478*(7368), 229-232.

German, C. R., & Elderfield, H. (1990). Application of the Ce anomaly as a paleoredox indicator: the ground rules. *Paleoceanography*, *5*(5), 823-833.

German, C. R., Higgs, N. C., Thomson, J., Mills, R., Elderfield, H., Blusztajn, J., ... & Bacon, M. P. (1993). A geochemical study of metalliferous sediment from the TAG Hydrothermal Mound, 26° 08′ N, Mid-Atlantic Ridge. *Journal of Geophysical Research: Solid Earth*, *98*(B6), 9683-9692.

Goldschmidt, V. M. (1954). Geochemistry. *Soil Science*, *78*(2), 156.

Grobler, N. J., & Botha, B. J. V. (1976). Pillow-lavas and hyaloclastite in the Ongeluk Andesite Formation in a road-cutting west of Griquatown, South Africa. *Trans. Geol. Soc. S. Afr*, *79*, 53-57.

Gumsley, A. P., Chamberlain, K., Bleeker, W., Söderlund, U., de Kock, M. O., Kampmann, T. C., Larsson, E. (2015). U-Pb TIMS and in-situ SIMS dating of baddeleyite and zircon from sub-volcanic sills of the Ongeluk Formation (Transvaal Supergroup) in the Griqualand West sub-basin, Kaapvaal Craton, with implications for Snowball Earth and the Great Oxygenation Event. *Paper presented at AGU-GAC-MAC-CGU Joint Assembly 2015, Montréal, Canada.*

Gutzmer, J., & Beukes, N. J. (1996). Mineral paragenesis of the Kalahari managanese field, South Africa. *Ore Geology Reviews*, *11*(6), 405-428.

Haymon, R. M., & Kastner, M. (1981). Hot spring deposits on the East Pacific Rise at 21 N: preliminary description of mineralogy and genesis. *Earth and Planetary Science Letters*, *53*(3), 363-381.

Hoashi, M., Bevacqua, D. C., Otake, T., Watanabe, Y., Hickman, A. H., Utsunomiya, S., & Ohmoto, H. (2009). Primary haematite formation in an oxygenated sea 3.46 billion years ago. *Nature Geoscience*, *2*(4), 301-306.

Høgdahl, O. T., Melsom, S. & Bowen, V. T. (1968). Neutron activation analysis of lanthanide elements in sea water. Central Inst. for Industrial Research, Oslo.

Holland, H. D. (1984). *The chemical evolution of the atmosphere and oceans*. Princeton University Press.

Holland, H. D. (2002). Volcanic gases, black smokers, and the Great Oxidation Event. *Geochimica et Cosmochimica Acta*, *66*(21), 3811-3826.

Hoyle, J., Elderfield, H., Gledhill, A., & Greaves, M. (1984). The behaviour of the rare earth elements during mixing of river and sea waters. *Geochimica et Cosmochimica Acta*, *48*(1), 143-149.

Inoue, A. (1995). Formation of clay minerals in hydrothermal environments. In: *Origin and mineralogy of clays* (pp. 268-329). Springer Berlin Heidelberg.

Isley, A. E. (1995). Hydrothermal plumes and the delivery of iron to banded iron formation. *The Journal of Geology*, 169-185.

James, H. L. (1954). Sedimentary facies of iron-formation. *Economic Geology*, *49*(3), 235-293.

Johannesson, K. H., Hawkins, D. L., & Cortés, A. (2006). Do Archean chemical sediments record ancient seawater rare earth element patterns? *Geochimica et Cosmochimica Acta*, *70*(4), 871-890.

Johnson, C. M., Skulan, J. L., Beard, B. L., Sun, H., Nealson, K. H., & Braterman, P. S. (2002). Isotopic fractionation between Fe (III) and Fe (II) in aqueous solutions. *Earth and Planetary Science Letters*, *195*(1), 141-153.

Johnson, C. M., Beard, B. L., Beukes, N. J., Klein, C., & O'Leary, J. M. (2003). Ancient geochemical cycling in the Earth as inferred from Fe isotope studies of banded iron formations from the Transvaal Craton. *Contributions to Mineralogy and Petrology*, *144*(5), 523-547.

Johnson, C. M., Roden, E. E., Welch, S. A., & Beard, B. L. (2005). Experimental constraints on Fe isotope fractionation during magnetite and Fe carbonate formation coupled to dissimilatory hydrous ferric oxide reduction. *Geochimica et Cosmochimica Acta*, *69*(4), 963-993.

Johnson, C. M., Beard, B. L., & Roden, E. E. (2008a). The iron isotope fingerprints of redox and biogeochemical cycling in modern and ancient Earth. *Annu. Rev. Earth Planet. Sci.*, *36*, 457-493.

Johnson, C. M., Beard, B. L., Klein, C., Beukes, N. J., & Roden, E. E. (2008b). Iron isotopes constrain biologic and abiologic processes in banded iron formation genesis. *Geochimica et Cosmochimica Acta*, *72*(1), 151-169.

Kappler, A., Pasquero, C., Konhauser, K. O., & Newman, D. K. (2005). Deposition of banded iron formations by anoxygenic phototrophic Fe (II)-oxidizing bacteria. *Geology*, *33*(11), 865-868.

Kasting, J. F., Eggler, D. H., & Raeburn, S. P. (1993). Mantle redox evolution and the oxidation state of the Archean atmosphere. *The Journal of geology*, 245-257.

Kasting, J. F., Pavlov, A. A., & Siefert, J. L. (2001). A coupled ecosystem-climate model for predicting the methane concentration in the Archean atmosphere. *Origins of Life and Evolution of the Biosphere*, *31*(3), 271-285.

Kato, Y., Suzuki, K., Nakamura, K., Hickman, A. H., Nedachi, M., Kusakabe, M., ... & Ohmoto, H. (2009). Hematite formation by oxygenated groundwater more than 2.76 billion years ago. *Earth and Planetary Science Letters*, *278*(1), 40-49.

Kim, K. H., Byrne, R. H., & Lee, J. H. (1991). Gadolinium behavior in seawater: a molecular basis for gadolinium anomalies. *Marine chemistry*, *36*(1), 107-120.

Kirschvink, J. L., Gaidos, E. J., Bertani, L. E., Beukes, N. J., Gutzmer, J., Maepa, L. N., & Steinberger, R. E. (2000). Paleoproterozoic snowball Earth: extreme climatic and geochemical global change and its biological consequences. *Proceedings of the National Academy of Sciences*, *97*(4), 1400-1405.

Kirschvink, J. L., & Kopp, R. E. (2008). Palaeoproterozoic ice houses and the evolution of oxygen-mediating enzymes: the case for a late origin of photosystem II. *Philosophical Transactions of the Royal Society of London B: Biological Sciences*, *363*(1504), 2755-2765.

Klein, C. (2005). Some Precambrian banded iron-formations (BIFs) from around the world: Their age, geologic setting, mineralogy, metamorphism, geochemistry, and origins. *American Mineralogist*, *90*(10), 1473-1499.

Klein, C., & Beukes, N. J. (1989). Geochemistry and sedimentology of a facies transition from limestone to iron-formation deposition in the early Proterozoic Transvaal Supergroup, South Africa. *Economic Geology*, *84*(7), 1733-1774.

Koeppenkastrop, D., & De Carlo, E. H. (1993). Uptake of rare earth elements from solution by metal oxides. *Environmental science & technology*, *27*(9), 1796-18

Konhauser, K. O., Hamade, T., Raiswell, R., Morris, R. C., Ferris, F. G., Southam, G., & Canfield, D. E. (2002). Could bacteria have formed the Precambrian banded iron formations? *Geology*, *30*(12), 1079-1082.

Konhauser, K. O., Amskold, L., Lalonde, S. V., Posth, N. R., Kappler, A., & Anbar, A. (2007). Decoupling photochemical Fe (II) oxidation from shallow-water BIF deposition. *Earth and Planetary Science Letters*, *258*(1), 87-100.

Konhauser, K. O., Kappler, A., & Roden, E. E. (2011). Iron in microbial metabolisms. *Elements*, *7*(2), 89-93.

Kopp, R. E., Kirschvink, J. L., Hilburn, I. A., & Nash, C. Z. (2005). The Paleoproterozoic snowball Earth: a climate disaster triggered by the evolution of oxygenic photosynthesis. *Proceedings of the National Academy of Sciences of the United States of America*, *102*(32), 11131-11136.

Krapež, B., Barley, M. E., & Pickard, A. L. (2003). Hydrothermal and resedimented origins of the precursor sediments to banded iron formation: sedimentological evidence from the Early Palaeoproterozoic Brockman Supersequence of Western Australia. *Sedimentology*, *50*(5), 979-1011.

Kuma, K., Nishioka, J., & Matsunaga, K. (1996). Controls on iron (III) hydroxide solubility in seawater: the influence of pH and natural organic chelators. *Limnology and Oceanography*, *41*(3), 396-407.

Kump, L. R., & Barley, M. E. (2007). Increased subaerial volcanism and the rise of atmospheric oxygen 2.5 billion years ago. *Nature*, *448*(7157), 1033-1036.

Laznicka, P. (1992). Manganese deposits in the global lithogenetic system: Quantitative approach. *Ore Geology Reviews*, *7*(4), 279-356.

Lee, J. H., & Byrne, R. H. (1993). Complexation of trivalent rare earth elements (Ce, Eu, Gd, Tb, Yb) by carbonate ions. *Geochimica et Cosmochimica Acta*, *57*(2), 295-302.

Lovley, D. R., Stolz, J. F., Nord, G. L., & Phillips, E. J. (1987). Anaerobic production of magnetite by a dissimilatory iron-reducing microorganism. *Nature*, *330*(6145), 252-254.

Lovley, D. R. (1991). Magnetite formation during microbial dissimilatory iron reduction. In *Iron biominerals* (pp. 151-166). Springer US.

Lyons, T. W., & Gill, B. C. (2010). Ancient sulfur cycling and oxygenation of the early biosphere. *Elements*, *6*(2), 93-99.

Lyons, T. W., Reinhard, C. T., & Planavsky, N. J. (2014). The rise of oxygen in Earth/'s early ocean and atmosphere. *Nature*, *506*(7488), 307-315.

Markl, G., Von Blanckenburg, F., & Wagner, T. (2006). Iron isotope fractionation during hydrothermal ore deposition and alteration. *Geochimica et Cosmochimica Acta*, *70*(12), 3011-3030.

Miyano, T., & Beukes, N. J. (1984). Phase relations of stilpnomelane, ferri-annite, and riebeckite in very low-grade metamorphosed iron-formations. *South African Journal of Geology*, *87*(2), 111-124.

Moore, J. M., Polteau, S., Armstrong, R. A., Corfu, F., & Tsikos, H. (2012). The age and correlation of the Postmasburg Group, southern Africa: constraints from detrital zircon grains. *Journal of African Earth Sciences*, *64*, 9-19.

Morris, R. C. (1993). Genetic modelling for banded iron-formation of the Hamersley Group, Pilbara Craton, Western Australia. *Precambrian Research*, *60*(1), 243-286.

Morris, R. C. (2012). Microplaty hematite—its varied nature and genesis.*Australian Journal of Earth Sciences*, *59*(3), 411-434.

Nel, C. J., Beukes, N. J., & De Villiers, J. P. R. (1986). The Mamatwan manganese mine of the Kalahari manganese field. *Mineral Deposits of Southern Africa*, *1*, 963-978.

Nelson, D. R., Trendall, A. F., & Altermann, W. (1999). Chronological correlations between the Pilbara and Kaapvaal cratons. *Precambrian Research*, *97*(3), 165-189.

Nozaki, Y., Zhang, J., & Amakawa, H. (1997). The fractionation between Y and Ho in the marine environment. *Earth and Planetary Science Letters*, *148*(1), 329-340.

Ohmoto, H., & Goldhaber, M. B. (1997). Sulfur and carbon isotopes. *Geochemistry of hydrothermal ore deposits*, *3*, 517-611.

Ohmoto, H., Watanabe, Y., Ikemi, H., Poulson, S. R., & Taylor, B. E. (2006). Sulphur isotope evidence for an oxic Archaean atmosphere. *Nature*, *442*(7105), 908-911.

Ohmoto, H., Watanabe, Y., Yamaguchi, K. E., Naraoka, H., Haruna, M., Kakegawa, T., ... & Kato, Y. (2006). Chemical and biological evolution of early Earth: constraints from banded iron formations. *Geological Society of America Memoirs*, *198*, 291-331.

Olson, S. L., Kump, L. R., & Kasting, J. F. (2013). Quantifying the areal extent and dissolved oxygen concentrations of Archean oxygen oases. *Chemical Geology*, *362*, 35-43.

Page, A. L. (1982). *Methods of soil analysis. Part 2. Chemical and microbiological properties*. American Society of Agronomy, Soil Science Society of America.

Pearce, N. J., Perkins, W. T., Westgate, J. A., Gorton, M. P., Jackson, S. E., Neal, C. R., & Chenery, S. P. (1997). A compilation of new and published major and trace element data for NIST SRM 610 and NIST SRM 612 glass reference materials. *Geostandards newsletter*, *21*(1), 115-144.

Pettijohn, F. J. (1975). Sedimentary rocks (3rd edition). *New York, Harper and Row*, 628 p.

Pickard, A. L. (2003). SHRIMP U–Pb zircon ages for the Palaeoproterozoic Kuruman Iron Formation, northern Cape Province, South Africa: evidence for simultaneous BIF deposition on Kaapvaal and Pilbara cratons. *Precambrian Research*, *125*(3), 275-315.

Planavsky, N., Bekker, A., Rouxel, O. J., Kamber, B., Hofmann, A., Knudsen, A., & Lyons, T. W. (2010). Rare earth element and yttrium compositions of Archean and Paleoproterozoic Fe formations revisited: new perspectives on the significance and mechanisms of deposition. *Geochimica et Cosmochimica Acta*, *74*(22), 6387-6405.

Planavsky, N. J., McGoldrick, P., Scott, C. T., Li, C., Reinhard, C. T., Kelly, A. E., ... & Lyons, T. W. (2011). Widespread iron-rich conditions in the mid-Proterozoic ocean. *Nature*, *477*(7365), 448-451.

Planavsky, N., Rouxel, O. J., Bekker, A., Hofmann, A., Little, C. T., & Lyons, T. W. (2012). Iron isotope composition of some Archean and Proterozoic iron formations. *Geochimica et Cosmochimica Acta*, *80*, 158-169.

Planavsky, N. J., Asael, D., Hofman, A., Reinhard, C. T., Lalonde, S. V., Knudsen, A., ... & Beukes, N. J. (2014). Evidence for oxygenic photosynthesis half a billion years before the Great Oxidation Event. *Nature Geoscience*, *7*(4), 283-286.

Poitrasson, F., Halliday, A. N., Lee, D. C., Levasseur, S., & Teutsch, N. (2004). Iron isotope differences between Earth, Moon, Mars and Vesta as possible records of contrasted accretion mechanisms. *Earth and Planetary Science Letters*, *223*(3), 253-266.

Polyakov, V. B., & Mineev, S. D. (2000). The use of Mössbauer spectroscopy in stable isotope geochemistry. *Geochimica et Cosmochimica Acta*, *64*(5), 849-865.

Poulton, S. W., & Canfield, D. E. (2011). Ferruginous conditions: a dominant feature of the ocean through Earth's history. *Elements*, *7*(2), 107-112.

Poulton, S. W., Fralick, P. W., & Canfield, D. E. (2004). The transition to a sulphidic ocean∼ 1.84 billion years ago. *Nature*, *431*(7005), 173-177.

Pourmand, A., Dauphas, N., & Ireland, T. J. (2012). A novel extraction chromatography and MC-ICP-MS technique for rapid analysis of REE, Sc and Y: Revising CI-chondrite and Post-Archean Australian Shale (PAAS) abundances. *Chemical Geology*, *291*, 38-54.

Qin, L., & Humayun, M. (2008). The Fe/Mn ratio in MORB and OIB determined by ICP-MS. *Geochimica et Cosmochimica Acta*, *72*(6), 1660-1677.

Quinn, K. A., Byrne, R. H., & Schijf, J. (2004). Comparative scavenging of yttrium and the rare earth elements in seawater: competitive influences of solution and surface chemistry. *Aquatic Geochemistry*, *10*(1-2), 59-80.

Raiswell, R. (1982). Pyrite texture, isotopic composition and the availability of iron. *American Journal of Science*, *282*(8), 1244-1263.

Rasmussen, B., Fletcher, I. R., Brocks, J. J., & Kilburn, M. R. (2008). Reassessing the first appearance of eukaryotes and cyanobacteria. *Nature*, *455*(7216), 1101-1104.

Rasmussen, B., Krapež, B., Muhling, J. R., & Suvorova, A. (2015). Precipitation of iron silicate nanoparticles in early Precambrian oceans marks Earth's first iron age. *Geology*, *43*(4), 303-306.

Reczko, B. F. F., Oberholzer, J. D., Eriksson, P. G., & Schreiber, U. M. (1995). A re-evaluation of the volcanism of the Palaeoproterozoic Pretoria Group (Kaapvaal craton) and a hypothesis on basin development. *Journal of African Earth Sciences*, *21*(4), 505-519.

Reineck, H.-E., and Wunderlich, F. (1968). Classification and origin of flaser and lenticular bedding. *Sedimentology, v. 11*, p. 99-104.

Reinhard, C. T., Planavsky, N. J., Robbins, L. J., Partin, C. A., Gill, B. C., Lalonde, S. V., ... & Lyons, T. W. (2013). Proterozoic ocean redox and biogeochemical stasis. *Proceedings of the National Academy of Sciences*, *110*(14), 5357-5362.

Riding, R., Fralick, P., & Liang, L. (2014). Identification of an Archean marine oxygen oasis. *Precambrian Research*, *251*, 232-237.

Rouxel, O., Dobbek, N., Ludden, J., & Fouquet, Y. (2003). Iron isotope fractionation during oceanic crust alteration. *Chemical Geology*, *202*(1), 155-182.

Rouxel, O. J., Bekker, A., & Edwards, K. J. (2005). Iron isotope constraints on the Archean and Paleoproterozoic ocean redox state. *Science*, *307*(5712), 1088-1091.

Rouxel, O., Shanks, W. C., Bach, W., & Edwards, K. J. (2008). Integrated Fe-and S-isotope study of seafloor hydrothermal vents at East Pacific Rise 9–10 N. *Chemical Geology*, *252*(3), 214-227.

Sahoo, S. K., Planavsky, N. J., Kendall, B., Wang, X., Shi, X., Scott, C., ... & Jiang, G. (2012). Ocean oxygenation in the wake of the Marinoan glaciation.*Nature*, *489*(7417), 546-549.

Satkoski, A. M., Beukes, N. J., Li, W., Beard, B. L., & Johnson, C. M. (2015). A redox-stratified ocean 3.2 billion years ago. *Earth and Planetary Science Letters*, *430*, 43-53.

Schauble, E. A. (2004). Applying stable isotope fractionation theory to new systems. *Reviews in Mineralogy and Geochemistry*, *55*(1), 65-111.

Schieber, J. (1999). Microbial mats in terrigenous clastics; the challenge of identification in the rock record. *Palaios*, *14*(1), 3-12.

Schoenberg, R., & von Blanckenburg, F. (2005). An assessment of the accuracy of stable Fe isotope ratio measurements on samples with organic and inorganic matrices by high-resolution multicollector ICP-MS. *International Journal of Mass Spectrometry*, *242*(2), 257-272.

Schutte, S. S. (2011). *Ongeluk volcanism in relation to the Kalahari manganese deposits* (Doctoral dissertation).

Scott, C., Lyons, T. W., Bekker, A., Shen, Y. A., Poulton, S. W., Chu, X. L., & Anbar, A. D. (2008). Tracing the stepwise oxygenation of the Proterozoic ocean. *Nature*, *452*(7186), 456-459.

Severmann, S., Johnson, C. M., Beard, B. L., German, C. R., Edmonds, H. N., Chiba, H., & Green, D. R. H. (2004). The effect of plume processes on the Fe isotope composition of hydrothermally derived Fe in the deep ocean as inferred from the Rainbow vent site, Mid-Atlantic Ridge, 36 14′ N. *Earth and Planetary Science Letters*, *225*(1), 63-76.

Sharma, M., Polizzotto, M., & Anbar, A. D. (2001). Iron isotopes in hot springs along the Juan de Fuca Ridge. *Earth and Planetary Science Letters*,*194*(1), 39-51.

Shen, Y., Knoll, A. H., & Walter, M. R. (2003). Evidence for low sulphate and anoxia in a mid-Proterozoic marine basin. *Nature*, *423*(6940), 632-635.

Sherrell, R. M., Field, M. P., & Ravizza, G. (1999). Uptake and fractionation of rare earth elements on hydrothermal plume particles at 9 45′ N, East Pacific Rise. *Geochimica et Cosmochimica Acta, 63*(11), 1709-1722.

Sholkovitz, E. R., Landing, W. M., & Lewis, B. L. (1994). Ocean particle chemistry: the fractionation of rare earth elements between suspended particles and seawater. *Geochimica et Cosmochimica Acta*, *58*(6), 1567-1579.

Siever, R. (1992). The silica cycle in the Precambrian. *Geochimica et Cosmochimica Acta*, *56*(8), 3265-3272.

Simonson, B. M. (1985). Sedimentological constraints on the origins of Precambrian iron-formations. *Geological Society of America Bulletin*, *96*(2), 244-252.

Skulan, J. L., Beard, B. L., & Johnson, C. M. (2002). Kinetic and equilibrium Fe isotope fractionation between aqueous Fe (III) and hematite. *Geochimica et Cosmochimica Acta*, *66*(17), 2995-3015.

Smith, A. J., Beukes, N. J., & Gutzmer, J. (2013). The composition and depositional environments of Mesoarchean iron formations of the West Rand group of the Witwatersrand Supergroup, South Africa. *Economic Geology*, *108*(1), 111-134.

Steinhoefel, G., Horn, I., & von Blanckenburg, F. (2009). Micro-scale tracing of Fe and Si isotope signatures in banded iron formation using femtosecond laser ablation. *Geochimica et Cosmochimica Acta*, *73*(18), 5343-5360.

Summons, R. E., Bradley, A. S., Jahnke, L. L., & Waldbauer, J. R. (2006). Steroids, triterpenoids and molecular oxygen. *Philosophical Transactions of the Royal Society of London B: Biological Sciences*, *361*(1470), 951-968.

Swart, Q. D. (2012). *Carbonate rocks of the Paleoproterozoic Pretoria and Postmasburg Groups, Transvaal Supergroup* (Doctoral dissertation).

Teng, F. Z., Dauphas, N., Huang, S., & Marty, B. (2013). Iron isotopic systematics of oceanic basalts. *Geochimica et Cosmochimica Acta*, *107*, 12-26.

Trendall, A. F. (1983). The Hamersley Basin. *Developments in Precambrian Geology*, *6*, 69-129.

Tsikos, H., & Moore, J. M. (1997). Petrography and geochemistry of the Paleoproterozoic Hotazel Iron-Formation, Kalahari manganese field, South Africa; implications for Precambrian manganese metallogenesis. *Economic Geology*, *92*(1), 87-97.

Tsikos, H., Matthews, A., Erel, Y., & Moore, J. M. (2010). Iron isotopes constrain biogeochemical redox cycling of iron and manganese in a Palaeoproterozoic stratified basin. *Earth and Planetary Science Letters*, *298*(1), 125-134.

Urey, H. C. (1947). The thermodynamic properties of isotopic substances. *Journal of the Chemical Society (Resumed)*, 562-581.

Waldbauer, J. R., Sherman, L. S., Sumner, D. Y., & Summons, R. E. (2009). Late Archean molecular fossils from the Transvaal Supergroup record the antiquity of microbial diversity and aerobiosis. *Precambrian Research*, *169*(1), 28-47.

Wang, Q., & Morse, J. W. (1996). Pyrite formation under conditions approximating those in anoxic sediments I. Pathway and morphology. *Marine Chemistry*, *52*(2), 99-121.

Welch, S. A., Beard, B. L., Johnson, C. M., & Braterman, P. S. (2003). Kinetic and equilibrium Fe isotope fractionation between aqueous Fe (II) and Fe (III). *Geochimica et Cosmochimica Acta*, *67*(22), 4231-4250.

Weyer, S., & Schwieters, J. B. (2003). High precision Fe isotope measurements with high mass resolution MC-ICPMS. *International Journal of Mass Spectrometry*, *226*(3), 355-368.

Whitehouse, M. J., & Fedo, C. M. (2007). Microscale heterogeneity of Fe isotopes in> 3.71 Ga banded iron formation from the Isua Greenstone Belt, southwest Greenland. *Geology*, *35*(8), 719-722.

Widdel, F., Schnell, S., Heising, S., Ehrenreich, A., Assmus, B., & Schink, B. (1993). Ferrous iron oxidation by anoxygenic phototrophic bacteria. *Nature*, *362*(6423), 834-836.

Wiesli, R. A., Beard, B. L., & Johnson, C. M. (2004). Experimental determination of Fe isotope fractionation between aqueous Fe (II), siderite and “green rust” in abiotic systems. *Chemical Geology*, *211*(3), 343-362.

Williams, L. A., & Crerar, D. A. (1985). Silica diagenesis, II. General mechanisms. *Journal of Sedimentary Research*, *55*(3).

Williams, H. M., McCammon, C. A., Peslier, A. H., Halliday, A. N., Teutsch, N., Levasseur, S., & Burg, J. P. (2004). Iron isotope fractionation and the oxygen fugacity of the mantle. *Science*, *304*(5677), 1656-1659.

Williams, H. M., Peslier, A. H., McCammon, C., Halliday, A. N., Levasseur, S., Teutsch, N., & Burg, J. P. (2005). Systematic iron isotope variations in mantle rocks and minerals: the effects of partial melting and oxygen fugacity. *Earth and Planetary Science Letters*, *235*(1), 435-452.

Wu, L., Percak-Dennett, E. M., Beard, B. L., Roden, E. E., & Johnson, C. M. (2012). Stable iron isotope fractionation between aqueous Fe (II) and model Archean ocean Fe–Si coprecipitates and implications for iron isotope variations in the ancient rock record. *Geochimica et Cosmochimica Acta*, *84*, 14-28.

Xu, Q., & Scott, S. D. (2005). Spherulitic pyrite in seafloor hydrothermal deposits: products of rapid crystallization from mixing fluids. In *Mineral deposit research: meeting the global challenge* (pp. 711-713). Springer Berlin Heidelberg.

Yamaguchi, K. E., Johnson, C. M., Beard, B. L., & Ohmoto, H. (2005). Biogeochemical cycling of iron in the Archean–Paleoproterozoic Earth: constraints from iron isotope variations in sedimentary rocks from the Kaapvaal and Pilbara Cratons. *Chemical Geology*, *218*(1), 135-169.

Zahnle, K., Claire, M., & Catling, D. (2006). The loss of mass-independent fractionation in sulfur due to a Palaeoproterozoic collapse of atmospheric methane. *Geobiology*, *4*(4), 271-283.

Zhu, X. K., O'Nions, R. K., Guo, Y., & Reynolds, B. C. (2000). Secular variation of iron isotopes in North Atlantic deep water. *Science*, *287*(5460).

Appendix

1. Scans drill-core GL36 (true scale)

293.25 cm
293.05 cm

293.05 cm
292.90 cm

292.90 cm
292.82 cm

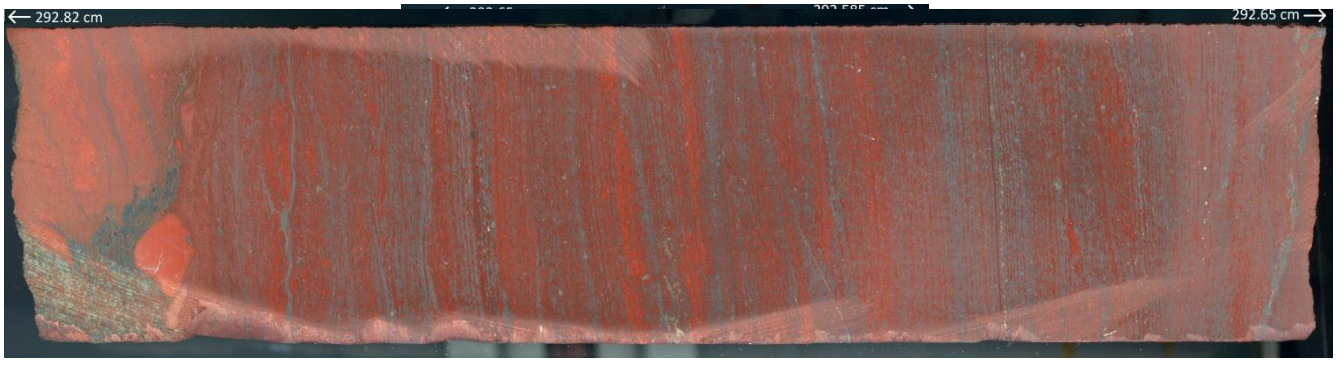
292.82 cm
292.65 cm

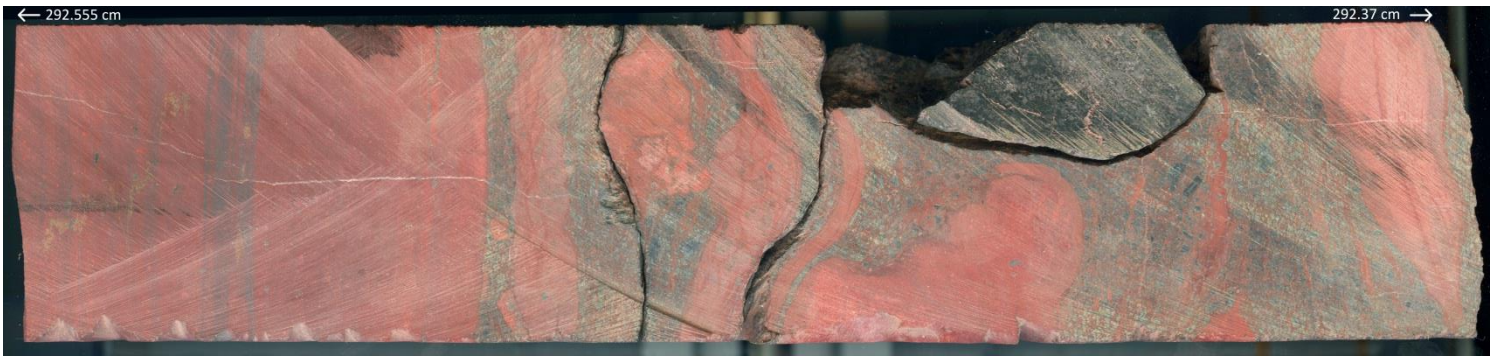
292.555 cm
292.37 cm

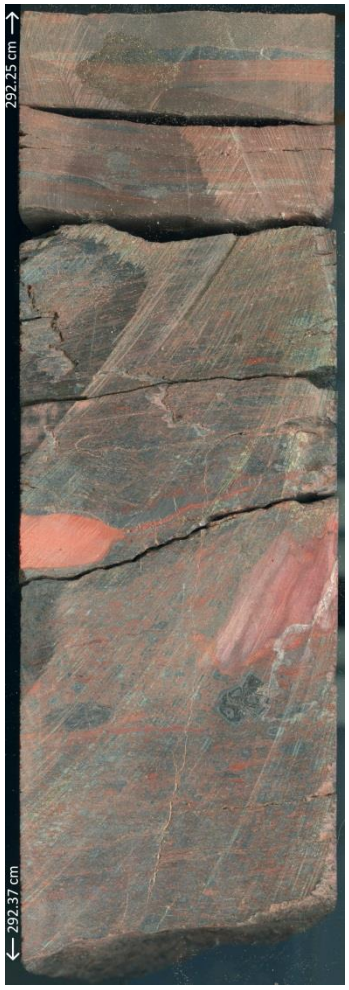
292.25 cm
292.37 cm

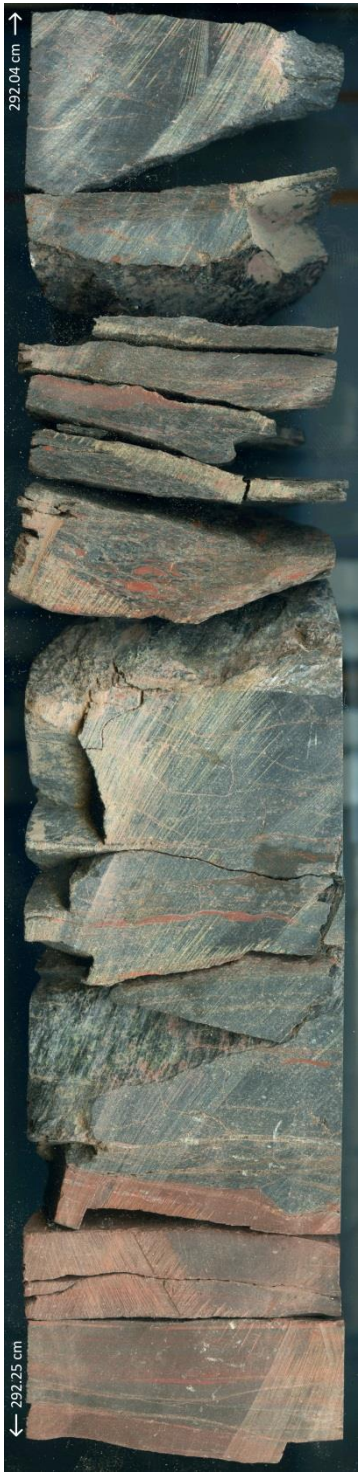
292.04 cm
292.25 cm

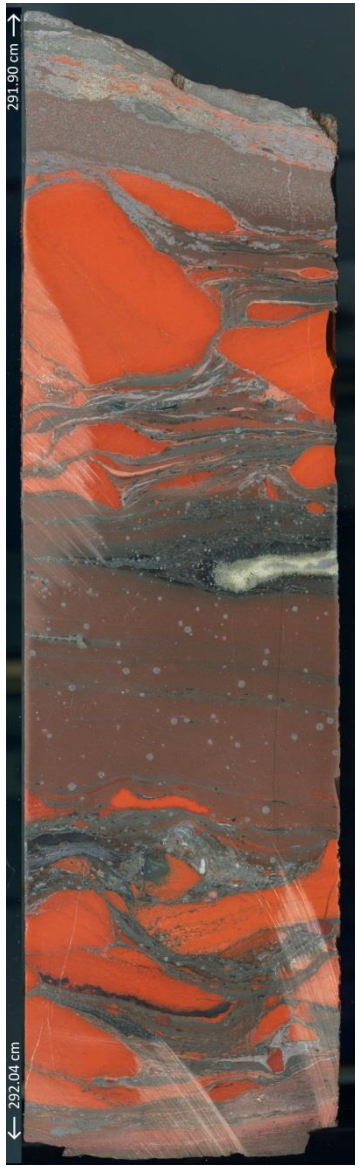
291.90 cm
292.04 cm

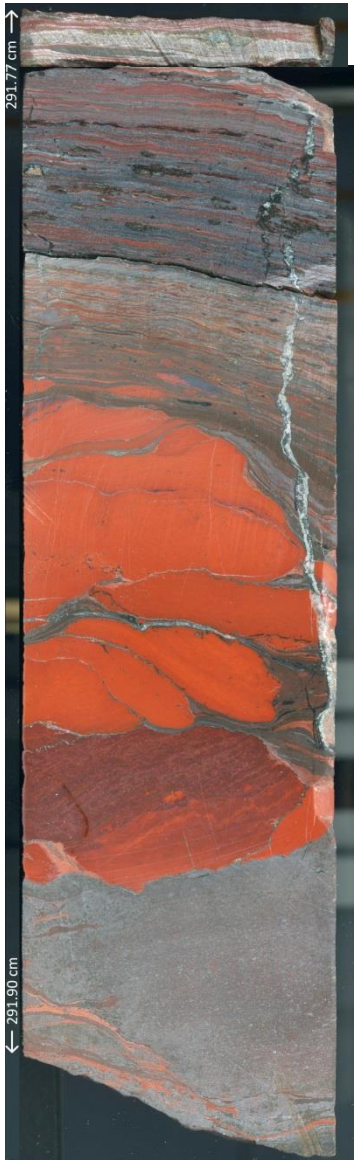
291.77 cm
291.90 cm

291.60 cm
291.77 cm

291.60 cm
291.49 cm

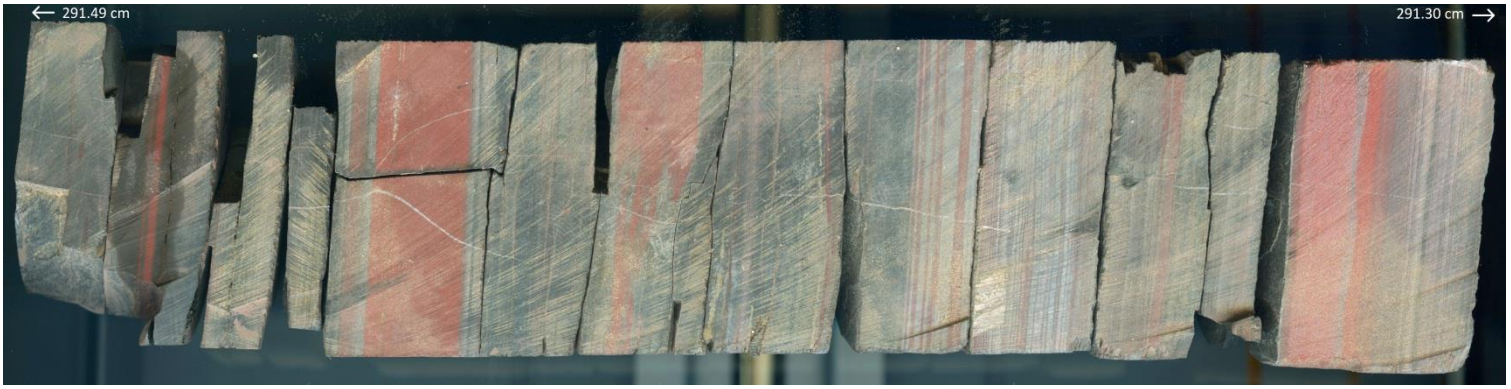
291.49 cm
291.30 cm

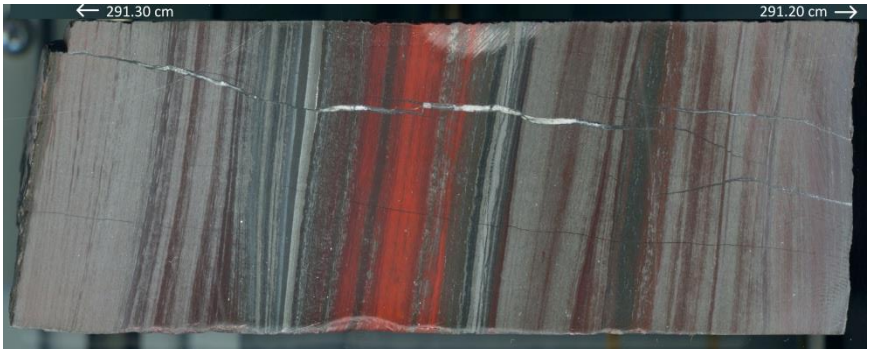
291.30 cm
291.20 cm

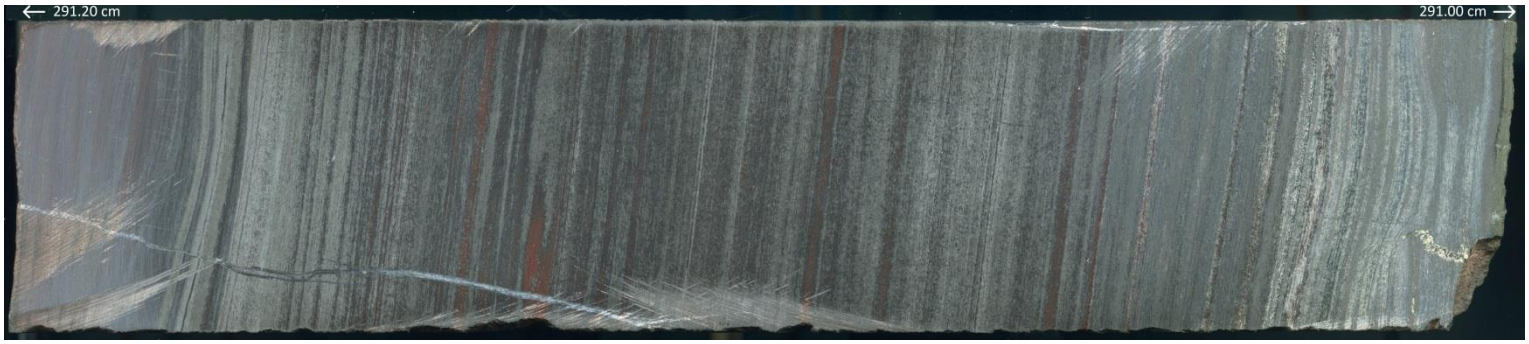
291.20 cm
291.00 cm

2. EMPA

2.1 Minerals

Table 1: Overview of all WDS point analyses. The term "1σ %" represents the 1 S.D. obtained from counting statistics. Elements are indicated with their oxide form, but it is important to note that the given weight percentages only represent the measured mass of the elements (atoms) and not that of oxygen. Elements lighter than F cannot be measured properly with WDS, but their total contribution to the mineral mass can be deduced from the deviation of the Total (mass %) from 100 %.

Thin-section	Mineral	SiO2 (wt %)	Si (1σ %)	Na2O (wt %)	Na (1σ %)	CaO (wt %)	Ca (1σ %)	SO3 (wt %)	S (1σ %)	K2O (wt %)	K (1σ %)	TiO2 (wt %)	Ti (1σ %)	Al2O3 (wt %)	Al (1σ %)	MgO (wt %)	Mg (1σ %)	FeO (wt %)	Fe (1σ %)	MnO (wt %)	Mn (1σ %)	Total (wt %)	Total (1σ %)
4	magnetite	1.08	1.73	-	-	0.05	15.44	0.03	54.01	0.00	100.00	0.08	8.57	0.01	169.44	0.02	48.47	92.56	0.20	0.03	41.44	93.86	439.30
6	magnetite	1.62	1.35	-	-	0.02	32.05	0.00	655.74	0.00	100.00	0.09	7.77	0.02	58.49	0.02	67.79	92.57	0.20	0.03	36.45	94.37	959.84
8	magnetite	1.09	1.73	-	-	0.07	10.04	0.02	67.82	0.00	100.00	0.10	7.36	0.00	100.00	0.03	33.48	93.41	0.20	0.05	23.30	94.78	343.93
	average	**1.26**	1.60	**-**	-	**0.05**	19.18	**0.02**	259.19	**0.00**	100.00	**0.09**	7.90	**0.01**	109.31	**0.03**	49.91	**92.85**	0.20	**0.04**	33.73	**94.34**	581.02
	1 S.D.	**0.30**				**0.03**		**0.01**		**0.00**		**0.01**		**0.01**		**0.01**		**0.49**		**0.01**		**0.46**	
6	stilpnomelane	52.11	0.21	-	-	0.02	35.51	0.02	61.24	2.19	0.93	0.05	12.47	4.80	0.67	9.02	0.48	23.15	0.42	1.34	1.55	92.70	113.48
6	stilpnomelane	50.83	0.21	-	-	0.02	36.72	0.00	100.00	0.35	2.72	0.07	9.77	4.56	0.70	14.14	0.38	22.10	0.43	1.16	1.69	93.23	152.62
8	stilpnomelane	48.11	0.22	-	-	1.11	1.37	0.00	100.00	0.91	1.49	0.06	11.41	5.17	0.65	9.69	0.47	24.47	0.41	1.17	1.70	90.69	117.72
8	stilpnomelane	48.28	0.22	-	-	0.03	23.80	0.03	42.49	2.01	0.97	0.06	10.31	5.13	0.65	9.70	0.47	25.37	0.40	1.12	1.73	91.73	81.04
8	stilpnomelane	46.86	0.22	-	-	0.04	16.12	0.00	100.00	3.02	0.78	0.04	16.37	5.16	0.65	10.56	0.45	24.12	0.41	1.41	1.51	91.21	136.51
	average	**49.24**	0.22	**-**	-	**0.24**	22.70	**0.01**	80.75	**1.70**	1.38	**0.06**	12.07	**4.96**	0.66	**10.62**	0.45	**23.84**	0.41	**1.24**	1.64	**91.91**	120.27
	1 S.D.	**2.16**				**0.49**		**0.02**		**1.06**		**0.01**		**0.27**		**2.04**		**1.26**		**0.13**		**1.05**	
4	minnesotaite	56.93	0.20	-	-	0.03	18.21	0.00	100.00	0.00	100.00	0.04	14.82	0.41	3.25	20.29	0.31	16.60	0.50	0.09	11.61	94.40	248.90
4	minnesotaite	55.92	0.20	-	-	0.05	12.63	0.05	29.40	0.00	100.00	0.05	14.13	0.46	3.00	20.82	0.31	16.44	0.50	0.11	9.40	93.90	169.57
6	minnesotaite	57.43	0.20	-	-	0.01	48.45	0.00	100.00	0.00	459.46	0.07	10.17	0.27	4.63	20.83	0.31	15.69	0.52	0.08	12.53	94.39	636.27
6	minnesotaite	57.98	0.20	-	-	0.03	21.24	0.01	114.89	0.00	100.00	0.08	8.97	0.27	4.57	21.42	0.30	14.95	0.53	0.09	12.36	94.83	263.06
6	minnesotaite	57.94	0.20	-	-	0.03	20.94	0.00	387.30	0.00	100.00	0.05	12.73	0.28	4.36	20.77	0.31	15.93	0.51	0.08	12.71	95.09	539.06
6	minnesotaite	56.71	0.20	-	-	0.03	20.83	0.00	435.89	0.01	44.36	0.05	14.34	0.56	2.65	21.94	0.30	14.79	0.53	0.08	12.42	94.17	531.52
6	minnesotaite	54.42	0.20	0.02	41.69	0.07	10.16	0.00	100.00	0.00	100.00	0.04	14.03	1.55	1.32	20.08	0.32	18.70	0.47	0.12	9.02	95.01	277.21
6	minnesotaite	55.23	0.20	0.00	100.00	0.03	19.41	0.01	83.81	0.00	100.00	0.04	16.02	1.49	1.35	20.57	0.31	16.18	0.50	0.12	9.17	93.66	330.77
15	minnesotaite	54.36	0.20	0.07	13.95	0.11	6.43	0.04	21.35	0.01	47.67	0.05	12.51	2.37	1.03	22.91	0.29	14.04	0.54	0.09	12.01	94.05	115.98
15	minnesotaite	56.78	0.20	0.01	87.83	0.04	15.85	0.00	317.98	0.00	100.00	0.04	16.54	2.12	1.07	19.56	0.32	14.98	0.52	0.15	7.65	93.68	547.96
	average	**56.37**	0.20	**0.03**	60.87	**0.04**	19.42	**0.01**	169.06	**0.00**	125.15	**0.05**	13.43	**0.98**	2.72	**20.92**	0.31	**15.83**	0.51	**0.10**	10.89	**94.32**	366.03
	1 S.D.	**1.34**		**0.03**		**0.03**		**0.02**		**0.00**		**0.01**		**0.82**		**0.96**		**1.30**		**0.02**		**0.52**	

Thin-section	Mineral	SiO2 (wt %)	Si (1σ %)	Na2O (wt %)	Na (1σ %)	CaO (wt %)	Ca (1σ %)	SO3 (wt %)	S (1σ %)	K2O (wt %)	K (1σ %)	TiO2 (wt %)	Ti (1σ %)	Al2O3 (wt %)	Al (1σ %)	MgO (wt %)	Mg (1σ %)	FeO (wt %)	Fe (1σ %)	MnO (wt %)	Mn (1σ %)	Total (wt %)	Total (1σ %)
4	Mn-calcite	1.67	1.20	-	-	51.65	0.18	0.19	12.22	0.08	6.42	0.04	20.03	0.07	14.38	0.53	2.51	0.95	2.49	3.59	0.89	58.77	60.32
4	Mn-calcite	0.10	8.54	-	-	54.79	0.17	0.05	34.01	0.01	31.53	0.02	34.00	0.02	54.32	0.26	4.37	0.65	3.21	3.48	0.90	59.38	171.05
4	Mn-calcite	0.65	2.12	-	-	48.00	0.19	0.02	58.21	0.01	54.58	0.02	39.15	0.44	3.03	3.94	0.76	1.33	1.99	3.54	0.89	57.95	160.92
8	Mn-calcite	0.31	3.55	-	-	57.66	0.17	0.17	12.34	0.01	41.98	0.05	12.92	0.03	29.95	0.13	6.82	0.58	3.48	4.21	0.82	63.16	112.03
	average	**0.69**	3.85	**-**	-	**53.03**	0.18	**0.11**	29.20	**0.03**	33.63	**0.03**	26.53	**0.14**	25.42	**1.22**	3.62	**0.88**	2.79	**3.71**	0.88	**59.82**	126.08
	1 S.D.	**0.70**				**4.15**		**0.09**		**0.04**		**0.02**		**0.20**		**1.82**		**0.34**		**0.34**		**2.31**	
17	calcite	0.18	5.24	0.02	39.81	56.92	0.17	0.02	40.82	0.00	100.00	0.06	10.68	0.08	11.92	0.17	5.65	1.79	1.67	1.09	1.78	60.33	217.74
17	calcite	0.21	4.76	0.01	56.86	56.39	0.17	0.02	39.97	0.00	100.00	0.02	33.11	0.01	138.01	0.11	8.23	0.50	3.82	2.13	1.19	59.40	386.12
19	calcite	0.10	8.55	0.00	176.93	56.24	0.17	0.01	39.63	0.00	195.87	0.01	44.56	0.01	88.70	0.11	6.98	0.56	3.51	1.07	1.76	58.12	566.66
19	calcite	0.09	9.88	0.00	975.47	58.30	0.17	0.01	63.89	0.00	262.06	0.00	100.00	0.00	100.00	0.12	7.15	0.61	3.34	0.57	2.68	59.70	1524.64
19	calcite	0.16	5.03	0.01	54.31	55.35	0.18	0.00	100.00	0.00	490.46	0.06	8.85	0.19	4.25	0.03	20.00	0.65	3.07	0.88	2.02	57.33	688.17
	average	**0.15**	6.69	**0.01**	260.68	**56.64**	0.17	**0.01**	56.86	**0.00**	229.68	**0.03**	39.44	**0.06**	68.58	**0.11**	9.60	**0.82**	3.08	**1.15**	1.89	**58.98**	676.67
	1 S.D.	**0.05**		**0.01**		**1.09**		**0.01**		**0.00**		**0.03**		**0.08**		**0.05**		**0.54**		**0.59**		**1.22**	
4	pyrite	0.41	1.96	-	-	0.02	23.97	67.71	0.41	0.00	100.00	0.04	10.79	0.00	100.00	0.03	21.23	30.72	0.25	0.00	100.00	98.92	358.61
4	pyrite	0.17	3.81	-	-	0.01	48.11	68.22	0.40	0.00	100.00	0.04	10.43	0.00	168.58	0.01	48.43	30.82	0.25	0.00	167.41	99.27	547.42
4	pyrite	0.29	2.50	-	-	0.01	40.76	68.39	0.40	0.00	100.00	0.04	10.88	0.01	49.06	0.05	11.77	30.95	0.25	0.02	30.50	99.75	246.12
15	pyrite	0.10	5.77	0.06	11.86	0.00	100.00	69.84	0.22	0.00	100.00	0.05	8.04	0.01	48.66	0.01	42.09	31.36	0.25	0.00	154.30	101.44	471.19
15	pyrite	0.06	9.43	0.10	7.74	0.00	100.00	68.62	0.22	0.00	100.00	0.04	9.52	0.02	39.06	0.00	185.25	31.36	0.25	0.00	100.00	100.19	551.47
15	pyrite	0.30	2.47	0.09	8.98	0.01	44.62	65.58	0.23	0.00	100.00	0.03	14.02	0.03	23.32	0.07	8.88	31.04	0.25	0.00	100.00	97.13	302.77
15	pyrite	0.21	3.16	0.08	9.16	0.01	33.37	66.41	0.23	0.00	100.00	0.04	9.10	0.02	38.92	0.07	8.08	30.78	0.25	0.01	87.48	97.64	289.75
	average	**0.22**	4.16	**0.08**	9.44	**0.01**	55.83	**67.82**	0.30	**0.00**	100.00	**0.04**	10.40	**0.01**	66.80	**0.03**	46.53	**31.00**	0.25	**0.01**	105.67	**99.19**	395.33
	1 S.D.	**0.11**		**0.01**		**0.01**		**1.32**		**0.00**		**0.01**		**0.01**		**0.03**		**0.24**		**0.01**		**1.37**	
8	Mn-ilmenite	1.70	1.27	0.00	100.00	0.00	144.70	0.02	49.79	0.00	100.00	48.83	0.16	0.20	6.96	0.84	2.19	37.43	0.32	10.44	0.49	99.45	405.88
8	Mn-ilmenite	0.76	2.12	0.01	187.81	0.01	70.23	0.01	132.29	0.00	100.00	49.97	0.16	0.26	5.62	0.35	4.12	37.82	0.32	10.17	0.50	99.35	503.17
8	Mn-ilmenite	0.09	11.27	0.00	100.00	0.00	713.74	0.00	182.57	0.00	100.00	51.17	0.16	0.05	24.20	0.07	15.88	38.17	0.31	10.51	0.49	100.07	1148.62
	average	**0.85**	4.89	**0.00**	129.27	**0.00**	309.56	**0.01**	121.55	**0.00**	100.00	**49.99**	0.16	**0.17**	12.26	**0.42**	7.40	**37.81**	0.32	**10.37**	0.49	**99.62**	685.89
	1 S.D.	**0.81**		**0.00**		**0.00**		**0.01**		**0.00**		**1.17**		**0.11**		**0.39**		**0.37**		**0.18**		**0.39**	

Thin-section	Mineral	SiO2 (wt %)	Si (1σ %)	Na2O (wt %)	Na (1σ %)	CaO (wt %)	Ca (1σ %)	SO3 (wt %)	S (1σ %)	K2O (wt %)	K (1σ %)	TiO2 (wt %)	Ti (1σ %)	Al2O3 (wt %)	Al (1σ %)	MgO (wt %)	Mg (1σ %)	FeO (wt %)	Fe (1σ %)	MnO (wt %)	Mn (1σ %)	Total (wt %)	Total (1σ %)
1	ankerite centre	0.18	5.42	0.00	100.00	27.80	0.25	0.00	199.00	0.26	2.99	0.04	15.36	0.04	26.41	17.82	0.35	3.42	1.13	11.37	0.48	60.93	351.39
1	ankerite centre	1.33	1.42	0.00	100.00	27.45	0.25	0.03	26.62	0.00	100.00	0.03	19.95	0.21	5.53	15.54	0.38	4.23	1.01	10.18	0.51	58.99	255.67
	average	**0.76**	3.42	**0.00**	100.00	**27.63**	0.25	**0.02**	112.81	**0.13**	51.50	**0.03**	17.66	**0.12**	15.97	**16.68**	0.37	**3.83**	1.07	**10.78**	0.50	**59.96**	303.53
	1 S.D.	**0.81**		**0.00**		**0.25**		**0.02**		**0.18**		**0.01**		**0.12**		**1.61**		**0.57**		**0.84**		**1.37**	
1	ankerite rim	0.59	2.37	0.00	275.84	26.42	0.25	0.01	69.25	0.00	138.91	0.03	21.73	0.01	95.03	11.58	0.45	10.05	0.64	6.08	0.66	54.77	605.13
1	ankerite rim	3.26	0.87	0.02	54.99	26.38	0.25	0.00	100.00	0.00	1473.07	0.03	20.95	0.00	5635.16	10.74	0.47	7.28	0.75	8.97	0.54	56.68	7287.05
	average	**1.92**	1.62	**0.01**	165.42	**26.40**	0.25	**0.01**	84.63	**0.00**	805.99	**0.03**	21.34	**0.01**	2865.10	**11.16**	0.46	**8.67**	0.70	**7.53**	0.60	**55.72**	3946.09
	1 S.D.	**1.89**		**0.01**		**0.03**		**0.01**		**0.00**		**0.00**		**0.01**		**0.59**		**1.96**		**2.04**		**1.35**	
19	feldspar	52.32	0.21	0.02	43.36	0.04	15.26	0.00	100.00	3.90	0.69	0.15	4.98	27.32	0.26	2.58	0.90	5.36	0.90	0.05	18.58	91.74	185.14
19	feldspar	53.35	0.21	0.04	21.86	0.03	22.55	0.02	45.28	4.32	0.65	0.09	7.17	26.63	0.26	3.01	0.82	4.43	0.99	0.04	22.78	91.96	122.57
19	feldspar	51.38	0.21	0.04	21.49	0.04	15.30	0.02	35.55	3.98	0.68	0.10	6.45	28.33	0.25	2.80	0.86	4.75	0.95	0.05	17.36	91.50	99.10
19	feldspar	51.87	0.21	0.02	59.64	0.03	23.44	0.01	82.82	3.68	0.71	0.08	8.54	28.06	0.25	2.39	0.93	5.27	0.90	0.05	17.94	91.45	195.38
19	feldspar	51.45	0.21	0.00	212.45	0.03	21.47	0.01	60.61	3.55	0.72	0.12	6.02	28.15	0.25	2.58	0.89	5.19	0.91	0.04	22.13	91.12	325.66
19	feldspar	51.03	0.21	0.01	69.44	0.05	14.41	0.02	43.08	3.71	0.71	0.07	9.02	26.95	0.26	2.75	0.86	5.55	0.88	0.05	18.49	90.19	157.36
19	feldspar	48.91	0.22	0.03	30.68	0.04	17.27	0.00	100.00	3.76	0.70	0.10	7.04	27.71	0.26	3.11	0.81	6.82	0.79	0.10	10.29	90.57	168.06
19	feldspar	53.12	0.21	0.02	40.49	0.08	8.33	0.02	29.06	3.49	0.73	0.09	7.60	27.45	0.25	3.02	0.82	4.25	1.02	0.06	14.47	91.62	102.98
	average	**51.68**	0.21	**0.02**	62.43	**0.04**	17.25	**0.01**	62.05	**3.80**	0.70	**0.10**	7.10	**27.58**	0.26	**2.78**	0.86	**5.20**	0.92	**0.06**	17.76	**91.27**	169.53
	1 S.D.	**1.39**		**0.01**		**0.02**		**0.01**		**0.27**		**0.02**		**0.60**		**0.25**		**0.80**		**0.02**		**0.61**	
17	titanite	30.70	0.26	0.00	100.00	27.20	0.25	0.00	100.00	0.00	365.71	34.50	0.21	2.74	0.91	0.55	2.48	2.04	1.56	0.05	23.34	97.78	594.72
17	titanite	30.36	0.27	0.02	50.38	23.73	0.27	0.00	100.00	0.00	110.77	29.50	0.22	4.32	0.70	2.64	0.94	5.23	0.91	0.12	9.16	95.93	273.62
19	titanite	30.77	0.26	0.01	68.47	26.34	0.25	0.01	63.89	0.01	57.88	32.65	0.21	3.11	0.84	0.96	1.71	3.12	1.22	0.10	10.93	97.08	205.66
19	titanite	31.27	0.26	0.00	7903.50	27.34	0.25	0.00	100.00	0.05	10.77	34.77	0.21	2.33	0.99	0.40	3.10	1.99	1.59	0.03	30.85	98.19	8051.52
19	titanite	26.42	0.29	0.07	15.57	24.58	0.26	0.02	32.74	0.04	13.39	31.96	0.22	6.44	0.56	1.25	1.42	2.40	1.41	0.08	13.94	93.26	79.80
	average	**29.90**	0.27	**0.02**	1627.58	**25.84**	0.26	**0.01**	79.33	**0.02**	111.70	**32.68**	0.21	**3.79**	0.80	**1.16**	1.93	**2.96**	1.34	**0.08**	17.64	**96.45**	1841.06
	1 S.D.	**1.97**		**0.03**		**1.61**		**0.01**		**0.02**		**2.14**		**1.66**		**0.89**		**1.35**		**0.04**		**1.98**	

Thin-section	Mineral	SiO2 (wt %)	Si (1σ %)	Na2O (wt %)	Na (1σ %)	CaO (wt %)	Ca (1σ %)	SO3 (wt %)	S (1σ %)	K2O (wt %)	K (1σ %)	TiO2 (wt %)	Ti (1σ %)	Al2O3 (wt %)	Al (1σ %)	MgO (wt %)	Mg (1σ %)	FeO (wt %)	Fe (1σ %)	MnO (wt %)	Mn (1σ %)	Total (wt %)	Total (1σ %)
17	hematite	1.66	1.35	0.03	41.76	0.07	10.19	0.02	36.82	0.00	100.00	1.94	0.85	1.17	1.84	0.89	2.25	84.58	0.21	0.08	15.06	90.45	210.33
	average	**0.91**	4.43	**0.02**	70.88	**0.11**	7.96	**0.01**	68.41	**0.00**	100.00	**1.37**	1.14	**0.65**	6.65	**0.48**	11.40	**87.04**	0.21	**0.05**	26.40	**90.64**	297.46
	1 S.D.	**1.06**		**0.02**		**0.05**		**0.02**		**0.00**		**0.80**		**0.73**		**0.59**		**3.47**		**0.04**		**0.26**	

Thin-section	Mineral	SiO2 (wt %)	Si (1σ %)	Na2O (wt %)	Na (1σ %)	CaO (wt %)	Ca (1σ %)	SO3 (wt %)	S (1σ %)	K2O (wt %)	K (1σ %)	TiO2 (wt %)	Ti (1σ %)	Al2O3 (wt %)	Al (1σ %)	MgO (wt %)	Mg (1σ %)	FeO (wt %)	Fe (1σ %)	MnO (wt %)	Mn (1σ %)	Total (wt %)	Total (1σ %)
2	chlorite	29.10	0.35	0.02	68.13	0.13	6.81	0.00	100.00	0.00	100.00	0.03	42.25	14.64	0.48	15.21	0.48	27.78	0.46	0.55	4.33	87.46	323.29
2	chlorite	29.30	0.35	0.02	63.81	0.05	17.05	0.00	100.00	0.00	603.20	0.03	52.52	14.22	0.49	15.36	0.47	27.38	0.47	0.47	4.92	86.82	843.28
2	chlorite	27.96	0.36	0.04	34.38	0.16	5.99	0.00	100.00	0.00	100.00	0.02	79.44	14.73	0.48	14.03	0.50	29.22	0.45	0.45	5.02	86.61	326.62
2	chlorite	28.31	0.36	0.00	100.00	0.05	16.52	0.02	70.59	0.00	444.74	0.01	137.17	14.71	0.48	15.57	0.47	27.79	0.46	0.50	4.57	86.95	775.36
2	chlorite	29.69	0.35	0.03	44.33	0.06	13.79	0.00	100.00	0.00	100.00	0.01	170.24	14.14	0.49	15.49	0.47	27.43	0.47	0.55	4.36	87.39	434.50
3	chlorite	28.74	0.36	0.02	48.93	0.12	7.63	0.02	62.34	0.01	56.72	0.08	17.02	15.65	0.47	16.16	0.46	26.66	0.47	0.39	5.47	87.85	199.87
3	chlorite	30.14	0.35	0.01	97.28	0.11	8.34	0.02	67.91	0.00	103.52	0.07	19.36	15.19	0.47	16.75	0.45	25.99	0.48	0.38	5.68	88.67	303.84
5	chlorite	27.64	0.36	0.03	38.64	0.11	8.15	0.00	100.00	0.00	120.82	0.01	142.60	16.04	0.46	17.64	0.43	24.19	0.50	0.35	6.14	86.01	418.10
5	chlorite	27.48	0.37	0.04	32.83	0.14	6.93	0.02	66.74	0.00	100.00	0.01	87.97	16.09	0.46	17.66	0.43	24.21	0.50	0.34	6.07	85.98	302.30
5	chlorite	28.00	0.36	0.01	98.46	0.12	7.77	0.00	100.00	0.01	82.13	0.04	35.17	15.87	0.46	17.68	0.43	23.86	0.50	0.35	5.93	85.93	331.21
5	chlorite	31.31	0.34	0.05	25.86	0.12	7.64	0.00	100.00	0.00	198.25	0.00	323.95	10.34	0.58	19.21	0.42	24.48	0.49	0.32	6.40	85.84	663.93
5	chlorite	31.61	0.34	0.03	36.79	0.13	7.18	0.03	49.91	0.01	80.76	0.00	337.66	10.35	0.58	19.32	0.42	24.23	0.50	0.34	6.07	86.05	520.21
5	chlorite	31.39	0.34	0.03	34.29	0.20	4.88	0.02	55.27	0.00	111.21	0.01	192.90	10.92	0.56	19.55	0.41	22.55	0.51	0.34	6.12	85.02	406.49
5	chlorite	27.72	0.36	0.01	132.26	0.07	11.88	0.00	100.00	0.00	100.00	0.02	68.20	16.06	0.46	16.79	0.45	25.05	0.49	0.32	6.50	86.04	420.60
5	chlorite	31.96	0.34	0.06	20.81	0.24	4.32	0.01	101.44	0.04	13.50	0.00	2382.18	12.40	0.53	19.29	0.41	21.83	0.52	0.37	5.80	86.21	2529.85
5	chlorite	31.71	0.34	0.06	22.67	0.23	4.53	0.03	37.28	0.05	12.37	0.01	106.90	12.42	0.52	19.29	0.41	22.37	0.52	0.41	5.26	86.58	190.80
5	chlorite	31.76	0.34	0.04	31.03	0.23	4.61	0.03	47.81	0.05	11.36	0.01	153.93	12.51	0.52	18.77	0.42	22.34	0.52	0.43	5.16	86.16	255.70
6	chlorite	33.13	0.27	-	-	0.09	7.66	0.01	100.00	0.00	68.56	0.07	9.59	9.66	0.48	19.56	0.33	24.64	0.40	0.33	3.91	87.49	191.20
6	chlorite	31.44	0.28	-	-	0.11	6.61	0.00	100.00	0.00	100.00	0.07	10.04	10.90	0.45	19.77	0.32	24.21	0.41	0.37	3.66	86.86	221.77
6	chlorite	32.06	0.28	-	-	0.15	5.24	0.02	435.89	0.00	23.86	0.07	9.34	10.93	0.45	20.10	0.32	23.22	0.42	0.32	3.97	86.88	479.77
7	chlorite	32.34	0.34	0.09	15.40	0.28	4.02	0.04	30.09	0.05	11.77	0.00	277.37	12.16	0.53	19.94	0.41	21.76	0.53	0.31	6.61	86.98	347.07
7	chlorite	32.16	0.34	0.12	12.28	0.28	3.96	0.02	52.95	0.06	10.04	0.00	100.00	12.13	0.53	20.11	0.40	21.60	0.53	0.30	6.85	86.77	187.88
7	chlorite	32.34	0.34	0.06	21.71	0.27	4.14	0.02	81.23	0.04	13.03	0.00	100.00	11.89	0.54	20.18	0.40	21.66	0.53	0.32	6.41	86.78	228.33

Thin-section	Mineral	SiO2 (wt %)	Si (1σ %)	Na2O (wt %)	Na (1σ %)	CaO (wt %)	Ca (1σ %)	SO3 (wt %)	S (1σ %)	K2O (wt %)	K (1σ %)	TiO2 (wt %)	Ti (1σ %)	Al2O3 (wt %)	Al (1σ %)	MgO (wt %)	Mg (1σ %)	FeO (wt %)	Fe (1σ %)	MnO (wt %)	Mn (1σ %)	Total (wt %)	Total (1σ %)
7	chlorite	30.90	0.34	0.02	52.02	0.08	10.46	0.00	100.00	0.01	75.73	0.03	46.26	12.23	0.53	19.34	0.42	23.35	0.51	0.32	6.48	86.28	292.75
7	chlorite	30.85	0.34	0.01	99.85	0.06	12.99	0.00	637.79	0.00	171.75	0.04	38.71	12.01	0.54	19.76	0.41	23.54	0.50	0.31	6.62	86.58	969.50
7	chlorite	31.70	0.34	0.06	20.67	0.11	8.03	0.01	168.09	0.01	65.27	0.01	100.48	10.30	0.59	19.17	0.42	24.54	0.49	0.34	6.09	86.25	370.47
7	chlorite	31.32	0.34	0.01	160.95	0.06	14.66	0.00	100.00	0.01	83.68	0.14	10.14	11.52	0.55	19.45	0.41	23.65	0.50	0.36	5.80	86.52	377.03
7	chlorite	31.79	0.34	0.00	252.67	0.08	9.79	0.00	100.00	0.00	157.06	0.59	3.25	11.07	0.56	18.93	0.42	23.53	0.50	0.36	5.80	86.35	530.39
7	chlorite	29.50	0.35	0.04	32.87	0.06	14.65	0.00	100.00	0.03	18.27	0.03	49.76	14.08	0.49	17.68	0.44	25.17	0.49	0.39	5.50	86.97	222.82
7	chlorite	30.65	0.35	0.04	30.32	0.05	16.33	0.00	723.50	0.03	20.10	0.04	33.05	12.22	0.53	18.62	0.43	24.63	0.49	0.30	6.67	86.58	831.77
8	chlorite	31.79	0.28	-	-	0.04	17.46	0.00	52.91	0.03	100.00	0.06	11.66	10.10	0.47	20.09	0.32	24.91	0.40	0.28	4.53	87.29	188.03
8	chlorite	31.57	0.28	-	-	0.04	15.91	0.00	100.00	0.00	100.00	0.06	11.76	10.28	0.47	20.13	0.32	24.37	0.41	0.28	4.60	86.72	233.75
8	chlorite	31.16	0.28	-	-	0.07	9.72	0.01	52.22	0.03	73.20	0.07	10.35	10.79	0.45	20.40	0.32	24.06	0.41	0.29	4.32	86.87	151.27
8	chlorite	29.92	0.29	-	-	0.04	16.54	0.00	52.22	0.03	100.00	1.35	1.17	14.71	0.38	15.99	0.36	24.90	0.40	0.38	3.65	87.31	175.01
8	chlorite	30.53	0.28	-	-	0.04	18.20	0.00	39.12	0.04	127.43	0.75	1.66	14.18	0.39	17.75	0.34	24.10	0.41	0.34	3.93	87.72	191.76
8	chlorite	31.03	0.28	-	-	0.05	13.16	0.00	127.47	0.01	405.82	0.04	14.51	10.72	0.46	20.27	0.32	23.92	0.41	0.27	4.59	86.32	567.02
8	chlorite	30.95	0.28	0.00	187.88	0.03	18.89	0.01	68.37	0.00	2794.78	0.09	7.38	14.17	0.39	19.28	0.33	23.42	0.41	0.31	4.17	88.27	3082.88
8	chlorite	31.33	0.28	0.00	100.00	0.04	18.12	0.03	28.21	0.00	100.00	0.17	4.47	14.12	0.39	19.19	0.33	22.90	0.42	0.27	4.62	88.03	256.84
8	chlorite	32.48	0.27	0.01	80.08	0.03	19.32	0.03	27.90	0.00	351.33	0.06	10.43	10.89	0.45	20.40	0.32	23.53	0.41	0.30	4.19	87.74	494.70
8	chlorite	31.54	0.28	0.00	551.75	0.09	7.89	0.03	27.94	0.00	100.00	0.31	2.77	12.83	0.41	18.64	0.34	23.94	0.41	0.36	3.70	87.74	695.49
8	chlorite	30.08	0.28	0.00	184.69	0.03	22.59	0.02	37.29	0.00	100.00	1.57	1.02	14.60	0.39	16.22	0.36	25.37	0.40	0.39	3.46	88.29	350.48
8	chlorite	31.40	0.28	0.01	72.65	0.05	13.77	0.00	100.00	0.01	95.33	0.28	2.95	12.82	0.41	19.82	0.32	23.20	0.42	0.34	3.92	87.93	290.05
8	chlorite	31.96	0.28	0.00	250.91	0.12	6.29	0.01	72.57	0.00	100.00	0.19	3.99	11.93	0.43	19.70	0.33	23.35	0.41	0.36	3.75	87.63	438.96
8	chlorite	32.07	0.28	0.00	404.48	0.10	7.02	0.03	28.98	0.00	100.00	0.22	3.57	12.11	0.43	20.27	0.32	23.24	0.42	0.39	3.55	88.43	549.05
8	chlorite	30.66	0.28	0.00	100.00	0.04	14.90	0.00	100.00	0.01	54.56	0.63	1.74	12.87	0.41	19.62	0.33	23.48	0.41	0.31	4.21	87.62	276.84
8	chlorite	31.36	0.28	0.02	37.11	0.06	10.80	0.02	49.09	0.00	114.19	0.12	5.97	12.37	0.42	19.53	0.33	23.98	0.41	0.37	3.63	87.83	222.23
8	chlorite	31.48	0.28	0.00	1073.05	0.04	16.38	0.02	35.55	0.00	320.68	0.21	3.71	12.07	0.43	19.66	0.33	24.52	0.40	0.33	3.99	88.33	1454.80
10	chlorite	30.25	0.35	0.02	55.20	0.10	8.83	0.01	107.05	0.01	79.01	0.12	11.47	13.63	0.50	18.61	0.42	24.09	0.50	0.33	6.35	87.17	269.68
10	chlorite	30.34	0.35	0.04	28.00	0.12	7.73	0.02	72.00	0.02	21.26	0.16	9.58	13.99	0.49	18.65	0.42	23.70	0.50	0.35	6.13	87.39	146.46
10	chlorite	30.37	0.35	0.00	397.35	0.10	8.86	0.01	96.47	0.01	45.07	0.27	6.08	13.86	0.50	18.60	0.42	24.28	0.50	0.35	5.81	87.85	561.41
10	chlorite	30.82	0.34	0.02	65.42	0.09	9.50	0.01	110.72	0.02	27.47	0.25	6.61	12.48	0.53	18.98	0.42	24.19	0.50	0.31	6.55	87.16	228.06
10	chlorite	30.64	0.35	0.03	43.54	0.11	7.91	0.01	234.67	0.01	39.84	0.11	12.35	12.97	0.52	18.81	0.42	24.30	0.50	0.32	6.57	87.31	346.67
10	chlorite	31.74	0.34	0.03	36.91	0.12	8.01	0.00	100.00	0.03	18.44	0.04	30.04	10.76	0.57	18.20	0.43	24.25	0.50	0.34	6.02	85.51	201.26
10	chlorite	30.25	0.35	0.03	49.36	0.13	6.90	0.00	100.00	0.02	25.03	0.11	12.52	12.02	0.54	18.18	0.43	26.07	0.48	0.39	5.50	87.20	201.11

Thin-section	Mineral	SiO2 (wt %)	Si (1σ %)	Na2O (wt %)	Na (1σ %)	CaO (wt %)	Ca (1σ %)	SO3 (wt %)	S (1σ %)	K2O (wt %)	K (1σ %)	TiO2 (wt %)	Ti (1σ %)	Al2O3 (wt %)	Al (1σ %)	MgO (wt %)	Mg (1σ %)	FeO (wt %)	Fe (1σ %)	MnO (wt %)	Mn (1σ %)	Total (wt %)	Total (1σ %)
10	chlorite	30.55	0.35	0.02	75.67	0.11	8.33	0.00	305.52	0.01	65.99	0.08	17.39	10.88	0.57	18.16	0.43	27.31	0.47	0.35	6.11	87.46	480.83
10	chlorite	30.45	0.35	0.01	120.79	0.18	5.54	0.03	46.26	0.03	21.12	0.31	5.35	13.51	0.50	18.39	0.43	24.31	0.50	0.32	6.31	87.53	207.15
11	chlorite	30.38	0.35	0.03	39.02	0.50	2.72	0.00	100.00	0.03	18.16	0.03	49.73	13.67	0.50	18.10	0.43	24.11	0.50	0.35	5.96	87.20	217.37
11	chlorite	30.02	0.35	0.01	143.48	0.30	3.80	0.01	87.59	0.03	18.56	0.04	31.50	13.65	0.50	18.07	0.43	24.13	0.50	0.33	6.33	86.59	293.04
11	chlorite	30.46	0.35	0.03	41.07	0.19	5.27	0.02	49.44	0.03	20.62	0.04	29.85	12.17	0.53	18.28	0.43	23.50	0.51	0.35	6.05	85.08	154.12
11	chlorite	31.17	0.34	0.03	40.19	0.23	4.66	0.01	93.29	0.04	14.71	0.04	30.69	12.07	0.54	18.58	0.42	23.06	0.51	0.31	6.73	85.54	192.08
11	chlorite	31.19	0.34	0.06	20.98	0.23	4.63	0.04	31.93	0.03	18.84	0.01	223.53	11.16	0.56	19.23	0.42	24.47	0.49	0.36	5.94	86.77	307.66
11	chlorite	29.68	0.35	0.02	58.12	0.26	4.25	0.03	42.88	0.03	16.03	0.14	10.19	12.60	0.52	18.31	0.43	23.81	0.50	0.37	5.61	85.25	138.88
11	chlorite	31.24	0.34	0.03	41.49	0.41	3.08	0.01	84.89	0.04	13.18	0.03	46.84	12.58	0.52	18.52	0.42	23.24	0.51	0.34	6.09	86.45	197.36
12	chlorite	30.77	0.34	0.04	38.33	0.11	8.13	0.01	100.21	0.02	25.35	0.08	17.77	10.74	0.57	17.98	0.43	25.73	0.48	0.35	5.98	85.83	197.59
12	chlorite	31.95	0.34	0.03	48.53	0.08	10.68	0.00	100.00	0.01	69.87	0.00	100.00	10.80	0.57	20.23	0.41	23.48	0.51	0.33	6.25	86.90	337.16
12	chlorite	32.03	0.34	0.03	47.07	0.08	10.01	0.00	100.00	0.02	33.66	0.00	100.00	10.79	0.57	20.12	0.41	23.39	0.51	0.31	6.56	86.76	299.13
12	chlorite	32.06	0.34	0.02	54.51	0.10	9.13	0.01	164.07	0.02	33.74	0.00	100.00	10.70	0.57	19.97	0.41	23.24	0.51	0.27	7.52	86.38	370.80
12	chlorite	30.34	0.35	0.04	31.74	0.10	8.50	0.01	151.32	0.03	20.54	0.23	6.83	13.02	0.51	18.42	0.43	24.45	0.49	0.32	6.39	86.96	227.10
12	chlorite	30.73	0.34	0.01	83.03	0.10	8.90	0.00	100.00	0.01	52.21	0.40	4.35	12.91	0.52	18.58	0.42	23.55	0.50	0.29	6.79	86.58	257.06
12	chlorite	30.55	0.35	0.00	100.00	0.10	8.75	0.01	95.34	0.02	21.17	0.27	5.96	13.21	0.51	18.70	0.42	23.92	0.50	0.29	7.03	87.08	240.03
12	chlorite	30.32	0.35	0.03	38.22	0.10	9.07	0.00	100.00	0.02	21.40	0.20	7.57	13.17	0.51	18.97	0.42	24.03	0.50	0.33	6.11	87.18	184.15
13	chlorite	31.14	0.34	0.04	32.47	0.29	3.87	0.02	52.10	0.02	30.20	0.20	7.67	10.69	0.57	18.72	0.42	24.07	0.50	0.38	5.39	85.58	133.53
13	chlorite	31.10	0.34	0.03	38.60	0.16	6.25	0.00	100.00	0.01	67.48	0.05	27.68	11.00	0.56	19.12	0.42	25.02	0.49	0.37	5.73	86.86	247.55
13	chlorite	31.60	0.34	0.04	36.63	0.20	5.15	0.02	64.91	0.01	44.00	0.00	778.17	10.85	0.57	18.22	0.43	24.85	0.49	0.39	5.48	86.17	936.17
13	chlorite	31.32	0.34	0.05	26.97	0.37	3.32	0.00	290.17	0.02	23.11	0.00	100.00	11.24	0.56	18.96	0.42	23.71	0.50	0.40	5.36	86.07	450.75
13	chlorite	31.01	0.34	0.03	47.73	0.06	13.74	0.00	100.00	0.00	139.41	0.63	3.10	12.62	0.52	18.52	0.43	25.00	0.49	0.32	6.37	88.19	312.13
13	chlorite	31.24	0.34	0.04	32.24	0.11	8.27	0.00	100.00	0.02	25.32	0.12	11.94	12.42	0.53	19.13	0.42	24.17	0.50	0.31	6.64	87.56	186.20
13	chlorite	32.30	0.34	0.05	28.47	0.14	6.63	0.04	35.28	0.01	84.61	0.16	9.31	12.07	0.54	18.82	0.42	24.02	0.50	0.33	6.15	87.93	172.25
14	chlorite	28.36	0.36	0.07	21.03	0.22	4.80	0.07	19.31	0.05	12.21	0.00	100.00	14.56	0.49	15.79	0.47	27.73	0.46	0.49	4.61	87.34	163.74
14	chlorite	30.80	0.34	0.07	19.47	0.24	4.30	0.04	30.94	0.06	9.66	0.01	201.48	14.15	0.49	15.73	0.47	26.32	0.48	0.55	4.25	87.97	271.88
14	chlorite	27.77	0.36	0.08	17.48	0.22	4.95	0.07	19.70	0.13	5.15	0.02	82.58	14.33	0.49	16.13	0.46	28.39	0.46	0.49	4.73	87.62	136.36
14	chlorite	28.49	0.36	0.14	11.78	0.17	5.89	0.01	150.23	0.01	47.63	0.00	100.00	14.06	0.49	15.28	0.48	28.39	0.46	0.49	4.76	87.04	322.08
14	chlorite	28.86	0.36	0.15	10.77	0.18	5.61	0.01	119.50	0.02	24.06	0.00	100.00	14.55	0.49	16.03	0.46	27.23	0.47	0.50	4.69	87.53	266.41
14	chlorite	28.58	0.36	0.16	10.18	0.11	8.12	0.02	61.20	0.02	22.55	0.00	100.00	14.35	0.49	15.32	0.48	28.51	0.46	0.48	4.79	87.55	208.63
14	chlorite	28.70	0.36	0.02	57.74	0.03	26.01	0.01	118.47	0.00	152.63	0.00	100.00	14.45	0.49	15.54	0.47	27.83	0.46	0.48	4.84	87.06	461.47

Thin-section	Mineral	SiO2 (wt %)	Si (1σ %)	Na2O (wt %)	Na (1σ %)	CaO (wt %)	Ca (1σ %)	SO3 (wt %)	S (1σ %)	K2O (wt %)	K (1σ %)	TiO2 (wt %)	Ti (1σ %)	Al2O3 (wt %)	Al (1σ %)	MgO (wt %)	Mg (1σ %)	FeO (wt %)	Fe (1σ %)	MnO (wt %)	Mn (1σ %)	Total (wt %)	Total (1σ %)
14	chlorite	27.34	0.37	0.01	99.61	0.12	8.08	0.00	2291.22	0.02	30.26	0.00	100.00	14.50	0.49	15.13	0.48	29.84	0.45	0.43	5.14	87.39	2536.10
14	chlorite	27.67	0.36	0.01	125.58	0.17	5.71	0.03	44.92	0.02	30.67	0.00	100.00	14.77	0.48	14.85	0.48	28.79	0.45	0.46	4.78	86.77	313.43
15	chlorite	28.52	0.29	0.05	20.15	0.10	7.30	0.02	46.90	0.01	44.01	0.05	13.55	14.82	0.38	15.28	0.38	28.20	0.38	0.46	3.10	87.51	136.44
15	chlorite	27.97	0.30	0.00	5411.54	0.06	10.63	0.01	67.76	0.00	100.00	0.04	17.88	15.85	0.37	18.22	0.34	25.95	0.39	0.35	3.73	88.45	5612.94
15	chlorite	27.73	0.30	0.05	21.66	0.11	6.54	0.04	23.01	0.01	101.18	0.06	11.41	15.98	0.37	18.91	0.33	25.29	0.40	0.34	3.93	88.50	169.13
15	chlorite	28.71	0.29	0.03	35.82	0.08	9.11	0.03	25.93	0.00	319.91	0.06	10.56	15.77	0.37	18.26	0.34	24.43	0.40	0.35	3.84	87.71	406.57
16	chlorite	28.34	0.36	0.12	12.68	0.11	8.32	0.00	100.00	0.00	100.00	0.00	359.89	14.35	0.49	15.95	0.46	27.27	0.47	0.48	4.74	86.62	587.41
16	chlorite	28.47	0.36	0.01	102.35	0.29	3.88	0.00	100.00	0.00	100.00	0.00	100.00	14.32	0.49	16.28	0.46	27.25	0.47	0.55	4.39	87.17	412.40
16	chlorite	27.56	0.37	0.01	77.88	0.28	4.06	0.00	100.00	0.00	100.00	0.00	100.00	14.74	0.48	16.31	0.46	27.67	0.46	0.53	4.47	87.10	388.18
16	chlorite	27.56	0.37	0.02	54.57	0.20	4.98	0.01	156.16	0.00	107.77	0.00	100.00	14.60	0.49	16.76	0.45	27.43	0.47	0.54	4.37	87.12	429.63
16	chlorite	28.38	0.36	0.02	61.16	0.16	6.16	0.00	100.00	0.00	100.00	0.01	203.64	14.07	0.49	15.40	0.47	27.94	0.46	0.53	4.38	86.50	477.12
16	chlorite	34.51	0.32	0.01	131.06	0.21	4.95	0.00	1161.12	0.00	100.00	0.01	95.78	11.56	0.55	18.45	0.42	22.80	0.51	0.36	5.84	87.91	1500.55
16	chlorite	35.01	0.32	0.02	72.92	0.27	4.05	0.00	321.50	0.01	52.87	0.00	100.00	12.08	0.53	17.88	0.43	22.82	0.51	0.34	6.15	88.43	559.28
	average Hotazel	**30.45**	0.33	**0.03**	144.60	**0.14**	8.90	**0.01**	136.45	**0.02**	111.46	**0.12**	93.41	**12.89**	0.49	**18.19**	0.41	**24.80**	0.47	**0.37**	5.32	**87.01**	488.70
	1 S.D.	**1.60**		**0.03**		**0.09**		**0.01**		**0.02**		**0.24**		**1.69**		**1.61**		**1.87**		**0.07**		**0.80**	
17	chlorite	26.24	0.31	0.00	100.00	0.01	116.26	0.01	87.67	0.00	100.00	0.10	6.74	18.72	0.34	13.70	0.40	28.92	0.37	0.50	2.89	88.20	414.98
17	chlorite	25.59	0.31	0.00	500.28	0.02	24.91	0.00	150.92	0.00	100.00	0.68	1.65	18.28	0.34	13.60	0.40	29.63	0.37	0.51	2.89	88.32	782.07
17	chlorite	26.67	0.30	0.01	81.09	0.11	6.63	0.04	20.62	0.00	100.00	0.18	4.22	18.01	0.35	16.48	0.36	25.79	0.39	0.46	3.11	87.75	217.07
17	chlorite	24.94	0.32	0.01	90.00	0.52	2.17	0.01	56.96	0.00	100.00	0.08	7.75	17.15	0.36	14.88	0.38	25.39	0.40	0.47	3.06	83.45	261.40
17	chlorite	26.07	0.31	0.00	100.00	0.06	10.90	0.00	854.39	0.00	100.00	0.06	9.94	18.62	0.34	13.56	0.40	28.97	0.37	0.54	2.79	87.89	1079.44
17	chlorite	26.55	0.30	0.02	47.59	0.25	3.53	0.02	34.99	0.00	100.00	0.14	5.14	16.77	0.36	15.63	0.37	27.37	0.38	0.53	2.80	87.28	195.46
17	chlorite	26.00	0.31	0.00	100.00	0.02	26.46	0.03	29.97	0.00	100.00	0.06	11.05	18.60	0.34	15.31	0.37	27.53	0.38	0.52	2.87	88.06	271.75
17	chlorite	27.02	0.30	0.00	361.42	0.02	36.18	0.00	100.00	0.00	100.00	0.05	11.92	17.94	0.35	15.66	0.37	26.89	0.38	0.51	2.84	88.09	613.76
19	chlorite	25.80	0.31	0.00	100.00	0.02	31.75	0.00	150.92	0.00	115.58	0.05	12.96	19.19	0.33	13.73	0.40	28.25	0.37	0.72	2.28	87.76	414.90
19	chlorite	25.36	0.31	0.00	689.65	0.02	39.60	0.01	56.96	0.00	100.00	0.08	7.91	19.45	0.33	13.59	0.40	28.57	0.37	0.68	2.37	87.76	897.90
19	chlorite	26.16	0.31	0.01	98.62	0.02	32.73	0.02	32.32	0.00	100.00	0.04	16.04	18.35	0.34	13.74	0.40	27.58	0.38	0.65	2.46	86.57	283.60
19	chlorite	25.68	0.31	0.00	100.00	0.05	13.55	0.00	430.11	0.00	104.24	0.12	5.70	19.67	0.33	13.06	0.41	28.91	0.37	0.70	2.33	88.20	657.35
19	chlorite	26.35	0.30	0.01	104.08	0.85	1.58	0.03	25.24	0.00	156.57	0.27	3.04	18.10	0.34	12.82	0.41	27.41	0.38	0.72	2.28	86.56	294.22
19	chlorite	25.86	0.31	0.00	7479.7	0.42	2.46	0.01	66.62	0.05	12.62	0.08	7.96	19.49	0.33	12.96	0.41	28.14	0.38	0.74	2.24	87.76	7573.0

Thin-section	Mineral	SiO2 (wt %)	Si (1σ %)	Na2O (wt %)	2 Na (1σ %)	CaO (wt %)	Ca (1σ %)	SO3 (wt %)	S (1σ %)	K2O (wt %)	K (1σ %)	TiO2 (wt %)	Ti (1σ %)	Al2O3 (wt %)	Al (1σ %)	MgO (wt %)	Mg (1σ %)	FeO (wt %)	Fe (1σ %)	MnO (wt %)	Mn (1σ %)	Total (wt %)	5 Total (1σ %)
19	chlorite	26.12	0.31	0.01	95.36	0.05	13.43	0.00	100.00	0.00	100.00	0.06	9.91	19.00	0.34	13.98	0.39	27.48	0.38	0.68	2.35	87.39	322.47
19	chlorite	25.46	0.31	0.00	220.29	0.03	19.91	0.05	17.81	0.00	100.00	0.06	10.50	19.85	0.33	14.11	0.39	27.89	0.38	0.66	2.41	88.11	372.33
19	chlorite	25.80	0.31	0.00	100.00	0.02	26.97	0.00	984.89	0.00	100.00	0.07	8.83	19.11	0.34	13.53	0.40	28.73	0.37	0.70	2.35	87.96	1224.46
19	chlorite	25.92	0.31	0.00	100.00	2.61	0.84	0.02	45.43	0.01	73.69	0.05	11.97	17.00	0.36	13.27	0.40	26.18	0.39	0.86	2.04	85.91	235.43
19	chlorite	24.27	0.32	0.00	284.15	1.90	1.00	0.01	84.85	0.00	100.00	0.06	10.84	19.46	0.33	13.21	0.40	27.16	0.38	0.69	2.32	86.76	484.59
	average Ongeluk	**25.89**	0.31	**0.00**	565.91	**0.37**	21.62	**0.01**	175.30	**0.00**	98.04	**0.12**	8.64	**18.57**	0.34	**14.04**	0.39	**27.73**	0.38	**0.62**	2.56	**87.36**	873.49
	1 S.D.	**0.62**		**0.01**		**0.71**		**0.01**		**0.01**		**0.15**		**0.91**		**1.04**		**1.13**		**0.11**		**1.16**	

2.2 Hematite-chert

Thin-section	SiO2 (wt %)	Si (1σ %)	Na2O (wt %)	Na (1σ %)	CaO (wt %)	Ca (1σ %)	SO3 (wt %)	S (1σ %)	K2O (wt %)	K (1σ %)	TiO2 (wt %)	Ti (1σ %)	Al2O3 (wt %)	Al (1σ %)	MgO (wt %)	Mg (1σ %)	FeO (wt %)	Fe (1σ %)	MnO (wt %)	Mn (1σ %)	Total (wt %)	Total (1σ %)
2	89.60	0.18	0.03	37.96	0.06	13.31	0.00	100.00	0.01	79.89	0.00	100.00	0.35	4.27	1.63	1.46	5.70	1.07	0.19	9.34	97.57	347.48
2	87.99	0.19	0.00	100.00	0.04	21.27	0.00	845.48	0.01	59.17	0.00	100.00	0.18	7.34	4.77	0.81	4.72	1.18	0.05	32.27	97.75	1167.71
2	94.86	0.18	0.00	100.00	0.02	36.42	0.00	100.00	0.00	255.00	0.00	100.00	0.18	7.25	0.15	7.52	3.07	1.49	0.09	17.95	98.37	625.81
2	93.46	0.18	0.00	232.89	0.03	22.92	0.00	646.07	0.01	37.48	0.01	106.78	0.17	7.39	0.20	5.81	3.85	1.32	0.15	11.34	97.90	1072.18
2	97.22	0.18	0.02	50.27	0.03	23.88	0.01	102.55	0.02	29.80	0.00	100.00	0.13	9.55	0.06	15.64	1.54	2.22	0.03	47.41	99.06	381.50
2	92.73	0.18	0.02	42.11	0.05	16.18	0.01	133.75	0.01	56.49	0.00	3106.59	0.16	8.41	0.10	10.52	5.71	1.06	0.06	27.32	98.84	3402.61
2	91.65	0.18	0.00	100.00	0.10	8.66	0.01	145.33	0.01	61.64	0.01	93.35	0.20	6.80	0.28	4.51	5.86	1.05	0.15	11.64	98.28	433.16
2	81.90	0.20	0.03	37.00	0.04	18.46	0.01	156.62	0.00	100.00	0.00	100.00	0.48	3.41	6.56	0.69	7.81	0.90	0.05	30.42	96.88	447.70
2	92.76	0.18	0.02	60.99	0.04	17.67	0.01	86.84	0.00	209.16	0.00	691.01	0.17	7.71	1.95	1.30	3.97	1.29	0.10	16.75	99.02	1092.90
2	90.86	0.18	0.02	56.26	0.09	9.69	0.00	100.00	0.02	33.42	0.01	204.92	0.19	7.06	0.40	3.66	6.69	0.98	0.22	8.48	98.49	424.65
2	89.27	0.18	0.01	101.27	0.07	12.10	0.00	100.00	0.00	118.09	0.01	231.54	0.17	7.64	0.34	4.06	7.86	0.90	0.24	8.01	97.97	583.79
2	83.21	0.19	0.03	40.63	0.10	8.60	0.01	175.16	0.01	48.16	0.02	73.92	0.13	10.31	0.23	5.44	13.68	0.67	0.12	14.58	97.53	377.66
2	92.37	0.18	0.03	37.56	0.12	7.48	0.00	267.92	0.01	77.02	0.00	100.00	0.16	7.69	0.18	6.34	3.93	1.30	0.09	17.68	96.89	523.17
2	96.04	0.18	0.04	28.09	0.05	14.82	0.01	109.14	0.01	63.78	0.00	100.00	0.17	7.70	0.13	8.50	2.68	1.61	0.09	16.71	99.22	350.53
2	70.10	0.21	0.03	36.77	0.04	21.49	0.00	399.15	0.01	61.95	0.01	111.77	0.31	5.03	11.15	0.53	13.09	0.69	0.11	14.68	94.85	652.27
2	92.68	0.18	0.01	82.92	0.05	15.07	0.00	2412.45	0.00	100.00	0.00	622.85	0.12	10.43	1.20	1.74	4.17	1.25	0.11	15.56	98.35	3262.45
2	87.81	0.19	0.01	133.13	0.09	10.05	0.00	100.00	0.02	21.13	0.05	25.95	0.32	4.52	0.42	3.47	8.49	0.86	0.22	8.81	97.43	308.11
2	91.50	0.18	0.01	88.63	0.08	10.19	0.01	118.89	0.01	45.94	0.01	91.96	0.14	9.08	0.31	4.25	5.88	1.05	0.15	12.60	98.11	382.77
2	83.19	0.19	0.08	17.23	0.13	7.31	0.07	20.56	0.02	31.87	0.02	75.71	0.13	9.70	0.22	5.76	12.42	0.71	0.10	16.18	96.37	185.22
2	65.58	0.22	0.53	4.54	0.53	2.60	0.54	4.24	0.02	30.41	0.02	66.04	0.15	8.48	0.36	3.93	15.74	0.62	0.08	19.39	83.56	140.47
2	92.19	0.18	0.01	71.72	0.13	7.18	0.00	100.00	0.00	236.03	0.00	100.00	0.16	7.71	0.27	4.68	5.27	1.11	0.20	9.03	98.24	537.64
2	76.13	0.20	0.06	20.93	0.06	14.39	0.01	173.29	0.01	86.47	0.01	120.75	1.09	1.97	3.11	1.06	19.27	0.56	0.05	37.42	99.79	457.04
2	92.67	0.18	0.01	73.56	0.04	18.87	0.00	100.00	0.00	121.32	0.00	100.00	0.18	7.00	1.10	1.82	4.82	1.16	0.14	12.53	98.97	436.44
2	89.28	0.18	0.01	180.31	0.08	11.18	0.02	59.36	0.01	93.78	0.03	51.06	0.17	7.59	0.39	3.67	8.03	0.89	0.22	8.60	98.23	416.62
2	92.29	0.18	0.02	54.92	0.09	9.48	0.01	149.02	0.01	95.57	0.02	74.49	0.12	11.04	0.22	5.66	5.88	1.05	0.14	12.95	98.78	414.36
2	91.05	0.18	0.03	38.71	0.16	6.00	0.00	100.00	0.01	35.96	0.02	79.24	0.10	12.71	0.17	7.05	7.56	0.92	0.11	15.67	99.21	296.44
2	89.37	0.18	0.02	48.17	0.07	12.24	0.01	225.93	0.02	22.36	0.02	67.25	0.11	12.13	0.12	9.81	9.31	0.82	0.11	14.15	99.15	413.04
2	85.17	0.19	0.02	42.08	0.09	9.82	0.01	133.01	0.01	90.85	0.05	26.70	0.14	8.90	0.27	4.89	11.25	0.74	0.20	8.88	97.21	326.06
2	77.65	0.20	0.03	44.66	1.75	1.31	0.00	100.00	0.00	474.44	0.00	100.00	0.24	6.02	7.75	0.63	8.14	0.88	0.06	24.46	95.62	752.60
2	88.97	0.18	0.01	86.04	0.07	11.61	0.00	255.65	0.01	39.47	0.01	226.29	0.17	8.03	0.55	2.94	8.15	0.88	0.16	11.51	98.10	642.60
2	89.89	0.18	0.01	124.87	0.09	9.83	0.01	221.79	0.01	36.54	0.03	50.25	0.16	8.55	0.49	3.09	7.26	0.94	0.27	7.33	98.20	463.37

Thin-section	SiO2 (wt %)	Si (1σ %)	Na2O (wt %)	Na (1σ %)	CaO (wt %)	Ca (1σ %)	SO3 (wt %)	S (1σ %)	K2O (wt %)	K (1σ %)	TiO2 (wt %)	Ti (1σ %)	Al2O3 (wt %)	Al (1σ %)	MgO (wt %)	Mg (1σ %)	FeO (wt %)	Fe (1σ %)	MnO (wt %)	Mn (1σ %)	Total (wt %)	Total (1σ %)
2	91.01	0.18	0.01	82.69	0.09	9.60	0.00	100.00	0.01	51.47	0.00	100.00	0.15	8.76	0.28	4.52	6.50	1.00	0.16	10.68	98.21	368.90
2	93.08	0.18	0.01	69.52	0.07	12.25	0.01	205.48	0.02	21.39	0.00	100.00	0.17	7.74	0.31	4.23	5.44	1.09	0.22	8.44	99.33	430.32
2	91.70	0.18	0.00	265.92	0.07	11.81	0.09	15.52	0.01	38.30	0.00	100.00	0.15	8.56	0.17	7.15	6.40	1.00	0.12	14.40	98.71	462.84
2	82.54	0.19	0.00	241.69	0.09	9.80	0.00	613.51	0.00	100.00	0.00	269.57	0.16	8.17	0.36	3.95	14.92	0.64	0.25	7.87	98.34	1255.39
2	89.21	0.19	0.02	52.35	0.10	8.67	0.02	75.94	0.01	79.46	0.00	100.00	0.29	4.90	2.60	1.12	6.17	1.02	0.16	11.14	98.57	334.79
2	90.57	0.18	0.01	103.13	0.08	9.96	0.01	170.11	0.01	99.04	0.03	47.27	0.19	7.06	0.52	3.05	6.90	0.96	0.19	10.12	98.50	450.88
2	89.15	0.18	0.01	93.14	0.07	11.57	0.00	100.00	0.01	43.46	0.04	30.77	0.17	7.73	0.37	3.82	9.16	0.83	0.18	9.73	99.18	301.23
2	87.42	0.19	0.01	120.58	0.11	8.25	0.00	100.00	0.01	44.26	0.03	45.80	0.11	11.20	0.28	4.78	10.49	0.77	0.15	11.69	98.60	347.52
2	92.68	0.18	0.01	183.66	0.11	8.48	0.02	66.53	0.02	28.33	0.00	100.00	0.17	7.76	0.32	4.10	5.73	1.06	0.22	8.62	99.27	408.72
2	88.89	0.19	0.00	227.80	0.06	13.29	0.00	100.00	0.01	59.82	0.00	309.83	0.11	11.71	0.16	7.35	9.82	0.80	0.10	16.19	99.16	746.98
2	86.63	0.19	0.02	54.37	0.09	9.74	0.00	249.89	0.01	59.72	0.00	896.75	0.12	10.75	0.31	4.41	10.87	0.76	0.22	8.54	98.27	1295.12
2	91.68	0.18	0.02	66.22	0.06	13.30	0.00	282.81	0.01	48.71	0.00	100.00	0.19	6.86	0.52	3.00	6.00	1.03	0.24	8.06	98.72	530.17
2	90.42	0.18	0.00	100.00	0.07	11.64	0.00	100.00	0.01	60.66	0.04	30.52	0.17	7.78	0.36	3.98	7.00	0.95	0.18	10.46	98.25	326.17
2	91.04	0.18	0.01	180.11	0.11	8.13	0.00	100.00	0.01	51.80	0.02	74.50	0.20	6.82	0.42	3.45	6.23	1.02	0.24	7.99	98.27	434.00
2	83.61	0.19	0.00	100.00	0.15	6.44	0.02	73.15	0.02	26.72	0.00	100.00	0.16	8.62	0.19	6.68	14.41	0.65	0.13	13.34	98.68	335.79
2	92.80	0.18	0.02	52.67	0.06	13.05	0.01	121.49	0.02	22.08	0.00	1247.92	0.14	9.42	0.27	4.76	5.05	1.14	0.15	12.02	98.52	1484.73
2	93.34	0.18	0.02	45.12	0.08	11.15	0.01	132.28	0.00	146.99	0.00	100.00	0.12	10.33	0.26	4.75	4.82	1.17	0.17	10.33	98.83	462.30
2	93.04	0.18	0.02	50.91	0.09	9.46	0.00	100.00	0.02	29.14	0.00	100.00	0.16	8.12	0.35	3.94	5.13	1.13	0.13	13.76	98.94	316.64
2	90.83	0.18	0.02	48.71	0.05	14.14	0.00	100.00	0.00	143.74	0.00	100.00	0.32	4.49	1.76	1.39	5.67	1.06	0.15	11.02	98.81	424.73
2	89.49	0.19	0.04	30.06	0.03	21.78	0.01	130.95	0.01	47.97	0.00	100.00	0.16	8.07	4.55	0.83	4.51	1.21	0.05	33.08	98.85	374.14
2	95.71	0.18	0.02	39.36	0.02	30.55	0.00	100.00	0.01	79.74	0.00	100.00	0.16	8.16	0.17	6.93	3.29	1.43	0.10	16.79	99.48	383.14
2	95.16	0.18	0.00	461.63	0.05	17.17	0.01	95.13	0.00	109.96	0.00	100.00	0.17	7.71	0.19	6.14	3.95	1.30	0.14	12.48	99.68	811.70
2	97.85	0.17	0.01	72.58	0.03	23.70	0.00	100.00	0.01	48.52	0.00	100.00	0.11	11.18	0.06	15.47	1.98	1.92	0.05	31.85	100.11	405.39
2	94.15	0.18	0.00	225.32	0.06	13.35	0.00	100.00	0.01	46.56	0.01	129.00	0.17	7.66	0.09	12.37	5.47	1.09	0.05	29.91	100.01	565.44
2	94.30	0.18	0.02	61.84	0.08	10.69	0.02	69.99	0.01	33.94	0.00	100.00	0.18	7.17	0.20	5.87	4.84	1.16	0.16	11.06	99.81	301.90
2	79.81	0.20	0.03	37.85	0.03	29.69	0.01	217.40	0.01	63.84	0.00	382.46	0.48	3.46	7.98	0.62	8.96	0.84	0.08	20.46	97.38	756.82
2	94.24	0.18	0.01	62.94	0.05	15.94	0.00	100.00	0.01	82.24	0.00	100.00	0.13	9.55	1.06	1.87	3.68	1.35	0.09	19.02	99.27	393.09
2	91.01	0.18	0.01	120.52	0.08	10.32	0.00	100.00	0.02	28.64	0.03	48.53	0.17	7.90	0.38	3.66	6.68	0.98	0.18	10.08	98.55	330.81
2	89.31	0.18	0.00	100.00	0.07	11.78	0.02	61.30	0.01	89.68	0.01	117.26	0.14	9.50	0.33	4.24	8.44	0.87	0.22	8.36	98.55	403.17
2	83.43	0.19	0.02	67.09	0.12	7.65	0.02	55.04	0.01	72.76	0.02	63.59	0.15	8.77	0.24	5.31	13.61	0.67	0.11	15.39	97.73	296.46
2	89.65	0.18	0.05	20.70	0.11	8.30	0.02	54.75	0.01	41.35	0.01	106.46	0.18	7.23	0.21	5.74	6.03	1.03	0.14	12.31	96.42	258.05

Thin-section	SiO2 (wt %)	Si (1σ %)	Na2O (wt %)	Na (1σ %)	CaO (wt %)	Ca (1σ %)	SO3 (wt %)	S (1σ %)	K2O (wt %)	K (1σ %)	TiO2 (wt %)	Ti (1σ %)	Al2O3 (wt %)	Al (1σ %)	MgO (wt %)	Mg (1σ %)	FeO (wt %)	Fe (1σ %)	MnO (wt %)	Mn (1σ %)	Total (wt %)	Total (1σ %)
2	95.02	0.18	0.01	107.69	0.08	10.42	0.00	100.00	0.00	141.17	0.00	347.75	0.14	8.88	0.15	7.59	4.40	1.23	0.13	12.62	99.94	737.53
2	72.70	0.21	0.04	28.98	0.04	18.86	0.00	100.00	0.00	100.00	0.00	485.26	0.32	4.77	10.35	0.55	12.34	0.71	0.17	10.11	95.96	749.45
2	93.58	0.18	0.01	118.88	0.04	19.56	0.01	134.48	0.01	65.36	0.00	529.00	0.12	10.93	1.41	1.57	3.88	1.30	0.09	17.35	99.15	898.61
2	89.35	0.18	0.01	136.26	0.10	9.19	0.00	1428.34	0.02	26.01	0.02	63.57	0.32	4.59	0.46	3.26	8.21	0.88	0.22	8.51	98.71	1680.79
2	93.15	0.18	0.02	56.77	0.09	9.13	0.00	100.00	0.01	33.85	0.00	595.06	0.15	8.65	0.28	4.59	5.57	1.08	0.20	9.09	99.47	818.40
2	86.55	0.19	0.02	58.82	0.09	9.62	0.02	59.23	0.01	65.38	0.05	24.56	0.10	13.04	0.19	6.44	12.44	0.71	0.11	15.69	99.57	253.68
2	73.05	0.21	0.46	4.80	0.46	2.90	0.42	5.10	0.02	28.33	0.03	39.74	0.15	8.70	0.27	4.79	13.80	0.67	0.06	27.13	88.72	122.37
2	89.95	0.18	0.02	42.97	0.11	8.23	0.00	100.00	0.00	112.25	0.01	188.26	0.16	8.02	0.33	4.10	8.11	0.88	0.19	9.97	98.89	474.86
2	76.21	0.20	0.08	16.26	0.06	12.73	0.00	100.00	0.01	95.51	0.00	366.98	1.12	1.94	3.02	1.08	19.10	0.56	0.07	25.11	99.67	620.37
2	92.73	0.18	0.02	50.99	0.04	17.62	0.00	100.00	0.01	37.34	0.01	178.90	0.13	10.10	1.09	1.84	4.75	1.18	0.11	14.89	98.90	413.04
2	89.79	0.18	0.00	405.19	0.09	9.94	0.01	221.29	0.01	68.41	0.01	93.48	0.17	7.80	0.39	3.65	8.09	0.88	0.21	8.95	98.76	819.77
2	92.98	0.18	0.03	40.69	0.08	10.56	0.00	100.00	0.01	46.69	0.02	68.93	0.13	9.64	0.23	5.45	5.91	1.05	0.14	12.79	99.52	295.98
2	91.09	0.18	0.02	48.21	0.18	5.61	0.00	100.00	0.02	30.36	0.02	55.16	0.11	11.91	0.15	7.51	7.62	0.91	0.11	15.36	99.32	275.21
2	89.91	0.18	0.01	85.49	0.09	9.59	0.00	100.00	0.01	45.90	0.01	93.45	0.12	10.22	0.13	8.50	9.18	0.83	0.08	21.34	99.55	375.50
2	86.75	0.19	0.01	100.74	0.09	9.65	0.00	3629.70	0.01	34.28	0.01	100.74	0.14	9.26	0.27	4.89	11.60	0.73	0.15	12.33	99.04	3902.51
2	78.83	0.20	0.01	88.47	1.73	1.32	0.00	8983.15	0.01	74.67	0.00	100.00	0.26	5.49	7.63	0.64	8.01	0.89	0.11	14.03	96.59	9268.86
2	90.13	0.18	0.01	135.21	0.07	11.98	0.00	286.45	0.01	42.71	0.02	67.62	0.19	7.03	0.64	2.58	7.78	0.90	0.19	9.81	99.04	564.47
2	91.04	0.18	0.02	59.93	0.09	9.01	0.04	31.54	0.01	53.18	0.03	44.61	0.16	8.08	0.48	3.18	7.08	0.95	0.24	8.00	99.18	218.66
2	92.15	0.18	0.01	100.02	0.10	8.54	0.00	100.00	0.01	54.41	0.02	70.50	0.13	9.78	0.27	4.67	6.55	0.99	0.16	11.20	99.40	360.29
2	93.82	0.18	0.00	100.00	0.08	10.10	0.00	413.99	0.01	50.69	0.01	142.83	0.16	8.19	0.29	4.48	5.21	1.12	0.17	10.62	99.76	742.20
2	92.54	0.18	0.01	138.24	0.10	8.95	0.06	22.04	0.01	41.78	0.02	74.90	0.12	10.47	0.16	7.14	6.35	1.01	0.11	16.25	99.47	320.96
2	83.00	0.19	0.00	100.00	0.08	10.42	0.00	100.00	0.01	86.60	0.02	68.09	0.11	11.91	0.36	4.04	14.90	0.64	0.23	8.71	98.71	390.60
2	89.35	0.18	0.00	302.89	0.08	10.78	0.02	77.40	0.01	87.36	0.00	262.25	0.28	5.11	2.69	1.10	6.22	1.01	0.14	12.17	98.79	760.25
2	90.94	0.18	0.03	33.84	0.05	17.29	0.01	162.65	0.01	64.36	0.03	51.16	0.21	6.39	0.56	2.81	6.96	0.96	0.20	9.55	98.99	349.19
2	89.51	0.18	0.02	65.13	0.08	11.32	0.03	41.73	0.01	39.53	0.05	26.76	0.19	6.94	0.40	3.68	9.19	0.83	0.19	9.99	99.66	206.09
2	87.61	0.19	0.01	137.41	0.09	10.10	0.00	100.00	0.02	28.47	0.01	132.66	0.12	10.65	0.30	4.56	10.53	0.77	0.18	9.80	98.86	434.61
2	92.80	0.18	0.00	239.39	0.12	7.33	0.00	100.00	0.02	30.40	0.00	379.98	0.18	7.31	0.32	4.17	5.47	1.09	0.19	9.39	99.11	779.24
2	89.23	0.18	0.00	1345.83	0.07	12.38	0.00	100.00	0.02	31.44	0.00	1158.39	0.11	12.06	0.16	7.38	9.98	0.79	0.13	13.34	99.69	2681.79
2	87.25	0.19	0.01	72.18	0.09	9.55	0.00	100.00	0.01	81.30	0.00	345.03	0.11	11.57	0.31	4.46	10.85	0.76	0.21	9.06	98.85	634.10
2	92.06	0.18	0.00	100.00	0.06	14.37	0.01	96.40	0.00	542.61	0.03	43.17	0.15	8.54	0.53	2.95	5.97	1.04	0.24	7.81	99.05	817.07
2	91.61	0.18	0.01	141.48	0.07	12.47	0.00	100.00	0.01	55.71	0.02	82.60	0.15	8.69	0.38	3.63	7.10	0.95	0.19	9.46	99.54	415.17
2	91.97	0.18	0.00	100.00	0.09	9.49	0.00	100.00	0.01	41.87	0.01	187.17	0.19	6.82	0.45	3.26	6.26	1.02	0.25	7.70	99.23	457.51

Thin-section	SiO2 (wt %)	Si (1σ %)	Na2O (wt %)	Na (1σ %)	CaO (wt %)	Ca (1σ %)	SO3 (wt %)	S (1σ %)	K2O (wt %)	K (1σ %)	TiO2 (wt %)	Ti (1σ %)	Al2O3 (wt %)	Al (1σ %)	MgO (wt %)	Mg (1σ %)	FeO (wt %)	Fe (1σ %)	MnO (wt %)	Mn (1σ %)	Total (wt %)	Total (1σ %)
2	84.12	0.19	0.01	93.65	0.14	6.70	0.01	96.86	0.00	710.76	0.04	33.97	0.15	8.94	0.19	6.71	14.68	0.65	0.11	14.52	99.46	972.95
2	93.84	0.18	0.00	967.39	0.08	10.79	0.00	100.00	0.02	26.09	0.00	100.00	0.16	7.82	0.27	4.60	5.01	1.14	0.17	10.39	99.55	1228.40
2	93.91	0.18	0.01	109.49	0.10	8.72	0.01	94.24	0.02	28.71	0.01	131.95	0.11	11.72	0.25	5.03	4.73	1.18	0.15	12.02	99.29	403.24
2	93.58	0.18	0.02	59.62	0.09	9.07	0.01	210.74	0.01	60.87	0.01	99.35	0.17	7.43	0.37	3.68	5.17	1.12	0.19	9.87	99.62	461.93
average	**89.14**	0.18	**0.03**	116.38	**0.12**	12.10	**0.02**	301.31	**0.01**	80.79	**0.01**	198.29	**0.19**	8.20	**1.08**	4.50	**7.64**	1.00	**0.15**	14.18	**98.39**	736.95
1 S.D.	**5.8**		**0.1**		**0.2**		**0.1**		**0.0**		**0.0**		**0.1**		**2.1**		**3.6**		**0.1**		**2.1**	

Thin-section	SiO2 (wt %)	Si (1σ %)	Na2O (wt %)	Na (1σ %)	CaO (wt %)	Ca (1σ %)	SO3 (wt %)	S (1σ %)	K2O (wt %)	K (1σ %)	TiO2 (wt %)	Ti (1σ %)	Al2O3 (wt %)	Al (1σ %)	MgO (wt %)	Mg (1σ %)	FeO (wt %)	Fe (1σ %)	MnO (wt %)	Mn (1σ %)	Total (wt %)	Total (1σ %)
14	78.19	0.20	0.00	100.00	0.04	19.49	0.00	100.00	0.00	275.09	0.00	100.00	0.10	12.89	0.07	17.32	20.16	0.55	0.00	100.00	98.56	725.54
14	59.67	0.23	0.01	245.44	0.02	33.14	0.01	102.21	0.00	100.00	0.00	840.03	0.22	6.94	0.33	4.63	36.63	0.40	0.01	152.14	96.91	1485.16
14	66.58	0.22	0.00	100.00	0.06	13.85	0.00	100.00	0.00	100.00	0.00	100.00	0.18	8.06	0.13	9.39	30.99	0.44	0.00	100.00	97.95	531.96
14	67.21	0.22	0.01	151.90	0.02	45.39	0.00	100.00	0.00	100.00	0.02	82.61	0.16	9.02	0.13	9.68	30.17	0.44	0.00	100.00	97.71	599.26
14	81.08	0.20	0.01	109.42	0.01	95.22	0.00	100.00	0.00	100.00	0.00	100.00	0.08	16.41	0.06	17.91	18.04	0.58	0.02	74.34	99.30	614.08
14	78.44	0.20	0.00	100.00	0.01	96.84	0.01	175.16	0.00	100.00	0.00	100.00	0.10	12.97	0.06	17.19	20.11	0.55	0.00	325.45	98.73	928.36
14	84.85	0.19	0.01	111.44	0.03	26.30	0.02	76.15	0.00	101.18	0.00	100.00	0.09	14.10	0.23	5.55	14.46	0.65	0.02	68.90	99.71	504.46
14	55.82	0.24	0.03	43.89	0.03	32.84	0.00	100.00	0.00	100.00	0.02	92.24	0.39	4.43	0.77	2.65	40.21	0.38	0.00	2602.38	97.26	2979.05
14	76.64	0.20	0.00	100.00	0.13	7.13	0.01	99.62	0.00	100.00	0.00	100.00	0.14	10.01	0.15	8.42	21.63	0.53	0.03	61.65	98.73	487.56
14	72.49	0.21	0.02	67.06	0.02	36.40	0.01	84.72	0.00	100.00	0.00	100.00	0.13	10.94	0.12	10.08	25.95	0.48	0.00	100.00	98.74	509.89
14	81.59	0.19	0.00	100.00	0.01	142.12	0.00	100.00	0.01	66.22	0.00	100.00	0.10	12.51	0.17	7.13	16.75	0.60	0.00	100.00	98.63	628.77
14	79.79	0.20	0.01	88.79	0.01	82.25	0.00	100.00	0.00	100.00	0.00	100.00	0.10	12.71	0.08	14.17	18.43	0.57	0.00	100.00	98.42	598.69
14	72.39	0.21	0.00	100.00	0.02	44.55	0.01	182.45	0.00	100.00	0.01	111.60	0.25	5.95	0.49	3.37	25.59	0.48	0.00	1174.71	98.75	1723.32
14	61.49	0.23	0.01	161.96	0.04	21.75	0.00	100.00	0.00	100.00	0.02	86.70	0.20	7.49	0.14	9.13	35.10	0.41	0.01	180.98	97.01	668.65
14	64.62	0.22	0.01	109.85	0.03	26.36	0.00	274.04	0.00	290.36	0.03	41.74	0.24	6.52	0.21	6.56	32.68	0.43	0.02	83.40	97.84	839.48
14	74.03	0.21	0.02	55.95	0.01	73.37	0.00	279.09	0.00	284.19	0.00	100.00	0.14	10.08	0.13	9.33	24.65	0.49	0.00	100.00	98.99	912.71
14	72.87	0.21	0.00	682.69	0.03	30.81	0.00	414.81	0.00	100.00	0.00	100.00	0.11	12.41	0.08	14.86	26.03	0.48	0.00	100.00	99.12	1456.27
14	68.39	0.22	0.01	96.11	0.03	27.95	0.02	57.36	0.00	100.00	0.01	170.75	0.15	9.85	1.58	1.60	27.99	0.46	0.00	510.28	98.18	974.58
14	79.13	0.20	0.00	100.00	1.42	1.47	0.01	132.71	0.00	100.00	0.00	100.00	0.13	10.03	0.06	18.92	17.94	0.58	0.02	79.01	98.71	542.92
14	60.10	0.23	0.00	100.00	0.03	32.31	0.00	100.00	0.00	100.00	0.00	502.91	0.30	5.28	0.26	5.57	37.22	0.40	0.02	96.65	97.93	943.35
14	73.17	0.21	0.00	100.00	0.02	50.93	0.00	100.00	0.00	100.00	0.00	100.00	0.15	9.40	0.09	13.32	25.22	0.49	0.00	606.20	98.64	1080.55
14	75.17	0.20	0.01	77.57	0.02	42.76	0.01	99.82	0.00	100.00	0.00	452.95	0.13	10.31	0.09	12.11	24.19	0.50	0.02	86.16	99.65	882.38
14	74.98	0.20	0.02	51.07	0.02	49.59	0.00	100.00	0.00	100.00	0.00	100.00	0.13	11.08	0.10	11.95	23.85	0.50	0.00	400.00	99.09	824.39
14	68.72	0.22	0.00	404.94	0.03	31.35	0.00	100.00	0.00	107.09	0.02	55.66	0.19	7.52	0.37	4.17	28.95	0.45	0.01	272.85	98.29	984.25

Thin-section	SiO2 (wt %)	Si (1σ %)	Na2O (wt %)	Na (1σ %)	CaO (wt %)	Ca (1σ %)	SO3 (wt %)	S (1σ %)	K2O (wt %)	K (1σ %)	TiO2 (wt %)	Ti (1σ %)	Al2O3 (wt %)	Al (1σ %)	MgO (wt %)	Mg (1σ %)	FeO (wt %)	Fe (1σ %)	MnO (wt %)	Mn (1σ %)	Total (wt %)	Total (1σ %)
14	70.01	0.21	0.01	146.83	0.01	65.06	0.00	100.00	0.00	100.00	0.00	100.00	0.13	10.72	0.09	14.08	28.60	0.46	0.01	208.17	98.85	745.53
14	60.69	0.23	0.01	104.30	0.08	11.49	0.01	121.38	0.00	100.00	0.00	100.00	0.24	6.37	0.20	6.90	36.21	0.40	0.00	100.00	97.44	551.07
14	74.87	0.20	0.03	43.34	0.02	49.90	0.01	152.85	0.00	100.00	0.03	46.77	0.17	8.19	0.09	12.27	24.18	0.50	0.02	76.67	99.41	490.69
14	78.14	0.20	0.00	209.18	0.03	26.99	0.01	111.65	0.00	222.19	0.03	47.87	0.09	14.57	0.10	11.60	19.80	0.55	0.00	100.00	98.20	744.80
14	68.85	0.22	0.01	228.63	0.02	48.38	0.01	199.51	0.00	100.00	0.01	93.66	0.16	9.15	0.14	8.79	28.57	0.46	0.00	100.00	97.76	788.80
14	67.30	0.22	0.03	44.02	0.08	10.86	0.01	180.01	0.00	100.00	0.00	100.00	0.46	3.69	1.20	1.88	28.88	0.45	0.01	183.22	97.96	624.35
14	82.43	0.19	0.03	42.29	0.02	38.09	0.00	100.00	0.00	312.93	0.00	100.00	0.14	9.41	0.11	10.24	16.79	0.60	0.00	100.00	99.52	713.75
14	74.33	0.21	0.01	178.29	0.01	86.65	0.00	100.00	0.00	100.00	0.01	128.81	0.12	11.12	0.09	12.10	24.72	0.49	0.01	172.02	99.30	789.69
14	75.76	0.20	0.02	74.69	0.03	27.72	0.02	73.32	0.00	100.00	0.00	100.00	0.15	9.07	0.12	9.71	22.79	0.51	0.00	100.00	98.88	495.22
14	79.10	0.20	0.01	202.39	0.02	38.99	0.00	100.00	0.00	693.09	0.00	796.06	0.14	9.49	0.08	13.70	20.45	0.54	0.01	117.12	99.82	1971.58
14	75.12	0.20	0.04	29.67	0.02	42.71	0.00	100.00	0.00	100.00	0.00	100.00	0.16	8.67	1.66	1.53	21.54	0.53	0.00	100.00	98.53	483.31
14	67.10	0.22	0.01	116.89	1.16	1.63	0.00	100.00	0.00	120.48	0.02	82.34	0.23	6.59	0.30	4.78	29.27	0.45	0.03	59.33	98.12	492.71
14	78.65	0.20	0.00	100.00	0.02	42.09	0.00	100.00	0.00	100.00	0.00	100.00	0.11	11.73	0.08	14.29	20.12	0.55	0.01	263.63	98.99	732.49
14	60.05	0.23	0.00	334.23	0.03	24.54	0.00	100.00	0.00	100.00	0.04	34.95	0.24	6.62	0.33	4.72	37.04	0.40	0.02	66.32	97.76	672.01
14	66.41	0.22	0.00	520.84	0.06	13.33	0.01	129.74	0.00	100.00	0.01	150.80	0.20	7.12	0.17	7.58	31.41	0.43	0.00	1247.03	98.28	2177.09
14	67.36	0.22	0.00	1581.72	0.02	41.65	0.00	100.00	0.00	100.00	0.02	61.00	0.17	8.26	0.17	7.58	30.08	0.44	0.01	284.79	97.83	2185.66
14	80.93	0.20	0.01	90.10	0.03	24.70	0.00	676.00	0.00	100.00	0.00	100.00	0.09	14.97	0.05	20.70	18.37	0.58	0.02	71.52	99.50	1098.77
14	78.50	0.20	0.01	194.09	0.03	25.51	0.00	483.57	0.00	100.00	0.00	100.00	0.08	17.54	0.08	14.62	19.95	0.55	0.01	217.23	98.65	1153.31
14	83.69	0.19	0.01	137.28	0.02	31.28	0.01	107.43	0.00	100.00	0.01	133.29	0.11	11.83	0.24	5.41	14.94	0.64	0.00	100.00	99.03	627.35
14	55.34	0.24	0.03	53.33	0.04	18.76	0.00	571.71	0.00	100.00	0.01	137.47	0.41	4.25	0.81	2.52	40.49	0.38	0.02	102.63	97.15	991.29
14	77.24	0.20	0.02	67.99	0.13	7.27	0.00	100.00	0.00	100.00	0.00	100.00	0.14	9.63	0.14	8.80	21.20	0.53	0.02	66.67	98.89	461.09
14	72.72	0.21	0.00	100.00	0.02	41.78	0.00	100.00	0.00	368.22	0.00	100.00	0.11	11.97	0.12	10.67	26.28	0.48	0.00	100.00	99.25	833.33
14	82.62	0.19	0.02	51.46	0.01	77.77	0.00	100.00	0.00	100.00	0.00	1242.00	0.08	16.43	0.20	6.34	16.43	0.61	0.02	71.77	99.38	1666.57
14	80.35	0.20	0.02	63.62	0.01	80.66	0.00	100.00	0.00	100.00	0.00	100.00	0.10	13.04	0.07	16.21	19.03	0.56	0.01	255.55	99.58	729.84
14	72.54	0.21	0.00	100.00	0.03	29.84	0.00	338.60	0.00	100.00	0.00	100.00	0.25	6.08	0.49	3.41	25.91	0.48	0.00	100.00	99.22	778.62
14	61.23	0.23	0.00	100.00	0.01	70.79	0.00	100.00	0.00	100.00	0.00	100.00	0.23	6.57	0.16	8.58	35.94	0.40	0.01	138.55	97.58	625.12
14	64.96	0.22	0.00	100.00	0.02	41.63	0.00	100.00	0.00	100.00	0.00	100.00	0.23	6.63	0.20	6.69	33.01	0.42	0.02	73.94	98.44	529.53
14	73.77	0.21	0.00	907.00	0.02	37.47	0.03	42.32	0.00	100.00	0.00	100.00	0.14	9.99	0.14	9.27	25.27	0.49	0.03	60.31	99.39	1267.06
14	71.56	0.21	0.00	100.00	0.02	47.49	0.00	100.00	0.00	193.30	0.02	81.18	0.13	10.71	0.09	12.81	27.20	0.47	0.00	100.00	99.02	646.17
14	68.35	0.22	0.01	203.55	0.01	70.31	0.01	169.34	0.00	100.00	0.03	46.83	0.16	8.95	1.55	1.62	28.21	0.46	0.00	100.00	98.33	701.28
14	79.97	0.20	0.00	100.00	1.46	1.44	0.02	64.14	0.00	100.00	0.00	100.00	0.13	10.24	0.04	25.04	16.93	0.60	0.02	91.34	98.57	493.00
14	59.32	0.23	0.01	83.63	0.02	52.01	0.00	100.00	0.00	162.22	0.01	102.21	0.29	5.52	0.26	5.58	37.78	0.39	0.02	70.73	97.73	582.52

Thin-section	SiO2 (wt %)	Si (1σ %)	Na2O (wt %)	Na (1σ %)	CaO (wt %)	Ca (1σ %)	SO3 (wt %)	S (1σ %)	K2O (wt %)	K (1σ %)	TiO2 (wt %)	Ti (1σ %)	Al2O3 (wt %)	Al (1σ %)	MgO (wt %)	Mg (1σ %)	FeO (wt %)	Fe (1σ %)	MnO (wt %)	Mn (1σ %)	Total (wt %)	Total (1σ %)
14	72.26	0.21	0.01	76.84	0.02	35.35	0.01	175.44	0.00	1227.86	0.00	100.00	0.17	8.49	0.10	11.63	26.28	0.48	0.02	69.94	98.88	1706.24
14	74.99	0.20	0.03	43.70	0.02	32.47	0.00	663.27	0.00	100.00	0.01	243.93	0.12	11.81	0.09	12.34	23.71	0.50	0.01	187.95	98.97	1296.17
14	75.26	0.20	0.03	41.06	0.03	30.49	0.00	100.00	0.00	100.00	0.01	250.68	0.14	9.72	0.11	11.21	23.51	0.51	0.00	100.00	99.08	643.87
14	68.05	0.22	0.01	118.24	0.01	58.26	0.01	92.80	0.00	100.00	0.02	69.19	0.19	7.50	0.37	4.30	29.43	0.45	0.03	54.13	98.12	505.09
14	70.17	0.21	0.01	90.63	0.06	13.74	0.00	100.00	0.00	100.00	0.00	100.00	0.13	10.55	0.10	11.85	28.45	0.46	0.00	100.00	98.93	527.44
14	60.59	0.23	0.01	126.36	0.11	8.51	0.00	100.00	0.00	100.00	0.00	100.00	0.24	6.31	0.21	6.66	36.76	0.40	0.00	867.28	97.92	1315.75
14	76.17	0.20	0.00	252.29	0.02	42.81	0.00	100.00	0.01	40.43	0.00	100.00	0.12	11.56	0.09	13.16	22.96	0.51	0.00	100.00	99.37	660.96
14	78.88	0.20	0.02	48.09	0.02	41.50	0.01	147.01	0.00	100.00	0.00	265.83	0.10	13.67	0.08	13.82	19.80	0.55	0.00	404.82	98.92	1035.49
14	70.49	0.21	0.00	804.51	0.01	66.08	0.01	144.15	0.00	100.00	0.00	100.00	0.15	9.27	0.14	8.68	28.16	0.46	0.03	62.45	98.99	1295.81
14	68.27	0.22	0.03	44.81	0.11	8.04	0.00	539.59	0.00	100.00	0.00	100.00	0.44	3.82	1.17	1.91	28.88	0.45	0.05	34.47	98.95	833.31
14	83.22	0.19	0.00	825.62	0.01	81.56	0.00	100.00	0.00	100.00	0.00	100.00	0.13	10.34	0.08	14.01	16.67	0.60	0.01	153.33	100.12	1385.65
14	72.72	0.21	0.00	507.06	0.03	23.91	0.00	627.32	0.00	100.00	0.00	100.00	0.15	9.17	0.09	13.29	26.88	0.47	0.00	100.00	99.88	1481.43
14	76.50	0.20	0.01	216.99	0.03	26.41	0.01	195.09	0.00	100.00	0.02	56.82	0.15	9.21	0.11	10.57	22.52	0.52	0.00	475.39	99.35	1091.20
14	78.79	0.20	0.01	150.16	0.01	55.56	0.01	153.23	0.00	250.29	0.01	93.61	0.14	9.50	0.10	11.71	21.50	0.53	0.01	169.93	100.59	894.72
14	76.07	0.20	0.02	70.55	0.01	54.12	0.01	85.30	0.00	180.82	0.00	100.00	0.13	10.38	1.10	1.95	21.46	0.53	0.02	68.38	98.83	572.23
14	66.74	0.22	0.00	100.00	1.48	1.42	0.02	79.00	0.00	100.00	0.02	85.18	0.27	5.72	0.26	5.45	29.26	0.45	0.01	138.11	98.05	515.55
average	**72.30**	0.21	**0.01**	184.50	**0.10**	39.91	**0.00**	162.53	**0.00**	144.39	**0.01**	148.44	**0.17**	9.57	**0.27**	9.55	**25.79**	0.49	**0.01**	217.50	**98.67**	917.09
1 S.D.	**7.19**		**0.01**		**0.31**		**0.01**		**0.00**		**0.01**		**0.08**		**0.37**		**6.47**		**0.01**		**0.75**	

3. Micro-XRF

XRF data are presented along the stratigraphic column as three-point averages of 1 mm laser point measurements. The results are qualitative.

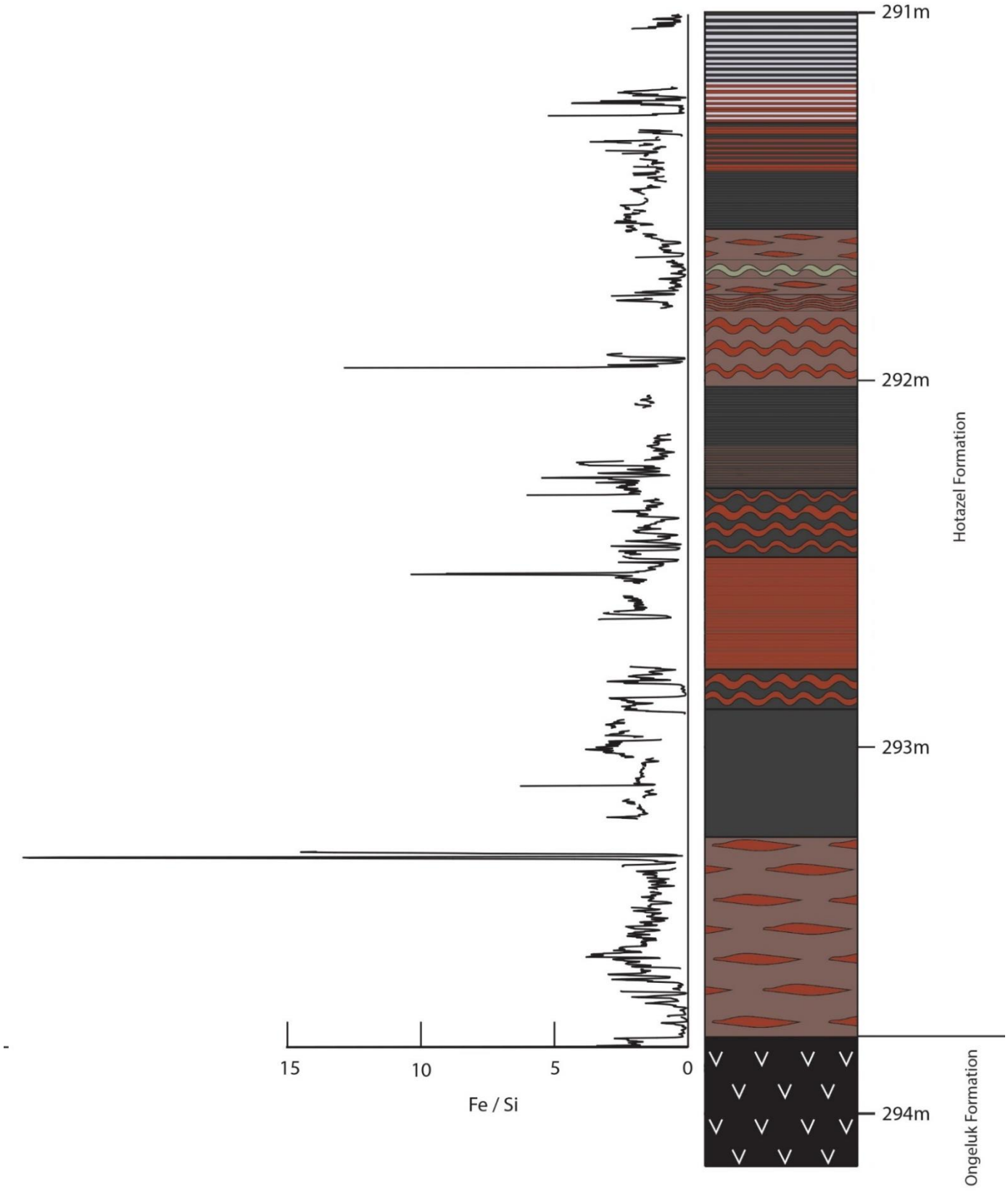

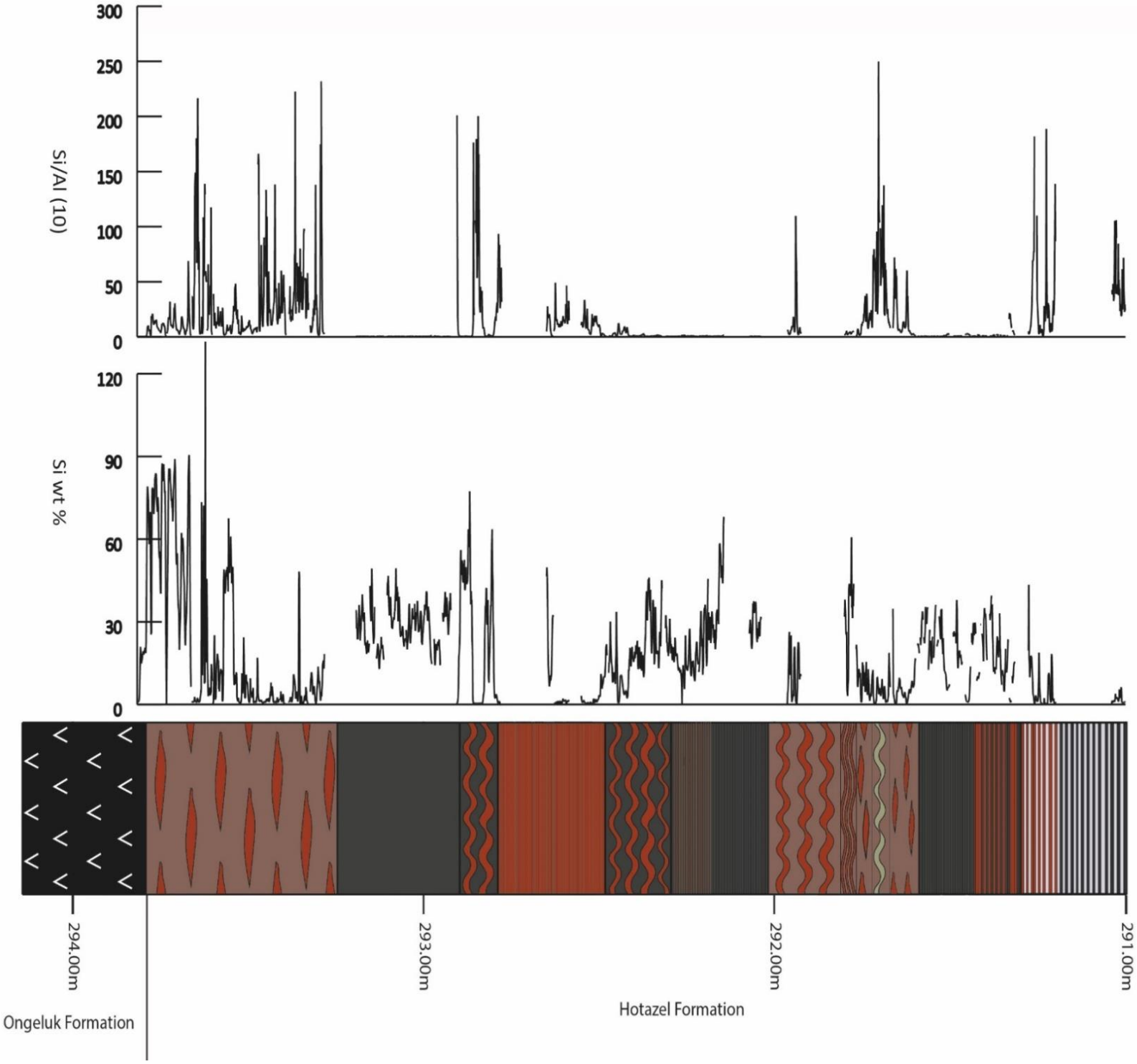
Si/Al (10)
300
250
200
150
100
50
0
Si wt %
120
90
60
30
0
294.00m
293.00m
292.00m
291.00m
Ongeluk Formation
Hotazel Formation

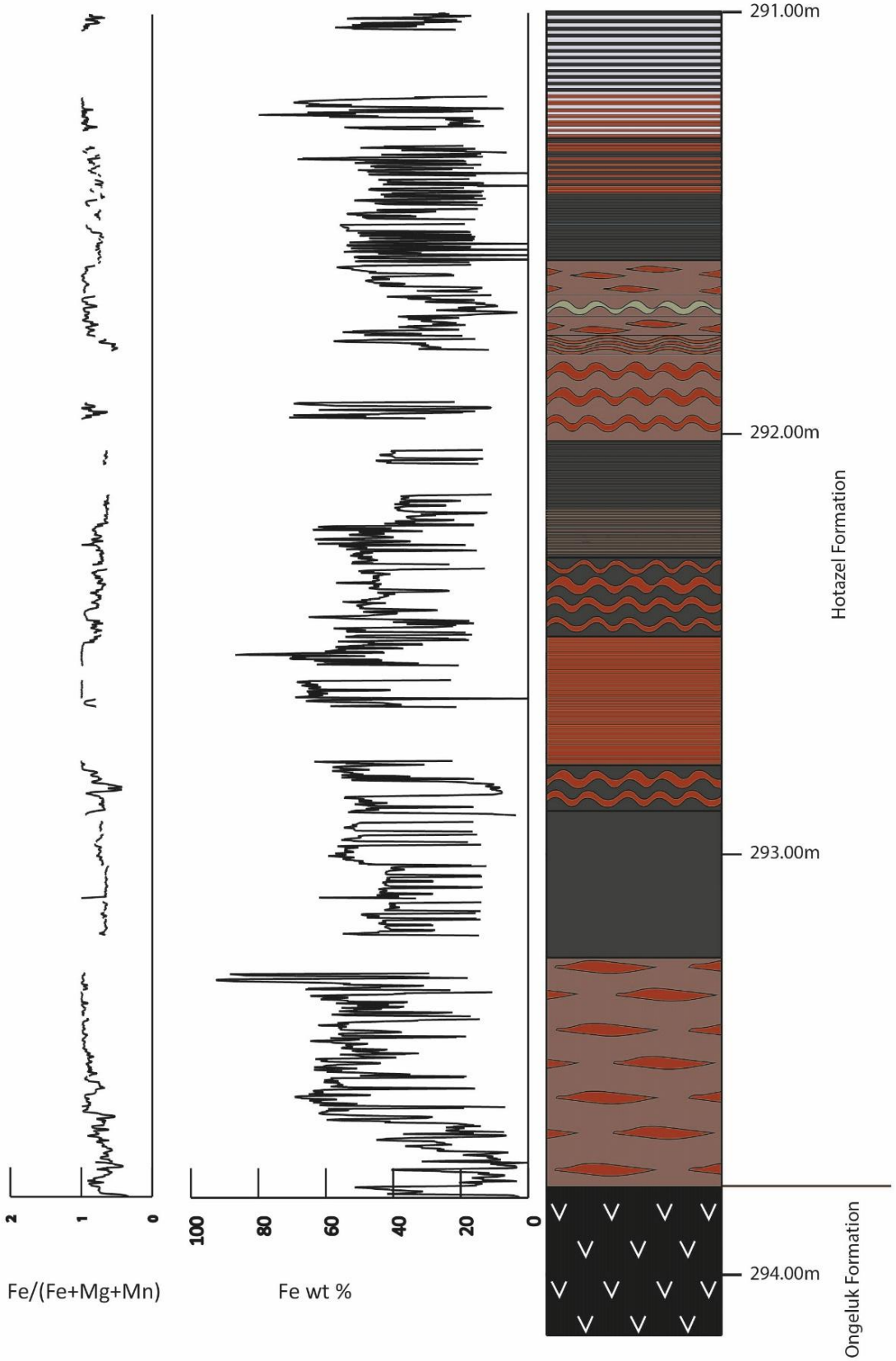
291.00m
292.00m
293.00m
294.00m
Hotazel Formation
Ongeluk Formation
Fe/(Fe+Mg+Mn)
2
1
0
Fe wt %
100
80
60
40
20
0

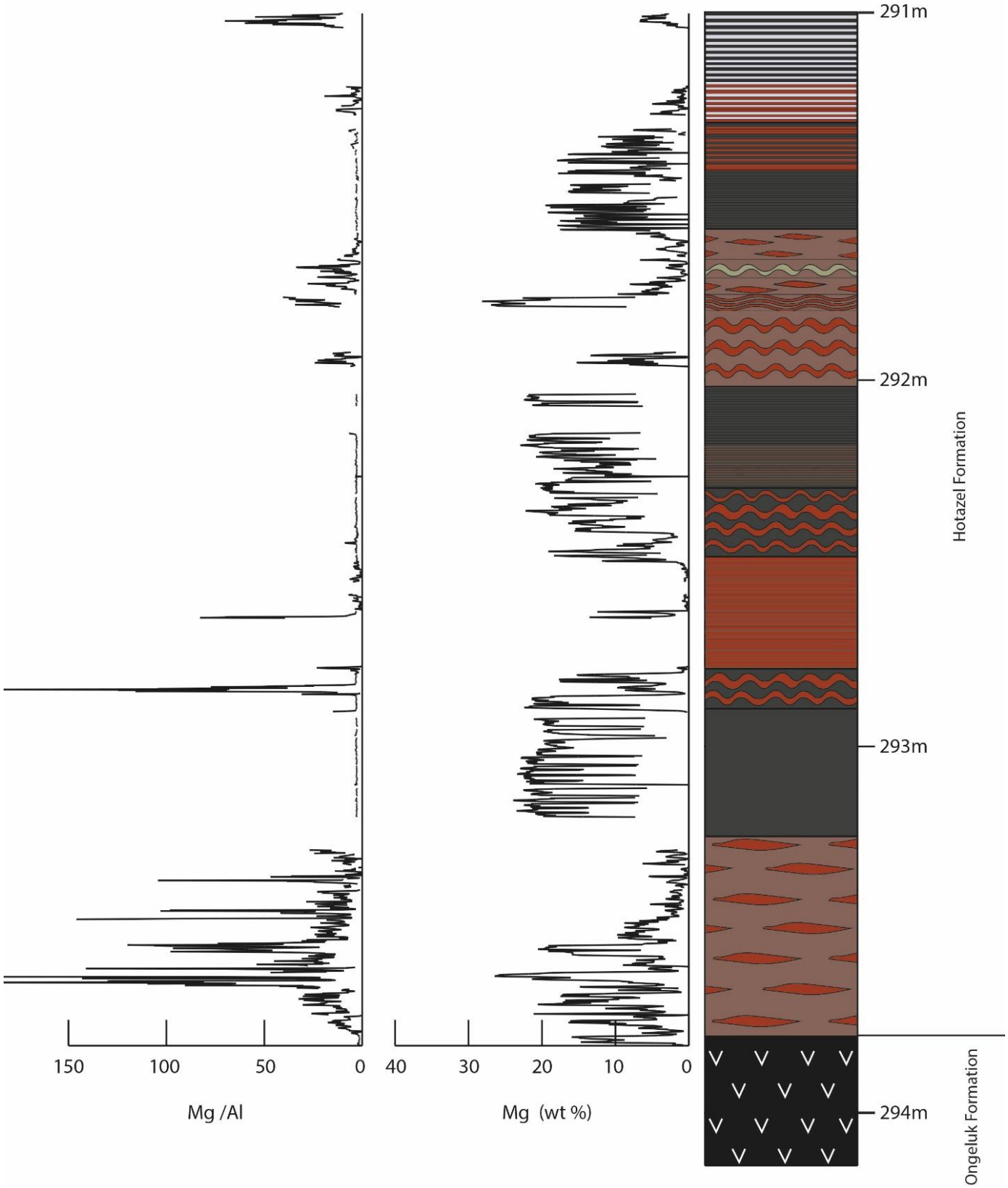
291m
292m
293m
294m
Hotazel Formation
Ongeluk Formation
150
100
50
0
Mg /Al
40
30
20
10
0
Mg (wt %)

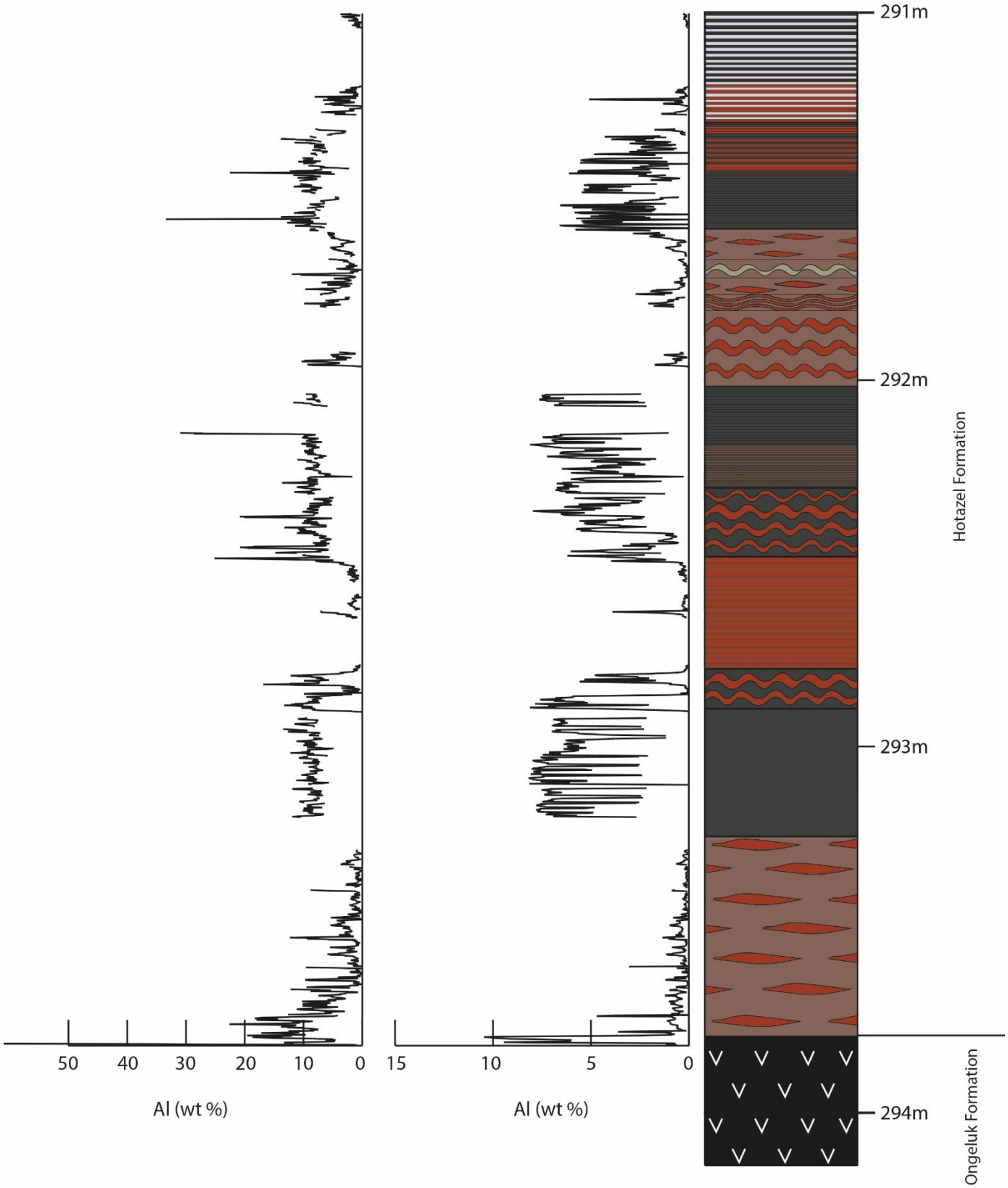
291m
292m
293m
294m
Hotazel Formation
Ongeluk Formation
50
40
30
20
10
0
Al (wt %)
15
10
5
0
Al (wt %)

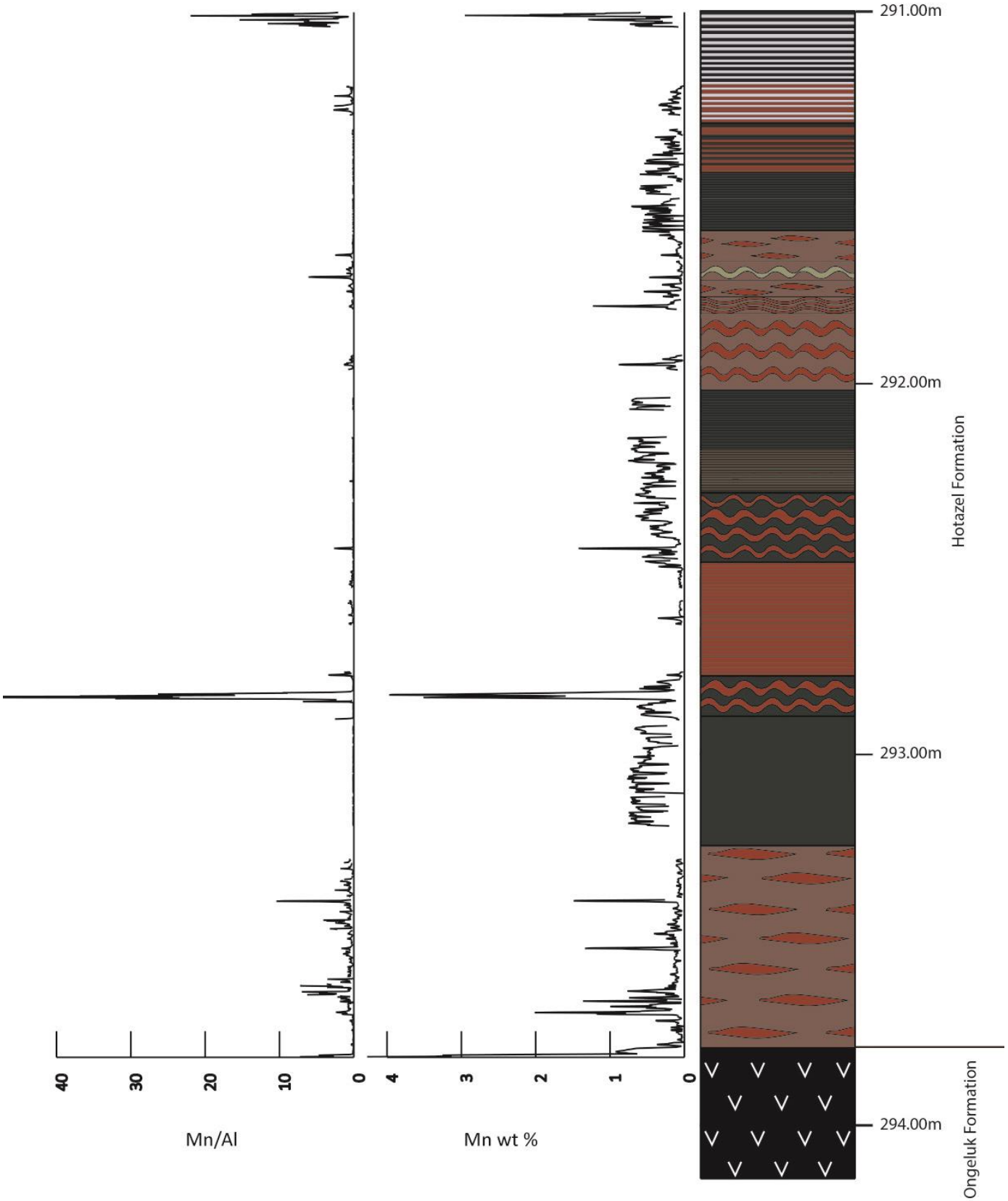
40
30
20
10
0
Mn/Al
4
3
2
1
0
Mn wt %
291.00m
292.00m
293.00m
294.00m
Hotazel Formation
Ongeluk Formation

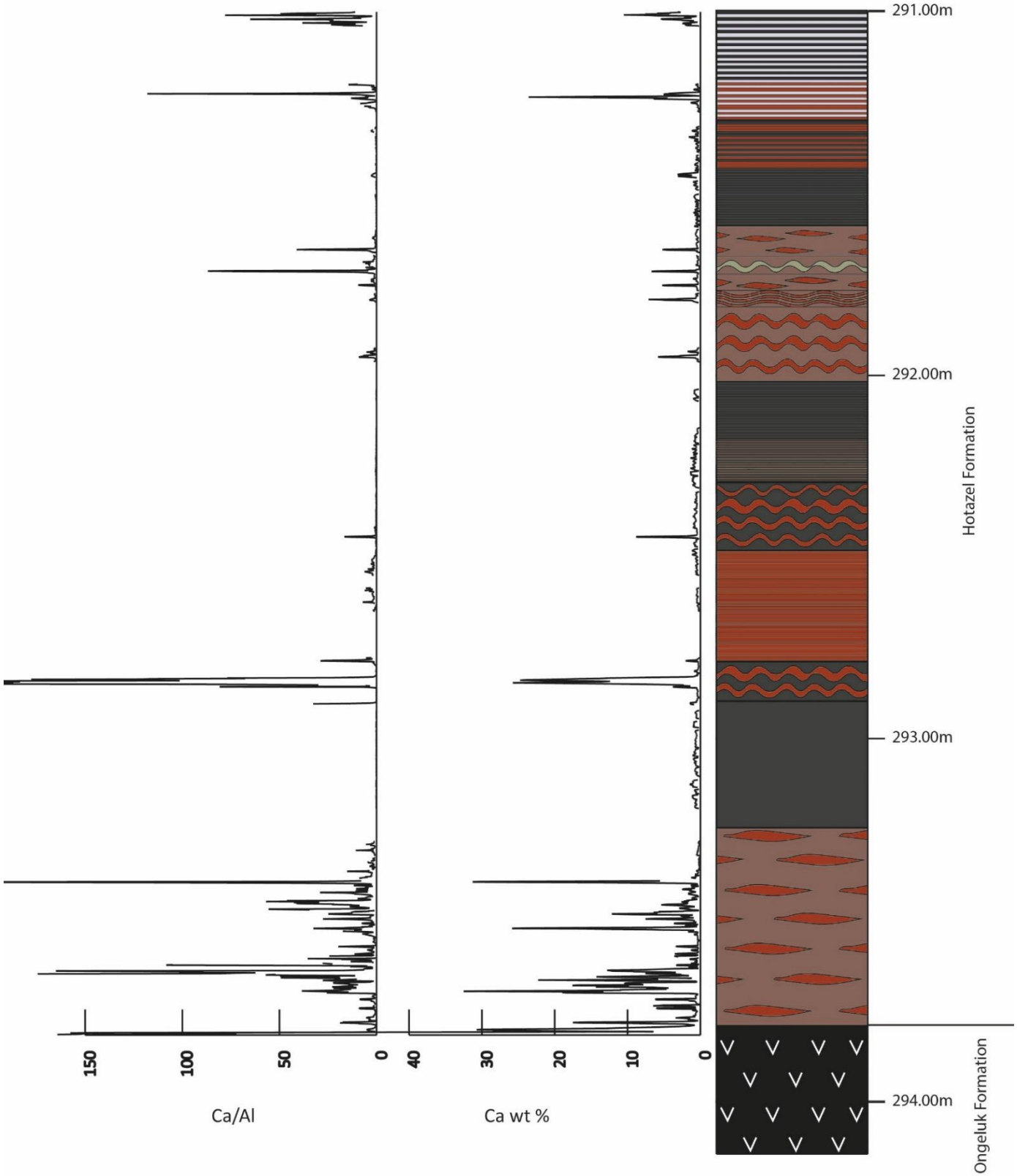
291.00m
292.00m
293.00m
294.00m
Hotazel Formation
Ongeluk Formation
150
100
50
0
Ca/Al
40
30
20
10
0
Ca wt %

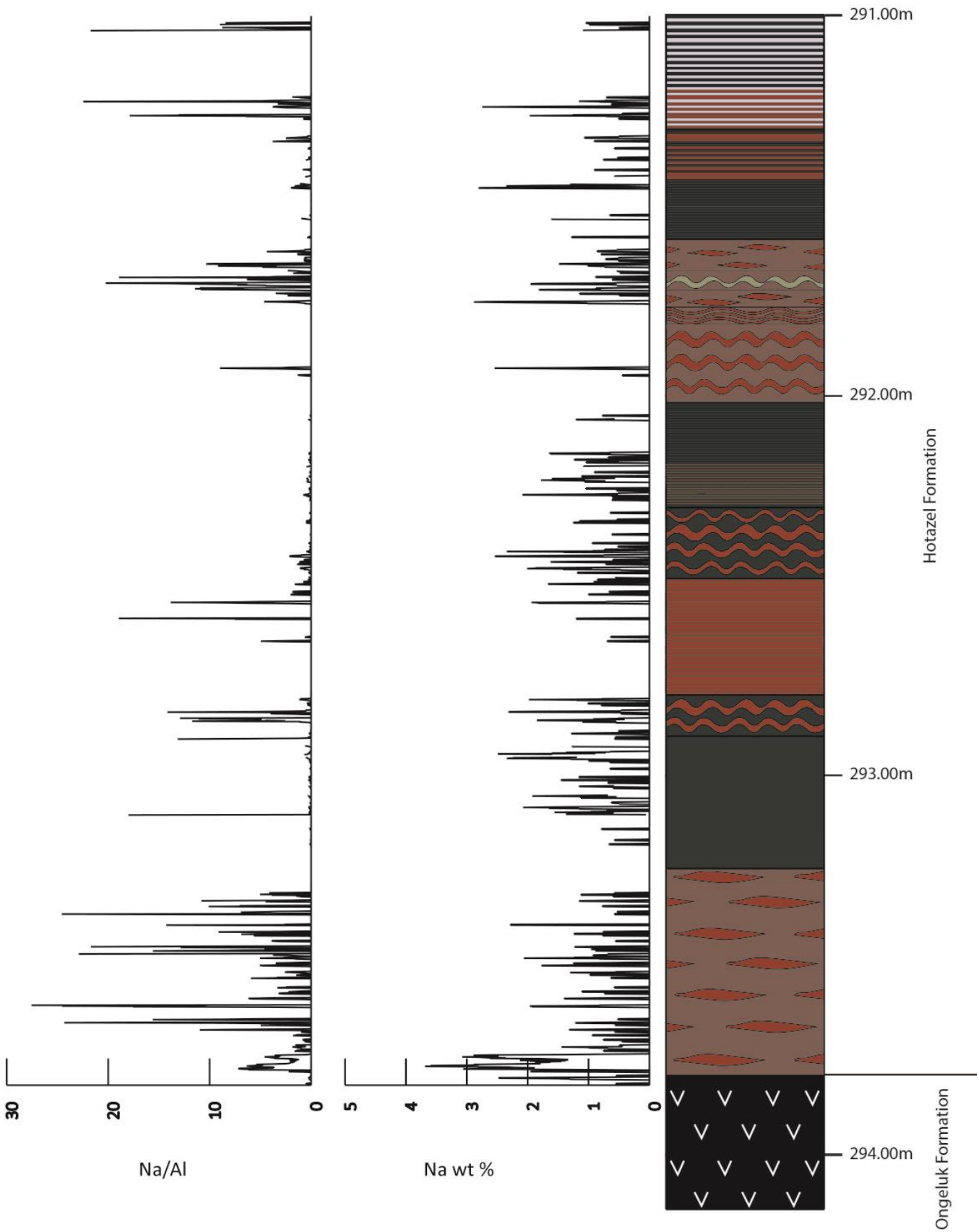
291.00m
292.00m
293.00m
294.00m
Hotazel Formation
Ongeluk Formation
30
20
10
0
Na/Al
5
4
3
2
1
0
Na wt %

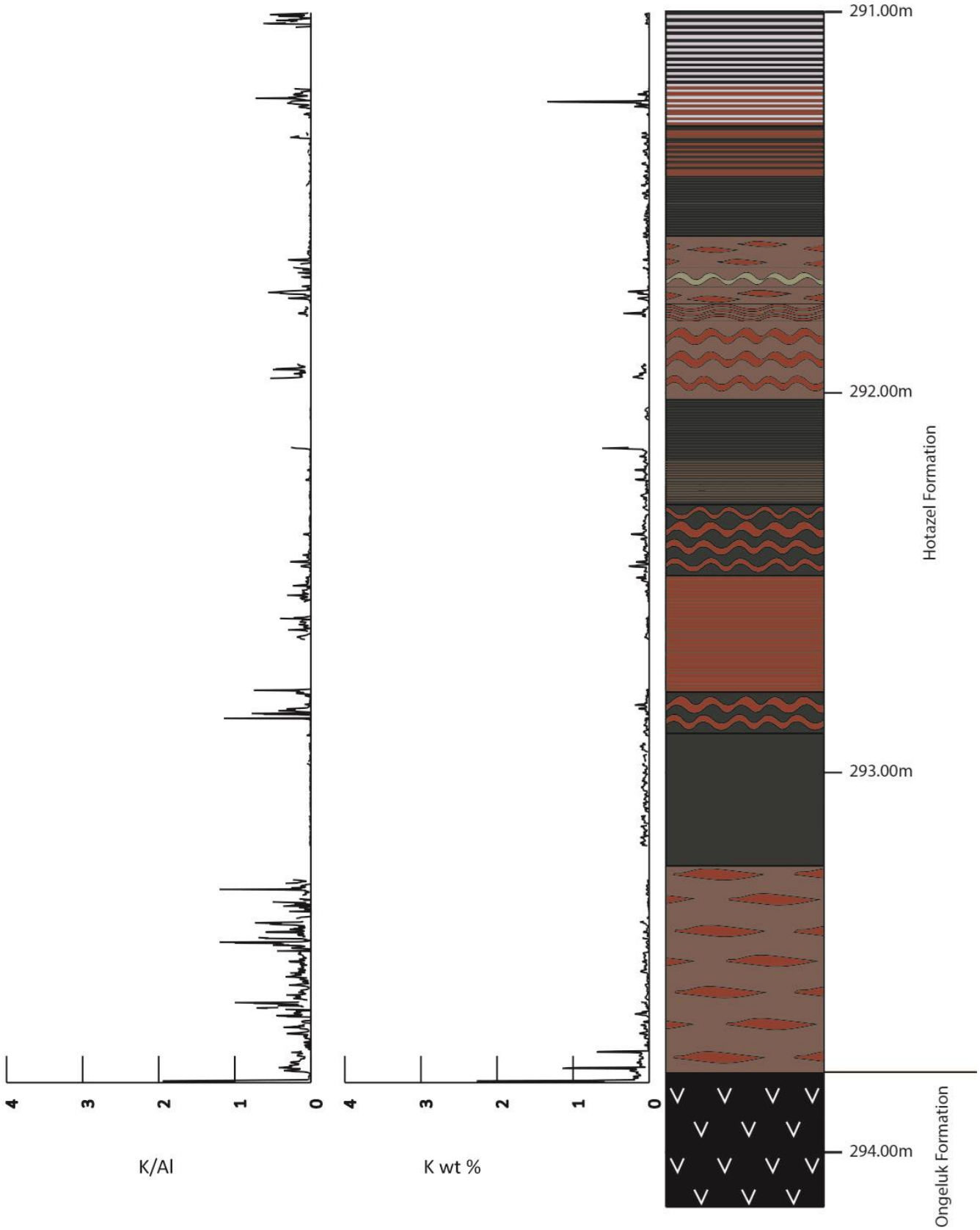
291.00m
292.00m
293.00m
294.00m
Hotazel Formation
Ongeluk Formation
K/Al
K wt %
4
3
2
1
0

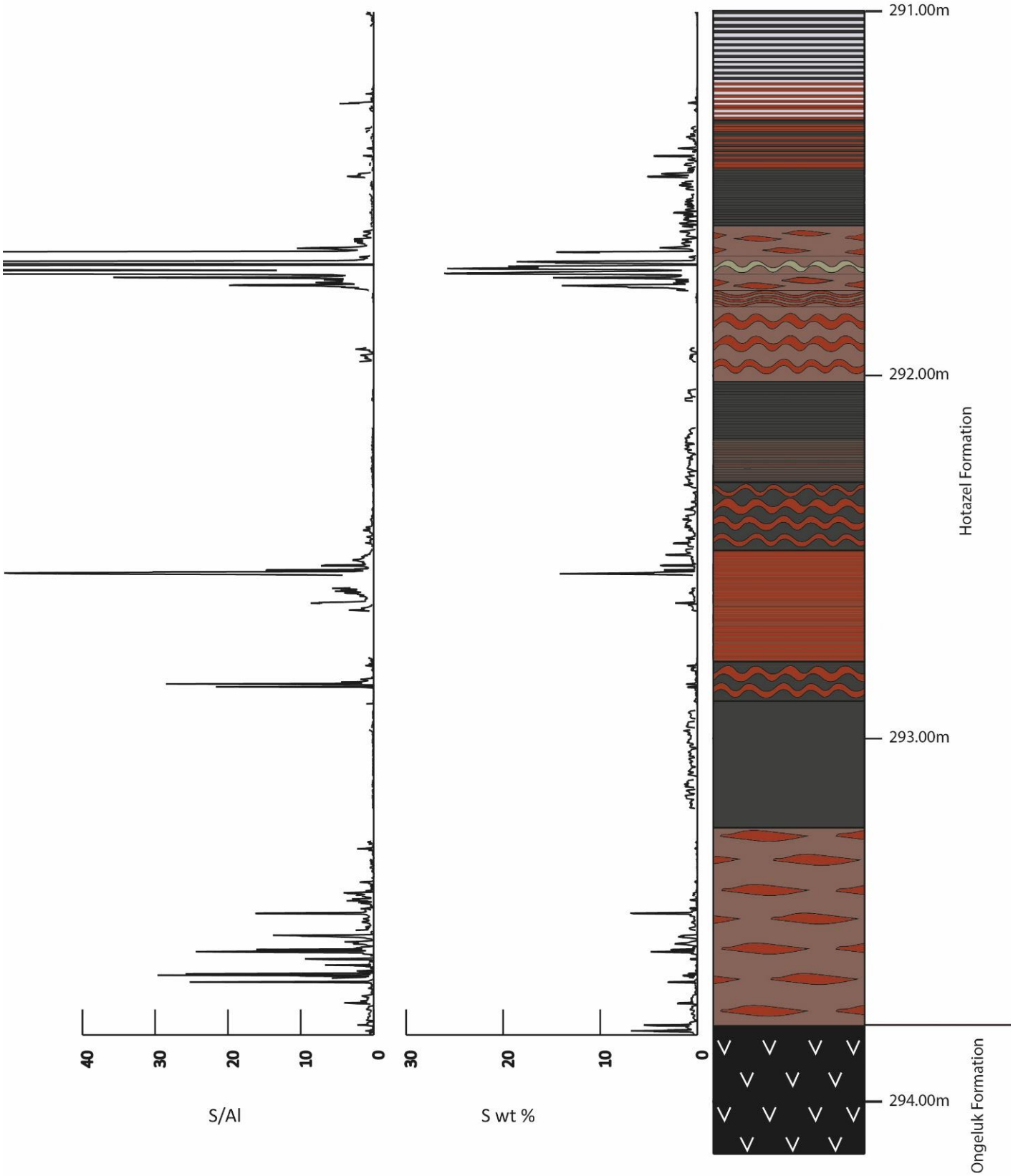
291.00m
292.00m
293.00m
294.00m
Hotazel Formation
Ongeluk Formation
S/Al
40
30
20
10
0
S wt %
30
20
10
0

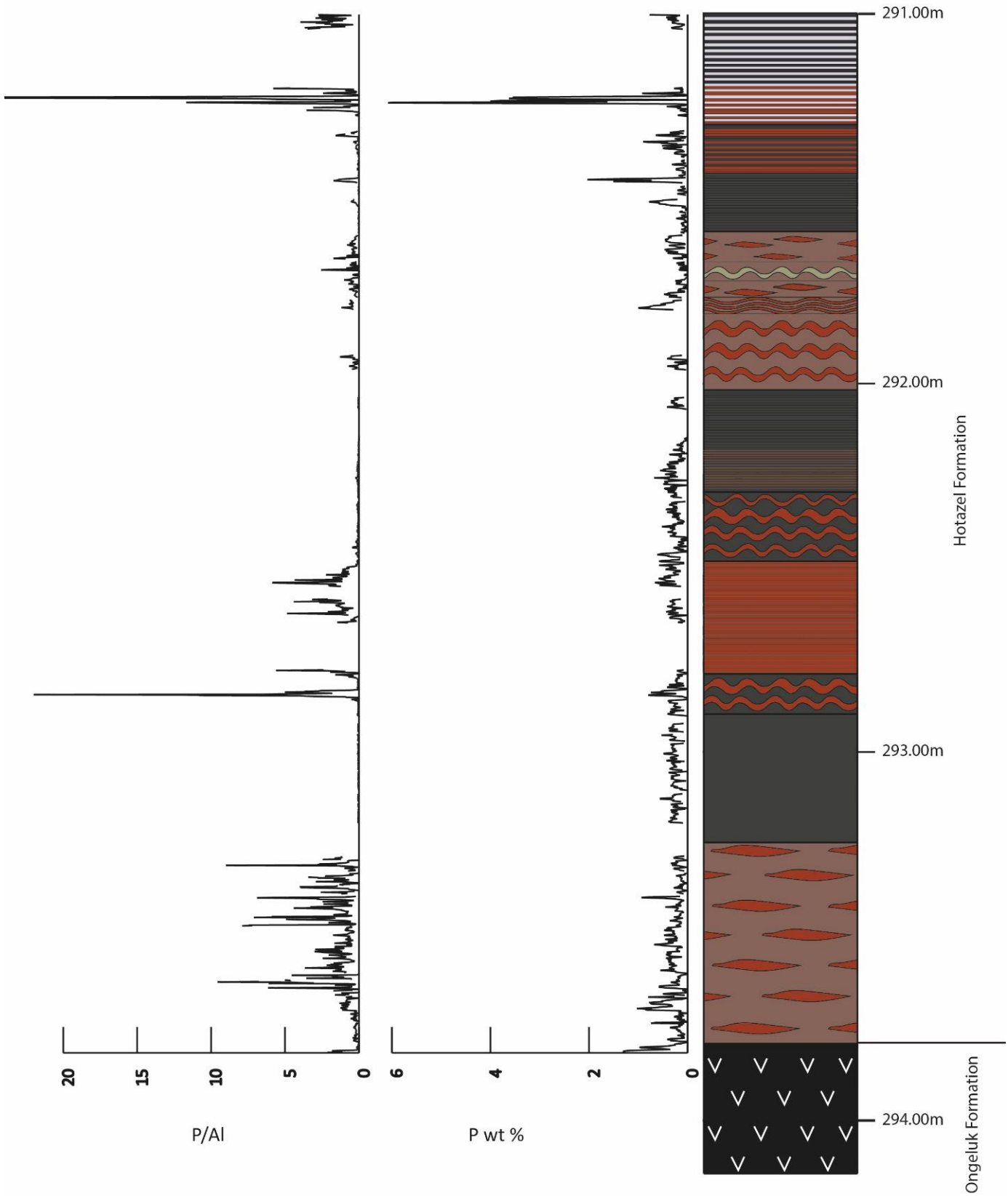
20
15
10
5
0
P/Al
6
4
2
0
P wt %
291.00m
292.00m
293.00m
294.00m
Hotazel Formation
Ongeluk Formation

4. LA-ICP-MS

4.1 Hematite-chert

Table 2: LA-ICP-MS determined major and trace elemental abundance (ppm) of all clean hematite-chert points and their mean per thin-section. 1 σ represents the counting statistics 1 σ error calculated in Glitter software (see Materials and methods); 1 S.D. is the standard deviation for the average elemental concentration of each thin-section. BDL stands for *below detection limit.*

	Mg24	1 σ	Mg26	1 σ	Al27	1 σ	Ca43	1 σ	Sc45	1 σ	Ti47	1 σ	Ti49	1 σ	V51	1 σ	Cr52	1 σ	Mn55	1 σ
Sample	ppm		ppm		ppm		ppm		ppm		ppm		ppm		ppm		ppm		ppm	
2-1	1096.3	289.28	1621.4	2128.21	349.71	12.65	946.86	62.74	0.939	0.09	16.58	10.71	5.02	0.71	2.54	0.11	0.196	0.075	185.52	6.65
2-2	915.14	247.05	1381.84	1862.53	245.28	8.94	717.99	56.75	1.33	0.1	6.76	4.84	3.26	0.61	2.81	0.13	0.526	0.079	104.45	3.77
2-3	1077.7	297.64	1601.53	2216.85	265.26	9.7	547.94	50.76	1.134	0.094	21.26	14.11	30.92	2.87	2.34	0.11	0.748	0.082	127.57	4.62
2-5	841.16	243.11	1286.56	1878.39	316.51	11.65	1104.81	66.61	1.111	0.093	BDL	226.56	14.15	1.45	3.11	0.14	0.812	0.083	125.76	4.6
2-6	1000.33	309.31	1522.87	2408.71	276.73	10.34	559.21	50.62	1.005	0.091	29.7	21.47	58.02	5.52	2.84	0.13	1.229	0.095	178.6	6.63
2-7	1023.15	323.5	1571.92	2553.45	242.33	9.1	561.27	50.89	1.096	0.093	11.89	8.94	5.63	0.76	2.76	0.13	0.571	0.076	122.43	4.57
2-8	1218.21	393.82	1876.59	3130.61	298.73	11.25	839.21	57.05	1.084	0.09	117.59	87.68	103.61	10.02	2.19	0.1	1.75	0.11	145.87	5.48
2-9	1121.73	370.72	1784.09	3056.46	299.9	11.35	703.78	53.75	1.228	0.093	463.99	352.06	215.02	20.95	2.56	0.12	3.03	0.16	148.87	5.62
2-10	1244.78	420.5	1959.17	3446.66	285.01	10.84	1116.01	69.32	0.869	0.093	6.52	5.45	12.34	1.36	2.96	0.14	0.57	0.08	166.64	6.33
average	**1059.83**		**1622.89**		**286.61**		**788.56**		**1.09**		**84.29**		**49.77**		**2.68**		**1.048**		**145.08**	
1 S.D.	**131.53**		**220.15**		**34.32**		**226.16**		**0.14**		**157.72**		**70.19**		**0.30**		**0.870**		**27.57**	
5-1	167828	239784.06	324628.5	1214740.4	1473.05	68.18	11112.83	1022.02	3.8	0.36	400.88	3612.89	1004.92	192.74	33.9	2.69	3.33	0.87	497.69	155.95
6-2	1203.72	271.3	1807.7	1978.83	432.41	15.27	1012.48	68.82	1.116	0.1	BDL	2.09	3.32	0.65	1.238	0.075	0.454	0.081	17.57	0.64
6-3	528.78	121.85	732.34	822.19	175.09	6.26	609.46	50.43	1.393	0.096	10.26	6.12	BDL	0.43	0.69	0.049	0.205	0.068	11.28	0.42
6-5	1590.36	383.21	2409.67	2847.75	443.84	15.83	1367.04	80.14	1.63	0.11	243.63	143.52	2.02	0.56	0.928	0.063	0.245	0.075	13.39	0.51
6-7	8160.62	12819.5	BDL	1363757.8	2887.87	124.32	3675.9	413.08	4.25	0.57	727.25	6440.07	859.43	147.77	24.26	1.75	2.94	0.8	183.35	51.99
average	**2870.87**		**1649.90**		**984.80**		**1666.22**		**2.10**		**327.05**		**288.26**		**6.78**		**0.961**		**56.40**	
1 S.D.	**3553.68**		**849.73**		**1274.77**		**1375.07**		**1.45**		**365.70**		**494.65**		**11.66**		**1.324**		**84.68**	

	Mg24	1 σ	Mg26	1 σ	Al27	1 σ	Ca43	1 σ	Sc45	1 σ	Ti47	1 σ	Ti49	1 σ	V51	1 σ	Cr52	1 σ	Mn55	1 σ
8-2	3631.61	1365.87	5663.58	11368.04	407.17	15.88	21740.92	1014.99	1.73	0.12	9.78	8.58	9.95	1.27	1.471	0.084	0.643	0.093	1686.3	65.86
8-3	5062.65	1944.53	8196.19	16888.16	358.19	14.04	40798.93	1910.55	1.24	0.1	BDL	76.14	11.7	1.43	1.739	0.092	0.838	0.09	2747.91	107.97
average	**4347.13**		**6929.89**		**382.68**		**31269.93**		**1.49**		**9.78**		**10.83**		**1.61**		**0.741**		**2217.11**	
1 S.D.	**1011.89**		**1790.83**		**34.63**		**13476.05**		**0.35**		-		**1.24**		**0.19**		**0.138**		**750.67**	
9-1	3544.24	5036	5557.04	18194.63	1066.16	50.01	1128.92	124.41	1.33	0.17	57.48	522.11	80.28	15.83	7.51	0.62	0.74	0.22	48.31	15.43
9-2	5462.79	7753.21	8131.77	25847.24	1382.95	65.09	3521.17	339.59	1.63	0.19	280.15	2550.3	81.71	16.22	5.87	0.49	1.18	0.33	66.66	21.39
average	**4503.51**		**6844.41**		**1224.56**		**2325.05**		**1.48**		**168.82**		**81.00**		**6.69**		**0.960**		**57.49**	
1 S.D.	**1356.62**		**1820.61**		**224.00**		**1691.58**		**0.21**		**157.45**		**1.01**		**1.16**		**0.311**		**12.98**	
11-2	14353.25	6109.21	24615.07	57764.43	2087.42	83.84	11246.14	567.38	1.33	0.17	2550.21	2365.36	6.55	1.28	5.54	0.28	0.87	0.15	1628.97	66.08
11-4	51994.68	98503.4	BDL	156703.97	299.34	13.23	42429.52	3552.61	BDL	0.42	76.86	722.87	9.01	2.79	3	0.28	BDL	0.39	6669.94	1863.95
average	**33173.97**		**24615.07**		**1193.38**		**26837.83**		**1.33**		**1313.54**		**7.78**		**4.27**		**0.870**		**4149.46**	
1 S.D.	**26616.51**		-		**1264.36**		**22049.98**		-		**1748.92**		**1.74**		**1.80**		-		**3564.50**	
13-2	2429.75	3678.9	26650.89	647077.56	863.27	37.94	1453.41	255.31	BDL	0.4	62.57	552.23	86.18	15.53	2.94	0.28	BDL	0.39	79.01	22.85
13-5	3086.54	4614.22	18115.88	230054.63	353.63	15.81	3485.32	338.54	BDL	0.27	80.12	707.52	86.69	15.59	1.96	0.18	0.65	0.3	49.59	14.48
13-8	1304.39	1915.83	4246.06	30640.72	681.35	30.53	501.27	170.56	BDL	0.31	70.49	624.47	119.55	21.86	3.59	0.3	2.15	0.59	40.89	12.17
13-9	793.11	1151.79	2063.72	11225.97	336.95	15.21	1142.32	111.77	1.01	0.12	16.97	150.99	30.45	5.67	3.14	0.24	1.24	0.32	29.59	8.95
13-10	963.84	1396.27	2427.38	12462.19	352.08	15.93	671.84	74.99	1.17	0.13	16.73	149.11	21.69	4.08	2.48	0.19	1.54	0.39	29.16	8.86
13-11	878.19	1269.22	2095.01	10190.96	392.04	17.79	990.51	101.53	0.99	0.12	47.34	422.36	36.34	6.83	3.99	0.31	2.28	0.57	33.63	10.26
13-12	891.15	1285.1	1979.72	9155.9	370.23	16.86	964.48	97.85	0.97	0.12	12.61	112.67	38.87	7.32	3.48	0.27	1.65	0.42	33.25	10.18
13-13	802.34	1154.62	1735.56	7654.98	386.44	17.65	1282.62	124.77	1.27	0.14	156.49	1400.61	196.99	37.03	3.95	0.31	2.34	0.59	38.89	11.97
average	**1393.66**		**7414.28**		**467.00**		**1311.47**		**1.08**		**57.92**		**77.10**		**3.19**		**1.693**		**41.75**	
1 S.D.	**875.10**		**9548.25**		**195.46**		**930.76**		**0.13**		**47.70**		**59.43**		**0.71**		**0.618**		**16.49**	
14-3	1493.67	261.74	1980.67	1618.32	500.58	17.14	2086.51	97.98	2.08	0.12	31.84	14.89	41.41	3.08	4.75	0.19	2.66	0.14	91.25	3.08
14-6	1888.96	355.85	2545.87	2268.61	586.6	20.21	3217.89	140.88	2.12	0.13	16.26	8.35	57.7	4.34	5.26	0.21	6.58	0.28	61.62	2.1

	Mg24	1 σ	**Mg26**	1 σ	**Al27**	1 σ	**Ca43**	1 σ	**Sc45**	1 σ	**Ti47**	1 σ	**Ti49**	1 σ	**V51**	1 σ	**Cr52**	1 σ	Mn55	1 σ
14-7	1411.71	270.61	1873.1	1703.22	558.94	19.29	1954.13	93.86	1.85	0.11	15.66	8.11	68.88	5.13	5.38	0.21	3.79	0.17	66.62	2.27
14-8	1554.57	303.47	2178.76	2023.28	417.03	14.43	1149.38	65.91	1.75	0.1	61.31	30.71	46.47	3.54	3.97	0.16	3.29	0.16	41.92	1.44
14-9	1951.77	388.29	2748.12	2608.19	724.23	25.07	2768.04	120.04	2.2	0.12	65.18	33.12	69.48	5.24	6.63	0.26	3.11	0.15	74.77	2.56
14-10	4000.9	811.67	5568.96	5405.39	1366.43	47.35	3830.55	156.87	2.11	0.11	89.91	46.3	81.63	6.16	6.49	0.25	58.49	2.24	117.24	4.02
14-12	811.39	1142.51	842.49	1765.37	434.56	22.2	948.16	106.19	1.64	0.18	43.41	416.47	54	11.95	4.57	0.42	2.72	0.82	43.12	15.39
14-13	732.11	1031.07	744.1	1538.44	408.7	20.96	958.41	107.17	1.55	0.17	120.89	1163	55.15	12.27	4.44	0.41	2.5	0.76	39.46	14.15
average	**1730.64**		**2310.26**		**624.63**		**2114.13**		**1.91**		**55.56**		**59.34**		**5.19**		**10.393**		**67.00**	
1 S.D.	**1018.33**		**1501.93**		**317.85**		**1085.24**		**0.25**		**36.68**		**13.24**		**0.96**		**19.479**		**27.15**	
16-4	2479.23	3496.87	3201.75	8356.68	230.22	11.35	2325.5	246.32	0.45	0.19	39.87	369.74	34.58	7.27	6.94	0.6	2.62	0.75	31.96	10.68
16-5	2185.52	3081.19	2701.39	6907.08	260.34	12.71	4193.06	406.55	1.12	0.14	59.28	551.1	90.56	18.73	4.58	0.39	2.45	0.69	33.99	11.41
16-6	2401.77	3382.65	2856.4	6895.42	258.18	12.76	2662.1	265.21	0.94	0.13	43.08	403.5	82.19	17.29	4.09	0.36	2.02	0.58	30.01	10.23
16-8	727.72	1024.53	813.92	1897.02	180.67	9.07	1178.28	133.35	0.83	0.15	95.29	897.27	46.05	9.86	3.86	0.35	1.15	0.35	27.37	9.42
16-9	710.2	999.75	815.58	1869.4	203.73	10.2	1550.8	161.54	1.25	0.15	30.09	284.09	48.04	10.3	3.96	0.35	1.69	0.5	27.01	9.35
average	**1700.89**		**2077.81**		**226.63**		**2381.95**		**0.92**		**53.52**		**60.28**		**4.69**		**1.986**		**30.07**	
1 S.D.	**902.83**		**1167.15**		**34.57**		**1172.76**		**0.31**		**25.60**		**24.54**		**1.29**		**0.593**		**2.98**	

	Fe57	1 σ	Cu63	1 σ	Zn66	1 σ	Ga69	1 σ	Rb85	1 σ	Sr88	1 σ	Y89	1 σ	Zr90	1 σ	Nb93	1 σ	Cs133	1 σ	Ba137	1 σ
Sample	ppm		ppm		ppm		ppm		ppm		ppm		ppm		ppm		ppm		ppm		ppm	
2-1	189745.7	152609.84	BDL	0.15	2.48	0.41	0.265	0.042	0.235	0.021	5.82	0.24	2.249	0.091	0.324	0.082	0.029	0.0049	0.0442	0.008	6.45	0.33
2-2	135762.8	112595.16	BDL	0.13	0.8	0.35	0.131	0.038	0.144	0.019	3.99	0.17	1.528	0.065	0.693	0.089	0.0527	0.007	0.0481	0.0081	4.01	0.23
2-3	81768	69941.01	BDL	0.12	2.3	0.4	0.088	0.034	0.083	0.017	0.959	0.054	1.11	0.051	0.223	0.076	0.044	0.0067	0.03	0.0076	0.637	0.068
2-5	185761.9	169097.77	BDL	0.14	2.31	0.4	0.444	0.044	0.233	0.022	6.95	0.3	2.066	0.086	0.943	0.091	0.0938	0.0082	0.0792	0.0087	7.58	0.4
2-6	131594.6	131651.23	BDL	0.12	1.42	0.36	0.13	0.036	0.183	0.02	2.096	0.099	1.687	0.073	1.43	0.11	0.156	0.012	0.06	0.008	1.92	0.13
2-7	140948.1	145552.91	BDL	0.12	0.93	0.34	0.214	0.037	0.206	0.02	2.54	0.12	1.421	0.063	0.686	0.082	0.0458	0.0061	0.0706	0.0088	2.4	0.15
2-8	112541.3	119976.86	BDL	0.11	3.59	0.49	0.146	0.035	0.163	0.019	1.903	0.092	1.768	0.077	0.955	0.087	0.0711	0.0073	0.065	0.0083	1.5	0.11

	Fe57	1 σ	Cu63	1 σ	Zn66	1 σ	Ga69	1 σ	Rb85	1 σ	Sr88	1 σ	Y89	1 σ	Zr90	1 σ	Nb93	1 σ	Cs133	1 σ	Ba137	1 σ
2-9	146358.9	161092.91	BDL	0.12	BDL	0.41	0.128	0.036	0.217	0.021	3	0.14	2.252	0.097	0.945	0.087	0.133	0.01	0.0691	0.0081	3.13	0.19
2-10	212441	241442.83	BDL	0.13	1.44	0.36	0.353	0.042	0.221	0.021	7.46	0.34	2.48	0.11	0.769	0.086	0.0602	0.0067	0.062	0.0087	7.54	0.43
average	**148546.9**		-		**1.91**		**0.211**		**0.187**		**3.858**		**1.840**		**0.774**		**0.076**		**0.059**		**3.907**	
1 S.D.	**40978.5**		-		**0.93**		**0.121**		**0.050**		**2.351**		**0.452**		**0.361**		**0.043**		**0.015**		**2.657**	
5-1	660132.6	3666962.3	1.6	0.37	213.09	46.01	0.419	0.084	0.666	0.09	9.81	0.95	37.72	3.41	7.78	0.74	1.97	0.17	0.559	0.071	6.91	0.88
6-2	41680.73	27238.69	3.12	0.22	1.54	0.4	BDL	0.037	0.177	0.025	0.869	0.054	1.183	0.056	BDL	0.08	0.0273	0.0065	0.0255	0.0084	1.09	0.1
6-3	59557.54	40053.5	BDL	0.11	0.83	0.31	0.225	0.038	0.141	0.02	0.941	0.052	0.559	0.03	0.121	0.071	0.0103	0.0045	0.034	0.0077	3.04	0.19
6-5	45879.29	32712.48	0.88	0.14	2.37	0.44	0.117	0.038	0.453	0.036	1.214	0.067	1.127	0.054	2.02	0.13	0.0106	0.005	0.0329	0.0085	3.43	0.22
6-7	5364386	BDL	BDL	0.62	BDL	3	BDL	0.29	0.427	0.095	7.92	0.72	19.21	1.57	1.38	0.42	1.34	0.12	0.074	0.038	10.96	1.3
average	**1377875.9**		**2.00**		**1.58**		**0.171**		**0.300**		**2.736**		**5.520**		**1.174**		**0.347**		**0.042**		**4.630**	
1 S.D.	**2657684.4**		**1.58**		**0.77**		**0.076**		**0.163**		**3.459**		**9.131**		**0.966**		**0.662**		**0.022**		**4.342**	
8-2	34280.27	45807.56	2.31	0.21	1.55	0.41	0.228	0.044	0.218	0.024	10.87	0.51	3.66	0.16	BDL	0.084	0.0391	0.0068	0.0306	0.0085	2.97	0.2
8-3	39563.29	54626.55	1.93	0.18	2.43	0.45	0.116	0.037	0.26	0.024	22.35	1.05	5.88	0.26	0.143	0.075	0.0816	0.0085	0.044	0.0084	2.87	0.19
average	36921.8		2.12		1.99		0.172		0.239		16.610		4.770		0.143		0.060		0.037		2.920	
1 S.D.	3735.7		0.27		0.62		0.079		0.030		8.118		1.570		-		0.030		0.009		0.071	
9-1	234678.7	1180220.4	BDL	0.18	6.11	1.47	0.294	0.063	0.46	0.062	2.55	0.26	4.42	0.41	0.92	0.13	0.203	0.023	0.083	0.015	4.74	0.61
9-2	172589.5	848673	2.27	0.5	10.39	2.42	0.403	0.076	0.279	0.045	3.38	0.34	9.94	0.93	1.2	0.16	0.164	0.021	0.063	0.015	4.22	0.56
average	**203634.1**		**2.27**		**8.25**		**0.349**		**0.370**		**2.965**		**7.180**		**1.060**		**0.184**		**0.073**		**4.480**	
1 S.D.	**43903.7**		-		**3.03**		**0.077**		**0.128**		**0.587**		**3.903**		**0.198**		**0.028**		**0.014**		**0.368**	
11-2	99304.02	161848.61	1.97	0.27	10.2	1.43	1.62	0.13	0.063	0.029	2.5	0.14	4.31	0.2	BDL	0.13	0.075	0.012	0.056	0.014	2.6	0.22
11-4	BDL	918688.06	6.68	1.25	5.48	1.94	BDL	0.15	BDL	0.071	4.63	0.41	12.74	1.01	BDL	0.32	0.076	0.02	BDL	0.03	2.86	0.39
average	**99304.0**		**4.33**		**7.84**		**1.620**		**0.063**		**3.565**		**8.525**		-		**0.076**		**0.056**		**2.730**	
1 S.D.	-		**3.33**		**3.34**		-		-		**1.506**		**5.961**		-		**0.001**		-		**0.184**	

	Fe57	1 σ	Cu63	1 σ	Zn66	1 σ	Ga69	1 σ	Rb85	1 σ	Sr88	1 σ	Y89	1 σ	Zr90	1 σ	Nb93	1 σ	Cs133	1 σ	Ba137	1 σ
13-2	621194	9195919	BDL	0.56	BDL	5.71	BDL	0.16	BDL	0.067	1.3	0.18	6.62	0.56	BDL	0.37	0.204	0.034	BDL	0.029	3.08	0.42
13-5	334406.9	3872318.3	2.87	0.63	3.94	1.33	BDL	0.1	0.27	0.053	1.94	0.2	10.27	0.86	BDL	0.25	0.152	0.021	0.082	0.022	3.14	0.39
13-8	401971.8	3458741	BDL	0.42	2.7	1.33	BDL	0.12	0.251	0.059	1.33	0.16	2.91	0.26	1.01	0.3	0.419	0.041	BDL	0.024	3.28	0.42
13-9	281618.5	2030023.6	2.68	0.52	14.19	2.97	0.131	0.038	0.124	0.022	1.17	0.11	3.23	0.28	1.11	0.13	0.156	0.014	0.039	0.0083	1.54	0.19
13-10	226089.7	1568331.3	2.53	0.49	0.89	0.38	0.087	0.035	0.099	0.019	0.925	0.092	1.36	0.12	1.12	0.13	0.11	0.011	0.0319	0.0076	1.27	0.16
13-11	309804.7	2072074.1	4.11	0.8	BDL	0.36	BDL	0.037	0.141	0.023	1.6	0.15	3.26	0.29	0.99	0.12	0.15	0.014	0.0249	0.0079	1.62	0.2
13-12	249724.5	1613295.3	3.22	0.63	BDL	0.34	BDL	0.033	0.14	0.023	1.24	0.12	3.58	0.32	2.32	0.22	0.149	0.014	0.0311	0.0077	1.55	0.19
13-13	274284.1	1714368.1	2.63	0.52	1.49	0.45	0.159	0.039	0.203	0.028	1.47	0.14	4.55	0.4	2.69	0.26	0.288	0.024	0.0306	0.008	2.12	0.26
average	**337386.8**		**3.01**		**4.64**		**0.126**		**0.175**		**1.372**		**4.473**		**1.540**		**0.204**		**0.040**		**2.200**	
1 S.D.	**126858.3**		**0.59**		**5.46**		**0.036**		**0.066**		**0.305**		**2.782**		**0.758**		**0.102**		**0.021**		**0.836**	
14-3	204557.5	95790.28	BDL	0.15	2.78	0.46	0.13	0.043	0.244	0.024	2.252	0.096	9.42	0.34	1.1	0.12	0.199	0.014	0.0474	0.0091	1.71	0.11
14-6	227000.7	117508.24	BDL	0.17	3.77	0.56	0.128	0.049	0.205	0.027	2.274	0.1	13.49	0.49	1.46	0.13	0.215	0.015	0.0368	0.0099	1.63	0.11
14-7	225819.1	119618.95	BDL	0.16	2.39	0.46	0.17	0.044	0.155	0.023	2.123	0.092	11.07	0.4	3.42	0.18	0.281	0.016	0.0605	0.0097	1.67	0.11
14-8	186380.6	101113.5	BDL	0.14	2.4	0.42	0.098	0.039	0.148	0.021	1.677	0.075	7.07	0.26	1.1	0.11	0.192	0.013	0.0381	0.0087	1.62	0.1
14-9	271441.3	150937.59	BDL	0.15	3.48	0.49	0.259	0.042	0.278	0.024	2.72	0.11	14.79	0.54	4.85	0.23	0.333	0.018	0.05	0.0088	1.548	0.098
14-10	234341.3	133660.25	BDL	0.13	20.23	1.61	0.553	0.045	0.441	0.028	2.51	0.1	15.15	0.55	5.1	0.24	0.272	0.015	0.0971	0.0095	1.7	0.1
14-12	173632.8	613872.44	BDL	0.2	1.5	0.49	0.137	0.038	0.192	0.03	1.8	0.2	6.51	0.68	1.95	0.22	0.213	0.021	0.0244	0.0081	1.43	0.21
14-13	181332.2	634087	BDL	0.2	1.5	0.49	0.147	0.038	0.148	0.026	1.93	0.22	6.29	0.66	2.59	0.28	0.231	0.023	0.0259	0.008	1.68	0.25
average	**213063.2**		-		**4.76**		**0.203**		**0.226**		**2.161**		**10.474**		**2.696**		**0.242**		**0.048**		**1.624**	
1 S.D.	**32871.3**		-		**6.31**		**0.149**		**0.099**		**0.353**		**3.701**		**1.609**		**0.049**		**0.023**		**0.094**	
16-4	100702.7	424930.47	3.51	0.8	1.29	0.76	BDL	0.067	BDL	0.032	1	0.12	4.78	0.47	0.49	0.15	0.09	0.014	BDL	0.015	1.94	0.29
16-5	71234.88	295723.19	3.56	0.78	2.04	0.59	0.171	0.042	0.105	0.022	2.35	0.25	11.83	1.15	0.98	0.12	0.245	0.023	0.0193	0.0079	3.26	0.43
16-6	67329.19	266978.91	3.18	0.72	2.86	0.78	0.202	0.047	0.072	0.021	1.67	0.18	6.92	0.69	0.69	0.1	0.224	0.022	BDL	0.0089	2.85	0.39
16-8	73356.98	282779.97	2.44	0.57	36.45	8.79	0.359	0.068	0.095	0.027	1	0.12	3.21	0.32	1.65	0.2	0.185	0.02	0.026	0.011	2.51	0.36
16-9	74731.7	284221.31	2.27	0.53	1.73	0.54	BDL	0.036	0.094	0.021	1.28	0.14	3.89	0.39	2.14	0.23	0.223	0.022	0.035	0.0091	2.5	0.35

	Fe57	1 σ	Cu63	1 σ	Zn66	1 σ	Ga69	1 σ	Rb85	1 σ	Sr88	1 σ	Y89	1 σ	Zr90	1 σ	Nb93	1 σ	Cs133	1 σ	Ba137	1 σ
average	**77471.1**		**2.99**		**8.87**		**0.244**		**0.092**		**1.460**		**6.126**		**1.190**		**0.193**		**0.027**		**2.612**	
1 S.D.	**13284.3**		**0.60**		**15.43**		**0.101**		**0.014**		**0.568**		**3.481**		**0.689**		**0.062**		**0.008**		**0.488**	

	La139	1 σ	Ce140	1 σ	Pr141	1 σ	Nd146	1 σ	Sm147	1 σ	Eu151	1 σ	Eu153	1 σ	Gd157	1 σ	Tb159	1 σ	Dy163	1 σ	Ho165	1 σ
Sample	ppm		ppm		ppm		ppm		ppm		ppm		ppm		ppm		ppm		ppm		ppm	
2-1	0.247	0.015	0.468	0.027	0.071	0.0062	0.231	0.024	0.089	0.015	0.024	0.0054	0.0239	0.0054	0.086	0.024	0.0285	0.0036	0.255	0.025	0.0702	0.0064
2-2	0.162	0.011	0.323	0.02	0.0392	0.0047	0.141	0.019	0.042	0.012	0.0199	0.0055	0.0185	0.0053	0.072	0.022	0.0236	0.0035	0.17	0.019	0.0528	0.0055
2-3	0.216	0.015	0.384	0.024	0.0463	0.0054	0.175	0.024	0.029	0.01	0.0128	0.0044	0.0185	0.0056	0.075	0.022	0.0131	0.0028	0.132	0.018	0.0241	0.0039
2-5	0.201	0.013	0.359	0.022	0.0451	0.0047	0.245	0.024	0.043	0.011	0.0215	0.0052	0.0283	0.0051	0.092	0.021	0.0217	0.003	0.224	0.022	0.0773	0.007
2-6	0.255	0.017	0.444	0.027	0.0535	0.0055	0.213	0.024	0.078	0.014	0.0218	0.0054	0.0196	0.0052	0.073	0.021	0.0107	0.0024	0.122	0.016	0.0407	0.0047
2-7	0.136	0.01	0.277	0.018	0.0335	0.0043	0.131	0.018	0.0184	0.0087	0.0174	0.0048	0.0197	0.005	0.056	0.019	0.0182	0.0029	0.169	0.019	0.0427	0.0049
2-8	0.293	0.019	0.54	0.033	0.0706	0.0069	0.283	0.03	0.054	0.013	0.0233	0.0055	0.0263	0.0056	0.094	0.023	0.0224	0.0033	0.185	0.021	0.0512	0.0057
2-9	0.439	0.027	0.658	0.04	0.0779	0.0073	0.306	0.031	0.066	0.014	0.0251	0.006	0.0204	0.0046	0.081	0.022	0.0208	0.0032	0.225	0.023	0.0613	0.0064
2-10	0.252	0.017	0.516	0.032	0.0742	0.0069	0.251	0.027	0.099	0.016	0.0407	0.0064	0.0243	0.0051	0.143	0.026	0.031	0.004	0.287	0.027	0.0959	0.0089
average	**0.245**		**0.441**		**0.057**		**0.220**		**0.058**		**0.023**		**0.022**		**0.086**		**0.021**		**0.197**		**0.057**	
1 S.D.	**0.088**		**0.119**		**0.017**		**0.061**		**0.027**		**0.008**		**0.004**		**0.024**		**0.007**		**0.055**		**0.022**	
5-1	30.99	3.84	46.97	5.32	4.97	0.72	21.56	2.71	3.4	0.51	1.77	0.24	1.82	0.26	4.64	0.67	0.544	0.084	3.88	0.62	0.89	0.14
6-2	0.699	0.04	1.033	0.057	0.139	0.012	0.525	0.054	0.116	0.024	0.0332	0.0078	0.0319	0.0071	0.098	0.027	0.011	0.0031	0.065	0.015	0.0298	0.0051
6-3	0.191	0.014	0.545	0.032	0.0336	0.0047	0.114	0.02	0.0128	0.0087	0.0163	0.0053	0.0149	0.0048	0.03	0.019	0.0057	0.0021	0.068	0.013	0.0108	0.0026
6-5	0.526	0.032	0.94	0.053	0.0797	0.0087	0.423	0.047	0.049	0.017	0.0152	0.0063	0.0286	0.0069	0.091	0.026	0.0037	0.0023	0.109	0.019	0.0263	0.0047
6-7	18.13	1.98	26.81	2.67	2.48	0.32	9.01	1.06	1.9	0.31	0.86	0.12	0.97	0.14	1.96	0.32	0.3	0.049	2.49	0.38	0.548	0.083
average	**4.887**		**7.332**		**0.683**		**2.518**		**0.519**		**0.231**		**0.261**		**0.545**		**0.080**		**0.683**		**0.154**	
1 S.D.	**8.832**		**12.987**		**1.199**		**4.332**		**0.921**		**0.419**		**0.472**		**0.944**		**0.147**		**1.205**		**0.263**	

	La139	1 σ	Ce140	1 σ	Pr141	1 σ	Nd146	1 σ	Sm147	1 σ	Eu151	1 σ	Eu153	1 σ	Gd157	1 σ	Tb159	1 σ	Dy163	1 σ	Ho165	1 σ
8-2	2.3	0.14	3.48	0.21	0.364	0.029	1.58	0.12	0.327	0.038	0.109	0.014	0.106	0.012	0.383	0.05	0.0574	0.0069	0.427	0.042	0.104	0.011
8-3	3.64	0.22	6.22	0.38	0.672	0.052	2.72	0.2	0.477	0.048	0.201	0.021	0.2	0.019	0.688	0.073	0.0916	0.0097	0.765	0.066	0.169	0.016
average	**2.970**		**4.850**		**0.518**		**2.150**		**0.402**		**0.155**		**0.153**		**0.536**		**0.075**		**0.596**		**0.137**	
1 S.D.	**0.948**		**1.937**		**0.218**		**0.806**		**0.106**		**0.065**		**0.066**		**0.216**		**0.024**		**0.239**		**0.046**	
9-1	2.12	0.27	2.82	0.33	0.293	0.046	1.22	0.17	0.232	0.049	0.135	0.023	0.139	0.025	0.32	0.065	0.0463	0.0093	0.389	0.071	0.094	0.017
9-2	5.41	0.69	7.95	0.93	0.79	0.12	3.64	0.49	0.77	0.13	0.361	0.055	0.375	0.059	0.87	0.15	0.126	0.022	0.98	0.17	0.226	0.038
average	**3.765**		**5.385**		**0.542**		**2.430**		**0.501**		**0.248**		**0.257**		**0.595**		**0.086**		**0.685**		**0.160**	
1 S.D.	**2.326**		**3.627**		**0.351**		**1.711**		**0.380**		**0.160**		**0.167**		**0.389**		**0.056**		**0.418**		**0.093**	
11-2	1.58	0.11	2.96	0.2	0.325	0.03	1.41	0.13	0.311	0.048	0.071	0.015	0.083	0.015	0.469	0.072	0.0661	0.0097	0.571	0.064	0.114	0.014
11-4	7.07	0.74	13.06	1.25	1.21	0.15	4.4	0.5	1.05	0.17	0.29	0.046	0.304	0.048	1.2	0.2	0.187	0.029	1.63	0.24	0.369	0.053
average	**4.325**		**8.010**		**0.768**		**2.905**		**0.681**		**0.181**		**0.194**		**0.835**		**0.127**		**1.101**		**0.242**	
1 S.D.	**3.882**		**7.142**		**0.626**		**2.114**		**0.523**		**0.155**		**0.156**		**0.517**		**0.085**		**0.749**		**0.180**	
13-2	3.64	0.41	6.44	0.66	0.78	0.11	2.72	0.34	0.69	0.13	0.188	0.037	0.129	0.03	0.78	0.16	0.114	0.021	0.89	0.15	0.18	0.03
13-5	5.08	0.58	7.69	0.8	0.91	0.12	4.04	0.48	0.7	0.11	0.164	0.029	0.154	0.028	1.02	0.16	0.131	0.021	1.11	0.17	0.24	0.036
13-8	2.14	0.25	3.85	0.41	0.41	0.059	1.73	0.22	0.348	0.065	0.092	0.022	0.062	0.019	0.389	0.097	0.058	0.012	0.469	0.082	0.107	0.019
13-9	1.51	0.18	2.55	0.28	0.311	0.044	1.33	0.16	0.305	0.047	0.086	0.013	0.075	0.012	0.373	0.058	0.0482	0.0076	0.394	0.062	0.087	0.013
13-10	0.529	0.064	1.05	0.11	0.111	0.016	0.449	0.06	0.143	0.026	0.0359	0.0071	0.0339	0.0067	0.123	0.028	0.0264	0.0047	0.18	0.03	0.0445	0.0073
13-11	1.53	0.18	2.75	0.3	0.336	0.048	1.49	0.19	0.342	0.053	0.062	0.011	0.091	0.014	0.421	0.065	0.0616	0.0096	0.384	0.061	0.078	0.012
13-12	1.46	0.18	2.59	0.29	0.329	0.047	1.24	0.16	0.263	0.042	0.066	0.011	0.066	0.011	0.367	0.058	0.0568	0.0089	0.432	0.068	0.094	0.015
13-13	2.26	0.27	3.73	0.41	0.477	0.068	1.87	0.23	0.411	0.061	0.113	0.016	0.107	0.016	0.535	0.08	0.081	0.012	0.564	0.088	0.12	0.018
average	**2.269**		**3.831**		**0.458**		**1.859**		**0.400**		**0.101**		**0.090**		**0.501**		**0.072**		**0.553**		**0.119**	
1 S.D.	**1.444**		**2.197**		**0.263**		**1.089**		**0.198**		**0.052**		**0.039**		**0.279**		**0.035**		**0.302**		**0.063**	
14-3	3.16	0.14	5.08	0.23	0.621	0.034	2.49	0.14	0.532	0.044	0.177	0.015	0.197	0.015	0.775	0.063	0.139	0.01	0.947	0.06	0.22	0.015
14-6	5.24	0.24	7.8	0.35	0.942	0.052	4.06	0.22	0.852	0.062	0.312	0.024	0.262	0.019	1.178	0.089	0.183	0.013	1.221	0.076	0.307	0.02

	La139	1 σ	Ce140	1 σ	Pr141	1 σ	Nd146	1 σ	Sm147	1 σ	Eu151	1 σ	Eu153	1 σ	Gd157	1 σ	Tb159	1 σ	Dy163	1 σ	Ho165	1 σ
14-7	3.88	0.18	6.21	0.28	0.733	0.041	3.13	0.17	0.629	0.047	0.221	0.017	0.211	0.015	0.936	0.071	0.14	0.01	1.058	0.065	0.257	0.017
14-8	2.37	0.11	3.94	0.18	0.45	0.026	2	0.12	0.418	0.036	0.129	0.012	0.137	0.012	0.605	0.052	0.0964	0.0077	0.733	0.049	0.157	0.011
14-9	5.13	0.24	8.33	0.38	1.022	0.056	4.35	0.23	0.938	0.062	0.318	0.023	0.309	0.02	1.349	0.094	0.203	0.014	1.457	0.086	0.383	0.024
14-10	6.3	0.29	9.23	0.43	1.197	0.066	4.94	0.26	0.923	0.06	0.349	0.024	0.368	0.023	1.392	0.096	0.225	0.015	1.616	0.094	0.377	0.023
14-12	2.25	0.33	3.78	0.5	0.426	0.073	1.87	0.28	0.394	0.07	0.124	0.021	0.116	0.02	0.59	0.1	0.09	0.016	0.73	0.13	0.164	0.03
14-13	2.19	0.32	3.66	0.49	0.428	0.074	1.85	0.28	0.356	0.064	0.103	0.018	0.137	0.024	0.506	0.089	0.086	0.015	0.66	0.12	0.172	0.031
average	**3.815**		**6.004**		**0.727**		**3.086**		**0.630**		**0.217**		**0.217**		**0.916**		**0.145**		**1.053**		**0.255**	
1 S.D.	**1.583**		**2.225**		**0.298**		**1.226**		**0.244**		**0.098**		**0.090**		**0.353**		**0.054**		**0.355**		**0.093**	
16-4	2.4	0.32	3.75	0.46	0.429	0.069	1.97	0.28	0.273	0.06	0.231	0.038	0.24	0.041	0.455	0.092	0.062	0.012	0.402	0.077	0.108	0.02
16-5	6.61	0.89	9.7	1.2	1.15	0.18	4.63	0.63	0.88	0.14	0.72	0.1	0.68	0.1	1.23	0.19	0.163	0.027	1.08	0.19	0.244	0.041
16-6	3.75	0.52	5.54	0.7	0.64	0.1	2.62	0.37	0.454	0.077	0.437	0.064	0.373	0.058	0.68	0.11	0.098	0.017	0.64	0.11	0.144	0.025
16-8	0.92	0.13	1.41	0.18	0.149	0.026	0.578	0.091	0.181	0.039	0.067	0.014	0.059	0.013	0.151	0.043	0.0242	0.0057	0.282	0.055	0.088	0.016
16-9	1.78	0.25	2.61	0.33	0.323	0.053	1.4	0.2	0.247	0.045	0.139	0.022	0.137	0.023	0.339	0.061	0.0447	0.0083	0.37	0.068	0.095	0.017
average	**3.092**		**4.602**		**0.538**		**2.240**		**0.407**		**0.319**		**0.298**		**0.571**		**0.078**		**0.555**		0.136	
1 S.D.	**2.221**		**3.231**		**0.385**		**1.533**		**0.283**		**0.264**		**0.244**		**0.415**		**0.055**		**0.322**		**0.064**	

	Er166	1 σ	Yb172	1 σ	Lu175	1 σ	Hf178	1 σ	Ta181	1 σ	Pb208	1 σ	Th232	1 σ	U238	1 σ
Sample	ppm		ppm		ppm		ppm		ppm		ppm		ppm		ppm	
2-1	0.295	0.024	0.611	0.051	0.0983	0.0067	0.0105	0.0051	0.0056	0.0023	1.229	0.073	0.0172	0.0021	0.0364	0.0036
2-2	0.215	0.02	0.497	0.045	0.0863	0.0067	0.0259	0.0065	BDL	0.0023	0.401	0.028	0.026	0.003	0.0412	0.0042
2-3	0.088	0.013	0.218	0.028	0.0435	0.005	0.0099	0.0062	BDL	0.0021	0.115	0.013	0.0279	0.0035	0.031	0.0038
2-5	0.3	0.025	0.646	0.056	0.1107	0.0075	0.0153	0.0063	BDL	0.0019	0.567	0.038	0.0509	0.0044	0.041	0.004
2-6	0.204	0.02	0.567	0.052	0.0965	0.007	0.0512	0.0082	BDL	0.0026	0.198	0.017	0.0618	0.0053	0.0352	0.0038
2-7	0.162	0.017	0.546	0.051	0.0978	0.0071	0.0161	0.0057	BDL	0.0019	0.325	0.025	0.0207	0.0026	0.0377	0.004
2-8	0.193	0.02	0.466	0.046	0.0973	0.0073	0.0108	0.0059	0.0079	0.0027	0.219	0.019	0.0471	0.0045	0.0329	0.0038
2-9	0.313	0.028	0.608	0.057	0.1018	0.0074	0.0374	0.0067	0.0259	0.0037	0.511	0.037	0.0422	0.0042	0.0469	0.0048

	Er166	1 σ	Yb172	1 σ	Lu175	1 σ	Hf178	1 σ	Ta181	1 σ	Pb208	1 σ	Th232	1 σ	U238	1 σ
2-10	0.358	0.031	0.595	0.056	0.0927	0.0069	0.0219	0.006	BDL	0.0021	0.661	0.046	0.0347	0.0035	0.0353	0.0038
average	**0.236**		**0.528**		**0.092**		**0.022**		**0.013**		**0.470**		**0.037**		**0.038**	
1 S.D.	**0.086**		**0.130**		**0.019**		**0.014**		**0.011**		**0.338**		**0.015**		**0.005**	
5-1	2.45	0.36	2.43	0.4	0.313	0.046	0.065	0.02	0.088	0.017	4.89	0.86	0.351	0.054	0.75	0.13
6-2	0.096	0.016	0.106	0.021	0.0116	0.0034	BDL	0.0049	BDL	0.0019	0.126	0.016	0.0061	0.0019	0.0152	0.003
6-3	0.06	0.011	0.052	0.013	0.0092	0.0024	BDL	0.0039	BDL	0.0019	0.314	0.025	0.0045	0.0014	0.0163	0.0027
6-5	0.07	0.014	0.095	0.02	0.0088	0.0031	0.047	0.011	BDL	0.0016	0.29	0.026	0.0114	0.0026	0.0229	0.0037
6-7	1.57	0.23	1.46	0.25	0.278	0.044	BDL	0.02	0.043	0.017	6.28	0.97	0.219	0.036	0.26	0.047
average	**0.449**		**0.428**		**0.077**		**0.047**		**0.043**		**1.753**		**0.060**		**0.079**	
1 S.D.	**0.747**		**0.688**		**0.134**		-		-		**3.019**		**0.106**		**0.121**	
8-2	0.325	0.032	0.319	0.039	0.0512	0.0054	0.0193	0.0058	BDL	0.0027	0.336	0.029	0.0334	0.004	0.023	0.0033
8-3	0.517	0.047	0.464	0.05	0.0709	0.0064	BDL	0.005	BDL	0.0024	0.308	0.026	0.0513	0.0052	0.0216	0.0031
average	**0.421**		**0.392**		**0.061**		**0.019**		-		**0.322**		**0.042**		**0.022**	
1 S.D.	**0.136**		**0.103**		**0.014**		-		-		**0.020**		**0.013**		**0.001**	
9-1	0.295	0.051	0.251	0.052	0.0494	0.0092	0.038	0.012	0.0073	0.0041	0.98	0.18	0.082	0.014	0.058	0.012
9-2	0.73	0.12	0.55	0.1	0.094	0.016	0.039	0.013	BDL	0.0041	1.68	0.31	0.116	0.019	0.049	0.011
average	**0.513**		**0.401**		**0.072**		**0.039**		**0.007**		**1.330**		**0.099**		**0.054**	
1 S.D.	**0.308**		**0.211**		**0.032**		**0.001**		-		**0.495**		**0.024**		**0.006**	
11-2	0.388	0.046	0.427	0.06	0.0671	0.0088	BDL	0.011	BDL	0.0044	0.352	0.037	0.0244	0.0046	0.0459	0.0068
11-4	1.15	0.16	1.1	0.18	0.196	0.029	0.032	0.017	0.025	0.011	0.457	0.081	0.061	0.012	0.0392	0.0097
average	**0.769**		**0.764**		**0.132**		**0.032**		**0.025**		**0.405**		**0.043**		**0.043**	
1 S.D.	**0.539**		**0.476**		**0.091**		-		-		**0.074**		**0.026**		**0.005**	

	Er166	1 σ	Yb172	1 σ	Lu175	1 σ	Hf178	1 σ	Ta181	1 σ	Pb208	1 σ	Th232	1 σ	U238	1 σ
13-2	0.68	0.11	0.51	0.099	0.105	0.019	0.064	0.029	BDL	0.012	1	0.17	0.192	0.029	0.055	0.012
13-5	0.73	0.11	0.65	0.11	0.121	0.018	0.034	0.018	BDL	0.0077	1.55	0.25	0.183	0.026	0.0415	0.0084
13-8	0.294	0.05	0.301	0.063	0.048	0.011	BDL	0.019	0.025	0.01	1.6	0.27	0.223	0.032	0.048	0.0098
13-9	0.257	0.038	0.265	0.044	0.0345	0.0055	0.0181	0.0065	0.0082	0.0028	0.454	0.077	0.097	0.014	0.0207	0.004
13-10	0.112	0.019	0.171	0.03	0.0227	0.0041	0.0398	0.0081	BDL	0.0022	0.384	0.066	0.0608	0.009	0.0222	0.0043
13-11	0.269	0.04	0.28	0.047	0.0429	0.0067	0.022	0.0073	0.0152	0.0037	0.463	0.079	0.158	0.022	0.0272	0.0052
13-12	0.314	0.046	0.351	0.057	0.0482	0.0072	0.0235	0.0066	0.006	0.0027	0.462	0.079	0.103	0.015	0.0288	0.0054
13-13	0.37	0.054	0.375	0.061	0.0565	0.0082	0.0231	0.0077	0.0124	0.0034	0.62	0.11	0.134	0.019	0.0321	0.006
average	**0.378**		**0.363**		**0.060**		**0.032**		**0.013**		**0.817**		**0.144**		**0.034**	
1 S.D.	**0.215**		**0.152**		**0.035**		**0.016**		**0.007**		**0.506**		**0.055**		**0.012**	
14-3	0.734	0.047	0.526	0.043	0.086	0.0065	0.0241	0.0065	0.0108	0.0029	1.42	0.075	0.241	0.014	0.0794	0.0062
14-6	0.889	0.057	0.736	0.057	0.1095	0.0079	0.0335	0.008	0.0182	0.0037	1.091	0.061	0.334	0.019	0.0698	0.0059
14-7	0.77	0.049	0.626	0.048	0.1031	0.0069	0.0541	0.0088	0.0171	0.0036	1.342	0.072	0.321	0.018	0.086	0.0065
14-8	0.512	0.035	0.503	0.041	0.0626	0.005	0.0149	0.0069	0.0126	0.0029	1.053	0.058	0.21	0.012	0.0614	0.0051
14-9	1.033	0.064	0.939	0.066	0.1461	0.0086	0.0554	0.0081	0.0197	0.0034	1.594	0.085	0.393	0.021	0.096	0.007
14-10	1.103	0.067	0.977	0.068	0.1478	0.0084	0.109	0.011	0.0249	0.0031	1.293	0.07	0.393	0.021	0.0932	0.0067
14-12	0.5	0.086	0.435	0.084	0.0594	0.0099	0.0292	0.0075	0.0202	0.0045	0.98	0.2	0.209	0.035	0.054	0.012
14-13	0.494	0.086	0.481	0.093	0.062	0.01	0.069	0.013	0.0132	0.0036	0.99	0.2	0.226	0.038	0.058	0.012
average	**0.754**		**0.653**		**0.097**		**0.049**		**0.017**		**1.220**		**0.291**		**0.075**	
1 S.D.	**0.242**		**0.210**		**0.036**		**0.030**		**0.005**		**0.225**		**0.079**		**0.016**	
16-4	0.259	0.048	0.304	0.064	0.065	0.012	0.027	0.011	BDL	0.0046	0.461	0.092	0.141	0.024	0.0393	0.0089
16-5	0.76	0.12	0.68	0.12	0.109	0.016	0.0259	0.0078	0.0156	0.0035	0.87	0.17	0.315	0.049	0.1	0.019
16-6	0.445	0.073	0.441	0.081	0.073	0.012	0.0179	0.0072	0.0101	0.003	0.71	0.14	0.294	0.047	0.08	0.016
16-8	0.236	0.043	0.23	0.048	0.0391	0.0077	0.0199	0.0091	BDL	0.0035	0.72	0.14	0.126	0.021	0.067	0.014
16-9	0.261	0.045	0.24	0.047	0.0422	0.0072	0.0288	0.0083	0.0085	0.003	0.75	0.15	0.186	0.03	0.072	0.015
average	**0.392**		**0.379**		**0.066**		**0.024**		**0.011**		**0.702**		**0.212**		**0.072**	
1 S.D.	**0.222**		**0.188**		**0.028**		**0.005**		**0.004**		**0.149**		**0.087**		**0.022**	

4.2 BCR-2G

Table 3: LA-ICP-MS determined major and trace elemental abundance (ppm) of BCR-2G reference material. 1 σ represents the counting statistics 1 sigma error calculated in Glitter software (see Materials and methods); 1 S.D. is the standard deviation for the average elemental concentration of BCR-2G. BDL stands for below detection limit. Almost all measured concentrations are lower than the accepted values (GeoRem) for the BCR-2G reference material and are outside of the 1 S.D. range (except for Mn and Cs). Bias % indicates the relative difference between the measured and accepted values.

	Mg24	1 σ	Mg26	1 σ	Al27	1 σ	Ca43	1 σ	Sc45	1 σ	Ti47	1 σ	Ti49	1 σ	V51	1 σ	Cr52	1 σ	Mn55	1 σ
Sample	ppm		ppm		ppm		ppm		ppm		ppm		ppm		ppm		ppm		ppm	
BCR-2G	26285.5	4473.4	36342.6	28575.7	69903.1	2382.0	45012.6	1679.3	33.70	1.13	15041.2	6825.7	16691.9	1157.5	449.5	16.2	17.87	0.68	1580.4	53.0
BCR-2G	29766.1	42089.4	42422.3	121221.2	69253.7	3303.6	43627.0	4092.8	32.70	2.83	6740.5	61911.6	15844.1	3181.8	435.8	36.0	17.44	4.72	1633.1	534.5
BCR-2G	28316.7	39892.3	34699.8	85329.4	67899.7	3327.1	42744.1	4132.4	31.94	2.87	6572.1	61404.1	15730.8	3281.5	437.2	37.6	17.49	4.94	1618.3	548.6
BCR-2G	27399.8	38571.0	29477.4	63524.7	68804.8	3481.0	43478.9	4352.8	32.34	3.03	6239.3	59535.9	15775.0	3438.8	443.5	40.0	17.24	5.11	1624.3	573.6
BCR-2G	26681.3	37606.4	26566.8	52882.5	70589.1	3660.4	44191.5	4542.5	33.86	3.27	6425.7	62330.3	16126.6	3633.3	445.3	41.6	17.22	5.29	1608.6	585.8
BCR-2G	27886.2	6018.6	40976.5	42690.1	67871.3	2369.8	43387.6	1694.8	31.90	1.10	14832.3	8007.4	15942.7	1220.1	442.6	16.6	16.77	0.67	1574.6	54.4
BCR-2G	38850.9	64565.2	BDL	617087.2	61559.0	2610.5	40403.2	3352.6	26.65	2.00	7020.4	62995.3	14709.1	2474.5	392.7	26.7	16.05	3.56	1547.6	432.6
BCR-2G	36594.9	58212.8	BDL	2621877.8	61537.7	2632.5	39064.5	3262.1	25.88	1.96	7126.7	63255.1	14171.0	2414.1	385.5	26.6	14.15	3.20	1482.3	418.3
BCR-2G	34804.9	53198.8	1011194.9	-	60959.5	2643.9	39067.2	3306.6	25.75	2.00	6541.7	57748.8	13997.7	2435.0	394.0	27.9	15.97	3.70	1484.1	426.3
BCR-2G	32457.9	48156.6	147698.1	1432525.6	61743.8	2724.3	37635.9	3247.5	23.98	1.92	6398.7	56558.4	14165.9	2530.4	392.5	28.6	14.76	3.53	1462.7	430.1
BCR-2G	33192.3	48329.1	93465.7	541074.6	67321.0	3020.5	44626.6	3904.3	32.55	2.58	7122.0	63295.1	15898.5	2915.1	426.2	31.9	16.72	4.09	1647.6	496.0
BCR-2G	31873.9	45614.1	61052.6	237251.7	69044.1	3178.1	44707.4	4026.8	32.88	2.71	7018.8	63139.1	15974.5	3044.6	435.0	34.0	17.20	4.39	1634.8	509.8
BCR-2G	30726.7	43713.4	51746.4	174764.1	68295.7	3187.5	44463.8	4069.1	33.08	2.78	6954.4	63044.1	16161.7	3144.1	439.5	35.1	17.91	4.68	1665.8	529.4
BCR-2G	43509.0	83454.6	BDL	120157.9	59304.1	2494.3	40771.5	3406.7	26.26	1.94	6998.3	66150.0	13854.0	2316.3	374.6	25.0	14.72	3.22	1552.0	434.3
BCR-2G	42695.9	76423.2	BDL	217845.5	61240.6	2579.3	41476.4	3443.7	26.04	1.94	7241.7	66618.1	14294.4	2386.2	389.5	26.1	15.34	3.37	1534.5	427.3
BCR-2G	29497.1	7607.8	44750.1	57204.6	69178.8	2482.4	44157.1	1805.0	32.72	1.15	15410.0	9583.0	16237.7	1365.6	442.6	17.3	16.68	0.69	1552.0	55.3
BCR-2G	30313.9	9165.4	47738.7	73519.8	67974.0	2513.4	43959.5	1889.1	31.93	1.16	15182.2	10725.9	15883.7	1462.5	435.6	17.7	16.76	0.74	1583.2	58.4
BCR-2G	31789.2	11458.6	51809.7	98667.3	68421.1	2630.9	44229.1	2020.3	32.51	1.22	15402.1	12525.5	15952.7	1630.6	431.4	18.5	16.75	0.77	1552.9	59.9
BCR-2G	33044.1	13505.0	55316.3	123251.6	67893.9	2695.0	43693.2	2097.6	31.78	1.24	14494.8	13021.6	15840.9	1747.0	428.9	19.2	16.65	0.81	1562.3	62.6
BCR-2G	26844.3	4973.9	38054.9	33259.9	69121.4	2370.4	43510.8	1644.3	32.46	1.10	14817.6	7120.5	16468.6	1174.6	443.2	16.2	16.83	0.65	1542.1	52.1
average BCRG2	32126.5		113332.1		66395.8		42710.4		30.55		9679.0		15486.1		423.2		16.53		1572.1	
1 S.D.	**5026.9**		**241249.1**		**3691.0**		**2183.7**		**3.29**		**4038.3**		**906.6**		**24.5**		**1.06**		**56.4**	
GeoRem value	21470.4		-		70925.7		50457.4		33.00		14100.0		14100.0		425.0		17.00		1550.0	
Georem 1 S.D.	542.8		-		2117.2		786.2		2.00		1000.0		1000.0		18.0		2.00		70.0	
bias (%)	49.6		-		6.4		15.4		7.44		31.4		9.8		0.4		2.79		1.4	

	Fe57	1 σ	Cu63	1 σ	Zn66	1 σ	Ga69	1 σ	Rb85	1 σ	Sr88	1 σ	Y89	1 σ	Zr90	1 σ	Nb93	1 σ	Cs133	1 σ	Ba137	1 σ
Sample	ppm		ppm		ppm		ppm		ppm		ppm		ppm		ppm		ppm		ppm		ppm	
BCR-2G	130517.8	58350.7	17.02	0.76	155.3	11.0	43.49	1.78	53.18	2.03	334.7	12.4	32.53	1.16	166.73	6.87	11.45	0.46	1.25	0.06	659.6	27.6
BCR-2G	185426.3	840060.4	16.79	3.54	138.1	31.3	38.47	4.61	49.21	5.69	312.7	31.4	30.20	2.86	156.56	14.96	10.81	0.88	1.13	0.14	624.6	78.4
BCR-2G	158507.2	637896.6	15.75	3.48	136.7	32.3	38.84	4.87	49.92	6.01	312.6	32.7	30.79	3.03	154.58	15.30	10.98	0.93	1.20	0.15	615.9	80.7
BCR-2G	136534.5	493910.8	16.62	3.87	139.4	34.5	39.61	5.24	50.35	6.36	322.6	35.3	31.27	3.22	160.44	16.55	11.20	0.99	1.26	0.17	646.7	89.0

	Fe57	1 σ	Cu63	1 σ	Zn66	1 σ	Ga69	1 σ	Rb85	1 σ	Sr88	1 σ	Y89	1 σ	Zr90	1 σ	Nb93	1 σ	Cs133	1 σ	Ba137	1 σ
Sample	ppm		ppm		ppm		ppm		ppm		ppm		ppm		ppm		ppm		ppm		ppm	
BCR-2G	122876.0	416478.0	16.66	4.03	138.2	35.4	40.38	5.55	50.01	6.54	330.1	37.4	32.10	3.42	162.97	17.34	11.52	1.05	1.19	0.16	658.5	94.0
BCR-2G	153681.8	94959.2	14.73	0.72	143.4	11.2	41.46	1.80	50.52	2.02	304.6	11.8	29.78	1.10	153.11	6.68	10.75	0.45	1.15	0.06	604.5	27.0
BCR-2G	BDL	-	11.63	2.03	129.8	24.4	37.32	3.59	48.18	4.58	270.9	22.4	26.96	2.13	141.19	11.49	10.08	0.69	0.98	0.10	536.4	54.8
BCR-2G	6062984.5	-	13.78	2.41	130.6	24.9	37.82	3.71	46.85	4.52	269.7	22.7	26.17	2.10	138.12	11.37	10.11	0.70	1.07	0.11	535.3	55.6
BCR-2G	822538.8	-	13.77	2.48	130.5	25.5	37.35	3.77	47.54	4.70	266.0	22.9	26.17	2.14	135.02	11.33	10.35	0.74	1.07	0.12	539.7	57.6
BCR-2G	444709.0	4513464.5	11.44	2.17	127.5	25.6	36.50	3.81	46.51	4.74	265.3	23.5	25.82	2.18	131.98	11.35	10.10	0.74	1.04	0.12	535.8	59.0
BCR-2G	336642.9	2527041.3	15.61	2.94	135.9	28.0	38.02	4.09	49.37	5.17	304.9	27.8	30.34	2.62	155.52	13.67	10.69	0.79	1.11	0.12	600.6	68.1
BCR-2G	244968.6	1398792.3	16.23	3.21	137.3	29.4	37.89	4.27	49.66	5.42	314.0	29.8	31.21	2.80	158.92	14.47	11.00	0.85	1.19	0.13	625.9	74.1
BCR-2G	220202.6	1133608.8	16.59	3.36	142.1	31.1	39.62	4.57	49.61	5.54	313.6	30.4	30.84	2.82	156.23	14.50	11.15	0.88	1.21	0.14	617.0	74.8
BCR-2G	BDL	2440624.5	13.31	2.23	133.6	24.8	36.57	3.44	48.78	4.57	272.6	22.3	25.94	2.02	136.28	11.03	10.05	0.68	1.07	0.11	548.4	55.1
BCR-2G	BDL	5401321.5	11.58	2.00	156.4	29.0	42.40	4.01	46.85	4.40	270.2	22.1	26.15	2.04	138.80	11.22	10.03	0.68	1.05	0.11	539.0	54.3
BCR-2G	170717.6	133183.5	16.14	0.82	145.6	12.5	40.99	1.88	49.74	2.08	311.5	12.7	30.47	1.16	154.02	7.12	10.90	0.48	1.12	0.06	607.2	28.9
BCR-2G	191278.1	185408.0	15.86	0.86	139.5	13.2	40.48	1.98	50.05	2.20	310.4	13.2	30.17	1.20	154.56	7.58	11.01	0.52	1.20	0.06	622.7	31.6
BCR-2G	211184.8	264411.0	15.86	0.92	138.2	14.5	40.18	2.11	49.90	2.33	315.8	14.3	30.47	1.28	156.34	8.25	10.94	0.55	1.19	0.07	622.3	34.2
BCR-2G	237811.7	362543.0	15.82	0.98	136.1	15.4	40.13	2.23	49.54	2.42	313.1	14.9	30.30	1.32	155.84	8.71	11.00	0.58	1.17	0.07	617.0	36.0
BCR-2G	139845.5	70808.9	17.12	0.78	157.2	11.5	41.64	1.73	50.24	1.94	316.8	11.9	30.99	1.11	159.92	6.69	11.24	0.45	1.17	0.05	630.7	26.9
average BCRG2	586495.7		15.12		139.6		39.46		49.30		301.6		29.43		151.36		10.77		1.14		599.4	
1 S.D.	**1421457.7**		**1.88**		**8.5**		**1.97**		**1.54**		**23.0**		**2.27**		**10.35**		**0.48**		**0.08**		**43.3**	
GeoRem value	125078.7		21.00		125.0		23.00		47.00		342.0		35.00		184.00		12.50		1.16		683.0	
Georem 1 S.D.	899.8		5.00		5.0		1.00		0.50		4.0		3.00		15.00		1.00		0.07		7.0	
bias (%)	368.9		28.02		11.7		71.56		4.89		11.8		15.90		17.74		13.86		1.65		12.2	

	La139	1 σ	Ce140	1 σ	Pr141	1 σ	Nd146	1 σ	Sm147	1 σ	Eu151	1 σ	Eu153	1 σ	Gd157	1 σ	Tb159	1 σ	Dy163	1 σ	Ho165	1 σ
Sample	ppm		ppm		ppm		ppm		ppm		ppm		ppm		ppm		ppm		ppm		ppm	
BCR-2G	24.34	1.07	52.78	2.31	6.48	0.33	27.27	1.31	6.34	0.32	1.83	0.10	1.83	0.09	6.33	0.37	0.985	0.057	6.23	0.32	1.20	0.07
BCR-2G	23.30	3.04	49.26	5.88	6.10	0.93	26.21	3.45	5.60	0.83	1.68	0.23	1.74	0.25	5.81	0.85	0.850	0.130	5.79	0.95	1.13	0.18
BCR-2G	22.92	3.12	49.67	6.19	6.05	0.96	25.77	3.54	5.87	0.91	1.74	0.25	1.70	0.26	5.87	0.90	0.840	0.140	5.79	0.99	1.11	0.18
BCR-2G	23.74	3.40	51.19	6.71	6.26	1.04	26.82	3.88	5.79	0.94	1.81	0.27	1.86	0.29	6.42	1.03	0.900	0.150	5.99	1.07	1.12	0.19
BCR-2G	24.60	3.66	52.29	7.12	6.53	1.13	27.74	4.17	6.64	1.12	1.86	0.29	1.80	0.30	6.26	1.05	0.940	0.170	6.06	1.13	1.20	0.22
BCR-2G	22.16	1.04	47.46	2.23	5.85	0.32	25.09	1.32	5.45	0.30	1.66	0.10	1.64	0.09	5.86	0.38	0.900	0.057	5.49	0.31	1.10	0.07
BCR-2G	19.83	2.10	42.24	4.07	5.18	0.64	22.38	2.39	4.94	0.60	1.45	0.16	1.53	0.18	4.61	0.57	0.721	0.092	4.44	0.60	0.91	0.12

	La139	1 σ	Ce140	1 σ	Pr141	1 σ	Nd146	1 σ	Sm147	1 σ	Eu151	1 σ	Eu153	1 σ	Gd157	1 σ	Tb159	1 σ	Dy163	1 σ	Ho165	1 σ
Sample	ppm		ppm		ppm		ppm		ppm		ppm		ppm		ppm		ppm		ppm		ppm	
BCR-2G	19.28	2.08	42.08	4.13	5.15	0.64	22.34	2.43	5.03	0.63	1.40	0.16	1.45	0.18	4.98	0.62	0.757	0.098	4.92	0.67	0.96	0.13
BCR-2G	19.68	2.18	41.68	4.20	5.23	0.67	22.25	2.49	4.99	0.64	1.45	0.17	1.39	0.17	4.70	0.61	0.708	0.095	4.58	0.64	0.94	0.13
BCR-2G	19.60	2.24	41.71	4.35	5.17	0.69	22.31	2.58	4.95	0.66	1.44	0.18	1.34	0.18	5.21	0.69	0.780	0.110	4.84	0.70	0.96	0.14
BCR-2G	22.07	2.60	46.92	5.04	5.83	0.80	25.15	2.97	5.52	0.73	1.62	0.20	1.64	0.21	5.70	0.75	0.850	0.120	5.40	0.80	1.07	0.15
BCR-2G	23.32	2.87	49.68	5.58	6.20	0.89	26.05	3.22	5.87	0.81	1.70	0.22	1.75	0.24	5.77	0.80	0.860	0.130	5.75	0.88	1.09	0.16
BCR-2G	23.17	2.92	49.05	5.64	6.05	0.88	25.75	3.26	5.85	0.83	1.69	0.22	1.69	0.23	6.04	0.85	0.840	0.130	5.71	0.90	1.12	0.17
BCR-2G	19.72	2.05	42.34	4.00	5.46	0.66	22.33	2.33	4.83	0.57	1.45	0.16	1.60	0.18	4.75	0.57	0.764	0.095	5.18	0.68	0.96	0.12
BCR-2G	20.40	2.13	42.95	4.08	5.42	0.66	22.57	2.37	5.08	0.61	1.45	0.16	1.45	0.17	5.22	0.63	0.754	0.095	5.56	0.73	0.98	0.13
BCR-2G	22.51	1.13	48.60	2.44	5.87	0.35	25.35	1.44	5.75	0.34	1.66	0.11	1.70	0.10	5.72	0.40	0.853	0.059	5.40	0.33	1.07	0.07
BCR-2G	22.67	1.22	49.50	2.67	6.04	0.39	25.74	1.58	5.61	0.36	1.74	0.13	1.75	0.11	5.86	0.44	0.833	0.063	5.82	0.39	1.10	0.08
BCR-2G	23.13	1.36	49.37	2.90	6.17	0.44	26.36	1.77	6.15	0.42	1.76	0.14	1.75	0.12	5.97	0.50	0.896	0.074	5.89	0.43	1.19	0.09
BCR-2G	22.68	1.42	48.76	3.06	6.07	0.46	26.04	1.88	5.87	0.44	1.72	0.15	1.70	0.13	5.80	0.52	0.861	0.077	5.78	0.45	1.10	0.10
BCR-2G	23.06	1.03	49.45	2.21	6.07	0.31	25.83	1.28	5.98	0.31	1.73	0.10	1.65	0.09	5.89	0.35	0.864	0.051	5.75	0.30	1.13	0.06
average BCRG2	22.11		47.35		5.86		24.97		5.61		1.64		1.65		5.64		0.838		5.52		1.07	
1 S.D.	**1.71**		**3.74**		**0.44**		**1.86**		**0.51**		**0.15**		**0.15**		**0.54**		**0.072**		**0.49**		**0.09**	
GeoRem value	24.70		53.30		6.70		28.90		6.59		1.97		1.97		6.71		1.020		6.44		1.27	
Georem 1 S.D.	0.30		0.50		0.40		0.30		0.07		0.02		0.02		0.07		0.080		0.06		0.08	
bias (%)	10.49		11.17		12.55		13.61		14.94		16.65		16.35		15.97		17.863		14.31		15.53	

	Er166	1 σ	Yb172	1 σ	Lu175	1 σ	Hf178	1 σ	Ta181	1 σ	Pb208	1 σ	Th232	1 σ	U238
Sample	ppm		ppm		ppm		ppm		ppm		ppm		ppm		ppm
BCR-2G	3.38	0.18	3.40	0.20	0.482	0.022	4.37	0.20	0.741	0.036	13.60	0.65	5.70	0.27	1.66
BCR-2G	3.15	0.48	3.01	0.50	0.451	0.063	4.14	0.55	0.626	0.090	10.60	1.95	5.11	0.76	1.60
BCR-2G	3.00	0.48	2.94	0.51	0.456	0.066	3.85	0.54	0.680	0.100	10.89	2.09	5.05	0.79	1.53
BCR-2G	3.36	0.56	3.20	0.59	0.440	0.067	4.18	0.61	0.700	0.110	10.88	2.20	5.26	0.86	1.63
BCR-2G	3.37	0.58	3.02	0.57	0.452	0.071	4.21	0.64	0.690	0.110	11.45	2.40	5.41	0.92	1.67
BCR-2G	2.97	0.18	3.12	0.21	0.461	0.023	3.90	0.19	0.684	0.037	13.44	0.69	5.05	0.26	1.51
BCR-2G	2.45	0.31	2.38	0.33	0.383	0.047	3.35	0.38	0.529	0.066	9.76	1.45	4.39	0.53	1.38
BCR-2G	2.68	0.34	2.45	0.35	0.410	0.051	3.52	0.40	0.580	0.073	9.77	1.47	4.46	0.55	1.38
BCR-2G	2.65	0.35	2.63	0.38	0.326	0.043	3.83	0.45	0.559	0.072	9.40	1.46	4.56	0.58	1.45
BCR-2G	2.59	0.35	2.16	0.33	0.429	0.056	3.12	0.38	0.586	0.078	9.56	1.53	4.36	0.57	1.37

	Er166	1 σ	Yb172	1 σ	Lu175	1 σ	Hf178	1 σ	Ta181	1 σ	Pb208	1 σ	Th232	1 σ	U238
Sample	ppm		ppm		ppm		ppm		ppm		ppm		ppm		ppm
BCR-2G	2.95	0.40	2.85	0.43	0.421	0.053	3.81	0.46	0.613	0.080	10.15	1.67	4.82	0.65	1.47
BCR-2G	3.14	0.45	3.02	0.47	0.426	0.056	3.96	0.50	0.665	0.090	11.46	1.98	5.09	0.72	1.62
BCR-2G	3.08	0.45	2.99	0.48	0.462	0.062	3.92	0.51	0.691	0.096	10.64	1.88	5.08	0.73	1.61
BCR-2G	2.85	0.35	2.73	0.37	0.391	0.047	3.49	0.39	0.622	0.075	10.62	1.54	4.68	0.56	1.46
BCR-2G	2.68	0.33	2.67	0.37	0.379	0.046	3.77	0.42	0.606	0.074	10.46	1.53	4.55	0.54	1.38
BCR-2G	3.00	0.19	2.96	0.21	0.420	0.022	3.87	0.20	0.653	0.037	12.73	0.71	5.15	0.28	1.54
BCR-2G	3.02	0.21	2.92	0.23	0.398	0.022	3.88	0.22	0.642	0.040	28.52	1.70	4.93	0.30	1.55
BCR-2G	3.29	0.25	2.99	0.26	0.473	0.027	4.14	0.25	0.704	0.047	11.16	0.73	5.29	0.35	1.58
BCR-2G	3.13	0.26	3.03	0.28	0.474	0.029	4.09	0.26	0.701	0.050	12.79	0.90	5.14	0.36	1.64
BCR-2G	3.18	0.18	3.13	0.19	0.424	0.020	4.12	0.19	0.692	0.035	65.24	3.16	5.16	0.25	1.54
average BCRG2	3.00		2.88		0.428		3.88		0.648		14.66		4.96		1.53
1 S.D.	**0.27**		**0.30**		**0.039**		**0.31**		**0.056**		**12.59**		**0.36**		**0.10**
GeoRem value	3.70		3.39		0.503		4.84		0.780		11.00		5.90		1.69
Georem 1 S.D.	0.04		0.03		0.005		0.28		0.060		1.00		0.30		0.12
bias (%)	19.03		15.04		14.930		19.92		16.897		33.24		15.90		9.55

4.3 REE + Y distribution patterns

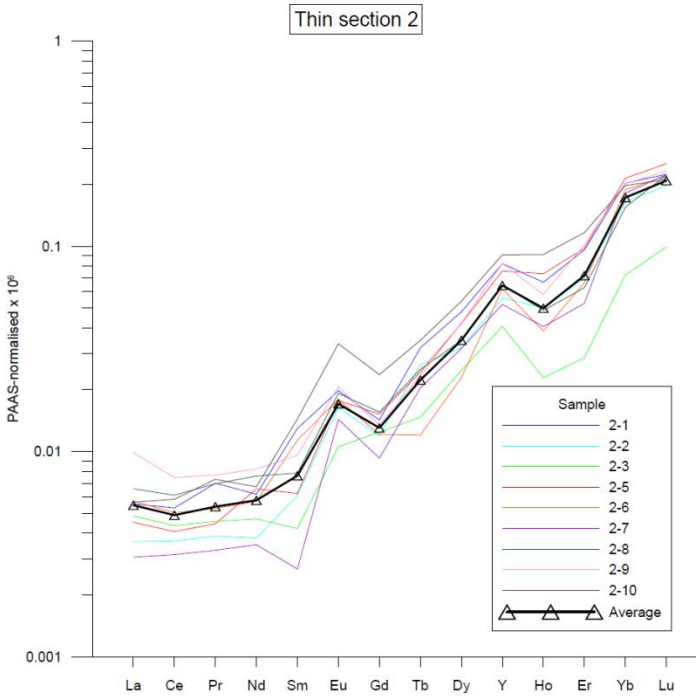

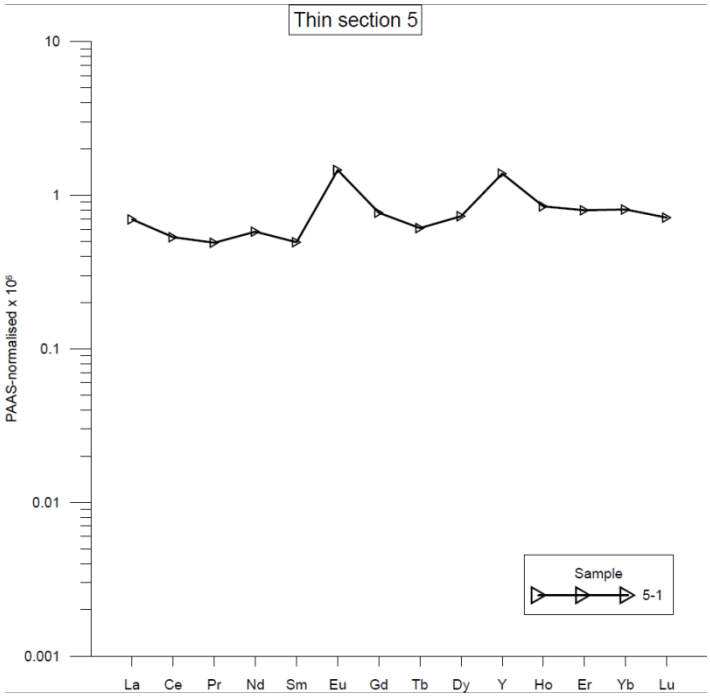

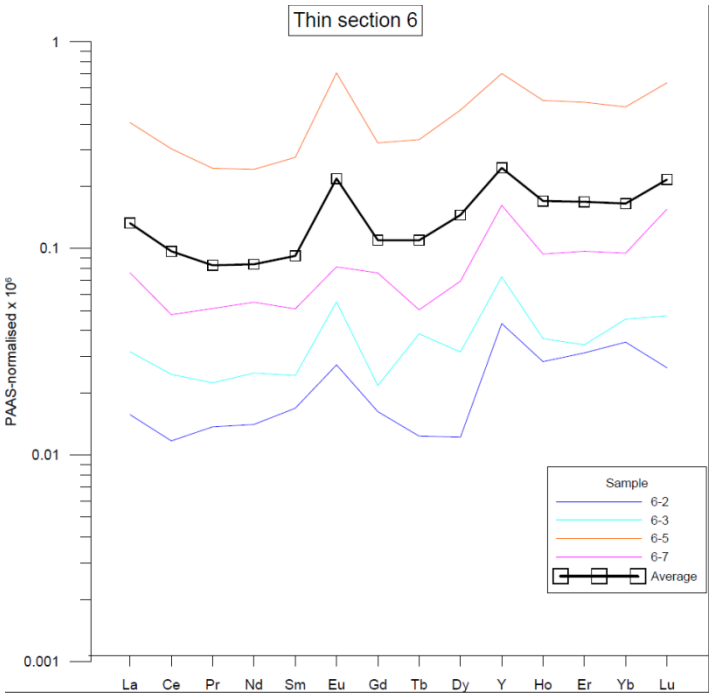

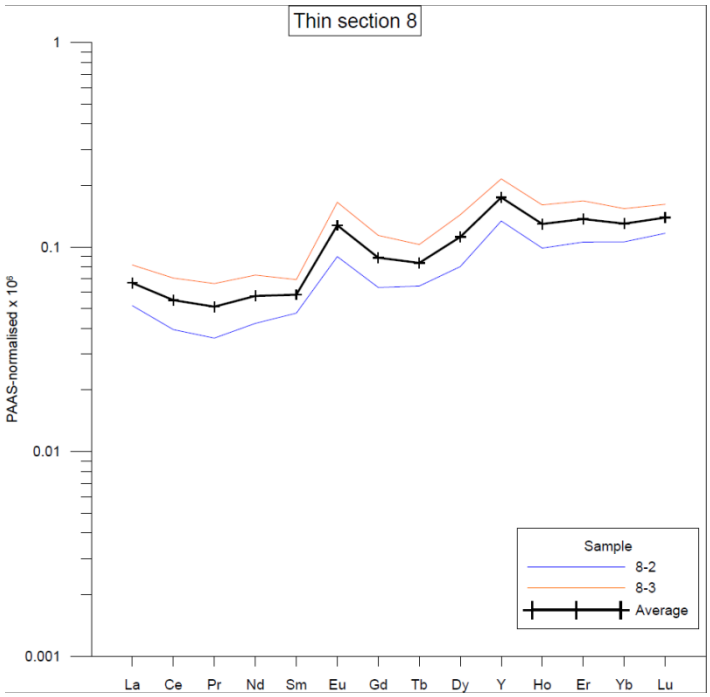

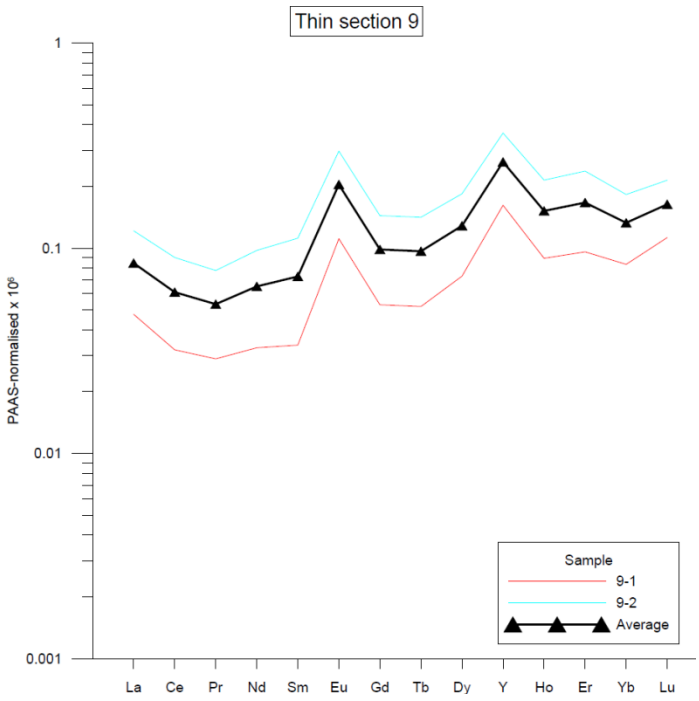
Thin section 9
PAAS-normalised x 10⁶
1
0.1
0.01
0.001
La Ce Pr Nd Sm Eu Gd Tb Dy Y Ho Er Yb Lu
Sample
9-1
9-2
Average

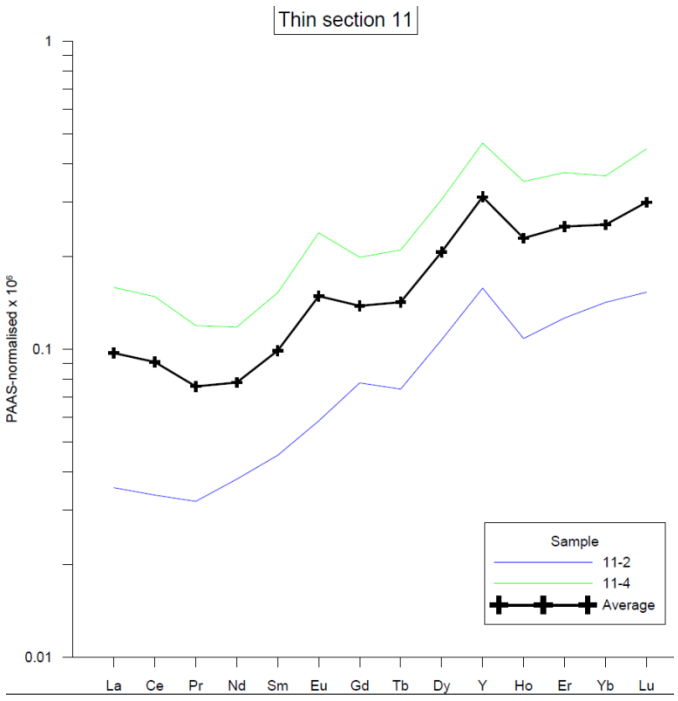
Thin section 11
PAAS-normalised x 10⁶
1
0.1
0.01
La Ce Pr Nd Sm Eu Gd Tb Dy Y Ho Er Yb Lu
Sample
11-2
11-4
Average

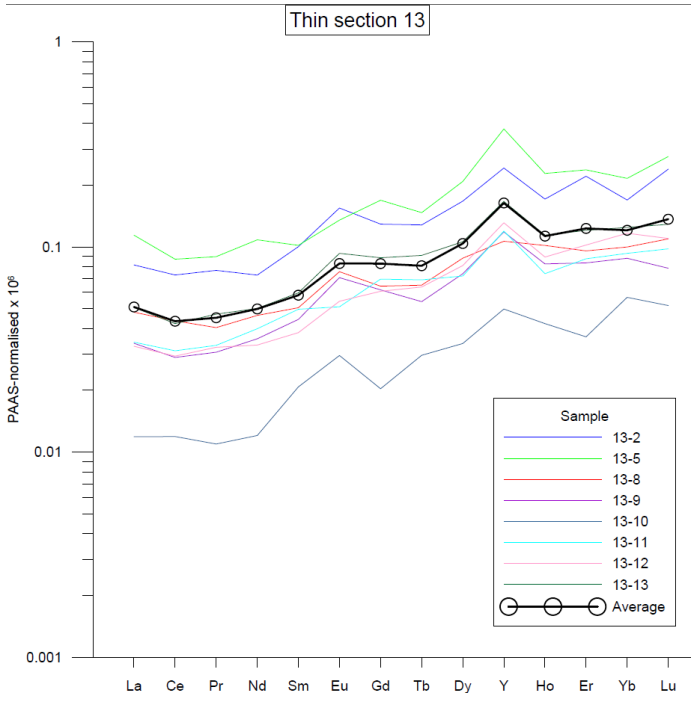
Thin section 13
PAAS-normalised x 10⁶
1
0.1
0.01
0.001
La Ce Pr Nd Sm Eu Gd Tb Dy Y Ho Er Yb Lu
Sample
13-2
13-5
13-8
13-9
13-10
13-11
13-12
13-13
Average

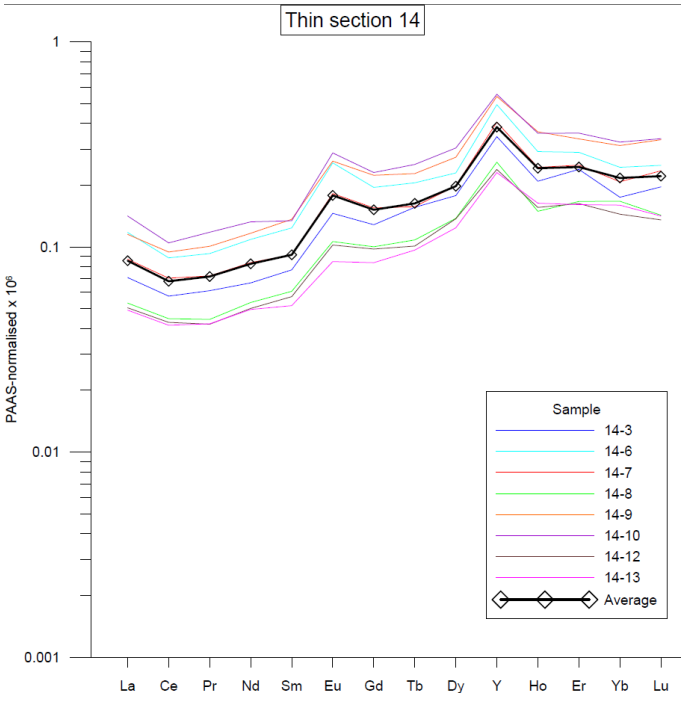
Thin section 14
PAAS-normalised x 10⁶
1
0.1
0.01
0.001
La Ce Pr Nd Sm Eu Gd Tb Dy Y Ho Er Yb Lu
Sample
14-3
14-6
14-7
14-8
14-9
14-10
14-12
14-13
Average

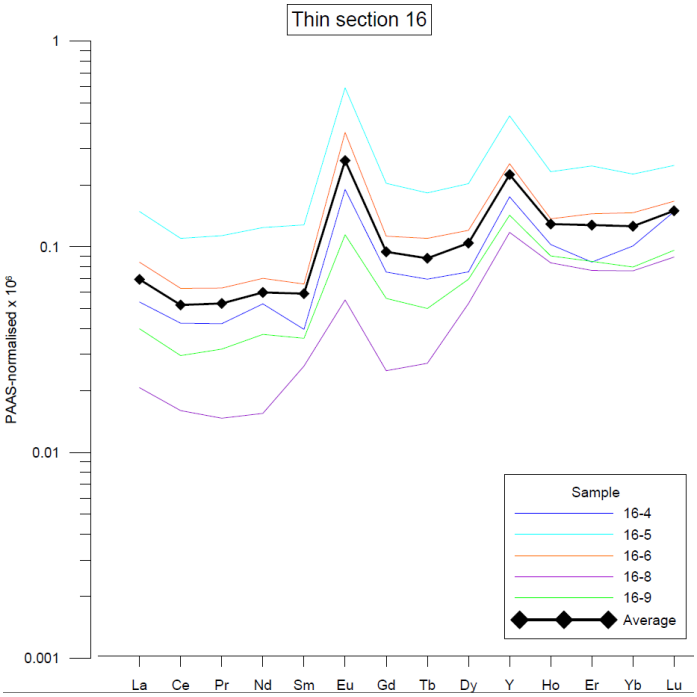
Thin section 16
PAAS-normalised x 10⁶
1
0.1
0.01
0.001
La Ce Pr Nd Sm Eu Gd Tb Dy Y Ho Er Yb Lu
Sample
16-4
16-5
16-6
16-8
16-9
Average

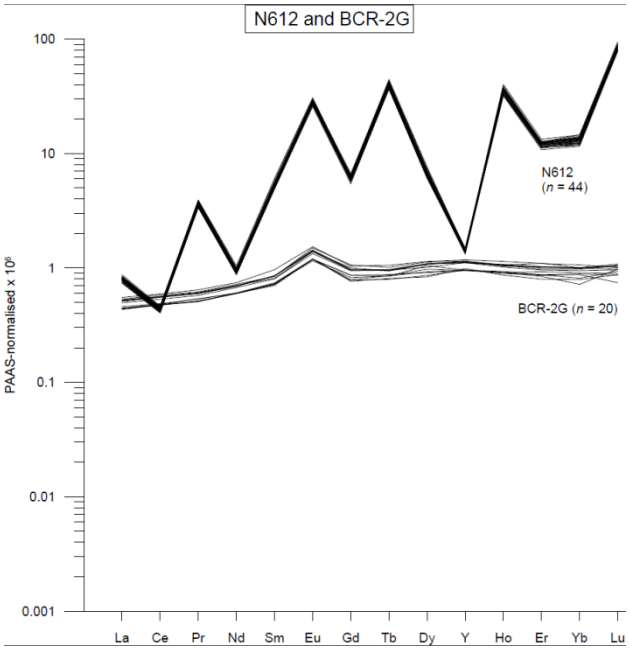
N612 and BCR-2G
PAAS-normalised x 10⁶
100
10
1
0.1
0.01
0.001
La Ce Pr Nd Sm Eu Gd Tb Dy Y Ho Er Yb Lu
N612
(n = 44)
BCR-2G (n = 20)

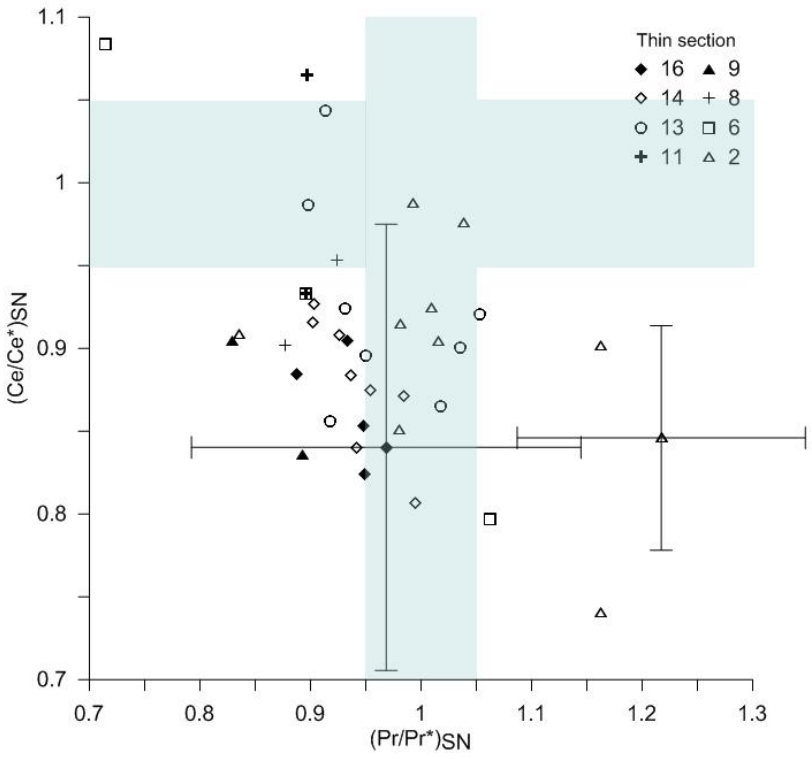
Thin section
16 9
14 8
13 6
11 2
(Ce/Ce*)SN
1.1
1
0.9
0.8
0.7
0.7 0.8 0.9 1 1.1 1.2 1.3
(Pr/Pr*)SN

5. XRD

2θ background subtracted plots from XRD results of HF1-7. Coloured bars represent the database mineral peak positions. Due to preferential alignment of the sample minerals (e.g. ankerite) the database peak height distribution may deviate from the measured peak height at the same 2θ.

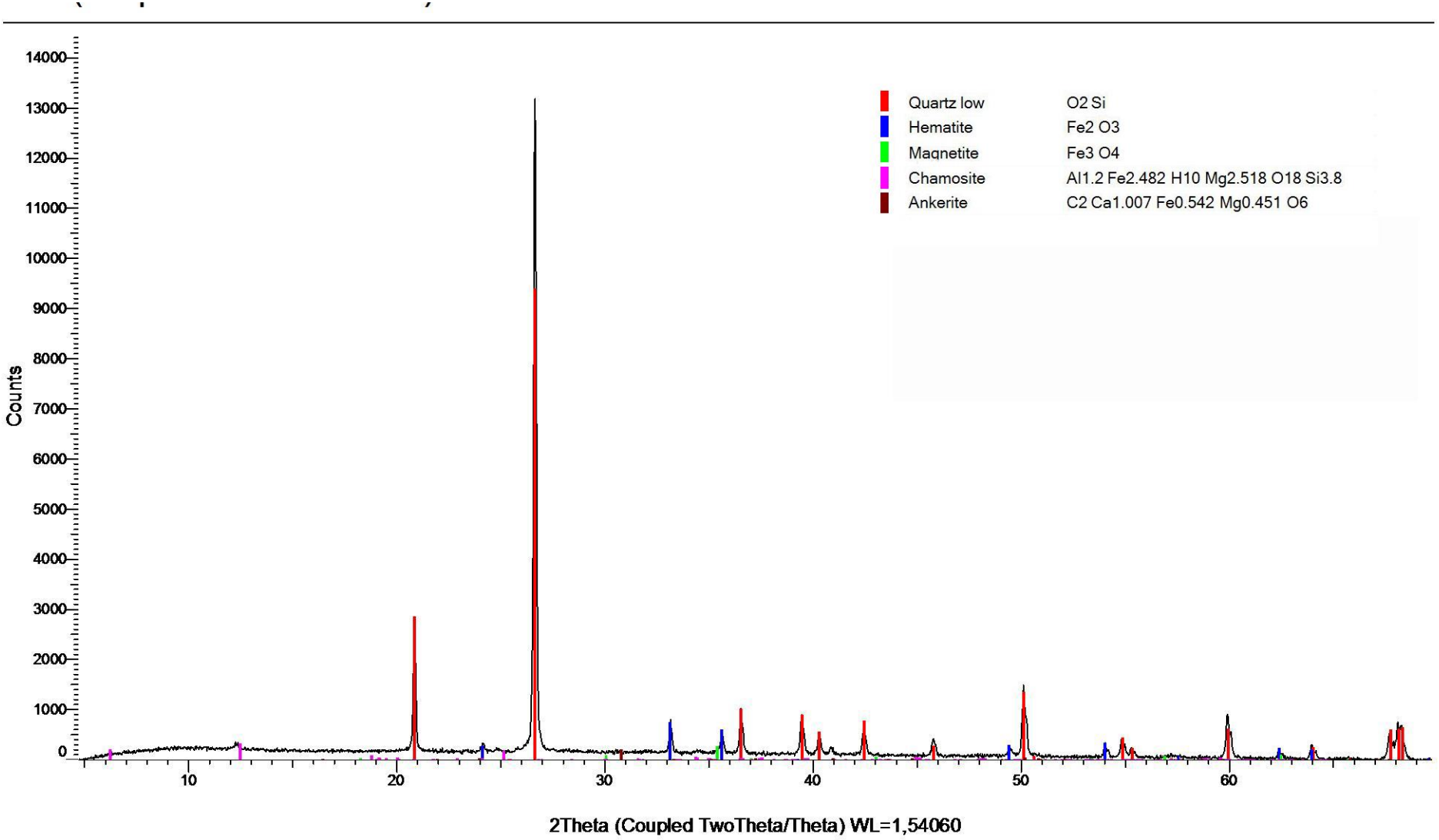

HF 2.1 (Coupled TwoTheta/Theta)

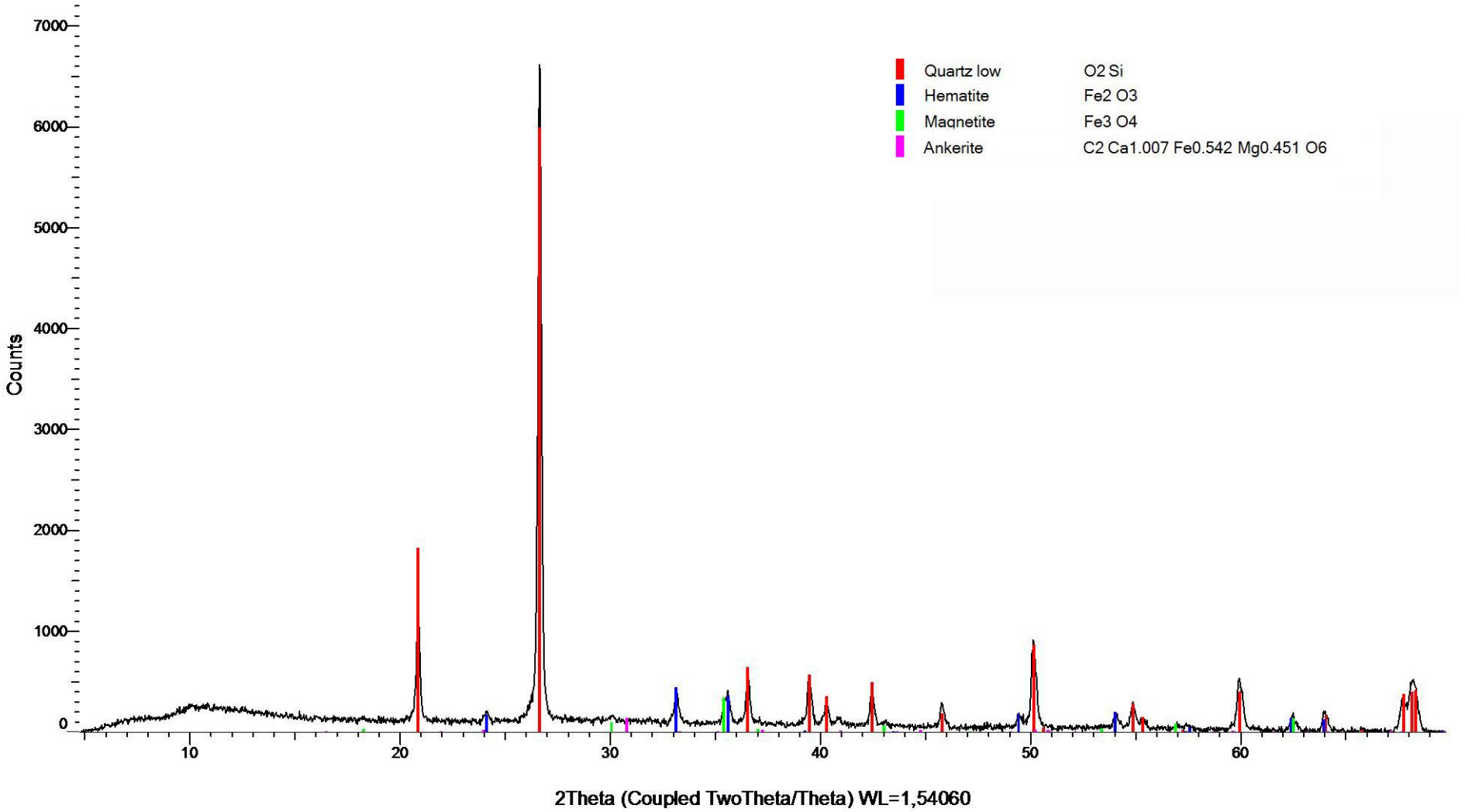

HF 3.1 (Coupled TwoTheta/Theta)

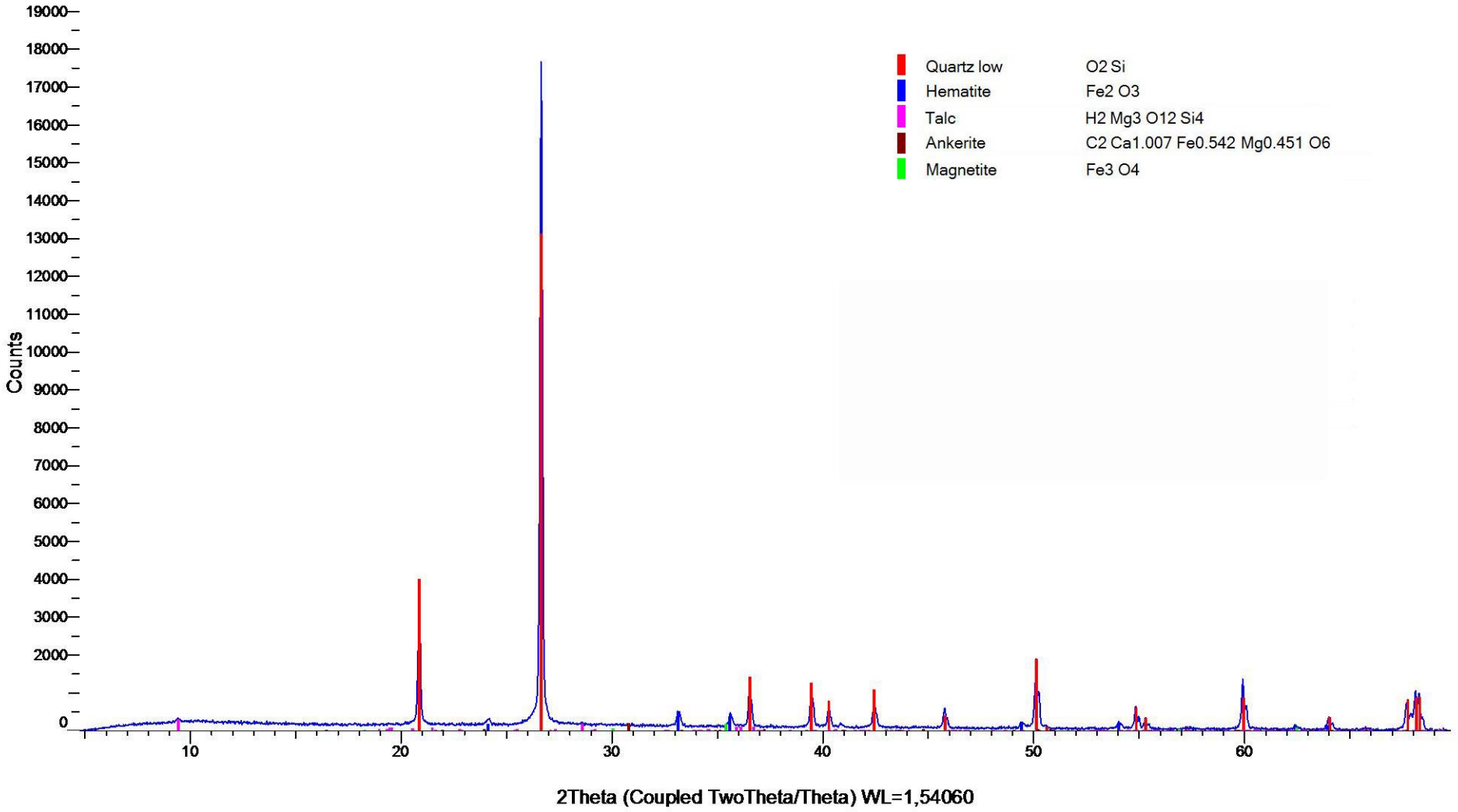

HF 4.1 (Coupled TwoTheta/Theta)

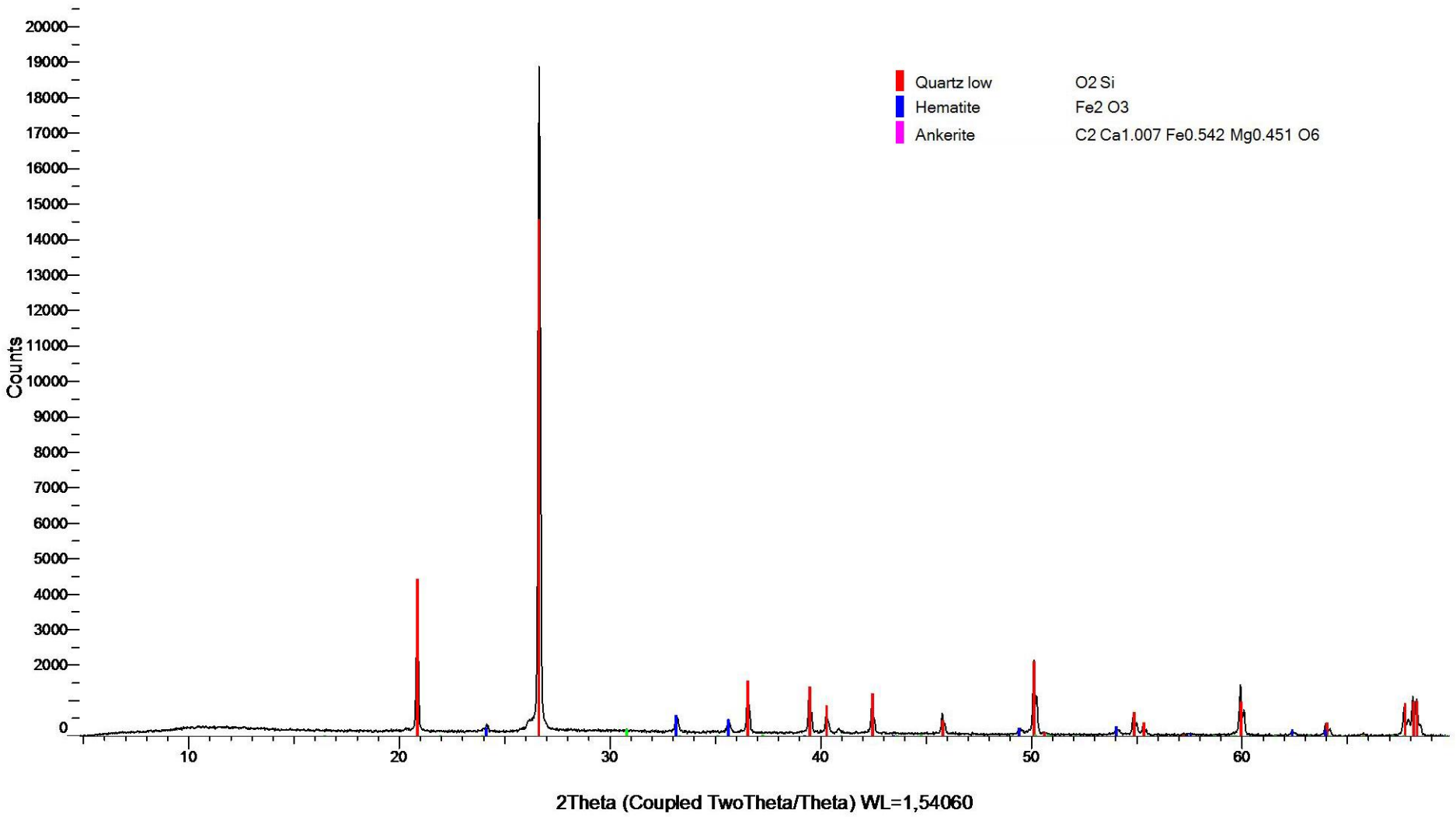

HF5 (Coupled TwoTheta/Theta)

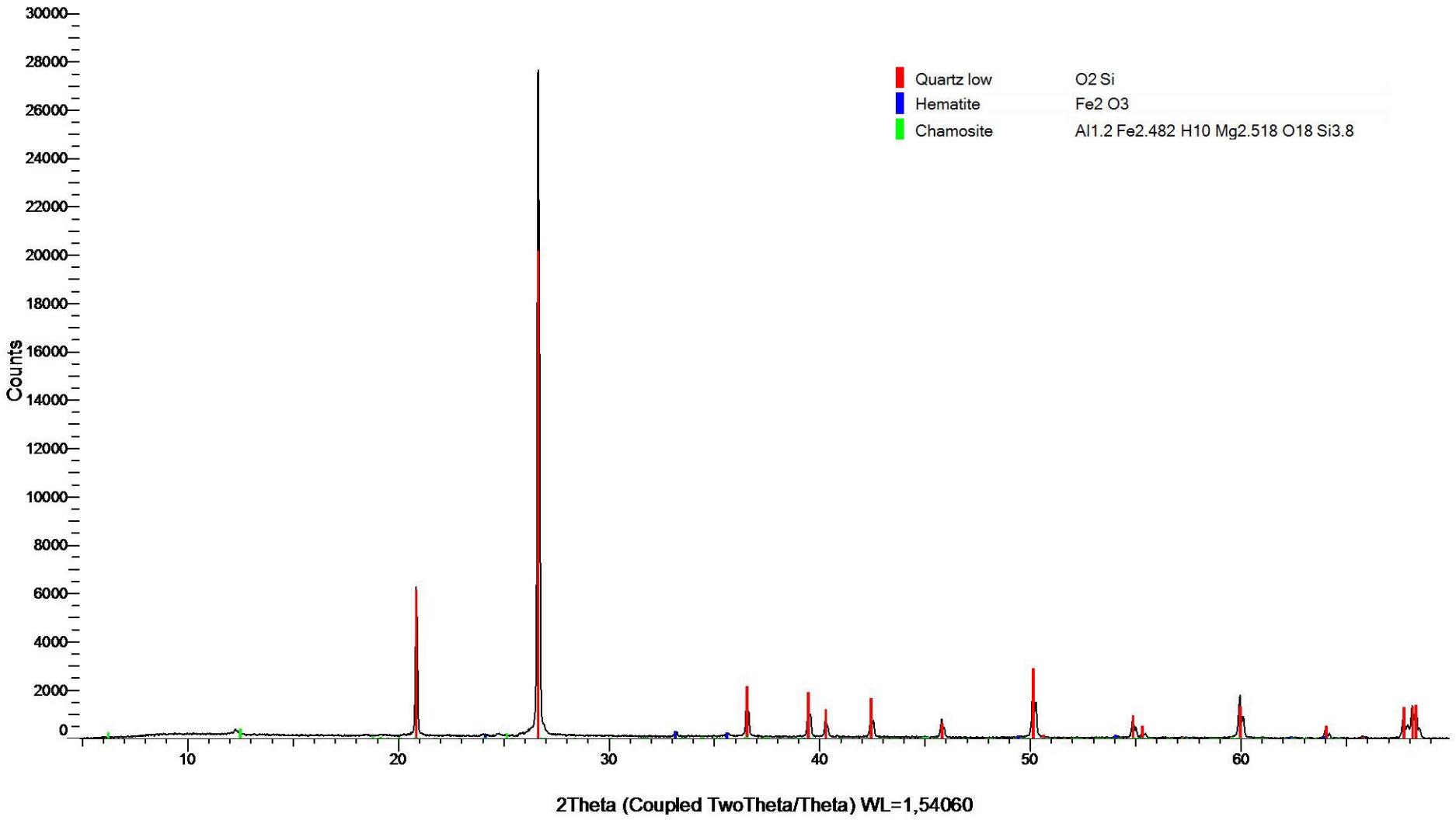

HF 6.1 (Coupled TwoTheta/Theta)

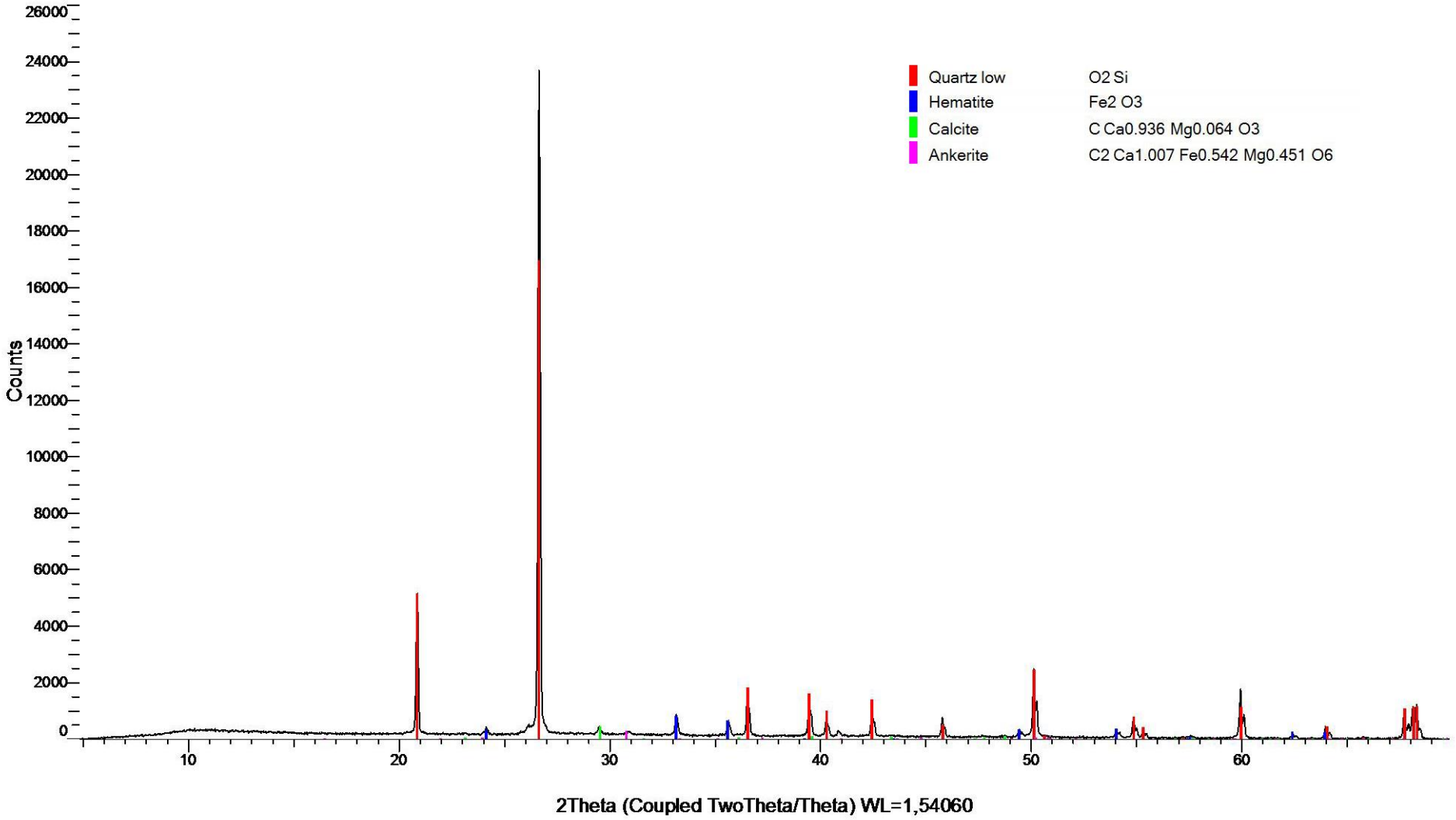

HF 7.1 (Coupled TwoTheta/Theta)

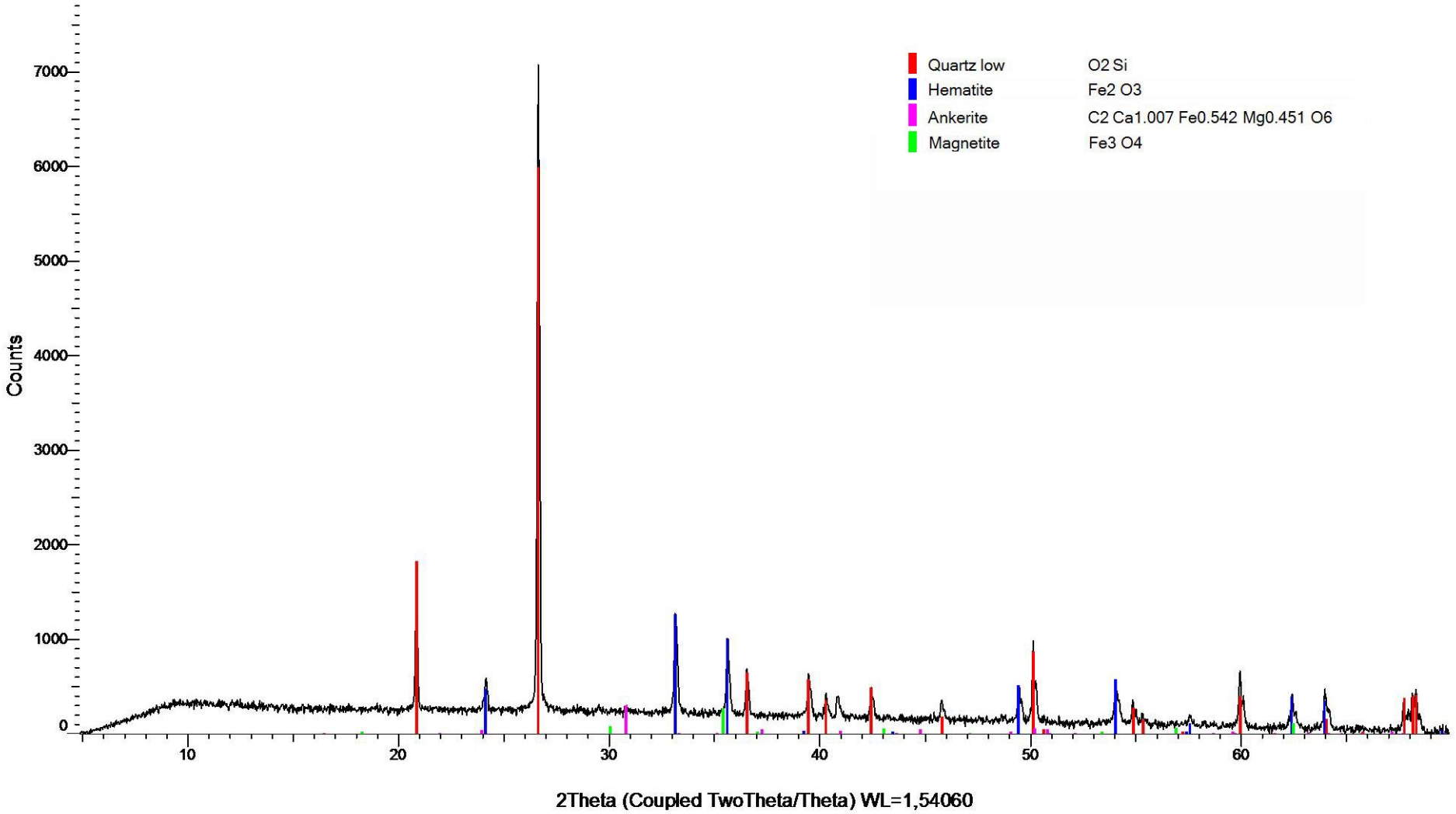

6. ICP-OES

6.1 Fe isotope sample chemistry

Table 4: ICP-OES major and trace element data of the Hotazel and Ongeluk Fe isotopes (HF1-7 and OF1-3) totally destructed samples and HCl digested samples (HF3,4,6 and 7 HCl). Values are reported in parts per million and represent the dry rock concentration. For the HCl digested samples the values represent the concentration in the dissolved part of the rock. The bias percentage is calculated from the difference between the processed standard ISE 921 and the accepted values (2013). BDL stands for below detection limit. Values below the Background Equivalent Concentration are displayed in italic; values indicated with " > " are above the line range and have an uncertainty of 10 % or higher.

Sample	Al 394.401 (µg/g)	B 208.959 (µg/g)	Ba 455.404 (µg/g)	Be 313.107 (µg/g)	Ca 315.887 (µg/g)	Co 230.786 (µg/g)	Cr 205.618 (µg/g)	Cu 324.754 (µg/g)	Fe 239.562 (µg/g)	K 766.491 (µg/g)	Li 670.780 (µg/g)	Mg 285.213 (µg/g)	Mn 257.611 (µg/g)
HF1	526.6	172.5	8.7	3.9	822.9	BDL	BDL	BDL	74773.4	BDL	BDL	1449.8	319.5
HF2	1470.4	159.9	20.9	3.9	2532.9	BDL	BDL	80.3	76632.3	*171.9*	BDL	1822.4	132.5
HF3	747.4	170.4	12.5	3.9	1563.9	56.9	BDL	*7.1*	40935.6	BDL	BDL	3044.8	128.4
HF4	2652.6	204.3	42.1	3.5	732.1	33.8	BDL	BDL	38992.8	1035.7	*9.5*	982.9	57.2
HF5	4023.9	153.9	7.9	3.6	320.7	BDL	*2.6*	BDL	21376.8	BDL	*9.5*	8276.7	164.8
HF6	*276.5*	218.6	31.2	4.9	10089.6	*25.1*	39.4	BDL	42289.0	BDL	BDL	1683.7	902.6
HF7a	1132.8	137.0	8.2	4.3	7963.0	BDL	*2.9*	BDL	173897.8	BDL	BDL	2217.7	445.5
HF7b	1081.7	221.3	10.4	6.2	7466.4	BDL	*4.7*	BDL	165618.0	BDL	BDL	2117.1	432.3
OF1	68504.6	80.2	8.6	5.1	17058.7	*26.0*	101.8	23.3	158348.3	BDL	*17.5*	64666.5	3405.1
OF2	59031.8	79.6	28.2	3.8	11900.1	30.3	78.2	636.3	120300.1	920.8	*26.5*	52480.9	3166.3
OF3	82594.3	80.3	119.1	5.3	37885.2	48.6	136.8	76.5	160474.4	5391.0	*44.1*	63275.9	4330.0
HF3 HCl	573.0	BDL	10.7	2.7	1419.4	110.8	BDL	13.4	20452.9	BDL	BDL	864.4	123.9
HF4 HCl	3053.6	BDL	53.1	3.3	587.9	29.0	BDL	8.9	14209.4	1331.3	*8.6*	529.5	47.5
HF6 HCl	*190.5*	BDL	26.5	4.6	9124.3	*22.3*	20.9	BDL	18328.6	BDL	BDL	1373.2	821.6
HF7a HCl	1050.7	BDL	10.4	5.7	7964.6	BDL	BDL	17.1	133268.0	BDL	BDL	1526.7	453.7
HF7b HCl	*1357.1*	BDL	*35.9*	22.4	10139.1	BDL	BDL	BDL	144201.9	BDL	BDL	1563.5	515.9
BHVO-1	91708.9	BDL	129.0	5.7	78399.3	34.4	279.3	138.1	84937.3	4483.5	*9.1*	42639.7	1273.9
JB-2	114210.0	BDL	222.8	4.2	73949.3	32.4	26.2	241.7	> 109581.1	3848.7	*12.7*	30602.8	1802.5
AGV-1	125643.2	BDL	1277.0	7.0	35310.7	*9.8*	*7.0*	61.1	48091.3	26226.6	*14.9*	9746.9	778.3
ISE921	56873.5	70.0	572.6	5.4	42451.0	10.8	118.4	95.6	32333.1	BDL	55.1	11825.6	1244.3
ISE921 acc. value	56800.0	-	563.0	2.1	43000.0	14.9	130.0	93.8	31900.0	19100.0	53.6	11100.0	1190.0
Bias (%)	0.1	-	1.7	156.3	1.3	27.8	8.9	1.9	1.4	-	2.8	6.5	4.6

Sample	Na 589.592 (µg/g)	Ni 231.604 (µg/g)	P 177.495 (µg/g)	Pb 220.353 (µg/g)	S 182.034 (µg/g)	Sc 424.683 (µg/g)	Si 251.612 (µg/g)	Sr 407.771 (µg/g)	Ti 334.187 (µg/g)	V 292.402 (µg/g)	Y 360.073 (µg/g)	Zn 206.200 (µg/g)	Zr 343.823 (µg/g)
HF1	340.6	BDL	218.6	BDL	270.7	BDL	906.6	3.9	59.3	BDL	*3.0*	8.4	BDL
HF2	*262.6*	BDL	513.5	BDL	1625.7	*2.3*	2103.9	3.6	118.4	*8.8*	*6.5*	30.7	*8.8*
HF3	*202.1*	321.2	209.5	BDL	BDL	*2.1*	673.8	*0.7*	*23.1*	BDL	BDL	*6.8*	BDL
HF4	*263.1*	BDL	168.6	BDL	*78.7*	*2.2*	1362.0	*1.3*	*35.1*	BDL	BDL	*4.4*	*5.1*
HF5	*217.2*	BDL	71.4	BDL	*78.3*	*2.6*	2127.7	*1.0*	116.9	*10.2*	BDL	46.5	*7.5*
HF6	*244.9*	BDL	107.6	BDL	*78.5*	BDL	1374.3	5.8	628.6	BDL	BDL	BDL	*16.0*
HF7a	*205.6*	BDL	670.8	BDL	*67.6*	*2.9*	777.4	3.2	56.5	*8.6*	*11.1*	*7.5*	*16.4*
HF7b	*264.1*	BDL	643.2	BDL	BDL	*3.6*	643.7	*2.6*	*55.7*	*8.9*	*11.5*	*8.3*	*14.6*
OF1	*231.4*	66.8	901.8	BDL	*72.7*	27.8	172.4	5.8	7646.0	283.8	33.6	197.8	161.8
OF2	*233.4*	112.3	629.8	BDL	658.3	21.7	391.8	3.5	5273.8	243.6	24.4	162.8	122.6
OF3	796.0	110.4	1207.9	BDL	144.0	36.6	722.1	9.4	10399.9	378.4	45.6	160.6	216.0
HF3 HCl	239.3	303.7	129.6	BDL	BDL	*1.9*	454.7	*0.5*	*15.0*	BDL	BDL	8.3	BDL
HF4 HCl	335.9	BDL	90.1	BDL	BDL	*2.3*	595.5	*1.0*	*36.0*	BDL	BDL	7.6	BDL
HF6 HCl	*360.6*	BDL	53.9	BDL	BDL	BDL	441.5	3.7	179.8	BDL	BDL	BDL	BDL
HF7a HCl	*322.9*	BDL	584.5	BDL	BDL	*3.6*	721.6	*2.1*	*40.5*	BDL	*9.9*	*5.7*	*11.4*
HF7b HCl	*1162.0*	BDL	601.2	BDL	BDL	*13.5*	2149.0	BDL	BDL	BDL	BDL	BDL	BDL
BHVO-1	15725.9	110.2	1131.0	BDL	BDL	*29.6*	802.1	399.1	> 16460.0	331.1	22.7	100.6	154.7
JB-2	15379.3	192.7	389.7	BDL	BDL	*54.0*	395.1	195.4	> 7485.3	623.3	22.0	120.7	47.8
AGV-1	31680.5	*11.2*	2237.6	*51.7*	BDL	*13.0*	207.4	679.5	> 6586.5	131.4	*17.7*	95.5	219.1
ISE921	5094.5	40.2	1385.2	177.3	725.5	10.1	152.3	173.8	> 3556.1	92.7	18.0	534.0	94.6
ISE921 acc. value	5540.0	42.4	1400.0	167.0	702.0	10.0	-	165.0	3700.0	90.0	26.2	522.0	245.0
Bias (%)	8.0	5.2	1.1	6.1	3.4	1.3	-	5.3	-	3.1	31.1	2.3	61.4

Table 5: ICP-OES data of the procedular blanks.

	Al 394.401 (µg/g)	B 208.959 (µg/g)	Ba 455.404 (µg/g)	Be 313.107 (µg/g)	Ca 396.847 (µg/g)	Co 230.786 (µg/g)	Cr 205.618 (µg/g)	Cu 324.754 (µg/g)	Fe 259.941 (µg/g)	K 766.491 (µg/g)	Li 670.780 (µg/g)	Mg 285.213 (µg/g)	Mn 257.611 (µg/g)
blank	1.055	*0.576*	*0.020*	*0.010*	*1.575*	< 0.0126	< 0.0022	< 0.0092	*0.029*	< 0.0606	< 0.0118	*0.153*	< 0.0031
blank HCl	< 0.0708	< 0.005	0.014	0.010	0.035	< 0.0123	< 0.0035	< 0.0103	< 0.0036	< 0.0127	< 0.0111	< 0.0719	< 0.0039

	Na 589.592 (µg/g)	Ni 231.604 (µg/g)	P 177.495 (µg/g)	Pb 220.353 (µg/g)	S 182.034 (µg/g)	Sc 424.683 (µg/g)	Si 251.612 (µg/g)	Sr 407.771 (µg/g)	Ti 334.187 (µg/g)	V 292.402 (µg/g)	Y 360.073 (µg/g)	Zn 206.200 (µg/g)	Zr 343.823 (µg/g)
blank	0.560	< 0.0013	< 0.012	< 0.0128	< 0.1114	< 0.0049	*0.382*	< 0.0003	*0.028*	< 0.0013	< 0.0002	0.008	< 0.0112
blank HCl	0.508	< 0.0007	< 0.0143	< 0.0129	< 0.0518	< 0.005	0.040	< 0.0027	< 0.006	< 0.001	< 0.0001	< 0.0042	< 0.0107

6.2 Sample digestion and preparation for anion-exchange chromatography

Table 6: Overview of the sample dissolution and processing data prior to anion-exchange chromatography. The value in red (from ISE92) is obtained from photospectrometry instead of calculated from ICP-OES data after sample digestion.

Sample	Weight rock powder (g)	Digestion method	Total acid solution (g)	Dilution	ICP OES aliquot (g)	Diluted aliquot (g)	Extra dilution ICP-OES	ICP-OES aliquot conc. Fe (µg/g)	Fe conc. in acid solution (µg/g)	Portion of sample for further processing (g)	Total Fe in processed sample (µg)	Volume processed sample (mL)	Volume loaded on column (mL)	Amount of Fe loaded (µg)
blank		TD			2.7	6.6			0.0	1.790	0.0	0.505	0.45	0.0
ISE921	0.119	TD	16.6	139.4	2.7	6.1	316.5	102.1	231.9	1.707	361.3	0.569	0.45	285.9
BHVO-1	0.107	TD	26.7	250.7	2.7	4.6	435.7	195.0	338.9	1.441	488.3	0.928	0.45	236.8
JB-2	0.099	TD	17.5	176.7	2.7	5.8	385.5	284.3	620.2	1.427	885.0	0.967	0.45	412.0
HF1	0.104	TD	16.1	154.9	0.1	5.1	7249.7	10.3	482.7	0.639	308.5	0.629	0.45	220.8
HF2	0.103	TD	16.3	158.2	0.1	5.0	7394.8	10.4	484.5	0.646	312.9	0.623	0.45	226.1
HF3	0.098	TD	16.4	167.4	2.7	5.7	355.7	115.1	244.5	1.666	407.2	0.639	0.45	286.8
HF4	0.099	TD	17.1	172.6	2.7	5.0	316.2	123.3	225.9	1.764	398.5	0.589	0.45	304.3
HF5	0.102	TD	16.7	164.2	2.7	5.4	327.5	65.3	130.2	4.120	536.3	0.565	0.45	427.0
HF6	0.088	TD	16.6	188.9	2.7	5.9	410.8	102.9	223.9	1.970	440.9	0.587	0.45	338.0
HF7a	0.095	TD	16.5	173.5	0.1	5.1	8212.8	21.2	1002.1	0.316	316.6	0.540	0.45	263.6
HF7b	0.065	TD	16.1	246.6	0.1	5.1	11805.4	14.0	671.6	0.469	314.8	0.572	0.45	247.7
blank HCl		HCl	14.9		2.6	4.9		0.0	0.0	2.257	0.0	0.540	0.45	0.0
AGV-1	0.082	TD	18.0	220.7	2.7	5.6	466.1	103.2	217.9	2.360	514.3	0.898	0.45	257.8
OF1	0.102	TD	16.8	164.4	0.1	5.1	7684.2	20.6	963.3	0.326	313.7	0.593	0.3	158.6
OF2	0.104	TD	16.7	160.1	0.1	5.1	7659.5	15.7	751.3	0.424	318.4	0.598	0.45	239.7
OF3	0.100	TD	16.7	167.7	0.1	5.1	7963.2	20.2	957.0	0.321	307.4	0.479	0.45	288.6
HF3 HCl	0.092	HCl	14.4	155.2	3.0	5.1	268.3	76.2	131.8	4.012	528.8	0.597	0.45	398.2
HF4 HCl	0.072	HCl	14.1	194.8	3.0	5.1	329.9	43.1	73.0	9.967	727.1	0.592	0.45	552.7
HF6 HCl	0.055	HCl	14.9	272.5	3.0	5.2	464.7	39.4	67.3	9.448	635.5	0.597	0.45	479.4
HF7 HCl a	0.049	HCl	14.6	300.2	0.1	5.2	14733.9	9.0	444.0	0.692	307.2	0.589	0.45	234.8
HF7 HCl b	0.013	HCl	15.4	1166.0	3.0	5.9	2243.2	64.3	123.7	5.232	647.1	0.548	0.45	531.5
IF-G		TD									524.0	0.926	0.45	254.7

6.3 Qualitiy control

Table 7: ICP-OES aliquot data for Fe purity check after column separation of the Fe isotope samples. The repeatability and measurement bias are obtained from calibration with an internal ICP-OES control standard.

	Al 396.152 (µg/g)	Ca 396.847 (µg/g)	Cd 214.439 (µg/g)	Co 238.892 (µg/g)	Cr 267.716 (µg/g)	Cu 324.754 (µg/g)	Fe 238.204 (µg/g)	K 766.491 (µg/g)	Mg 279.553 (µg/g)	Mn 257.610 (µg/g)	Na 588.995 (µg/g)	Ni 216.555 (µg/g)	Pb 220.353 (µg/g)	S 181.972 (µg/g)	Zn 334.502 (µg/g)
blank	BDL	BDL	BDL	BDL	BDL	BDL	0.010	BDL	BDL	BDL	0.227	BDL	BDL	BDL	BDL
ISE921	BDL	BDL	BDL	BDL	BDL	BDL	2.344	BDL	BDL	BDL	BDL	BDL	BDL	BDL	BDL
BHVO-1	BDL	BDL	BDL	BDL	BDL	BDL	2.207	BDL	BDL	BDL	BDL	BDL	BDL	BDL	BDL
JB-2	BDL	BDL	BDL	BDL	BDL	BDL	3.827	BDL	BDL	BDL	BDL	BDL	BDL	BDL	BDL
HF1	BDL	BDL	BDL	BDL	BDL	BDL	2.171	BDL	BDL	BDL	BDL	BDL	BDL	BDL	BDL
HF2	BDL	BDL	BDL	BDL	BDL	BDL	2.247	BDL	BDL	BDL	BDL	BDL	BDL	BDL	BDL
HF3	BDL	BDL	BDL	BDL	BDL	BDL	2.048	BDL	BDL	BDL	BDL	BDL	BDL	BDL	BDL
HF4	BDL	BDL	BDL	BDL	BDL	BDL	2.118	BDL	BDL	BDL	0.110	BDL	BDL	BDL	BDL
HF5	BDL	BDL	BDL	BDL	BDL	BDL	3.273	BDL	BDL	BDL	BDL	BDL	BDL	BDL	BDL
HF6	BDL	BDL	BDL	BDL	BDL	BDL	2.604	BDL	BDL	BDL	BDL	BDL	BDL	BDL	BDL
HF7	BDL	BDL	BDL	BDL	BDL	BDL	2.515	BDL	BDL	BDL	BDL	BDL	BDL	BDL	BDL
HF7d	BDL	BDL	BDL	BDL	BDL	BDL	2.463	BDL	BDL	BDL	BDL	BDL	BDL	BDL	BDL
blank HCl	0.440	BDL	BDL	BDL	BDL	BDL	0.019	BDL	BDL	BDL	BDL	BDL	BDL	0.034	BDL
AGV-1	BDL	BDL	BDL	BDL	BDL	BDL	2.536	BDL	BDL	BDL	BDL	BDL	BDL	BDL	BDL
OF1	BDL	BDL	BDL	BDL	BDL	BDL	1.377	BDL	BDL	BDL	BDL	BDL	BDL	BDL	BDL
OF2	BDL	BDL	BDL	BDL	BDL	BDL	1.185	BDL	BDL	BDL	BDL	BDL	BDL	BDL	BDL
OF3	0.064	BDL	BDL	BDL	BDL	BDL	2.548	BDL	BDL	BDL	0.136	BDL	BDL	BDL	BDL
HF3 HCl	BDL	BDL	BDL	BDL	BDL	BDL	4.061	BDL	BDL	BDL	BDL	BDL	BDL	BDL	BDL
HF4 HCl	BDL	BDL	BDL	BDL	BDL	BDL	5.366	BDL	BDL	BDL	BDL	BDL	BDL	BDL	BDL
HF6 HCl	BDL	BDL	BDL	BDL	BDL	BDL	4.729	BDL	BDL	BDL	BDL	BDL	BDL	BDL	BDL
HF7a HCl	BDL	BDL	BDL	BDL	BDL	BDL	2.360	BDL	BDL	BDL	BDL	BDL	BDL	BDL	BDL
HF7b HCl	BDL	BDL	BDL	BDL	BDL	BDL	5.136	BDL	BDL	BDL	BDL	BDL	BDL	BDL	BDL
IF-G	BDL	BDL	BDL	BDL	BDL	BDL	2.475	BDL	BDL	BDL	BDL	BDL	BDL	BDL	BDL
% Repeatability	0.4	0.5	0.1	0.6	0.3	0.4	0.5	0.3	0.3	0.3	0.5	0.2	0.3	-	0.4
% Measurement bias	6.4	12.9	-	7.7	6.7	5.9	5.8	-0.8	10.1	5.8	3.3	6.5	8.9	-	6.8

Table 8: ***Above:*** **Evaluation of the total Fe content of the procedular blanks.** ***Below:*** **Evaluation of the Na-contaminated samples and procedular blanks (values represent ICP-OES aliquot concentrations).**

	Fe conc. ICP-OES aliquot (µg/g))	Dilution	Fe conc. Sample (µg/g)	Total Fe (ng)
blank	0.009591	50	0.47955	959.1
blank HCl	0.018808	50	0.9404	1880.8

Sample	Fe 238.204 (µg/g)	Na 588.995 (µg/g)	Na/Fe	Na/Fe (%)
blank	0.010	0.227	23.649	2364.9
HF4	2.118	0.110	0.052	5.2
OF3	2.548	0.136	0.054	5.4

Table 9: Column yield calculation.

Sample	Fe conc. ICP-OES aliquot after chromatography (µg/g)	Dilution	Fe conc. Sample (µg/g)	Total Fe collected from column (µg)	Column yield (%)
ISE921	2.34	50	117.2	234.4	82.0
BHVO-1	2.21	50	110.4	220.7	93.2
JB-2	3.83	50	191.3	382.7	92.9
HF1	2.17	50	108.6	217.1	98.3
HF2	2.25	50	112.4	224.7	99.4
HF3	2.05	50	102.4	204.8	71.4
HF4	2.12	50	105.9	211.8	69.6
HF5	3.27	50	163.6	327.3	76.6
HF6	2.60	50	130.2	260.4	77.0
HF7a	2.51	50	125.7	251.5	95.4
HF7b	2.46	50	123.1	246.3	99.4
AGV-1	2.54	50	126.8	253.6	98.4
OF1	1.38	50	68.9	137.7	86.8
OF2	1.18	50	59.2	118.5	49.4
OF3	2.55	50	127.4	254.8	88.3
HF3 HCl	4.06	50	203.1	406.1	102.0
HF4 HCl	5.37	50	268.3	536.6	97.1
HF6 HCl	4.73	50	236.5	472.9	98.7
HF7 HCl a	2.36	50	118.0	236.0	100.5
HF7 HCl b	5.14	50	256.8	513.6	96.6
IF-G	2.46	50	123.	247.5	97.2

7. Photospectrometry

		Total Fe in processed sample (µg)	
Sample	Volume processed sample (mL)	*ICP-OES data prior to processing*	*Photospectric data after processing*
ISE921	0.57	361.3	361
HF3	0.64	407.2	424
HF4	0.59	398.5	419
HF5	0.57	536.3	618
HF6	0.59	440.9	474
HF7	0.54	316.6	328
OF3	0.48	307.4	317

8. MC-ICP-MS

8.1 Fe isotopes

Table 10: MC-ICP-MS Fe isotope data for all analytes of session 1, 2 and 3, including the instrumental mass bias drift, signal intensity matching difference and $^{54}Cr/^{54}Fe$ and $^{58}Ni/^{58}Fe$ interferences. 2 S.E. is the standard error of the mean for each analyte Fe isotope ratio, calculated from the measured intensities. 2 S.D. represents internal standard deviation of the average Fe isotopic value for each sample, calculated from the individual analytes.

Session 1

Sample	$\delta^{56/54}Fe$ [‰]	2 S.E.	$\delta^{57/54}Fe$ [‰]	2 S.E.	$\delta^{58/54}Fe$ [‰]	2 S.E.	$\delta^{57/56}Fe$ [‰]	2 S.E.	$^{56/54}Fe$ mass bias drift [‰]	$^{57/56}Fe$ mass bias drift [‰]	signal intens. match. diff. [%]	$\delta^{57}Fe/\delta^{56}Fe$	$\delta^{56/54}Fe/\delta^{57/56}Fe$	$^{54}Cr/^{54}Fe$	$^{58}Ni/^{58}Fe$	^{56}Fe (V)
HanFe	0.332	0.030	0.460	0.062	0.825	0.502	0.127	0.073	-0.05	-0.06	3.16	1.38	2.61	5E-05	2E-03	10.459
HanFe	0.225	0.032	0.305	0.063	0.846	0.587	0.080	0.063	0.07	0.08	2.19	1.36	2.81	5E-05	1E-03	10.446
HanFe	0.303	0.043	0.456	0.076	0.840	1.056	0.153	0.074	0.01	0.02	0.14	1.50	1.99	4E-05	2E-03	6.775
HanFe	0.282	0.037	0.448	0.069	0.734	0.770	0.165	0.061	-0.05	0.04	5.00	1.59	1.71	5E-05	2E-03	6.778
HanFe	0.338	0.034	0.514	0.104	-0.625	0.786	0.175	0.095	0.00	-0.04	3.62	1.52	1.93	4E-05	3E-03	6.885
HanFe	0.282	0.035	0.402	0.092	0.350	0.822	0.120	0.091	-0.04	0.00	3.14	1.42	2.36	4E-05	3E-03	6.959
HanFe	0.317	0.044	0.465	0.067	1.005	0.892	0.147	0.071	0.00	-0.05	2.54	1.47	2.15	5E-05	2E-03	6.696
HanFe	0.321	0.048	0.443	0.092	-0.082	0.676	0.122	0.084	-0.02	-0.03	2.38	1.38	2.64	4E-05	3E-03	6.917
average	**0.300**		**0.436**		**0.487**		**0.136**									
2 S.D.	**0.074**		**0.123**		**1.140**		**0.061**									
BHVO-1	0.070	0.024	0.078	0.067	0.009	0.506	0.008	0.063	-0.02	-0.06	-0.03	1.11	8.72	4E-05	8E-05	10.133
BHVO-1	0.043	0.038	0.068	0.090	0.043	0.831	0.025	0.084	0.06	0.02	4.09	1.59	1.71	4E-05	9E-04	6.818
BHVO-1	0.114	0.041	0.177	0.097	-0.256	0.801	0.063	0.086	0.01	0.04	0.25	1.55	1.81	4E-05	1E-03	6.581
average	**0.075**		**0.108**		**-0.068**		**0.032**									
2 S.D.	**0.072**		**0.121**		**0.328**		**0.056**									
JB-2	0.044	0.037	0.107	0.074	0.246	0.522	0.063	0.070	0.02	0.05	0.25	2.42	0.70	4E-05	-5E-05	10.134
JB-2	0.051	0.037	0.049	0.078	0.127	0.871	-0.002	0.078	0.06	0.06	0.93	0.96	-22.33	4E-05	3E-04	6.791
average	**0.048**		**0.078**		**0.187**		**0.030**									
2 S.D.	**0.010**		**0.081**		**0.169**		**0.092**									

Sample	$\delta^{56/54}$Fe	2 S.E.	$\delta^{57/54}$Fe	2 S.E.	$\delta^{58/54}$Fe	2 S.E.	$\delta^{57/56}$Fe	2 S.E.	$^{56/54}$Fe	$^{57/56}$Fe	signal intens.	δ^{57}Fe/δ^{56}Fe	$\delta^{56/54}$Fe/$\delta^{57/56}$Fe	^{54}Cr/^{54}Fe	^{58}Ni/^{58}Fe	56Fe (V)
AGV-1	-0.070	0.027	-0.076	0.063	-0.361	0.534	-0.006	0.055	0.02	0.03	1.84	1.09	11.05	5E-05	3E-04	10.344
AGV-1	0.001	0.036	-0.010	0.063	0.021	0.670	-0.011	0.063	-0.01	-0.06	3.07	-8.45	-0.10	4E-05	3E-04	6.824
AGV-1	-0.026	0.029	-0.093	0.078	-0.079	0.708	-0.068	0.071	0.02	-0.06	2.58	3.61	0.38	4E-05	8E-04	7.025
average	**-0.031**		**-0.060**		**-0.140**		**-0.028**									
2 S.D.	**0.071**		**0.088**		**0.397**		**0.068**									
IF-G	0.683	0.032	0.954	0.100	0.513	0.753	0.270	0.086	0.03	0.01	-0.89	1.40	2.53	4E-05	1E-03	6.587
IF-G	0.638	0.033	0.940	0.067	1.671	0.817	0.302	0.070	0.00	-0.02	-0.33	1.47	2.11	4E-05	-2E-04	6.841
average	**0.644**		**0.926**		**1.126**		**0.282**									
2 S.D.	**0.073**		**0.073**		**1.164**		**0.035**									
HF1	-0.240	0.035	-0.327	0.086	-0.720	0.580	-0.087	0.065	0.01	0.02	0.87	1.36	2.75	5E-05	9E-04	10.202
HF1	-0.240	0.038	-0.321	0.079	-0.096	0.649	-0.080	0.070	0.00	0.00	0.38	1.33	2.99	4E-05	1E-03	6.685
HF1	-0.284	0.050	-0.362	0.081	0.340	0.690	-0.078	0.065	-0.01	-0.05	-0.41	1.27	3.67	4E-05	9E-04	6.630
average	**-0.255**		**-0.336**		**-0.158**		**-0.082**									
2 S.D.	**0.051**		**0.045**		**1.065**		**0.010**									
HF2	-0.321	0.028	-0.448	0.062	-0.975	0.517	-0.127	0.056	0.03	0.02	-0.49	1.40	2.52	4E-05	2E-04	10.199
HF2	-0.302	0.056	-0.411	0.078	-0.534	0.564	-0.109	0.066	-0.03	0.01	-0.22	1.36	2.78	4E-05	7E-04	6.700
HF2	-0.315	0.034	-0.397	0.100	-0.952	0.803	-0.081	0.090	-0.02	0.00	-0.26	1.26	3.88	4E-05	9E-04	6.672
average	**-0.313**		**-0.419**		**-0.820**		**-0.106**									
2 S.D.	**0.019**		**0.053**		**0.496**		**0.046**									
HF3	-0.378	0.047	-0.518	0.074	-1.479	0.918	-0.140	0.061	-0.01	0.08	-9.26	1.37	2.70	4E-05	1E-03	6.111
average	**-0.378**		**-0.518**		**-1.479**		**-0.140**									
2 S.D.	-		-		-		-									
HF4	-0.488	0.035	-0.768	0.057	-1.458	0.544	-0.281	0.050	-0.09	-0.09	7.86	1.57	1.74	4E-05	8E-04	11.190
HF4	-0.494	0.038	-0.757	0.077	-1.224	0.630	-0.264	0.067	-0.04	-0.04	8.69	1.53	1.87	4E-05	1E-03	7.301
average	**-0.491**		**-0.763**		**-1.341**		**-0.272**									
2 S.D.	**0.009**		**0.015**		**0.331**		**0.024**									

Sample	$\delta^{56/54}$Fe	2 S.E.	$\delta^{57/54}$Fe	2 S.E.	$\delta^{58/54}$Fe	2 S.E.	$\delta^{57/56}$Fe	2 S.E.	$^{56/54}$Fe	$^{57/56}$Fe	signal intens.	δ^{57}Fe/δ^{56}Fe	$\delta^{56/54}$Fe/$\delta^{57/56}$Fe	^{54}Cr/^{54}Fe	^{58}Ni/^{58}Fe	^{56}Fe (V)
HF5	-1.120	0.052	-1.696	0.094	-2.447	0.575	-0.578	0.065	0.17	0.06	6.13	1.52	1.94	4E-05	4E-04	10.221
HF5	-1.065	0.043	-1.530	0.079	-1.374	0.893	-0.465	0.060	0.07	0.00	0.68	1.44	2.29	4E-05	3E-04	6.817
HF5	-1.014	0.038	-1.511	0.089	-2.129	0.795	-0.498	0.074	-0.05	0.01	0.29	1.49	2.04	4E-05	6E-04	6.739
average	**-1.066**		**-1.579**		**-1.983**		**-0.514**									
2 S.D.	**0.106**		**0.204**		**1.102**		**0.116**									
HF6	-0.903	0.034	-1.315	0.067	-1.832	0.639	-0.412	0.076	-0.03	0.08	-0.33	1.46	2.19	4E-05	2E-03	6.843
HF6	-0.957	0.044	-1.406	0.106	-1.434	0.722	-0.449	0.101	0.01	0.03	-0.77	1.47	2.13	4E-05	1E-03	6.683
average	**-0.930**		**-1.361**		**-1.633**		**-0.431**									
2 S.D.	**0.076**		**0.128**		**0.564**		**0.052**									
HF7a	-0.522	0.045	-0.725	0.067	-1.379	1.047	-0.203	0.060	0.02	0.06	-2.18	1.39	2.58	4E-05	1E-03	6.279
HF7a	-0.470	0.031	-0.666	0.097	-1.161	0.898	-0.196	0.091	0.00	0.00	-3.56	1.42	2.40	4E-05	9E-04	6.575
average	**-0.496**		**-0.695**		**-1.270**		**-0.199**									
2 S.D.	**0.074**		**0.084**		**0.308**		**0.010**									
HF7b	-0.500	0.038	-0.701	0.084	-1.366	0.764	-0.201	0.084	0.06	0.00	-2.92	1.40	2.49	4E-05	2E-03	6.481
average	**-0.500**		**-0.701**		**-1.366**		**-0.201**									
2 S.D.	-		-		-		-									
OF1	-0.693	0.039	-1.108	0.094	-1.258	0.887	-0.416	0.084	0.03	0.08	-1.04	1.60	1.67	4E-05	1E-03	6.495
OF1	-0.686	0.029	-1.015	0.092	-1.279	0.709	-0.330	0.092	-0.02	-0.01	0.49	1.48	2.08	4E-05	2E-03	6.758
OF1	-0.716	0.043	-1.048	0.078	-1.355	0.769	-0.332	0.071	-0.05	-0.02	0.02	1.46	2.15	4E-05	1E-03	6.753
average	**-0.698**		**-1.057**		**-1.297**		**-0.359**									
2 S.D.	**0.032**		**0.095**		**0.102**		**0.098**									
OF2	-0.713	0.054	-1.076	0.081	-1.495	0.871	-0.363	0.071	-0.05	-0.07	-2.36	1.51	1.96	4E-05	3E-02	6.504
OF2	-0.735	0.037	-1.067	0.104	-1.818	0.962	-0.332	0.100	0.00	0.01	-2.09	1.45	2.21	4E-05	3E-02	6.680
OF2	-0.732	0.046	-1.081	0.078	-1.970	0.811	-0.349	0.074	-0.02	0.02	-1.17	1.48	2.10	4E-05	3E-02	6.731
average	**-0.727**		**-1.075**		**-1.761**		**-0.348**									
2 S.D.	**0.023**		**0.014**		**0.484**		**0.031**									

Sample	$\delta^{56/54}$Fe	2 S.E.	$\delta^{57/54}$Fe	2 S.E.	$\delta^{58/54}$Fe	2 S.E.	$\delta^{57/56}$Fe	2 S.E.	$^{56/54}$Fe	$^{57/56}$Fe	signal intens.	δ^{57}Fe/δ^{56}Fe	$\delta^{56/54}$Fe/$\delta^{57/56}$Fe	^{54}Cr/^{54}Fe	^{58}Ni/^{58}Fe	^{56}Fe (V)
OF 3	-0.660	0.041	-1.005	0.089	-1.913	0.872	-0.345	0.087	0.01	0.04	-4.67	1.52	1.92	4E-05	1E-03	6.554
OF 3	-0.639	0.050	-0.980	0.091	-1.474	0.646	-0.342	0.091	-0.05	-0.07	-3.08	1.53	1.87	4E-05	7E-04	6.651
average	**-0.649**		**-0.993**		**-1.693**		**-0.343**									
2 S.D.	**0.030**		**0.034**		**0.621**		**0.004**									

Session 2

	$\delta^{56/54}$Fe	2 S.E.	$\delta^{57/54}$Fe	2 S.E.	$\delta^{58/54}$Fe	2 S.E.	$\delta^{57/56}$Fe	2 S.E.	$^{56/54}$Fe	$^{57/56}$Fe	signal intens.	δ^{57}Fe/δ^{56}Fe	$\delta^{56/54}$Fe/$\delta^{57/56}$Fe	^{54}Cr/^{54}Fe	^{58}Ni/^{58}Fe	^{56}Fe (V)
HanFe	0.229	0.035	0.347	0.054	0.176	0.564	0.118	0.051	-0.06	-0.07	-0.80	1.51	1.94	5E-05	3E-03	11.278
HanFe	0.239	0.036	0.348	0.069	0.416	0.485	0.109	0.048	-0.02	0.00	-1.55	1.46	2.20	5E-05	2E-03	11.103
HanFe	0.230	0.032	0.308	0.046	0.809	0.564	0.077	0.045	0.00	0.01	-0.66	1.34	2.98	5E-05	2E-03	11.281
average	**0.233**		**0.334**		**0.467**		**0.101**									
2 S.D.	**0.011**		**0.046**		**0.639**		**0.042**									
BHVO	-0.021	0.037	-0.057	0.067	-0.227	0.465	-0.036	0.052	0.05	0.03	2.55	2.71	0.58	4E-05	7E-04	11.606
BHVO	-0.020	0.031	-0.072	0.061	0.132	0.524	-0.053	0.048	0.03	-0.01	2.34	3.66	0.38	4E-05	7E-04	11.346
average	**-0.020**		**-0.065**		**-0.047**		**-0.044**									
2 S.D.	**0.002**		**0.022**		**0.508**		**0.024**									
HF3 HCl	-0.207	0.043	-0.248	0.052	-0.158	0.422	-0.041	0.045	0.07	0.01	-0.40	1.20	5.02	4E-05	3E-04	11.320
HF3 HCl	-0.149	0.031	-0.265	0.067	-0.539	0.643	-0.115	0.060	0.05	0.04	-0.13	1.77	1.29	4E-05	1E-03	11.127
average	**-0.178**		**-0.256**		**-0.348**		**-0.078**									
2 S.D.	**0.081**		**0.024**		**0.539**		**0.105**									
HF4 HCl	-0.250	0.031	-0.344	0.057	-0.253	0.477	-0.093	0.050	0.01	0.03	-0.26	1.37	2.68	4E-05	2E-04	11.349
HF4 HCl	-0.272	0.027	-0.411	0.060	-0.456	0.586	-0.139	0.047	0.03	0.02	-2.09	1.51	1.96	4E-05	5E-04	11.003
average	**-0.261**		**-0.377**		**-0.355**		**-0.116**									
2 S.D.	**0.031**		**0.095**		**0.287**		**0.064**									

	$\delta^{56/54}$Fe	2 S.E.	$\delta^{57/54}$Fe	2 S.E.	$\delta^{58/54}$Fe	2 S.E.	$\delta^{57/56}$Fe	2 S.E.	$^{56/54}$Fe	$^{57/56}$Fe	signal intens.	δ^{57}Fe/δ^{56}Fe	$\delta^{56/54}$Fe/$\delta^{57/56}$Fe	^{54}Cr/^{54}Fe	^{58}Ni/^{58}Fe	^{56}Fe (V)
HF6 HCl	-0.636	0.026	-0.927	0.058	-1.219	0.448	-0.291	0.053	-0.03	0.01	-5.77	1.46	2.19	4E-05	1E-03	10.774
HF6 HCl	-0.731	0.032	-1.103	0.072	-1.201	0.480	-0.372	0.066	0.04	-0.03	-6.62	1.51	1.96	4E-05	4E-04	10.552
average	**-0.684**		**-1.015**		**-1.210**		**-0.332**									
2 S.D.	**0.135**		**0.250**		**0.026**		**0.115**									
HF7a HCl	-0.572	0.033	-0.829	0.056	-1.243	0.405	-0.256	0.046	0.05	0.08	0.14	1.45	2.23	4E-05	7E-04	11.349
average	**-0.572**		**-0.829**		**-1.243**		**-0.256**									
2 S.D.	-		-		-		-									
HF7b HCl	-0.553	0.031	-0.856	0.056	-1.002	0.527	-0.303	0.055	0.06	-0.02	0.22	1.55	1.83	4E-05	5E-04	11.389
average	**-0.553**		**-0.856**		**-1.002**		**-0.303**									
2 S.D.	-		-		-		-									

Session 3

	$\delta^{56/54}$Fe	2 S.E.	$\delta^{57/54}$Fe	2 S.E.	$\delta^{58/54}$Fe	2 S.E.	$\delta^{57/56}$Fe	2 S.E.	$^{56/54}$Fe	$^{57/56}$Fe	signal intens.	δ^{57}Fe/δ^{56}Fe	$\delta^{56/54}$Fe/$\delta^{57/56}$Fe	^{54}Cr/^{54}Fe	^{58}Ni/^{58}Fe	^{56}Fe (V)
ISE921	-0.229	0.035	-0.303	0.066	-0.062	0.535	-0.074	0.064	-0.04	-0.02	-2.03	1.32	3.11	5E-05	3E-03	10.906
ISE921	-0.133	0.031	-0.241	0.059	-0.495	0.629	-0.108	0.054	-0.08	-0.05	-0.85	1.81	1.24	5E-05	3E-03	10.298
average	**-0.181**		**-0.272**		**-0.279**		**-0.091**									
2 S.D.	**0.136**		**0.087**		**0.612**		**0.048**									

8.2 Quality control

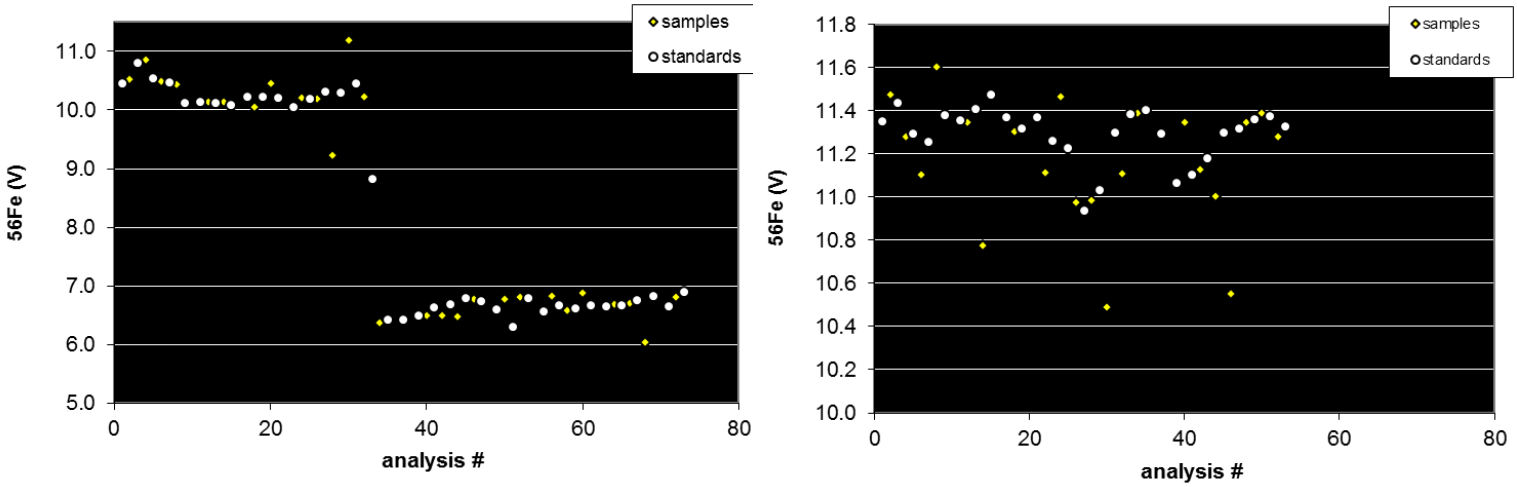

Figure 1: Plot of the ^{56}Fe intensity (V) of standard (IRMM-014) and samples of MC-ICP-MS session 1 (left) and session 2 right). Notice the major drop in intensity of the plasma in session 1 after analysis number 36.

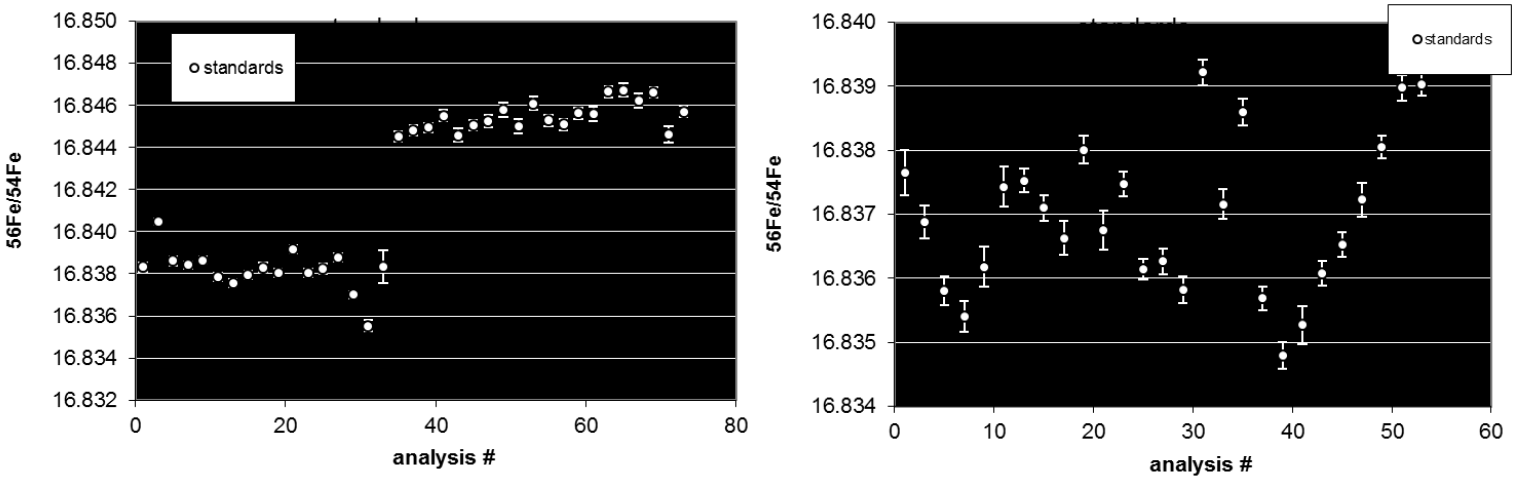

Figure 2: Plot of the ^{56}Fe-^{54}Fe ratio of the bracketing standard IRMM during MC-ICP-MS session 1 (left) and 2 (right). The mass bias drift during session 1 is quite constant, apart from the major shift to higher $^{56}Fe/^{54}Fe$ after analysis number 36; for session 2 the mass bias drift has a higher variability, especially in the middle part of the session. Therefore, all samples of run 2 have been rejected.

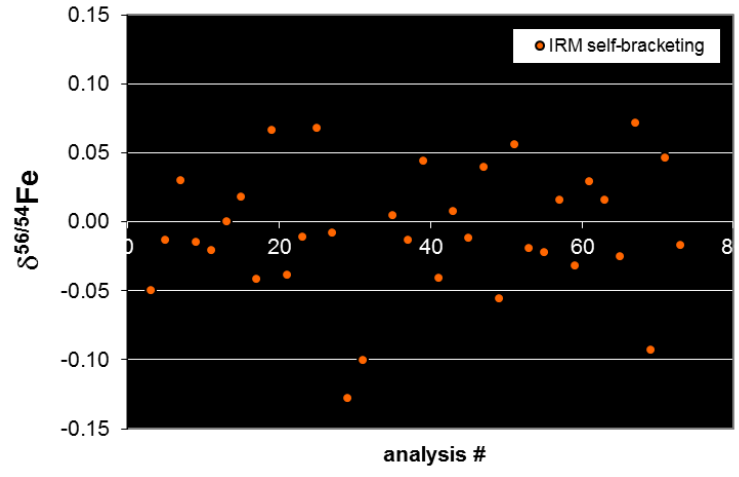

Figure 3: IRMM self-bracketing of MC-ICP-MS session 1.

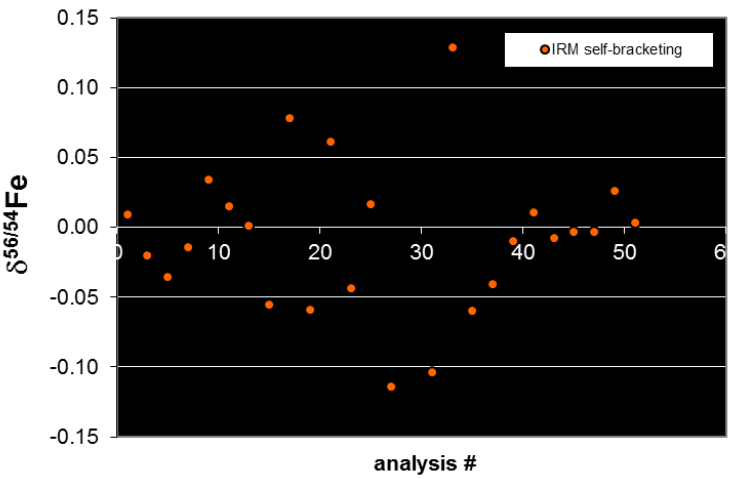

Figure 1: IRMM self-bracketing of MC-ICP-MS session 2.

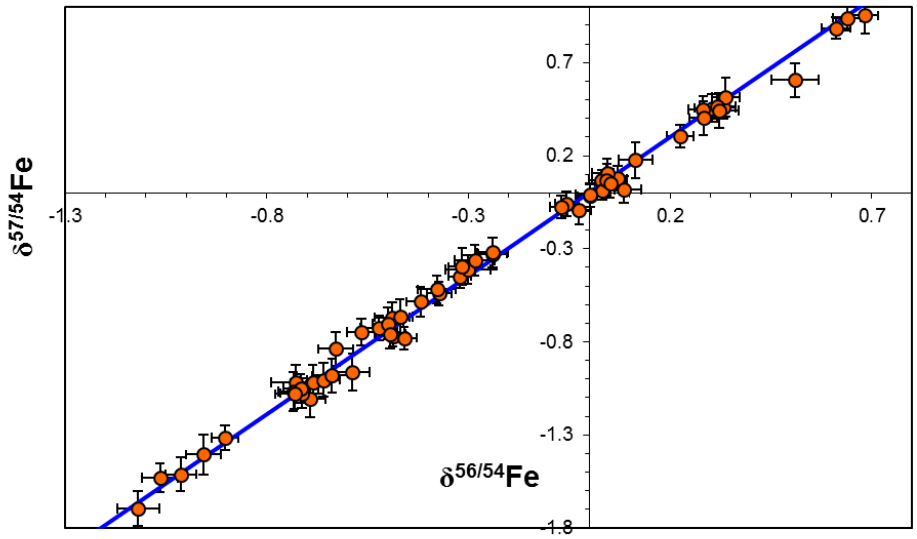

Figure 3: $\delta^{57}Fe$ vs. $\delta^{56}Fe$ plot of MC-ICP-MS session 1 results (3 runs) of samples (HF1-7, OF1-3) and reference materials (BHVO-1, JB-2, AGV-1, IF-G2). Sample that do not overlap the mass dependent fractionation line with their 2 S.D. uncertainty bars have been rejected.

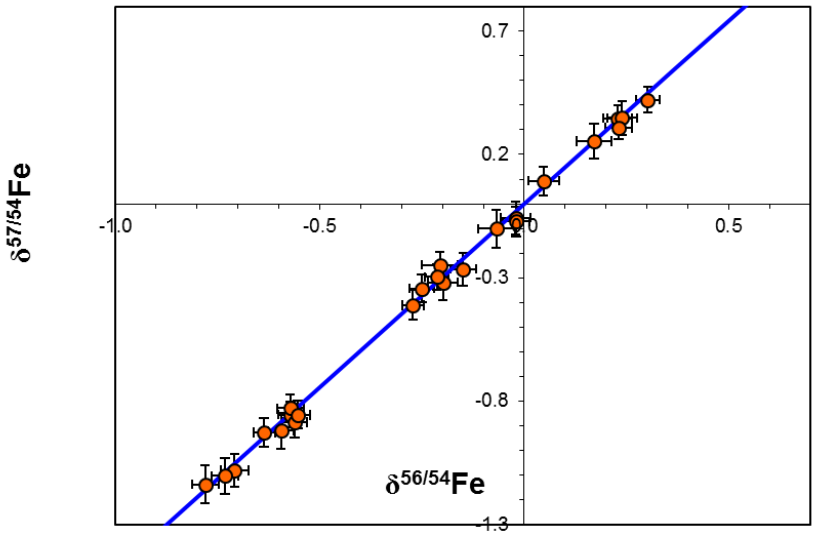

Figure 6: $\delta^{57}Fe$ vs. $\delta^{56}Fe$ plot of MC-ICP-MS session 2 results (3 runs) of samples (HF3, 4, 6 7a and 7b) and reference materials (BHVO-1). Samples that do not overlap the mass dependent fractionation line with their 2 S.D. uncertainty bars have been rejected.